JOURNAL
OF
APPLIED PHYSICS

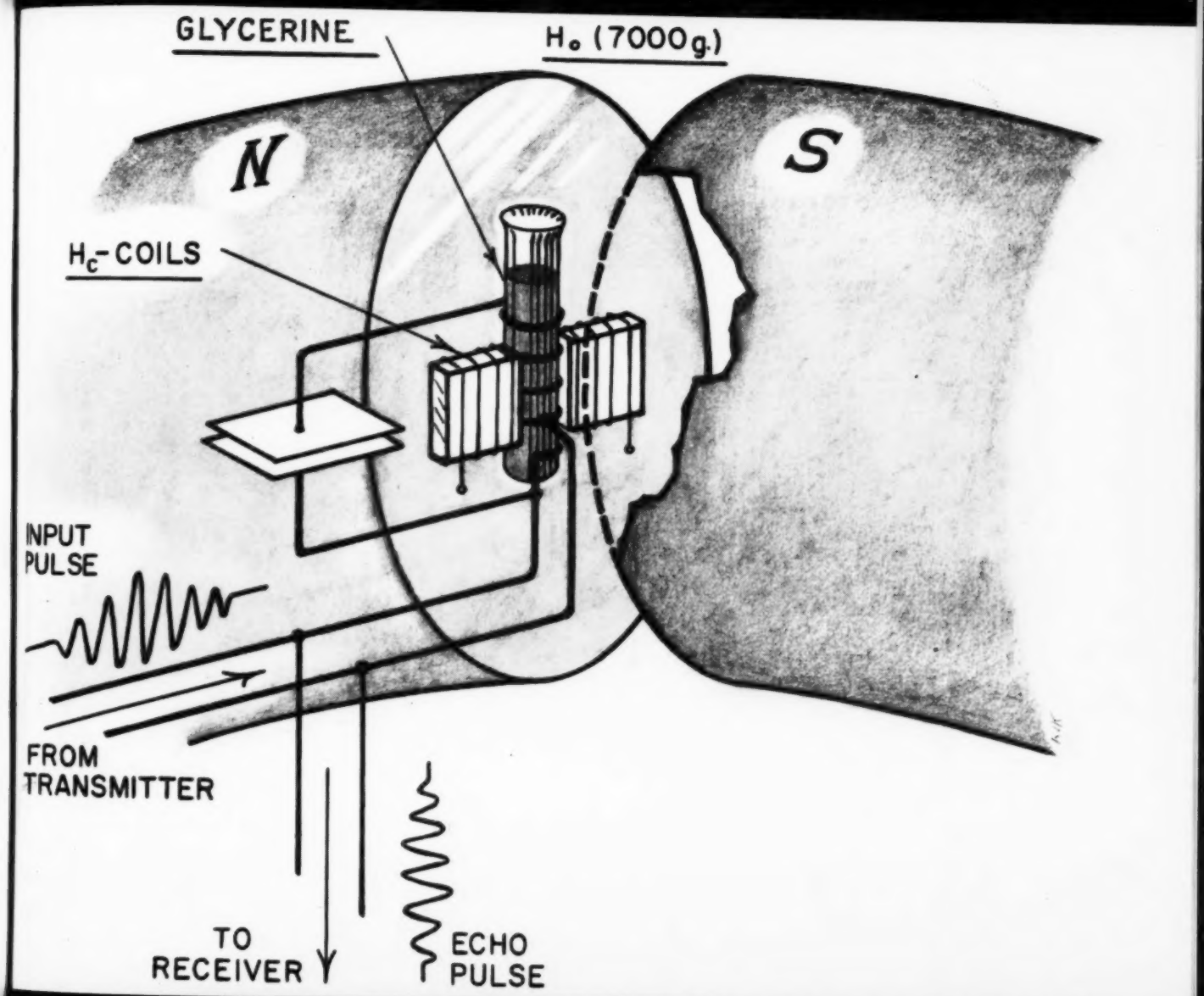

Norelco® X-RAY DIFFRACTION EQUIPMENT GROWS WITH YOUR RESEARCH NEEDS...

This is the fundamental research tool for film recording X-ray analysis. Automatic control provides 50 MA and 60 KVP. Exclusive four-window X-ray tube — *in choice of target materials* — offers multiple sources for operating as many as four cameras simultaneously or any combination of cameras with one or two goniometers — a time-saving feature for advanced techniques or automatic recordings.

Numerous precision built X-ray diffraction cameras are available for a wide range of work. These include two powder cameras, a precision back reflection camera, micro camera, flat plate camera and the new single crystal cylindrical camera, each of which may be mounted on most existing equipment. Additional cameras for special purpose applications are available.

Simply adding a wide range goniometer and the electronic circuit panel forms the basis for diffractometric work in which automatic recordings can be made using a choice of either scintillation, proportional or Geiger detectors.

Addition of the Spectograph further extends the versatility of the apparatus by permitting rapid qualitative and quantitative analyses or determinations of elements present in a sample regardless of free or combined state. High-intensity X-ray tubes and a variety of spectrographic holders are available for use with odd samples in fluorescence analysis studies.

With Norelco X-ray diffraction equipment, you can start with the basic units and build on a piece-by-piece basis, arriving at complete flexibility in techniques of X-ray analysis methods.

A Norelco PRODUCT NORTH AMERICAN PHILIPS COMPANY, INC.

Serving Science and Industry

750 South Fulton Avenue, Mount Vernon, N. Y.

In Canada: Rogers Majestic Electronics Ltd., 11-19 Brentcliffe Road, Leaside, Toronto 17, Ontario

JOURNAL OF APPLIED PHYSICS

Vol. 26, No. 11 NOVEMBER, 1955

In This Issue

Restoration of Resistivity and Lifetime in Heat Treated Germanium . . . R. A. Logan and M. Schwartz 1287

Low Magnetic Saturation Ferrites for Microwave Applications . . . . . L. G. Van Uitert 1289

Small-Angle X-Ray Scattering from Precipitates in Cold-Worked Al-Ag and Al-Zn . . . . . J.-P. Jan 1291

Electrical Analog of the Eddy-Current-Limited Domain-Boundary Motion in Ferromagnetics . . . . . G. Brouwer 1297

Deterioration of Luminescent Phosphors under Positive Ion Bombardment . . . . . J. R. Young 1302

Variation of Elastic Wave Velocity with Frequency in Fused Quartz and Armco Iron . . . . . D. S. Hughes and J. M. Kennel 1307

Ultrashort Light and Voltage Pulses Applied to Silver Halide Crystals by Turbine-Driven Mirror and Spark-Gap Switch . . . . . J. H. Webb 1309

Deformation of an Explosively Loaded Aluminum Single Crystal . . . . . John S. Rinehart 1315

Influence of Pulsed Magnetic Fields on the Reversal of Magnetization in Square-Loop Metallic Tapes . . . . . D. S. Rodbell and C. P. Bean 1318

Spin Echo Serial Storage Memory . . . . . A. G. Anderson, R. L. Garwin, E. L. Hahn, J. W. Horton, G. L. Tucker, and R. M. Walker 1324

Improved Wave Diagram Procedure for Shock Reflection from an Open End of a Duct . George Rudinger 1339

Theory of Remagnetization of Thin Tapes . . . . . H. Ekstein 1342

Reflection of a Compression Wave from a Symmetrical Wedge . . . . . R. W. Skulski and D. Weimer 1344

Theoretical Basis for Measuring the Saturation Emission of Highly Emitting Cathodes under Space-Charge-Limited Conditions . . . . . C. R. Crowell 1353

On the Transient Behavior of Semiconductor Rectifiers . . . . . B. R. Gossick 1356

Photoelectric Yields in the Vacuum Ultraviolet . . . . . W. C. Walker, N. Wainfan, and G. L. Weissler 1366

Some Monte Carlo Calculations of Gamma-Ray Penetrations . . . . . J. F. Perkins 1372

Relative Influence of Majority and Minority Carriers on Excess Noise in Semiconductor Filaments . . . . . Leon Bess 1377

Hysteresis Loops of Mixtures of Ferromagnetic Micropowders . . . . . C. P. Bean 1381

Letters to the Editor:

- Generation of Submillimeter Waves . . . . . H. Motz and K. B. Mallory 1384
- Observations of Cathode Arc Tracks . . . . . H. S. Dunkerley and D. L. Schaefer 1384
- Harmodotron—a Beam Harmonic, Higher-Order Mode Device for Producing Millimeter and Submillimeter Waves . . . . . P. D. Coleman and M. D. Sirkis 1385
- Breakup of Hollow Electron Beams . . . . . H. F. Webster 1386
- Mass Absorption Coefficient of Carbon for CuKα Radiation . . . . . D. R. Chipman 1387
- Effects of Ambient Atmosphere on the Stability of Barium Titanate . . . . . J. R. Anderson, G. W. Brady, W. J. Merz, and J. P. Remeika 1387
- Shot Noise in *p-n-p* Transistors . . . . . G. H. Hanson 1388
- Erratum: Elastic Constants of Germanium between 1.7° and 80°K . . . . . M. E. Fine 1389

Books Reviewed 1389

Books Received 1390

Announcements 1390

Proceedings of the Electron Microscope Society of America 1391

Index to Advertisers xxxii

JOURNAL OF APPLIED PHYSICS

A journal of applications of physics to other sciences and to industry

Published by the

American Institute of Physics

GOVERNING BOARD

Allen V. Astin
Robert F. Bacher
H. A. Bethe
J. W. Buchta
S. A. Goudsmit
Deane B. Judd
Hugh S. Knowles
W. H. Markwood, Jr.
William F. Meggers
Philip M. Morse
Brian O'Brien
Harry F. Olson
R. F. Paton
Eric Rodgers
Ralph A. Sawyer
Frederick Seitz
William Shockley
H. D. Smyth
J. H. Van Vleck
Mark W. Zemansky

OFFICERS AND STAFF

Frederick Seitz
Chairman, Governing Board

Henry A. Barton
Director

George B. Pegram
Treasurer

Wallace Waterfall
Executive Secretary

Theodore Vorburger
Advertising Manager

Ruth F. Bryans
Publication Manager

Edith I. Neftel
Circulation Manager

Kathryn Setze
Assistant Treasurer

Melvin Loos
Consultant on Printing

Editor
Robert L. Sproull

Editorial Board

Maurice A. Biot
Walker Bleakney
Wallace J. Eckert
Elmer Hutchisson
D. O. North
Louis A. Pipes
W. R. Smythe
Arthur V. Tobolsky
A. M. Weinberg

THE JOURNAL OF APPLIED PHYSICS is devoted to the application of physics to other sciences, to engineering, and to industry. Previous to 1937, this journal was called PHYSICS.

The JOURNAL OF APPLIED PHYSICS welcomes articles of two distinct kinds: (1) Descriptions of new results in experimental or theoretical physics which are of general interest to applied physicists. The author should explain his contribution in such a way that a physicist or engineer in another field of specialization can appreciate its objectives and essential features. (2) Critical reviews of particular areas of applied physics. Authors contemplating writing such reviews should correspond with the Editor before they begin writing.

The JOURNAL OF APPLIED PHYSICS welcomes letters to the editor which describe in a few words the content of laboratory reports and theses and which tell readers how they may obtain copies of such reports.

Manuscripts should be submitted to the Editor, Rockefeller Hall, Cornell University, Ithaca, New York. Authors should read the "Information for Contributors," facing page 1 of the January issue, before writing articles or letters. The *Style Manual* of the American Institute of Physics is also helpful to writers preparing manuscripts for journals published by the American Institute of Physics. It can be obtained for $1.00 from the American Institute of Physics, 57 East 55th Street, New York 22, New York.

Corrected proofs and all correspondence concerning papers in the process of publication should be addressed to the Publication Manager, American Institute of Physics, 57 East 55 Street, New York 22, New York.

Subscriptions, renewals, and orders for back numbers should be addressed to the American Institute of Physics, 57 East 55 Street, New York 22, New York.

Subscription Price	U.S. and Canada	Elsewhere
To members of the American Institute of Physics and Affiliated Societies	$10.00	$11.00
To all others	12.00	14.00

Back Number Prices

Yearly back number rate when complete year is available: $15.00.
Single copies: $1.50 each.

Changes of address should be sent to the American Institute of Physics.

Advertising rates supplied on request. Orders, advertising copy, and cuts should be sent to the American Institute of Physics.

Entered as second class matter January 22, 1937, at the Post Office at Lancaster, Pennsylvania, under the Act of March 3, 1879. Accepted for mailing at the special rate of postage provided for in paragraph (d-2), section 34.40, P. L. & R. of 1948, authorized May 2, 1932.

Journal
of
Applied Physics

Volume 26, Number 11 November, 1955

Restoration of Resistivity and Lifetime in Heat Treated Germanium

R. A. Logan and M. Schwartz
Bell Telephone Laboratories, Incorporated, Murray Hill, New Jersey
(Received July 20, 1955)

Experiments are described in which minority carrier lifetime and resistivity of germanium are altered by the addition of copper by diffusion, under conditions where extraneous chemical contamination is minimized. This copper is then gettered by heating the samples in contact with liquid lead or gold, and the resistivity and lifetime are substantially restored. The gettering process in interpreted in terms of the low distribution coefficient of copper in the ternary system which copper and germanium form with the getter.

INTRODUCTION

C. S. FULLER[1] has shown that when metals such as gold, silver, antimony, zinc, and tin are wetted to the surface of a germanium wafer, there is a marked reduction in the copper contamination of the sample in subsequent heat treatment. Furthermore, he has shown that where carrier lifetime was decreased by heat treatment, substantial improvements could be achieved by heating the sample in contact with these metals.

Recently the distribution coefficient of copper (the ratio of concentration in the solid to that in the liquid) was measured[2] in the ternary system which copper and germanium form with several metals. It was found that the distribution coefficient of copper in the ternary system formed with lead and germanium was 6.3×10^{-6} at 700°C for dilute solid solutions. When lead is replaced by tin or indium, this coefficient is reduced by a factor of about 10 and, with gold, the distribution coefficient is reduced by a factor of about 30. This suggests that these elements would be very effective in "gettering" copper out of germanium. The gettering process is, of course, assisted by the fast diffusion of copper in germanium.

The changes in resistivity of germanium which are produced by heat treatment are known[3] to be due primarily to copper that enters the crystal lattice. In addition, copper[4] is known to be a recombination center. However, there are other sources of recombination centers such as nickel,[4] plastic deformation,[5] dislocations,[5,6] or quenched-in imperfections.[7] When lifetime is decreased by heat treatment, it is usually difficult to identify unambiguously, the recombination centers that caused the decrease.

In the experiments described here, it is shown that in germanium, where lifetime and resistivity have been markedly changed by the addition of copper during heat treatment, the crystal can be substantially restored to its original resistivity and lifetime by heating in contact with lead or gold. These results suggest that the same effect might be produced by other metals where the the distribution coefficient of copper in the copper-germanium-metal system is small.

Some of the important characteristics of a liquid gettering agent are the following:

(1) The solubility of germanium in the liquid phase should be low so as to minimize loss of the germanium sample by the alloying. Alternatively, one can overcome this by using alloys of the gettering agent with germanium, which are saturated with germanium at the gettering temperature.

(2) The distribution coefficient for copper in the copper-germanium-gettering agent ternary system should be small.[2]

It is convenient to perform the gettering at temperatures where the diffusion coefficient of copper is suffi-

[1] C. S. Fuller (private communication).
[2] C. D. Thurmond and R. A. Logan, J. Phys. Chem. (to be published).
[3] C. S. Fuller and J. D. Struthers, Phys. Rev. **87**, 526 (1952).
[4] Burton, Hull, Morin, and Severiens, J. Phys. Chem. **57**, 853 (1953).
[5] Pearson, Read, Jr., and Morin, Phys. Rev. **93**, 666 (1954).
[6] R. A. Logan and M. Schwartz, Phys. Rev. **95**, 46 (1954).
[7] R. A. Logan, Phys. Rev. **91**, 757 (1953).

TABLE I.

A. Experiment with lead as gettering agent.

Sample number	Original values prior to experiments $\lvert N_D-N_A\rvert$/cc	τ(μsec)	After copper plating and heating 1 hour at 700°C $\lvert N_D-N_A\rvert$/cc	τ(μsec)	After heating 1 hour at 700°C in contact with lead $\lvert N_D-N_A\rvert$/cc	τ(μsec)
1	$\sim 2\times 10^{12}(N)$	~600	$6.0\times 10^{14}(P)$	8	$3.6\times 10^{13}(P)$	72
2	$\sim 2\times 10^{12}(N)$	~600	$1.6\times 10^{15}(P)$	3	$5.0\times 10^{12}(P)$	86
3	$\sim 2\times 10^{12}(N)$	~600	$1.1\times 10^{15}(P)$	5	$9.0\times 10^{12}(N)$	136

B. Experiment with gold as gettering agent.

Sample number	Original values prior to experiments $\lvert N_D-N_A\rvert$/cc	τ(μsec)	After copper plating and heating 1 hour at 750°C $\lvert N_D-N_A\rvert$/cc	τ(μsec)	After gold plating and heating 1½ hours at 700°C $\lvert N_D-N_A\rvert$/cc	τ(μsec)
1	$\sim 5\times 10^{13}(N)$	~900	$4.5\times 10^{15}(P)$	<1	$3\times 10^{13}(N)$	392
2	$\sim 5\times 10^{13}(N)$	~900	$6.3\times 10^{15}(P)$	<1	...	350
3	Control sample, gold plated and heated 1½ hours at 700°C.					
	$\sim 5\times 10^{13}(N)$	~900	...	...	$6\times 10^{13}(N)$	364
4	Control sample, not plated but heated 1½ hours at 700°C.					
	$\sim 5\times 10^{13}(N)$	~900	...	...	$2.5\times 10^{13}(N)$	20

ciently high so that in a time of the order of minutes, copper will diffuse out of germanium samples of dimensions customarily used in device applications. The diffusion constant of copper in germanium is 2.8×10^{-5} cm²/sec throughout the temperature range 700°C–900°C.[8] Hence at 700°C, for example, the mean diffusion length in one minute is 0.016 in.

EXPERIMENTAL PROCEDURE

The experiments described here were performed at 700°C. Since the solubility of germanium in liquid lead is small (5 atomic percent) at this temperature, only a small amount of lead germanium alloy is formed. Although liquid gold dissolves more germanium (35 atomic percent at 700°C), again, only a small amount of alloy is formed since gold can be electroplated on germanium, and only a thin layer of gold need be used (~0.0001 in.).

The germanium used in these experiments was in the form of rods, about ⅛ in. × ⅛ in. × 1 in., which were cut from crystals having intrinsic room-temperature resistivity and high body lifetime. Resistivity of the rods was measured by the two-point probe technique at dry-ice temperature where there was a negligible contribution to conductivity by thermally generated carriers. The difference between the donor and acceptor concentrations, N_D-N_A, can be then obtained from the resistivity measurement.[9] Lifetimes were measured at room temperature by the method of Haynes and Hornbeck.[10]

After recording the resistivity and lifetime of the experimental samples, a visible, uniform layer of copper was plated on the samples, and they were then heated in a cleaned quartz tube under an atmosphere of helium at 700°C. The quartz was cleaned by soaking for five minutes in 48% HF, rinsing in de-ionized water and heating to the softening point in an oxy-hydrogen flame.

The samples were then lapped to remove any copper-rich phase which formed, and the resistivity and lifetime were measured again. Since the resistivity of the copper-doped rods was low (~1 ohm-cm), the resistivities in this case were measured at room temperature, and N_D-N_A was again calculated.

The next operation was to remove the copper which had been dissolved in the crystal and to observe the effect of this gettering on resistivity and lifetime.

The samples were first cleaned[7] by etching in CP_4 and soaking in an aqueous solution of KCN. The metal which was to act as the gettering agent was next applied to the surface of the sample. Gold was applied by electroplating. Spectroscopically pure lead was applied in the form of wafers of area comparable to a surface of the sample and 0.020 in. thick. The lead wafers were cleaned by etching[11] and soaked in an aqueous solution of KCN. It was not ascertained whether this cleaning of the lead was necessary. However a copper content of 0.005 atom percent in the lead would produce a concentration of 10^{13} per cc in the germanium.[2] The wafer was wetted on the sample by heating the sample and lead on a chemically cleaned molybdenum foil with a Bunsen burner. The molybdenum foil was cleaned by soaking in HCl, rinsing in de-ionized water, then soaking in an aqueous solution of KCN, and finally rinsing again in de-ionized water.

Samples treated in this way were wrapped in chemically cleaned molybdenum foil and sealed in cleaned quartz tubes under an atmosphere of helium. The tubes were heated at 700°C for one to one and one-half hours. The heating time was chosen such that the copper atoms would be able to diffuse to the wafer surface where they would be gettered by the alloyed metal.

After this heating, excess lead was removed by preferential etching,[11] and the alloyed regions were removed by lapping. Resistivity and lifetime were then measured.

[8] Fuller, Struthers, Ditzenberger, and Wolfstirn, Phys. Rev. **93**, 1182 (1954).
[9] M. B. Prince, Phys. Rev. **92**, 681 (1953).
[10] J. R. Haynes and J. A. Hornbeck, Phys. Rev. **90**, 152 (1953).

[11] The lead was etched in one part superoxol (H_2O_2), one part acetic acid, and five parts water.

RESULTS

The results of experiments studying gold and lead as gettering agents are presented in Table I. The impurity concentrations listed in the table are determined from the resistivity measurements.[9] The mark "N" or "P" after the impurity concentration refers to resistivity type of the sample, as determined from the sign of the thermoelectric voltage (thermal probe technique).

CONCLUSIONS

The experiments confirm the remarkable degree to which copper can be extracted from the germanium lattice. The resistivity and lifetime of germanium which is copper doped by heat treatment can be substantially restored by heating in contact with a gettering agent such as lead or gold. These results are in agreement with the earlier results of Fuller.[1] In addition, as observed by Fuller,[1] the presence of a metal such as lead or gold on the germanium surface will reduce or prevent copper contamination during heat treatment.

The present experiments indicate that gold is more effective than lead as a gettering agent. There are possibly two reasons for this. In the first place, the distribution coefficient of copper in dilute solution in the copper-gold-germanium system is 1/30 that in the copper-lead-germanium system. Hence, the level of copper contamination in germanium would be reduced more by gettering with a given amount of gold than by the same amount of lead. Secondly, gold was electroplated over the entire sample whereas lead was only applied to one side of the sample. In the electroplated sample, not only would copper atoms have a shorter distance to diffuse on the average, but the samples would be protected from any copper contaimination present in the heating system. The latter factor is not negligible since the heating procedure used in removing the copper with gold, i.e., heating 1½ hours at 700°C, reduced the lifetime to 20 μsec in a control sample without a getter. In this case, N_D-N_A was essentially unchanged from its original value.

In previous work[6,7] it was shown that germanium samples could be heated at high temperature (~850°C) and yet maintain body lifetime in excess of 100 μsec and alter N_D-N_A by only $\sim 10^{12}$/cc. This required the use of procedures to avoid chemical contamination and plastic deformation. In the present experiments, the electrical characteristics of germanium are altered by diffusing copper into the samples, and are then restored by gettering the copper. Although the resistivity was restored to very nearly its original value, the lifetime never returned to its original high value. This may be due to the small impurity concentration that remained in the samples or may be ascribed to plastic deformation during the heat treatment.

JOURNAL OF APPLIED PHYSICS VOLUME 26, NUMBER 11 NOVEMBER, 1955

Low Magnetic Saturation Ferrites for Microwave Applications

L. G. VAN UITERT
Bell Telephone Laboratories, Murray Hill, New Jersey
(Received June 3, 1955)

Low magnetic saturation ferrites suitable for microwave applications can be prepared in the magnesium aluminum ferrite system. These ferrites can be prepared to possess also relatively high permeabilities at carrier frequencies. Curie temperatures, coercive forces, magnetic saturations at 25°C, and initial permeabilities at 0.1 megacycle/sec for such materials are given.

INTRODUCTION

MAGNESIUM aluminum ferrites have proven to be of considerable utility in nonreciprocal devices operating in the lower microwave region. The decrease of magnetic saturation obtained by substituting aluminum for iron in magnesium ferrite effectively reduces the frequency at which ferromagnetic resonance occurs.[1] Members of this series containing manganese additions and having magnetic saturations up to 1400 gauss have been found to be useful for Faraday rotation applications at 4000 megacycles.[2] A low saturation member (No. 6 in Table I) has been found to possess a relatively narrow ferromagnetic resonance peak as low as 160 megacycles.[3]

PREPARATION OF SAMPLES

Ferrite samples having the compositions listed in Table I were prepared by calcining mixtures of $MgCO_3$, $MnCO_3$, $Al(OH)_3$, and Fe_2O_3 at 1000°C, ball milling, including a binder, pressing, and firing at 1400°C and lower temperatures in oxygen. The 1400°C firing temperature produced near maximum density in the the samples. Density varied from 4.36 to 4.14 grams/cm^3 with increasing aluminum concentration. Samples fired

[1] A. Fairweather *et. al.*, Repts. Phys. Soc. Progr. Phys. **15**, 142–172 (1952).
[2] Van Uitert, Schafer, and Hogan, J. Appl. Phys. **25**, 925–926 (1954).
[3] Suhl, Van Uitert, and Davis, submitted to J. Appl. Phys.

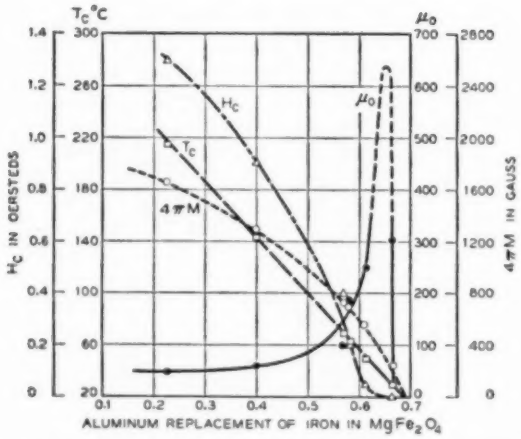

FIG. 1. Magnetic properties as a function of aluminum content.

at 1350°C and lower temperatures did not achieve these densities.

DISCUSSION

Those applications of ferrites which utilize circumferential components of magnetization to obtain resonance isolation such as the ferrite helices in traveling wave tube applications,[4] require the use of materials which possess reasonably high dc permeabilities. The samples fired at 1400°C maintain a relatively high value of permeability, as shown in Table I and Fig. 1. In this case, permeability at first drops as the aluminum content is increased and then, beyond 0.2 aluminum, increases to 300–600 in the compositions whose Curie temperatures are just above room temperature. In less dense magnesium aluminum ferrites, obtained by firing at 1350°C and lower, the permeabilities of the materials were found to vary from about 40 in magnesium ferrite to very low values with the increase of aluminum content. Measurements made by J. S. Cook[5] of these Laboratories using a helix made from a high density material having a low frequency permeability of 100 and a magnetic saturation ($4\pi M$) of 900 gauss, show that these low magnetic saturation ferrites have sufficient dc permeability to enable them to be successfully used in helical form for ferromagnetic resonance isolation applications below 1000 megacycles.

In Table I, the values at 25°C of the initial permeabilities (μ_0) at 0.1 megacycle, coercive forces (Hc) in oersteds, and magnetic saturation ($4\pi M$) in gauss for the materials fired at 1400°C are listed. The Curie temperatures (Tc) in degrees centigrade and the densities (D) in grams per cubic centimeter for these samples are also given.

The dc resistivities of these materials all lie in the vicinity of 10^{10} ohm-centimeters.

[4] Cook, Kompfner, and Suhl, Proc. Inst. Radio Engrs. **42**, 1188 (1954).

[5] Unpublished results.

TABLE I. Composition.

No.	Mg	Al	Fe	Mn	$4\pi M$ gauss	Tc °C	Hc oersteds	$\mu 0$	D g/cm³
1	1.143	0.229	1.771	0.114	1660	215	1.30	48	4.36
2	1.143	0.400	1.600	0.114	1280	145	0.90	54	4.30
3	1.180	0.572	1.428	0.118	734	70	0.40	100	4.20
4	1.098	0.583	1.417	0.121	700	64	0.21	190	4.20
5	1.075	0.624	1.376	0.118	542	51	0.06	250	4.16
6	1.042	0.676	1.324	0.120	270	30	0.002	302	4.14

The compositions listed in Table I are calculated so that the sum of the trivalent ions of aluminum and iron equals two in accordance with the equation for magnesium aluminum ferrites $Mg_{1.0}Al_xFe_{2-x}O_4$. In Fig. 1, the physical properties of the compositions given in Table I are plotted *versus* their listed aluminum contents. In this treatment the essentially fixed amount of manganese present is considered to contribute to the properties of the samples in a consistent way, and the magnesium present in excess of the amount required to combine with the other elements present to form spinel-type structures is treated as a second phase. The validity of this treatment of the data is supported by the fact that the Curie temperatures of the material are a linear function of the aluminum content. This is the one function plotted that may be expected to be unifluenced by the amount of nonmagnetic second phase present.

The curve for μ_0 is estimated to peak between compositions 5 and 6 at over 600, since μ_0 for the sample on the high aluminum content side of it (No. 6) is increased to 620 by decreasing the temperature of measurement to 20°C, and μ_0 for the sample on the low side of it (No. 5) is increased to 660 by increasing the temperature of measurement to 40°C. Thus it is indicated that a peak of comparable height lies between them at 25°C, the temperature at which the remaining data were obtained.

The magnetic saturation values are reduced by the fraction of second phase present. Coercive force is increased and initial permeability decreased much more significantly by the presence of a second phase. The third composition listed in Table I has the largest amount of excess magnesium present. In the figure it can be seen that Hc is higher and μ_0 lower than would otherwise be expected for this sample.

The low level of coercive force obtained in the range of the initial permeability peak indicates that crystal anisotropy is quite small, if not zero, in this vicinity.

ACKNOWLEDGMENTS

The author wishes to thank J. H. Scaff and F. Schnettler for constructive comments on the text; F. J. Dempsey and C. E. Hedden for making measurements; and F. Swanekamp for preparing the materials.

Small-Angle X-Ray Scattering from Precipitates in Cold-Worked Al-Ag and Al-Zn

J.-P. JAN*
Department of Physics, University of Illinois, Urbana, Illinois
(Received April 2, 1955)

A study of aging in cold-worked Al–Ag and Al–Zn alloys during the first stage of precipitation was made, by means of small-angle x-ray scattering. (a) The rate of growth of the Ag or Zn clusters was very little affected by cold-work. (b) Evidence was found that the amount of clustered solute is not altered by aging. (c) The clusters were deformed by cold-work, giving rise to an anisotropic small-angle scattering. This cannot be explained by large amounts of glide taking place in a limited number of slip planes, but rather speaks in favor of zones of homogeneous deformation. The deformation of precipitated particles by cold-work is a new and powerful means of investigating the mechanism of plastic deformation in the interior of a material.

1. INTRODUCTION

IT is widely accepted today that precipitation in Al–Ag alloys occurs in two distinct stages. In the first stage or pre-precipitation, the alloy contains zones of spherical symmetry, rich in solute atoms, and coherent with the parent matrix. At least 50% of the silver, and possibly all the silver, is already clustered after quenching from the equilibrium solid solution. On annealing, the zones grow in size, but after a certain time depending on the temperature, there is a transition to a second stage of precipitation: the precipitate then consists of platelets of hexagonal structure, parallel to the (111) planes of the parent matrix. The behavior of Al–Zn is about the same. These views are supported by numerous experiments and theoretical studies, among others those by Guinier,[1–3] Walker and Guinier,[4] Belbeoch and Guinier,[5] Köster *et al.*,[6–10] Hirano,[11] even though an x-ray investigation, carried out by Geisler and Hill,[12] led to different conclusions, which will not be discussed here.

The present study deals with two different effects of cold-work. The first one concerns the rate of precipitation, about which there are few experimental data: Gayler[13] and Graf and Guinier[14,15] found that plastic deformation increases the rate of precipitation in Al–Cu. The importance of the effect was emphasized by Seitz.[16]

The second one is the deformation of the precipitate particles by cold-work, which was clearly demonstrated by the small-angle x-ray scattering technique used in particle-size determination. It is a new effect and brings valuable information on the mechanism of plastic deformation.

2. PREPARATION OF THE SAMPLES

The alloys were prepared according to the technique described by Ellwood.[17] High-purity materials were melted in an alumina crucible at 750°C, stirred several times and cast into a cylindrical graphite mold. A rod was machined, which was submitted to a homogenization heat-treatment, consisting of repeated cycles of annealing and cold-work by swaging, and controlled by metallographic examination.

The composition, determined from the weight of the constituents before melting, was 10 and 30% Ag or Zn in weight. The samples were usually foils near the optimum thickness for x-ray transmission, i.e., 0.05–0.10 mm depending on the composition. The final thickness was obtained either directly by cold-rolling or by etching. A solution of NaOH 3N followed by conc. HNO_3 was the most suitable etchant.

Polycrystalline samples were used, unless otherwise specified. A few single crystals were grown by the strain-anneal method.

3. X-RAY SMALL-ANGLE SCATTERING UNIT

The unit is shown on Fig. 1. The source was a General Electric CA–7 x-ray tube with line focus and Cu target. The radiation was monochromatized by a Johann-Johansson bent quartz crystal, which gave a good separation of the K_α doublet. It was even possible, by careful adjustment, to reflect one of the components only and obtain a sharper focus.

The detector was a film (in front of which a Cu strip absorbed the main beam) or a Geiger counter, placed at the focus of the monochromator, at 8 cm from the sample. It was mounted on an arm which could rotate about a vertical axis passing through the sample. A motor driven screw moved a carriage which controlled

* Now at the National Research Council of Canada, Ottawa, Canada.
[1] A. Guinier, Z. Metallkunde **43**, 217 (1952).
[2] A. Guinier, Métaux, corrosion, usure **18**, 209 (1943).
[3] A. Guinier, Acta Cryst. **5**, 121 (1952).
[4] C. B. Walker and A. Guinier, Acta Metallurgica **1**, 568 (1953).
[5] B. Belbeoch and A. Guinier, Compt. rend. **238**, 1003 (1954); Acta Metallurgica **3**, 370 (1955).
[6] W. Köster and F. Braumann, Z. Metallkunde **43**, 193 (1952).
[7] Köster, Steinert, and Scherb, Z. Metallkunde **43**, 202 (1952).
[8] Glocker, Köster, Scherb, and Ziegler, Z. Metallkunde **43**, 208 (1952).
[9] G. Ziegler, Z. Metallkunde **43**, 213 (1952).
[10] U. Dehlinger and H. Knapp, Z. Metallkunde **43**, 223 (1952).
[11] K. Hirano, J. Phys. Soc. Japan **8**, 603 (1953).
[12] A. H. Geisler and J. K. Hill, Acta Cryst. **1**, 238 (1948).
[13] M. L. V. Gayler, J. Inst. Metals **72**, 543 (1946).
[14] R. Graf and A. Giunier, Compt. rend. **238**, 819 (1954).
[15] R. Graf and A. Guinier, Compt. rend. (Paris) **238**, 2175 (1954).
[16] F. Seitz, Advances in Physics **1**, 43 (1952).
[17] F. C. Ellwood, J. Inst. Metals **80**, 217 (1952).

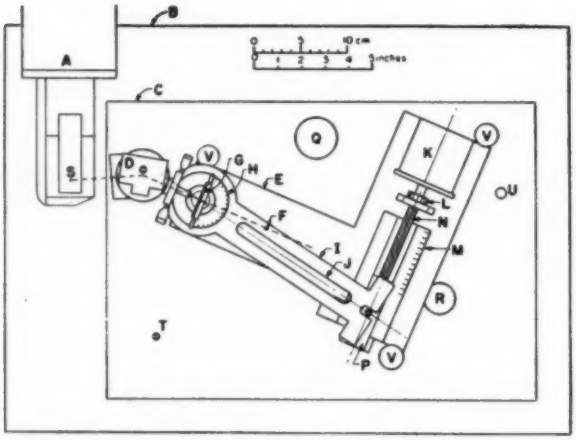

FIG. 1. Schematic diagram of the small-angle scattering unit. (A) X-ray tube; (B) brass base plate; (C) limit of the area enclosed by the helium box; (D) crystal-holder; (E) base of the camera; (F) focus; (G) sample-holder; (H) graduated circle to measure angle btw. sample and beam; (I) rotating arm; (J) slot for film-holder or Geiger counter; (K) electric motor; (L) micrometer; (M) scale to measure the translation of the carriage; (N) screw to control the motion of the carriage; (O) center of the reflecting crystal; (P) carriage; (Q) Kovar seals and O-ring gasket for electrical connections; (R) high voltage Kovar seal for Geiger counter; (S) x-ray source; (T) helium inlet; (U) helium outlet; (V) leveling screws for camera. The rotating arm is shown at 10° from its normal position; the supports for the crystal-holder, the film-holder and the Geiger counter are not represented.

the rotation of the arm. The translation of the carriage was measured by a pointer moving along a scale and a micrometer. The sample-holder could rotate, its position being determined by a graduated circle.

The x-ray beam was collimated by two vertical slits, and its angular width was 10 ft only, to reduce the scattering from the crystal itself; in this way, the small-angle scattering could be measured at 30 ft to the main beam.

Monochromator, sample, and detector were shielded which lead and enclosed in a box which could be filled with helium: this gas gives a negligible scattering.

Some measurements were made with a special camera, consisting of pinholes aligned with the x-ray source, and of a film-holder. White radiation was used. This setup had cylindrical symmetry, which was not the case for the monochromator and slit system, and was used to detect small anisotropies.

4. METHOD TO MEASURE THE PARTICLE SIZE

Guinier[18] calculated the intensity scattered at a small angle ϵ by a dilute system of N identical particles randomly oriented:

$$I = Nn^2 \exp\left(-\frac{4\pi^2 R^2 \epsilon^2}{3\lambda^2}\right), \tag{1}$$

where I is measured in electron units; n is the number of electrons per particle; λ is the wavelength of the radiation; R is a length called the *radius of gyration* of a particle; it is defined by:

$$R^2 = \frac{1}{n}\int \rho r^2 dV, \tag{2}$$

integrated over the particle; r is the distance from the electronic center of gravity to the volume element dV; ρ is the electronic density (number of electrons per unit volume). A homogeneous sphere of radius a has a radius of gyration

$$R = a\sqrt{\frac{3}{5}}. \tag{3}$$

The standard way of determining the radius of gyration consists of plotting log I *vs* ϵ^2, determining the slope of the straight line obtained, and using formula (1). In our case, unfortunately, the system of particles was not dilute, and, in cold-worked samples, the zones were not randomly oriented. The interpretation of the patterns was more complicated and will be described now.

A non-cold-worked sample, immediately after quenching from the solid solution, furnishes a ring pattern [Fig. 2(a)], which is explained by Walker and Guinier[4] in the following manner. During quenching, the solute atoms diffuse to form clusters, and they leave

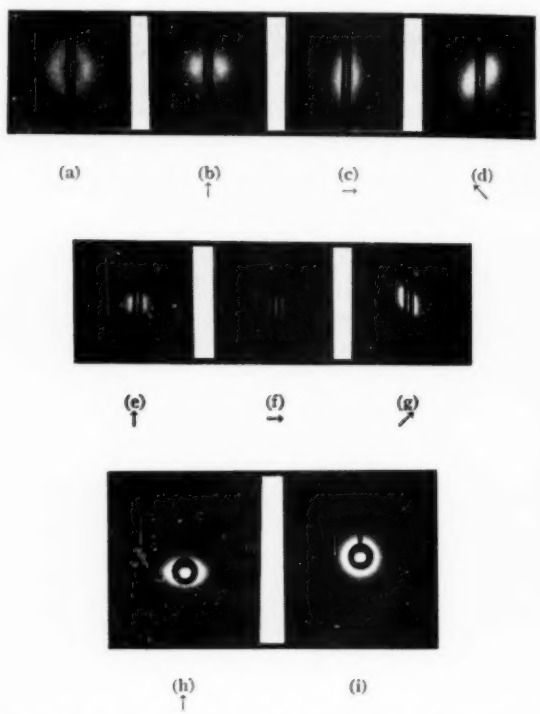

FIG. 2. Effect of cold-work on the small-angle x-ray scattering from quenched Al–Ag (30 wt %) samples; (a)–(g) Cu$K\alpha$ radiation; (a) before cold-work; (b)(c)(d) after 50% reduction in cross section by cold-rolling in the direction of the arrow; (e)(f)(g) after 95% cold-rolling; (h)(i) white Cu radiation and pinhole collimator; (h) polycrystal after 50% cold-rolling in the vertical direction; (i) single crystal before cold-work.

[18] A. Guinier, Ann. phys. **12**, 161 (1939).

behind them an impoverished shell. The scattering intensity can be described by the formula

$$I=Nn^2\left[\exp\left(-\frac{2\pi^2R^2\epsilon^2}{3\lambda^2}\right)-\exp\left(-\frac{2\pi^2R'^2\epsilon^2}{3\lambda^2}\right)\right]^2 \quad (4)$$

where n is now the number of excess electrons in one cluster (excess above the number of electrons in an equal volume filled with the average density) and is also the number of electrons missing in the shell; R and R' are the radii of gyration of the clusters and of the surrounding shells respectively. The intensity distribution calculated from (4) agrees well with the observed one. For large angles (larger than the angle corresponding to the maximum intensity), the second exponential can be neglected because $R'>R$, and (4) reduces to (1). The radii of gyration R of the clusters can therefore be determined in the standard way if the large angles only are taken into account.

The values of R obtained thus should be considered as an average size of the clusters, which certainly have different radii: as a matter of fact, the log I *vs* ϵ^2 curves showed departures from the linearity.

Another complication arises in the cold-worked samples only. The clusters formed during quenching are already present before cold-work. After cold-rolling, the small-angle scattering depends on the orientation of the sample (Fig. 2). The clusters have been deformed and possess a common orientation. If we represent them by an *average ellipsoid* of principal axes a,b,c, we can define three principal "radii of gyration"

$$R_X=a\sqrt{\frac{3}{5}},\quad R_Y=b\sqrt{\frac{3}{5}},\quad R_Z=c\sqrt{\frac{3}{5}}. \quad (5)$$

OY is perpendicular to the plane of rolling, and OZ is the rolling direction. Figure 3 shows how R_X and R_Z were determined, with the rolling direction respectively parallel and perpendicular to the slits of the collimator. The scattered intensity was measured along Ox on the x-ray film. R_Y cannot be measured directly, because the plane of the sample should then be parallel to the x-ray beam. It can be determined indirectly by orienting the sample at an angle to the x-ray beam. If the rolling

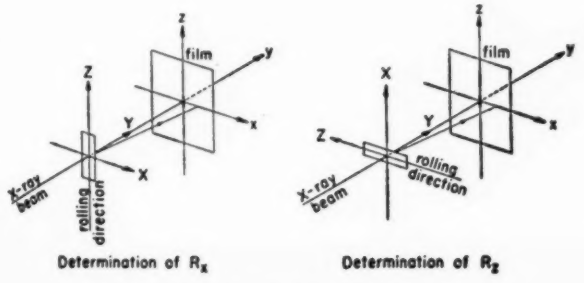

FIG. 3. Orientation of a cold-worked sample for determining the radii of gyration.

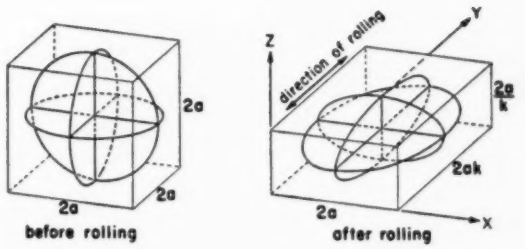

FIG. 4. Average effect of cold-rolling on the Ag or Zn zones in the first stage of precipitation.

direction is vertical, the same as for the determination of R_X (Fig. 3), but if the plane of rolling is at 45° to the x-ray beam, a quantity R_i is measured, from which R_Y can be calculated by means of the relationship

$$R_i^2=\tfrac{1}{2}(R_X^2+R_Y^2). \quad (6)$$

A more precise mathematical formulation of the anisotropic scattering is given in Appendix.

5. EXPERIMENTAL RESULTS

A. Anisotropy Produced by Cold-Work

(1) The average effect of cold-work on the shape of the clusters is an elongation in the rolling direction and a flattening perpendicular to the plane of rolling, the third dimension and the volume remaining unchanged (Fig. 4):

$$R_X=R;\quad R_Y=\frac{R}{k};\quad R_Z=kR. \quad (7)$$

R is the radius of gyration before cold-work, and R_X, R_Y, R_Z, are the principal radii of gyration after cold-work. The quantity

$$k=\frac{R_Z}{R_X} \quad (8)$$

measures the deformation; we call it the *anisotropy ratio*. In a typical case, $R=11.4$ A, $R_X=11.0$ A, $R_Y=9.0$ A, $R_Z=14.1$ A, $R^3=1480\cong R_XR_YR_Z=1400$.

(2) The anisotropy ratio is an increasing function of the amount of cold-work, but it is smaller than the elongation produced by cold-rolling (Table I, Fig. 5).

(3) In the course of aging following cold-work, R_X and R_Z tend to become equal (Table II). The anisotropy is created by cold-work, but the subsequent growth of the clusters tends to make them isotropic.

B. Rate of Precipitation

The samples were always submitted to cold-work immediately after quenching from the solid solution. They were aged simultaneously with non-cold-worked samples, x-ray pictures being taken in the course of aging. The results are shown in Table II. Al-Zn ages more rapidly than Al-Ag. The aging of the Al-Ag at

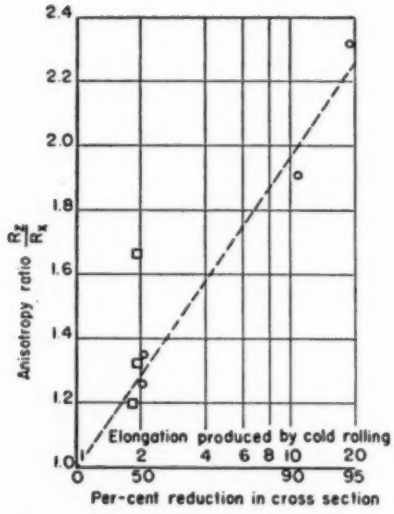

FIG. 5. Anisotropy of the Ag or Zn zones for various amounts of cold-work.

room temperature is very slow, but detectable after several months.

The size of the clusters in the cold-worked samples is described by three numbers, R_X, R_Y, R_Z. To compare them with the non-cold-worked ones, R_X must be used, according to Sec. 5A. Table II shows that the particle-size is slightly smaller in the cold-worked samples (Fig. 6), except for Al–Zn aged 8 hours at 100°C.

C. Amount of Clustered Solute

Evidence was found that the amount of clustered solute remains unchanged in the course of aging. This confirms the view supported by Walker and Guinier[4] that, in Al–Ag, most of the silver is clustered already right after quenching.

The optical density δ_0 of the films corresponding to zero angle was determined by extrapolation and reduced to equal exposure times; δ_0 is a relative measure of N_0n^2, as shown by formula (1), if the adjustment of the camera, the irradiated area on the sample and the conditions of development of the film remain the same. N_0 is the number of clusters per unit volume. Assuming also

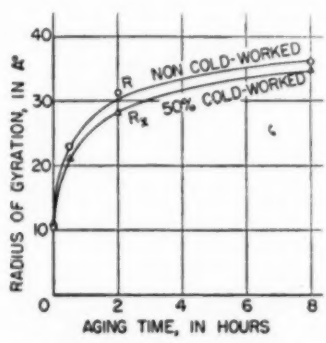

FIG. 6. Increase in size of the Ag clusters in Al—30 wt % Ag aged at 160°C.

that the number of electrons per particle, n, is proportional to the third power of the radius of gyration, R^3, we can write the following proportionalities:

$$\delta_0 \sim N_0 n^2; \quad \frac{\delta_0}{R^3} \sim N_0 n; \quad \frac{\delta_0}{R^6} \sim N_0. \tag{9}$$

Table III shows that, in spite of all the experimental errors linked to such a determination, N_0n rather than N_0n^2 or N_0 remains of the same order of magnitude in the course of aging. The number of clusters per unit volume decreases, but their total mass remains constant.

6. DISCUSSION AND CONCLUSIONS

A. Rate of Precipitation

The first stage of precipitation in Al–Ag and Al–Zn should be considered as a rearrangement of the clustering, with an increase of the average size of the clusters and a decrease of their number, rather than a nucleation and growth of particles from a homogeneous matrix, which becomes progressively depleted. Our results show that, in most cases, cold-work slows down very slightly the growth of the zones. Plastic deformation creates vacancies, which should favor diffusion, and also dislocations, which might hinder it by trapping solute atoms, the latter effect being larger than the former. A study of the second stage, which is more like the precipitation in Al–Cu mentioned in the introduction, might well lead to a different result, but the cluster size would then be more difficult to estimate.

TABLE I. Effect of the amount of cold-work on the anisotropy ratio.

Alloy	Percent reduction in cross section	Anisotropy ratio $k=R_Z/R_X$
Al—30 wt % Zn	46	1.20
30 wt % Zn	48	1.32
30 wt % Zn	48	1.66
Al—30 wt % Ag	52	1.35
30 wt % Ag	51	1.26
30 wt % Ag	91	1.91
30 wt % Ag	95	2.32

B. Anisotropy Effect

An explanation of the effect must be based on an atomic mechanism of plastic deformation. In fact, the clusters cover only a few lattice spacings, and plastic deformation in a metal is not homogeneous.

Experiments show that glide is restricted to certain regions, which appear on the surface of a plastically deformed sample as visible *slip bands*. Each slip band can be resolved into *slip lines* by the electron microscope as found by Heidenreich and Shockley,[19] Brown,[20]

[19] R. D. Heidenreich and W. Shockley, Bristol Conference on Strength of Solids (1947), p. 57.
[20] A. F. Brown, Advances in Physics 1, 427 (1952).

Kuhlmann-Wilsdorf and Wilsdorf,[21] and Noggle.[22] Kuhlmann and Wilsdorf[21] found that the spacing between slip lines on pure aluminum is 400 A on the average, each slip line corresponding to an amount of glide varying from 0 to 1200 A, with an average of 300–400 A.

The connection between the surface observations and the internal mechanism is still a matter of discussion. Let us assume that each slip line corresponds to one slip plane and that the above figures are valid for our alloys. Some of the spherical clusters would be cut by a glide plane; they become two distinct clusters, because the glide distance is much larger than their diameter. Most of them would be untouched, because their size is much smaller than the distance between two glide planes. If this were true, the majority of the clusters would remain spherical, and the average anisotropy effect should be very small; it should even be contrary to the one we observe as shown in Appendix.

The discrete distribution of the glide planes assumed here is therefore in contradiction with the experimental results. On the other hand, these would be readily explained if each slip line corresponded to a layer of homogeneous deformation in the interior of the material. This view is supported experimentally by Fujita, Suzuki, and Yamamoto,[23] and theoretically by H. and T. Suzuki,[24] who imagined a dislocation mechanism somewhat analogous to the one used to describe twinning. Twinning itself could explain the observations, but it would be very unlikely to occur in a face-centered cubic crystal.

Another possibility would be a nonsphericity of the clusters before cold-work; plastic deformation would give rise to a preferred orientation. Walker and Guinier[4] found that a single crystal of Al–Ag produces a small-angle scattering which does not depend on its orientation. We even found that the scattering from a polygonized single crystal of Al–Ag is also isotropic. Although this does not prove directly the sphericity of each individual cluster, it speaks in its favor.

In conclusion, the results constitute evidence that plastic deformation in Al–Ag and Al–Zn takes place by zones of homogeneous deformation rather than large amounts of glide in a limited number of glide planes. Experiments on single crystals deformed in tension and single slip could show if there is a simple orientation of the elongated clusters with respect to the lattice, and tell us whether glide or twinning is operative. Preliminary experiments, done on Al—10 wt % Ag single crystals, grown from a wire, showed that an extension produced an elongation of the clusters in the direction of tensile stress.

The anisotropy effect is a powerful tool for direct investigation of the mechanism of plastic deformation. The particles of precipitate in an age-hardening alloy are agents giving information about what is going on in the *interior* of the material. For instance, the precipitates of the second stage in Al–Ag, platelets parallel to the (111) planes, could be used; the way they change their orientation in a deformed crystal could tell us if there is single or double slip. The zones of the first stage are particularly favorable, because they cause little distortion of the lattice; Al and Ag have almost the same atomic radius, and the Ag atoms remain at the nodes of the Al lattice. The method can in some cases be used for nonmetals. Rohloff[25] deformed silver chloride containing spherical colloidal particles of silver, and studied their deformation by means of optical methods. Rohloff's anisotropy results are in agreement with the data described here.

TABLE II. Experimental results on aging.

Aged during	Non-cold-worked R, in A	Cold-worked Rx	Cold-worked Rz	Percent reduction in cross section
Al—30 wt % Ag aged at room temperature				
0	9.8	10.3	13.8	52
3 months	10.3	...	...	
7 months	11.4	11.0	14.1	
Al—30 wt % Ag aged at 160°C				
0	10.5	11.2	...	50
30 min	23.3	21.1	...	
2 hours	31.5	28.2	...	
8 hours	36.3	34.8	...	
24 hours	the second stage appears			
Al—30 wt % Zn aged at room temperature				
0	16.3	18.7	24.6	48
8 months	28.8	29.3	...	
Al—30 wt % Zn aged at 100°C				
0	18.3	17.1	28.3?	48
30 min.	24.9	21.1	24.5	
2 hours	28.1	26.4	28.2	
8 hours	36.8	37.5	37.9	
24 hours	too large to be measured			
Al—30 wt % Zn aged at 160°C				
0	17.0	17.2	20.7	46
30 min.	37.7	34.5	34.2	

TABLE III. Estimate of the relative density of clusters Al—30 wt % Ag aged at 160°C. Arbitrary units.

Time	$\delta_0 \sim N_0 n^2$	$\frac{\delta_0}{R^3} \sim N_0 n$	$\frac{\delta_0}{R^6} \sim N_0$
0	20	175	1490
30 min	113	90	71
2 hours	330	105	34
8 hours	632	132	26

[21] D. Kuhlmann-Wilsdorf and H. Wilsdorf, Acta Metallurgica 1, 394 (1953).
[22] T. S. Noggle (to be published).
[23] Fujita, Suzuki, and Yamamoto (to be published).
[24] T. Suzuki, Science Repts. Tôhoku Univ. **6**, 309 (1954); H. Suzuki, (to be published).
[25] E. Rohloff, Z. Physik **132**, 643 (1952).

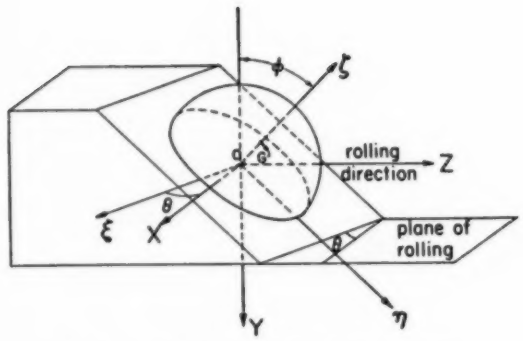

FIG. 7. Radii of gyration of a half-sphere.

7. ACKNOWLEDGMENTS

This work was supported by the U. S. Office of Ordnance Research, the "Bourse Félix Bonjour" of the University of Lausanne, Switzerland, and the "Kommission zur Förderung der wissentschaftlichen Forschung für Arbeitsbeschaffung," Switzerland.

The author wishes to express his gratitude to Professor J. S. Koehler, who directed this work, supplying many leading ideas and criticising thoroughly any argument or reasoning to the greatest benefit of the experiments, to Professor A. Guinier, for his help and his kind interest in this research, to Dr. H. Lambot, Dr. C. B. Walker, Dr. A. Kelly, and Mr. T. S. Noggle for their valuable comments and suggestions, and to all those who collaborated in making this work possible.

APPENDIX

In order to calculate the small-angle scattering from a distribution of homogeneous half-spheres with various orientations, we need first the scattering from a single half-sphere. According to Guinier[18] the radius of gyration $R_{\mathbf{i}}$ in the direction of a unit vector $\mathbf{i}$ is given by

$$R^2_{\mathbf{i}}=\frac{3}{n}\int \rho(\mathbf{i}\cdot\mathbf{r})^2 dV, \tag{9}$$

of which (2) is an average for random orientation of the particles. It is convenient to calculate the integral in a coordinate system in which the half-sphere is symmetrically oriented (Fig. 7). The angle between the normals to the glide plane ($O\zeta$) and to the plane of rolling (OY) is φ. The intersection $O\xi$ between the glide plane and the plane of rolling is at an angle θ to the axis OX (OX is perpendicular to the rolling direction OZ in the rolling plane). The radius vector $\mathbf{r}$ has its origin at the electronic center of gravity G of the half-sphere. If a is the radius of the sphere:

$$\mathbf{OG}=\left(0,0,\frac{3a}{8}\right);\ \mathbf{r}=\left(\xi,\eta,\zeta-\frac{3a}{8}\right);\ n=\frac{2}{3}\pi\rho a^3. \tag{10}$$

The unit vectors along OX and OZ are

$$\mathbf{i}_X=(\cos\theta,\ -\sin\theta\cos\varphi,\ -\sin\theta\sin\varphi), \tag{11}$$

$$\mathbf{i}_Z=(\sin\theta,\ \cos\theta\cos\varphi,\ \cos\theta\sin\varphi). \tag{12}$$

Formula (9) then gives the radii R_X and R_Z used in Secs. 4 and 5:

$$R^2_X=\frac{3a^2}{5}-\frac{27a^2}{64}\sin^2\theta\sin^2\varphi, \tag{13}$$

$$R^2_Z=\frac{3a^2}{5}-\frac{27a^2}{64}\cos^2\theta\sin^2\varphi. \tag{14}$$

They are equal when $\theta=45°$.

$$\begin{aligned}&\text{If}\quad 0°\leq\theta<45°,\quad R_Z<R_X;\\ &\text{If}\quad 45°<\theta\leq 90°,\quad R_Z>R_X;\end{aligned} \tag{15}$$

The measurements furnish a quadratic average of R_X and R_Z. For a random orientation of the half-spheres these averages are equal, and there is no anisotropy.

The actual orientations of the half-spheres are not known, but we can try to use the following model: by cold-work, Al and Ag tend to have a [112] direction parallel to the rolling direction and a (110) plane parallel to the plane of rolling. The averages obtained by assuming that all the (111) glide planes were equally probable, led to no anisotropy.

Actually, there are certainly more glide planes with values of θ comprised between 0° and 45°, than with values between 45° and 90°. The inequalities (15) show that the average R_Z should be smaller than the average R_X, the opposite of the observed anisotropy. The introduction of spheres sliced by a nondiametral plane would lead qualitatively to the same result.

Thus, the model of the sliced spheres either leads to no anisotropy at all, or to an anisotropy contrary to the one we observe.

JOURNAL OF APPLIED PHYSICS VOLUME 26, NUMBER 11 NOVEMBER, 1955

Electrical Analog of the Eddy-Current-Limited Domain-Boundary Motion in Ferromagnetics

G. BROUWER
Philips Research Laboratories, N. V. Philips' Gloeilampenfabrieken, Eindhoven, Netherlands
(Received November 26, 1954; revised manuscript received June 15, 1955)

The observed losses in a ferromagnetic core are always greater than those calculated on the basis of a homogeneous permeability. In a magnetization process by domain-boundary displacements the permeability is certainly not homogeneous, but attains extreme values in the domain walls. As a result of this concentration of the changes in magnetic flux the dispersion curves of the initial permeability as a function of frequency show a shift of the dispersion region towards lower frequencies with increasing domain size. This is the well-known eddy-current anomaly encountered in laminated cores. An electric-circuit model was utilized to determine the eddy-current distribution and domain-boundary motion in a number of idealized cases.

1. INTRODUCTION

WHEN the losses of a ferromagnetic core are calculated on the basis of a homogeneous permeability they are generally found to be exceeded by the actually measured losses. This phenomenon is known as the eddy-current anomaly.[1]

The magnetization process in a ferromagnetic material is associated with: (1) the simultaneous rotation of all the spins within a domain and (2) the displacement of the boundaries between the adjacent domains. The ferromagnetic models treated in this paper are chosen in such a way that only the domain-boundary displacements are possible. Consequently any change in the magnetic induction is restricted to the domain boundaries. It may be shown quite generally that such a concentration of changes in the magnetic flux leads to an increase in the eddy-current losses.[1,2] This will be analyzed in a number of special cases.

The equations governing the motion of the domain walls will be shown to be of the diffusion type. This allows for an approximate treatment by means of an electrical network as reviewed by Kron.[3] All illustrations in this paper have been obtained by means of such a diffusion analog.

2. MATHEMATICAL FORMULATION OF THE PROBLEM

The domain structure of a polycrystalline material is generally rather complicated and a certain idealization of the ferromagnetic will be necessary. The model adopted in this paper is given in Fig. 1. It consists of a lamination of ferromagnetic material in which the preferred spin-orientations are assumed to be parallel to the z-axis. The free surfaces are parallel to the xz-plane and stable wall positions are assumed to be parallel to the yz-plane. The lamination thickness is denoted by b and the wall spacing by $2a$. The magnetization process is considered to be a two-dimensional case containing the variables x and y.

When a small external alternating magnetic field H_{z0} is directed along the z-axis the walls will start to oscillate about the equilibrium positions and eddy-currents will be created, which tend to decrease the original field. At low frequencies the domain boundaries will move as rigid planes, but at higher frequencies a non-uniform motion will result from the finite penetration-depth of the magnetic field. The process is governed by the Maxwell equations, which give in this particular case:

$$\frac{\partial^2 H_z}{\partial x^2}+\frac{\partial^2 H_z}{\partial y^2}=\sigma\frac{\partial B_z}{\partial t}. \tag{1}$$

The units are expressed in the Giorgi system, σ denotes the conductivity of the ferromagnetic, H_z the local magnetic field in the z-direction, B_z the associated induction. The latter has an appreciable value only at the position of the domain walls. Hence Eq. (1) may be reduced to a fixed-boundary value problem of the two-dimensional Laplace equation

$$\frac{\partial^2 H_z}{\partial x^2}+\frac{\partial^2 H_z}{\partial y^2}=0 \tag{2}$$

and the boundary conditions

$$\frac{\partial H_z}{\partial x}=\pm\mu_{zt}\sigma a\frac{\partial H_z}{\partial t} \tag{3}$$

and $H_z=H_{z0}$ at the free surfaces. By application of symmetry considerations Eq. (3) may be derived from Eq. (1) by integrating over the wall with respect to x and neglecting the contribution of the second term in Eq. (1). The right-hand term in Eq. (3) represents the

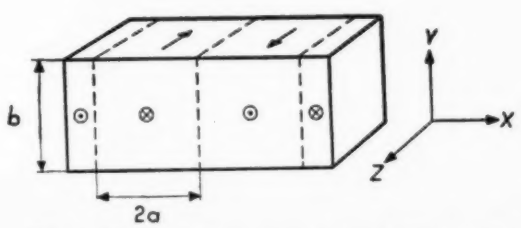

FIG. 1. Idealized ferromagnetic domain structure.

[1] Williams, Shockley, and Kittel, Phys. Rev. **80**, 1090 (1950).
[2] L. Néel, Ann. inst. Fourier, Grenoble **3**, 301 (1952).
[3] G. Kron. Elec. Eng. **67**, 672 (1948).

influence of the domain-boundary displacements as the concentrated effect of an area of width $2a$ and an apparent static value of the over-all permeability μ_{st}. The motion of the wall and its thickness are neglected as soon as the relations (2) and (3) are introduced.

The eddy currents may be expressed in terms of H_z by means of the equalities

$$i_x=\frac{\partial H_z}{\partial y} \tag{4}$$

$$i_y=-\frac{\partial H_z}{\partial x}. \tag{5}$$

Consequently the eddy currents are flowing along lines of constant H_z in the xy-plane.

Equation (1) is of the type belonging to the diffusion in inhomogeneous media. In the next section it will be shown how this partial differential equation and associated boundary-conditions, represented by Eqs. (2) and (3), may be solved by electric-network analog methods.

3. ELECTRIC-CIRCUIT MODEL OF THE DOMAIN-BOUNDARY MOTION IN A CONDUCTING FERROMAGNETIC

It is well known that an approximate solution of Eq. (2) may be obtained by the application of a square-meshed network of resistors R, as shown in Fig. 2(a). Provided the boundary conditions of the latter satisfy similar relations as in the ferromagnetic case the potential to earth V is equivalent to the local magnetic field H_z. The boundary condition at the free surfaces is simulated by short circuits connected to the output of a grounded alternating-voltage generator of angular frequency ω_2 and a constant voltage V_0. The same periodicity as of the domain structure is obtained by means of suitable connections which have the effect of closing the network in itself in one direction. It is easily verified that the condition (3) is satisfied by the introduction of condensers C between earth and midway taps of the resistor network corresponding to the position of the domain boundaries, provided the model law

$$nRC\omega_2=b^2\mu_{st}\sigma\omega_1 \tag{6}$$

holds. The number of subdivisions of the network equivalent to the thickness b of the ferromagnetic material is denoted by n, which also determines the degree of accuracy in the approximation. The angular frequency of the applied field H_{zo} is indicated by ω_1. The model frequency ω_2 is not necessarily equal to ω_1 but may be chosen in a convenient range if the relaxation time nRC is matched.

The model of a nonconducting ferromagnetic of the same type is given in Fig. 2(b). As the domain-boundary motion is no longer damped by eddy currents a frequency-independent permeability will result as long as no other complications are present. This reference model is convenient in order to express the over-all permeability of the conducting material as a function of frequency in terms of directly measurable model-quantities as is done in the following equations:

$$\frac{\mu(\omega_1)}{\mu_{st}}=\frac{1}{bH_{zo}}\int_0^b H_z(\omega_1)dy$$

$$\approx\frac{1}{nV_0}\left[\sum_{k=1}^{n-1}V_k(\omega_2)+V_0\right]$$

$$=\frac{1}{n\dot{V}_0C}\left[\sum_{k=1}^{n-1}\dot{V}_k(\omega_2)C+\dot{V}_0C\right]$$

$$=\frac{I_2(\omega_2)}{I_3(\omega_2)}=\frac{G_2(\omega_2)}{G_3(\omega_2)} \tag{7}$$

in which $\mu(\omega_1)$ is the over-all permeability of the ferromagnetic case at angular frequency ω_1, I_2 is the input current of model $2a$, I_3 of model $2b$, $G_2(\omega_2)$ the input admittance of the former at model frequency ω_2, and $G_3(\omega_2)$ the same quantity of model $2b$. All integrals and summations are taken at the position of a domain boundary or at the equivalent position in the model.

By means of relation (7) the complex permeability as a function of frequency may be derived from the models $2a$ and $2b$ by comparing their input admittances. This is done by bridge methods.

The eddy-current distribution may be plotted by intersecting the potential distribution V by planes of constant V, spaced equidistantly. The magnitude of the current density is to be derived from relations (4) and (5). As the deviation of a domain boundary is proportional to the local field, the relative shape of a wall

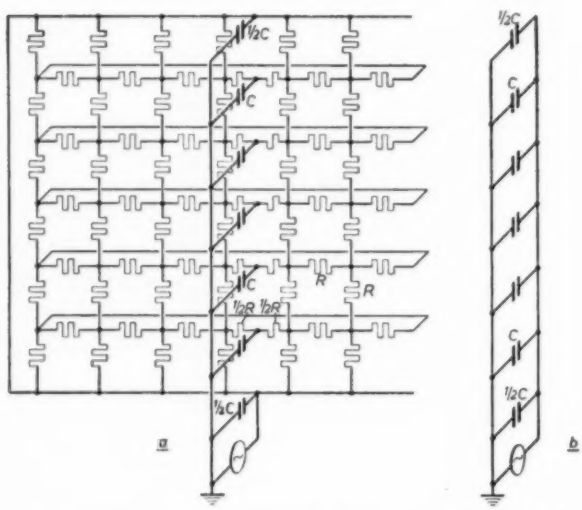

FIG. 2. Electric circuit model of the domain boundary motion in (a) a conducting ferromagnetic, (b) a nonconducting ferromagnetic.

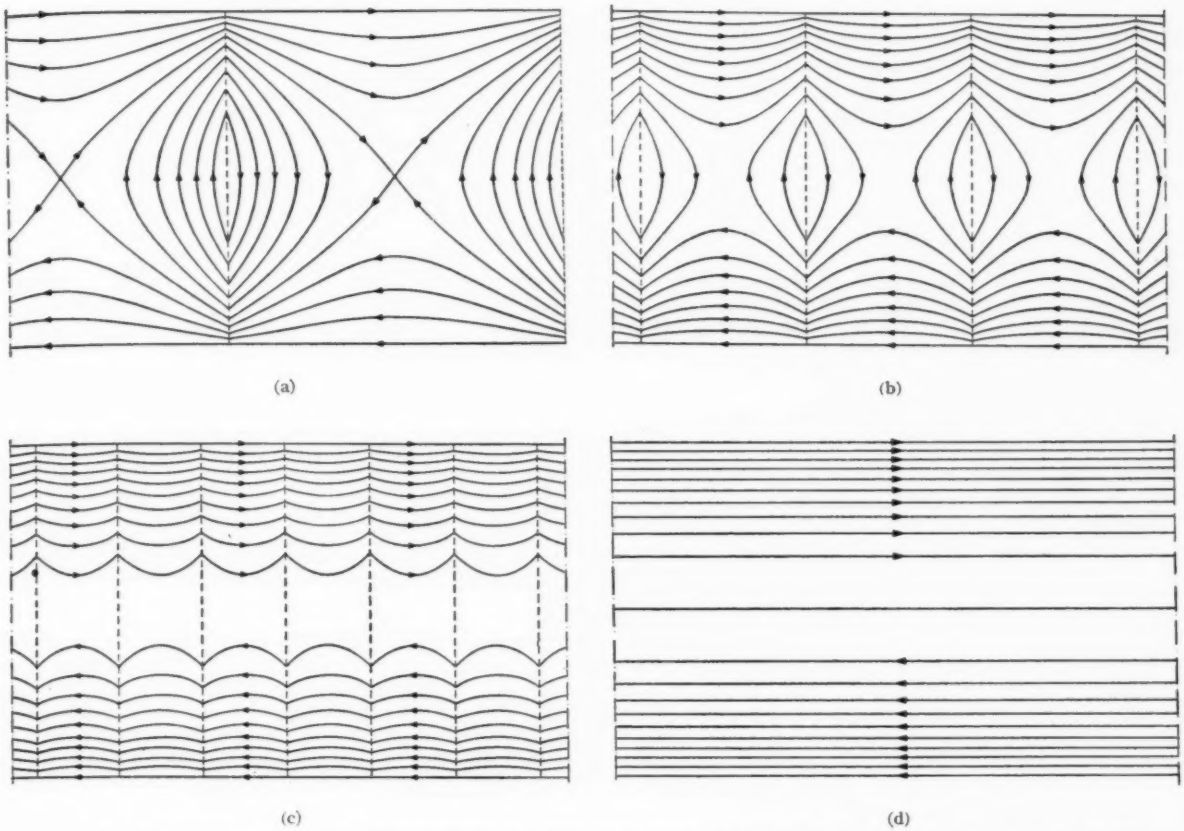

FIG. 3. Low-frequency eddy-current distribution in a ferromagnetic with domain structure. Walls are dashed. (a) Wall spacing equal to lamination thickness, (b) and (c) gradually decreasing domain size, and (d) homogeneous material in comparison. The over-all permeability and frequency are kept constant.

can also be determined. The speed of the wall is proportional to the charging current of the local condenser.

The potentials V are of a complex nature and both in-phase and out-of-phase components should be measured in order to obtain full information about the system. The in-phase part of V gives the situation when the external magnetic field attains a maximum value, whereas the second component belongs to the situation in which the driving field just goes through zero. The case of intermediate phase of the applied magnetic field may be derived by standard graphical methods from the data mentioned above.

The measurements of the potentials were made in the following way, which proved to be convenient. From the output signal of the generator three equally large signals were derived, having a phase lag of 90°, 180°, and 270° consecutively. This was achieved by means of an integrator and two phase-invertors. All four signals could be attenuated independently by means of calibrated potentiometers. By adding a suitable combination of signals to the unknown potential V the resulting signal could be reduced to zero. Both components of V with appropriate sign were then given by the readings of the potentiometers.

4. RESULTS AND DISCUSSION

(a) In a first series of measurements the influence of the domain size on the low-frequency eddy-current pattern was investigated. In Fig. 3(a) the current distribution is given for the case in which the wall spacing equals the lamination thickness. The domain boundaries and the free surfaces are both perpendicular to the plane of drawing, the former being indicated by dashed lines and the latter by solid lines on top of and

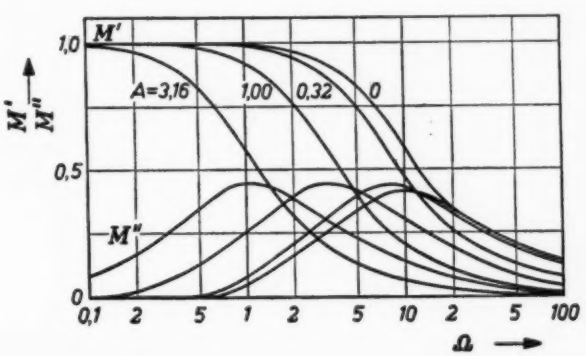

FIG. 4. The complex permeability $M'+jM''$ as a function of the frequency Ω with the domain size A as parameter, expressed in reduced quantities.

at the bottom of Fig. 3(a). The eddy currents are drawn in full. The material has a periodical structure. The wall spacing is gradually decreased in Figs. 3(b) and (c), until the material becomes homogeneous in Fig. 3(d). The over-all permeability is kept constant in this process. From Fig. 3 it will be clear that the assumption of a homogeneous permeability leads to a miscalculation of the eddy-current distribution and dissipation when the domain size becomes comparable to the lamination thickness.

(b) Next the influence of the domain size on the dispersion of the permeability due to eddy-current damping was studied. The result of this investigation, given in Fig. 4, could be kept quite general by the introduction of dimensionless quantities. The real and imaginary parts of the over-all permeability M' and M'' are expressed as fractions of the static value of the initial over-all permeability. A characteristic frequency ω_0 is defined by the relation $\omega_0 b^2 \mu_{si} \sigma = 1$ and Ω is defined by $\Omega = \omega_1/\omega_0$. The domain size is characterized by $A = 2a/b$, in which $2a$ is the wall spacing and b the lamination thickness. From Fig. 4 may be deduced that the peak in the losses shifts to lower frequencies as the domain size increases. The dispersion curve of the homogeneous

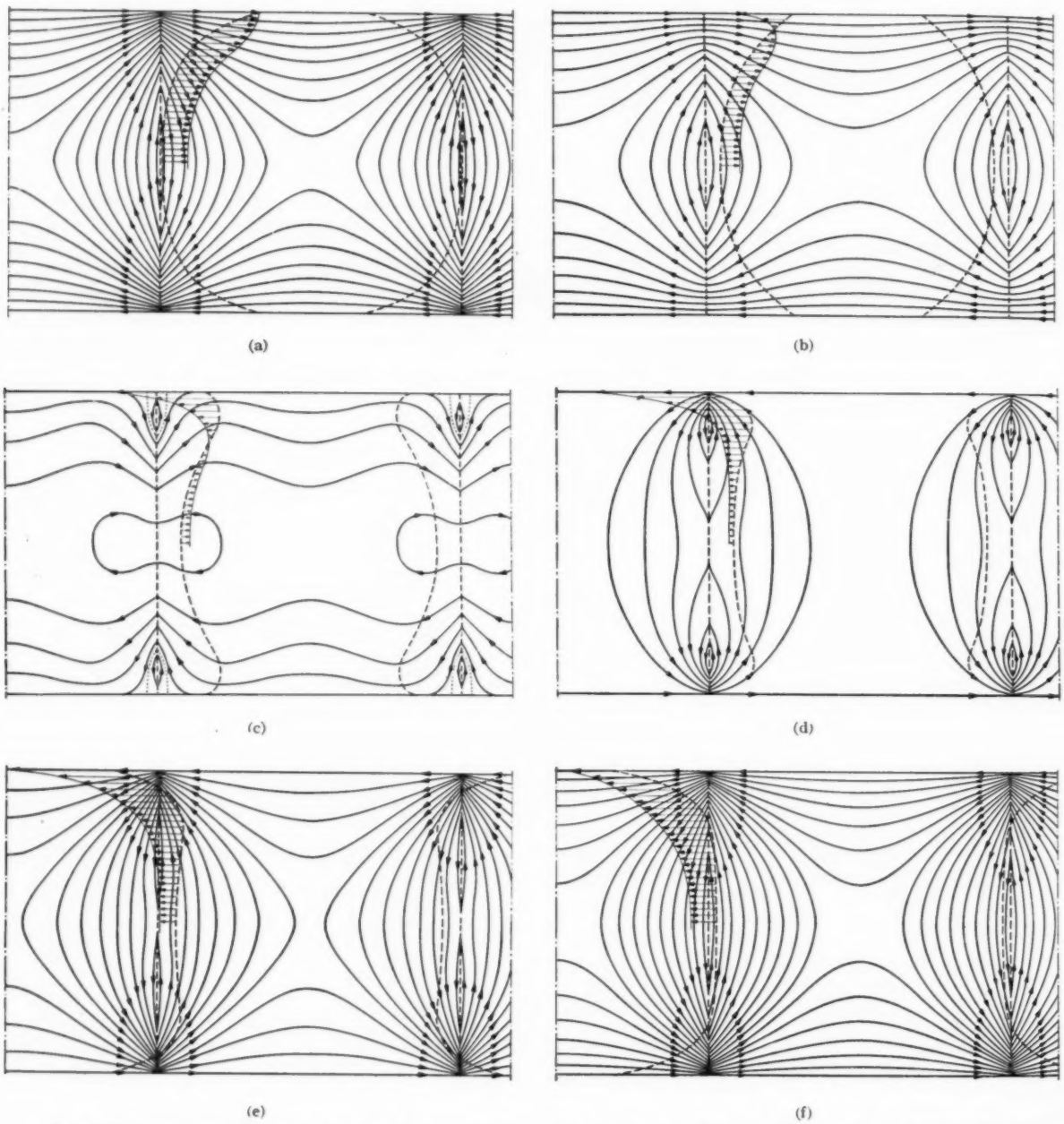

FIG. 5. Six consecutive stages in the high-frequency magnetization process during half a period. Wall displacements indicated by dashed lines, on an exaggerated scale, speed marked by arrows. (a) Maximum value of applied magnetic field, (b) reversal of rotational sense of eddy-currents in areas bounded by dotted lines, (d) zero external field.

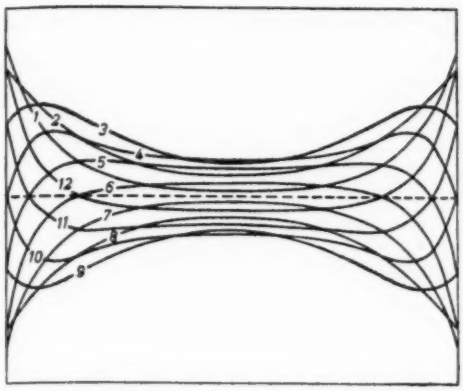

FIG. 6. Motion of domain boundary corresponding to the case of Fig. 5.

material corresponding to $A=0$ cannot be expected to give dependable results in the case of thin laminations with coarse domain structure. The usual eddy-current corrections of the permeability are incorrect in such a case, thus leading to the eddy-current anomaly.

(c) The case of Fig. 3(a) was studied at frequencies in the dispersion region, where the eddy-current distribution and domain-wall motion are of a much more complicated character than at low frequencies. In Figs. 5(a) to (f) six consecutive stages of the magnetization process are shown, having a phase difference of 1/12th of a period. Besides the equilibrium position the actual shape of the domain wall is indicated by a dashed line. The displacements are drawn on an exaggerated scale, but are assumed to be infinitely small. The speed of the wall is marked by arrows. The situation of Fig. 5(a) corresponds to a maximum value of the applied magnetic field. At the edges the wall has attained its extreme deviation from the equilibrium position and there the motion is just going to be reversed. The discontinuities in the flow lines of the eddy currents at the intersections with a moving domain boundary are caused by the concentration of the changes in magnetic flux in the wall. The discontinuities disappear locally when the latter has zero speed, as may be seen in Fig. 5(b). The interior part of the domain wall is always seen to be lagging behind the motion of the edges. In Fig. 5(c) a reversal of the rotational sense of the eddy currents about the generating source is observed in small areas near the edges of the walls. These areas, bounded by dotted lines, are gaining in importance in the next phase of the magnetization process and in Fig. 5(d) a complete reversal of all the eddy currents is obtained. The external magnetic field now goes through zero and accordingly the edges of the wall are in the equilibrium position. In the next figures the progress of the diffusion of the perturbation-areas into the ferromagnetic may be observed. In Fig. 5(f) half a cycle is almost completed and, but for the signs, the next development of the magnetization process is a repetition of what has already been shown. A peak in the power dissipation is, of course, corresponding to a maximum eddy-current density.

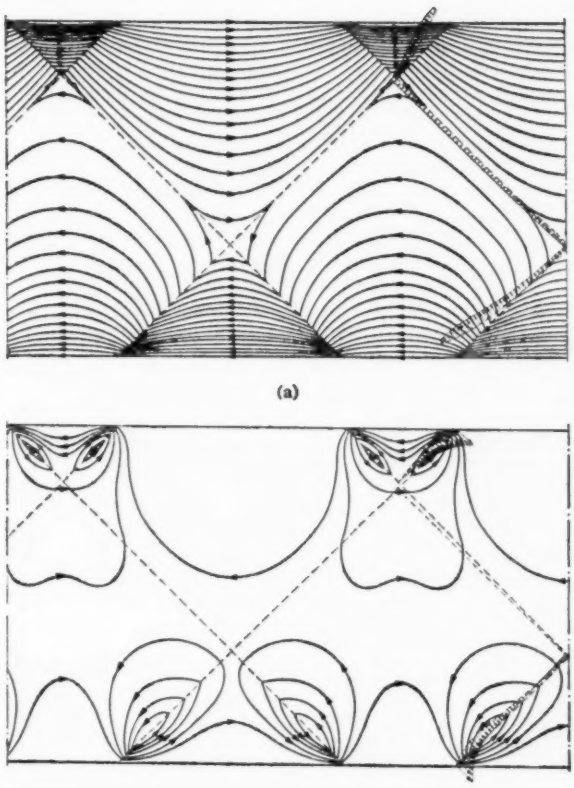

FIG. 7. Eddy-current distribution in a more complicated domain-structure. (a) Maximum value of external field, (b) zero value.

The motion of the domain wall during a complete cycle is reviewed in Fig. 6 and exhibits typical diffusion characteristics.

(d) At last a more complicated domain structure was investigated as is shown in Fig. 7. There are two systems of equidistant boundaries intersecting each other at right angles. The situation of Fig. 7(a) corresponds to a maximum value of the applied magnetic field, which is zero in Fig. 7(b). In this case also the resulting eddy-current distribution is quite different from what could be expected on the basis of a homogeneous permeability.

5. CONCLUSION

In a conducting ferromagnetic the elementary skin-effect theory, based upon a homogeneously distributed permeability breaks down as soon as the spacing of the domain boundaries becomes comparable to the lamination thickness. As a result of the inhomogenities introduced by the domain structure the dispersion peak is shifted to lower frequencies with increasing domain size.

Deterioration of Luminescent Phosphors under Positive Ion Bombardment

J. R. YOUNG
General Electric Research Laboratory, Schenectady, New York
(Received April 15, 1955)

The reduction of cathodoluminescence efficiency of phosphors has been observed after bombarding with H^+, H_2^+, He^+, Ne^+, N_2, and A^+ ions having energies from 1 to 25 kev. Detectable deterioration could be observed after a bombardment of less than 10^{-9} coul/mm² of ions (5×10^{11} ions/cm²). The deterioration could be annealed out at temperatures between 450° and 700°C. Results indicate that light 25-kev ions probably penetrate 0.1μ to 0.2μ into the phosphor.

INTRODUCTION

IT has been known for many years that luminescent phosphors deteriorate under prolonged bombardment by high-energy ions.[1–5] Examples of this deterioration may be found in magnetic deflection cathode-ray tubes having electron guns without ion traps, where a dark central spot appears on the screen because of negative ion bombardmant, and more recently in unaluminized television picture tubes where x-burn occasionally occurs due to positive ion bombardment of the screen.[6,7] Little quantitative information is available concerning the deterioration of phosphors under low-energy ion bombardment. Hanle and Rau[5] studied the luminescence induced by 15–35 kev positive ions and the decrease of this luminescence with time. They found only a slight dependence of the deterioration upon ion energy but a strong dependence upon ion mass, with the deterioration increasing with ion mass. The luminescence per particle, produced by ions heavier than He^+, was small and made observations difficult.

It is well known that an ion moving through a gas or solid will lose energy by different mechanisms, depending upon its velocity.[8,9] For velocities above about 2×10^8 cm/sec most of the energy is lost by ionization and excitation of the atoms in the solid. This type of energy loss in an inorganic phosphor should produce a large amount of luminescence but little deterioration. For ion velocities below 2×10^8 cm/sec much of the energy will be lost by elastic collisions with atoms in the phosphor. Energy lost by elastic collisions will produce little light but many displaced atoms and lattice defects.[9] This usually results in a decrease in the luminescence efficiency of the phosphor. It is therefore the low-velocity ions which produce much of the deterioration but little luminescence. It is possible to study the deterioration of phosphors by ion bombardment to lower ion energies if another technique is employed, namely, the use of electrons to excite the phosphor deteriorated by ion bombardment. The latter method was employed in this investigation.

It should be noted that ions pick up or lose electrons in matter depending primarily upon the ion velocity.[8,9] Therefore, regardless of the ion's original charge, very soon after entering the material it has a charge characteristic of its velocity. Thus, the deterioration produced by a bombarding atom, of a given velocity, should be the same whether the atom is positive, negative or neutral.

EXPERIMENTAL TECHNIQUE

Unless otherwise specified the powder phosphor used in these studies was a standard blue emitting ZnS:Ag with 0.001% Ag.* The phosphor was settled in triply distilled water without binder to 10 mg/cm² on microscope slides having a tin oxide transparent conducting coating. With reasonable handling care no difficulty was encountered in the phosphor failing to adhere to the slide. The transparent conducting film was used to insure that the phosphor remained at the desired potential during ion bombardment and electron excitation.

Ion bombardment was accomplished in a demountable tube shown schematically in Fig. 1. Positive ions were produced by electron bombardment of a gas which was introduced through a small capillary controlled leak. The positive ion gun was made from a standard

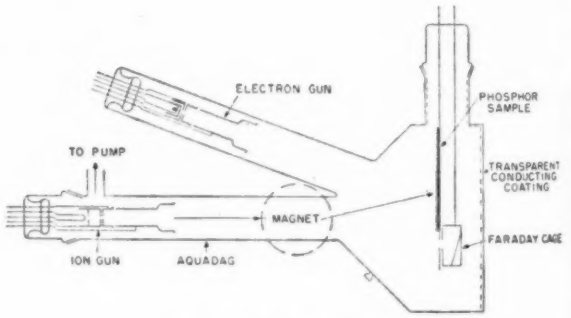

FIG. 1. Experimental tube.

[1] C. H. Bachman and C. W. Carnahan, Proc. Inst. Radio Engrs. **26**, 529 (1938).
[2] L. F. Broadway and A. F. Pearce, Proc. Phys. Soc. (London) **51**, 335 (1939).
[3] C. H. Bachman, J. Appl. Phys. **11**, 83 (1940).
[4] G. Leibman, Nature **157**, 228 (1946).
[5] W. Hanle and K. H. Rau, Z. Physik **133**, 297 (1952).
[6] Laponsky, Ozeroff, Thornton, and Young, Internal G. E. Publication.
[7] de Gier, Kleisma, and Peper, Philips Tech. Rev. **16**, 26 (1954).
[8] N. Bohr, Danske Mat. Fys. Medd. **18**, No. 8 (1948).
[9] J. C. Slater, J. Appl. Phys. **22**, 237 (1951).

* Obtained through the courtesy of D. E. Kinney, G. E. Chemical Products Works, Cleveland, Ohio.

5TP4 electron gun by modifying the first grid and using a tungsten ribbon as an electron source (see Fig. 1). Positive ions used were: H^+, H_2^+, He^+, Ne^+, N_2^+, and A^+. The ion beam could be accelerated up to 25 kev and focused into a uniform spot from 1 to 5 mm in diameter. A 2.5-mm diameter spot was usually employed.

Deflection of the ion beam was accomplished by an electromagnet (see Fig. 1). The ion current could be measured by deflecting the ion beam downward into the specially constructed Faraday cage. A 5-mm entrance slit in the Faraday cage enabled easy measurement of the total current in the 2.5-mm diameter ion beam. Total ion currents of between 10^{-9} and 10^{-11} ampere were used, resulting in a current density of 2×10^{-10} to 2×10^{-12} ampere/mm^2. The deterioration was the same regardless of the ion current density used as long as the total number of ions striking a unit area was identical. This ion current could be maintained constant within 5% for periods up to 3 hours, the longest exposure employed in this investigation. The samples were bombarded with from 10^{-10} to 10^{-6} coul/mm^2 or, expressed differently, from 5×10^{10} to 5×10^{14} ions/cm^2. After bombarding the phosphor with a known quantity of ions the deterioration produced was observed visually and with a multiplier phototube while the phosphor was excited by electrons from the electron gun. The electron gun was of the 5TP4 electrostatic type with a LaB_6[10] cathode and a grid having a 2-mil aperture. This provided an electron beam of small dimensions with which to excite separately various regions of the deteriorated phosphor. It was found that the electron beam could not be focused equally well at all electron accelerating energies but at all energies it was possible to keep the beam smaller than 0.5 mm in diameter. With the small electron beam diameter the uniformity of the deterioration could be checked. The deterioration was found to be quite uniform and thus indicates that the ion beam was uniform.

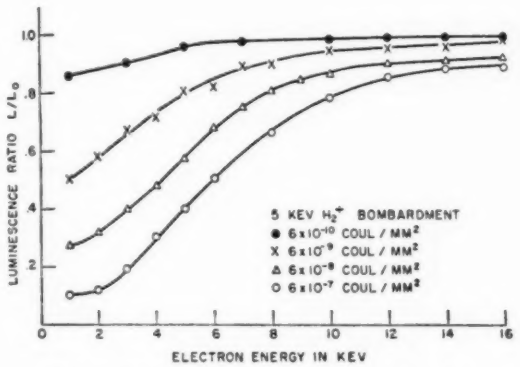
LUMINESCENCE RATIO L/L₀
ELECTRON ENERGY IN KEV
5 KEV H₂⁺ BOMBARDMENT
● 6x10⁻¹⁰ COUL / MM²
X 6x10⁻⁹ COUL / MM²
△ 6x10⁻⁸ COUL / MM²
○ 6x10⁻⁷ COUL / MM²

FIG. 2. Deterioration of ZnS:Ag produced by different quantities of 5 kev H_2^+ ions.

[10] J. M. Lafferty, J. Appl. Phys. **22**, 299 (1951).

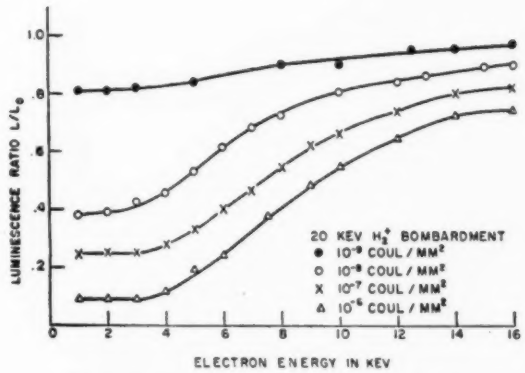

FIG. 3. Deterioration of ZnS:Ag produced by different quantities of 20 kev H_2^+ ions.

Luminescence measurements were made using a 5819 multiplier phototube. Luminescence was measured with the electron beam striking only the deteriorated portion of the phosphor and this luminescence compared to that when the electrons struck only the adjacent undeteriorated phosphor. The ratio of the luminescence obtained with the electrons striking the deteriorated phosphor to the luminescence when the electrons were striking the undeteriorated phosphor L/L_0 has been called the luminescence ratio.

Since the multiplier phototube sensitivity changes with wavelength, it was necessary to determine the change in emission spectrum of the phosphor after prolonged ion bombardment. Spectrum analyses made on several samples used in these experiments did not show a detectable spectrum shift. Therefore a correction was not necessary.

EXPERIMENTAL RESULTS

Since the deterioration effects were observed under electron excitation it was necessary to know the luminescence-energy characteristics of the phosphor. It was found that the standard relation

$$L=K(E-E_0)^n \qquad (1)$$

was satisfied if E_0 was assumed to be 150 ev and $n=1.3$ for electron energies between 1 and 20 kev. L is the luminescence, K a constant, E the exciting electron energy, and E_0 the electron energy necessary to penetrate the so-called dead layer.[11] The luminescence-current characteristics were found to be linear up to 1 μa/cm^2, the highest current density used in these experiments.

A. Deterioration *vs* Quantity of Ions

The deterioration produced by different quantities of ions was observed for ions of various energies. Results obtained for 5- and 20-kev H_2^+ ions are shown in Figs. 2 and 3. It was possible to detect the deterioration

[11] G. F. J. Garlick, *Advances in Electronics II* (Academic Press, Inc., New York, 1950), p. 159.

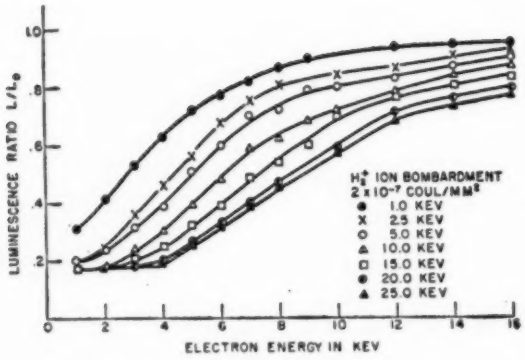

FIG. 4. Deterioration of ZnS:Ag produced by different energy H_2^+ ions.

visually with a luminescence ratio of 0.9 or lower, when the entire slide was excited by electrons. It is noticed that less than 10^{-9} coul/mm² was sufficient to produce visible deterioration at low electron excitation energies for both 5- and 20-kev H_2^+ ions. Also after about 10^{-6} coul/mm² bombardment at either 5- or 20-kev energy the deterioration was visible at electron excitation energies above 16 kev. A similar dependence upon the quantity of ions was obtained with the heavier ion components except the specific values were different (see Figs. 7 and 8).

B. Deterioration *vs* Ion Energy

Typical results obtained on the dependence of deterioration upon ion energy are shown for H_2^+ ions in Fig. 4. Here the quantity of ions striking a unit area was kept constant at 2×10^{-7} coul/mm². Observations were made at ion energies from 1 to 25 kev. It was possible to detect the deterioration visually up to quite high electron energies on these samples. The deterioration was found to be greater for ions having higher energies except at low-energy electron excitation where the luminescence ratio was almost constant.

It is to be expected that the higher-energy ions will penetrate further into the phosphor than lower-energy ions. Therefore, the deterioration depth will be greater for the high-energy ions. It is noticed that the constant

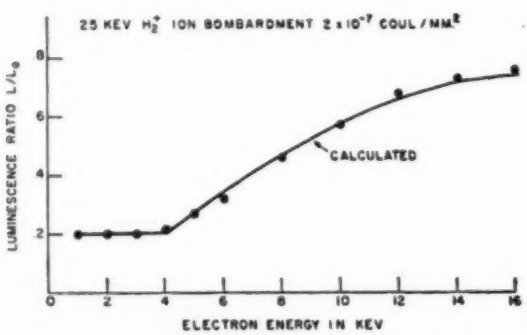

FIG. 5. Deterioration of ZnS:Ag produced by 25 kev H_2^+ ions. Curve is the best fit of Eq. (3).

luminescence ratio extends to higher electron exciting energies if the sample has been bombarded by higher-energy ions. Thus it would appear that the constant luminescence ratio region is the region where exciting electrons are being completely stopped in the deteriorated portion of the phosphor. When the luminescence ratio starts increasing the electrons are probably beginning to penetrate the deteriorated portion of the phosphor. If this is true, the break in the curve will give an indication of the depth of penetration of the ions in the phosphor. Also, since the brightness ratio under 1-kev electrons is about the same for 2.5 and 25 kev H_2^+ ions, it would seem that the deterioration per unit volume was roughly the same for the different ion energies, the total deteriorated volume being greater for high-energy ions because of the greater depth of penetration.

An expression may be derived to describe the luminescence ratio curves by using the luminescsnce-voltage characteristics of the phosphor, Eq. (1), and assuming (1) deterioration uniform with depth of ion penetration and (2) a constant amount of electron energy lost in the deteriorated region for electrons which penetrate the region (shown to be approximately true by Koller and Alden[12]). In the case where the electrons do not penerate the deteriorated region the luminescence ratio will be a constant

$$L/L_0=R_1 \text{ if } E\leq E_1 \tag{2}$$

and in the case where the electron beam does penetrate the deteriorated region the expression turns out to be

$$L/L_0=R_1\left(\frac{E_1-E_0}{E-E_0}\right)^n + \left(1-\frac{E_1-E_0}{E-E_0}\right)^n \quad \text{if } E\geq E_1 \tag{3}$$

where R_1 is given by (2), E_1 is the electron energy at which electrons just penetrate the deteriorated region, E is the energy of the exciting electrons, and n the exponent in the luminescence-voltage relationship (1).

It is possible to fit the foregoing expression to the experimental data quite well in some cases, as is shown in Fig. 5. From the best fit of expressions (2) and (3), values of E_1 were established. If the electron penetration law is known, the depth of penetration of the ions may be calculated. Although the Thomson[13]-Whiddington[14] law has been verified by many observers for metals and gases, some recent observations indicate it may not be accurate for phosphors.[12,15,16] However, it was used

[13] L. R. Koller and E. D. Alden, Phys. Rev. **83**, 684 (1951).
[13] J. J. Thomson, *Conduction of Electricity Through Gases* (Cambridge University Press, London, 1933), third edition, Vol. II, p. 109.
[14] R. Whiddington, Proc. Roy. Soc. (London) **89**, 554 (1914).
[15] P. H. Dowling and J. R. Sewell, J. Elec. Chem. Soc. **100**, 22 (1953).
[16] W. Ehrenberg and J. Frank, Proc. Phys. Soc. (London) **66**, 1057 (1953).

in this case to obtain an estimate of the ion penetration depth. In the form used here,

$$X_1=\frac{E_1^2}{b} \tag{4}$$

where X_1 is the depth of penetration of electrons having energy E_1 and b is a constant equal to $4\times10^{11}\ \rho$ volts^2 cm^{-1}, where ρ is the density of the material.[17]

The results obtained for H_2^+ are typical and are shown in Fig. 6. These results indicate a linear variation in ion penetration with energy and a penetration of about 0.1 micron for 25-kev H_2^+ ions. The linear variation of calculated penetration depth with energy was also found for the heavier ions. A linear dependence between range and energy has been found for fission fragments[18] in gases having velocities of the same order as the ions used here and has been predicted by Bohr.[8] Recent observations on the penetration of nitrogen ions in photographic emulsion also show a linear dependence

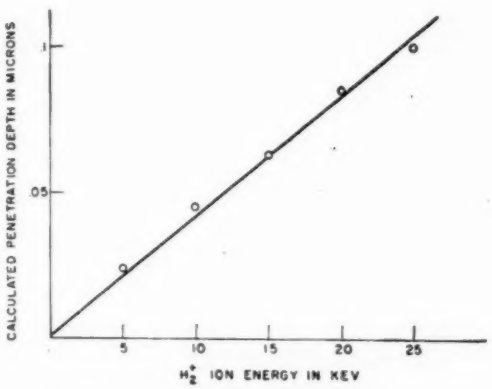

FIG. 6. Penetration depth-energy relationship for H_2^+ ions in ZnS:Ag.

with energy.[19] Also, the calculated penetration depths are in rough agreement with some recent observations made by the author on the penetration of aluminum films by ions.

C. Deterioration *vs* Ion Mass

The dependence of the deterioration upon ion mass was observed and typical results obtained are shown in Figs. 7 and 8. The dependence of the deterioration of the different mass ions upon energy was similar to that obtained for H_2^+ (see Fig. 4).

It is noticed in Fig. 7 that the deterioration by light ions increases with mass regardless of the excitation energy of the electrons. However, in Fig. 8 the deterioration by heavier ions decreases with mass at the high excitation energies and is about the same for low-energy electron excitation. If one considers the volume

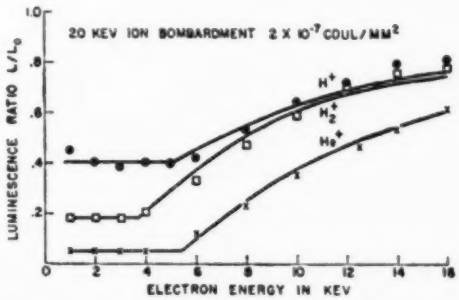

FIG. 7. Deterioration of ZnS:Ag produced by 20 kev H^+, H_2^+, and He^1 ions. Curves are the best fit of Eq. (3).

of the phosphor in which deterioration occurs, the deterioration per unit volume should be greater for the heavier ions. This is because the closer the mass of the bombarding ion to the atoms making up the solid, the more energy will be transferred per collision to the recoil atoms, and more atoms displaced per unit volume.[20] Therefore, the same energy is dissipated in a smaller volume in the case of the slower, heavier ions resulting in their shorter range. The range of the different ions is important in explaining these results since a heavy ion which has produced much deterioration per unit volume may extend such a short distance into the phosphor that only a small fraction of the exciting electron energy is lost in the deteriorated portion of the phosphor. This is believed to be the reason for the increased luminescence ratio with mass for the heavier ions in Fig. 8 for high electron excitation energies. However, in Fig. 7 the ranges of the light ions are similar, so the increased deterioration per unit volume will be the controlling factor in explaining the lower luminescence ratio with increasing mass for all electron excitation energies. Also, a 20-kev H^+ ion has a velocity of about 2×10^8 cm/sec, so a significant portion of the energy will be dissipated by nondeteriorating electronic excitation and ionization processes.[8,9,21]

It was possible to determine the range of the heavier ions in the same manner as discussed previously. Within the limits of experimental error the range energy rela-

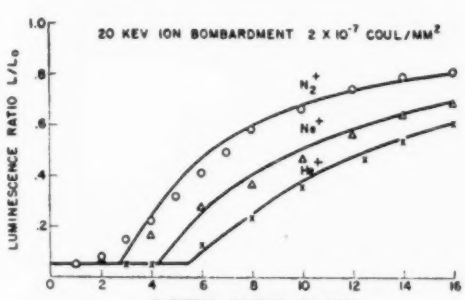

FIG. 8. Deterioration of ZnS:Ag produced by 20 kev He^+, Ne^+, and N_2^+ ions. Curves are the best fit of Eq. (3).

[17] H. M. Terrill, Phys. Rev. **24**, 616 (1924).
[18] J. K. Bøggild, Phys. Rev. **60**, 827 (1941).
[19] H. L. Reynolds and A. Zucker, Phys. Rev. **96**, 393 (1954).
[20] F. Seitz, Discussions Faraday Soc. No. 5, 271 (1949).
[21] K. H. Juergen Rottgardt, Z. angew. Phys. **6**, 160 (1954).

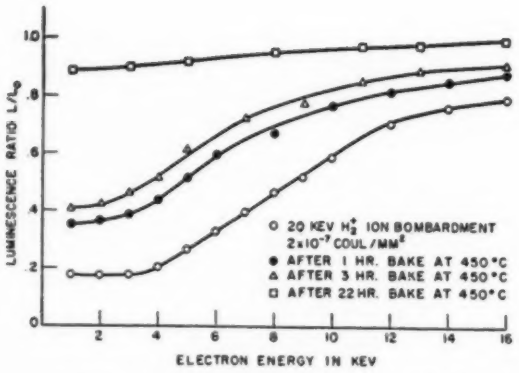
LUMINESCENCE RATIO L/L_0
ELECTRON ENERGY IN KEV
○ 20 KEV H_2^+ ION BOMBARDMENT
2×10^{-7} COUL/MM²
● AFTER 1 HR. BAKE AT 450°C
△ AFTER 3 HR. BAKE AT 450°C
□ AFTER 22 HR. BAKE AT 450°C

FIG. 9. The effect of heat treatment on H_2^+ ion deteriorated ZnS:Ag.

tionship was always linear. At a given energy the range of the different ions appeared to be roughly inversely proportional to the square root of the atomic number of the ion. Bohr predicts a $Z^{-\frac{1}{2}}$ dependence for heavy fission fragments in gases where Z is the atomic number of the fragment.[8] In the case of the molecular ions H_2^+ and N_2^+ it is assumed that they dissociate upon entering the phosphor and should therefore be treated as having one-half the energy of the bombarding molecules. This will account partially for the fact that the range of H_2^+ is less than He^+ and for the range of N_2^+ being less than Ne^+. Table I shows the calculated penetration depth for the different 20-kev ions studied.

D. Annealing

From the type of damage produced by ion bombardment of phosphors it would be expected that the deterioration could be annealed out by heating the phosphor.[9,21] This was found to be the case and the results obtained for H_2^+ ions are shown in Fig. 9. After a 30-hour bake at 450°C no deterioration was observable. A longer period of time and a temperature from 450° to 700°C was required in the case of the heavier ions. The luminescence efficiency of the phosphor remained constant during the annealing up to 450°C, with the phosphor sample in air. However, when the samples were baked for long periods of time in air at 500°C, the over-all efficiency diminished. Samples baked at 500°C or higher were baked in a nitrogen atmosphere. These observations are similar to those reported for ZnS phosphor deteriorated by neutron and alpha-particle irradiation.[22]

TABLE I. Ion energy 20 kev.

Positive ion	Calculated range in microns
H^+	0.16
H_2^+	0.08
He^+	0.18
Ne^+	0.11
N_2^+	0.05
A^+	0.05

E. Deterioration *vs* Type of Phosphor

In an effort to determine how different phosphors were affected by the positive ion bombardment, various samples obtained from different suppliers were bombarded with a constant quantity, 1.5×10^{-8} coul/mm², of 10-kev H_2^+ ions. The luminescence ratio at 5-kev electron excitation energy was measured after this bombardment. Results obtained indicated that slight variations do occur among the different ZnS and ZnCdS components, with L/L_0 differing by up to 20%. However, in the case of Zn_2SiO_4 about 10 times the number of ions are required to produce the same deterioration as in the case of ZnS or ZnCdS.

[22] A. W. Smith and J. Turkevich, Phys. Rev. **94**, 857 (1954).

JOURNAL OF APPLIED PHYSICS VOLUME 26, NUMBER 11 NOVEMBER, 1955

Variation of Elastic Wave Velocity with Frequency in Fused Quartz and Armco Iron*

D. S. HUGHES AND J. M. KENNEL
Physics Department, University of Texas, Austin, Texas
(Received June 8, 1955)

The velocity dispersion in fused quartz and in Armco iron was investigated by measuring the resonant frequency of small cylinders using quartz crystals on the ends as drivers and detectors. With x-cut crystals and y-cut crystals the computed velocities of the dilatational waves in the range 2.0–5.0 Mc and shear waves in the range 1.5–3.0 Mc decrease with frequency. This decrease in both cases is regarded as unreasonably large and is ascribed primarily to sample geometry. Simple standing plane waves, either dilatational or shear, cannot satisfy the boundary conditions in a free cylinder. A mosaic crystal was then constructed of sectors of y-cut crystals such that the driver generated and the detector transmitted only torsional waves. With these crystals and viscous coupling between the crystals and sample, the velocity in fused quartz was constant within ±1 m/s for the frequency range 0.6–3.0 Mc. The velocity in Armco iron was constant within ±2 m/s in the range 0.5–1.5 Mc and decreased about 10 m/s in the range 1.5–3.0 Mc.

INTRODUCTION

SEVERAL experimenters have searched for velocity dispersion in solids or have obtained data indirectly in the course of other work. Bhagavantam and Ramavataram[1] report no dispersion in brass and aluminum over the range 1–10 Mc. Mason and McSkimin[2] using aluminum in the range 2–15 Mc, Roth[3] using aluminum and magnesium in the range 5–100 Mc, and Roderick and Truell[4] using fused quartz and steel at 5 Mc and up, all report no dispersion. The last three experimenters used the echo times of modulated pulses.

APPARATUS AND METHOD

The actual resonant modes of a free solid are complicated functions of the shape of the solid as well as the elastic parameters. A short cylindrical rod can vibrate in many other modes than the simple ones where the length of the rod is an integral number of half wavelengths. Bancroft[5] has worked out the solution in detail for waves of a combination dilatational, shear type for infinite rods. When the wavelength is large compared to the rod diameter these waves travel with a velocity determined by Young's modulus. When the wavelength is small compared with the rod diameter the solutions give several possible velocities depending upon the mode of transmission.[5]

These more complex modes of vibration do not consist of plane waves traveling parallel to the axis of the cylinder. On the other hand, using either x- or y-cut crystals on the ends of the rod, the input wave is primarily a plane wave traveling parallel to the axis. On the theory that these complex modes required time to build up, the apparatus shown in Fig. 1 was assembled. The signal generator is a General Radio model 1001-A. The frequency meter is a Bendix BC-221-M which was checked against a General Radio secondary frequency standard. The accuracy of the frequency determination should be ±0.005%. The pulse gate can either be left open and a continuous drive used or the Hewlitt-Packard pulse generator can be used to give modulated pulse drive. Figure 2(a) shows the pulse applied to the driver crystal by this system. The length of this pulse is in general very long compared with the time through the sample. Figure 2(b) shows the received pulse on an expanded sweep, and Fig. 2(c) shows the received pulse with the sweep the same as in 2(a). Referring to Fig. 2(b), it is obvious that the successive reflections are reinforcing each other, and thus the sample length is an integral number of half wavelengths. This method was very successful in locating the longitudinal resonance modes. A slight shift in frequency causes the successive reflections to interfere and the pattern disappears. Unfortunately, since only six to eight reflections can be detected, the accuracy of setting the frequency was 0.1% as compared with 0.03% with continuous waves. It was found, however, that the approximately correct resonant frequency having been located by this method, it was possible in nearly every case to switch to continuous drive and locate the frequency with greater precision.

In order to avoid spurious resonances from the crystal holder it is necessary that no energy be reflected from

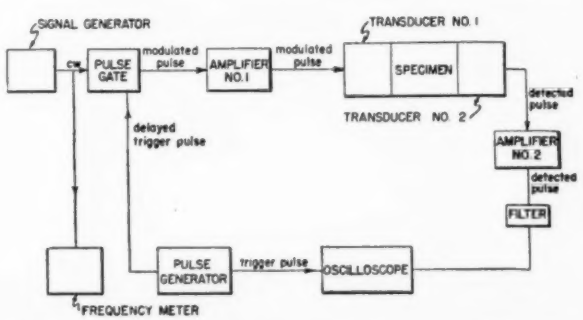

FIG. 1. Block diagram of apparatus for modulated pulses.

* This work was supported by research grants from the Shell Oil Company and the Humble Oil and Refining Company, and by an equipment loan from the Office of Naval Research.

[1] S. Bhagavantam and T. Ramavataram, Proc. Indian Acad. Sci. A32, 197 (1950).
[2] W. P. Mason and H. J. McSkimin, J. Acoust. Soc. Am. 19, 464 (1947).
[3] W. Roth, J. Appl. Phys. 19, 901 (1948).
[4] R. L. Roderick and R. Truell, J. Appl. Phys. 23, 267 (1952).
[5] Dennison Bancroft, Phys. Rev. 59, 588 (1941).

the backing material. Since some support for the crystal is required, the holder shown in Fig. 3 was designed. The felt, if dry, offers zero impedance to the crystal. The driver and detector were similar and mounted on carriages on an optical bench. The sample was suspended by fine wires from a third carriage. All samples and crystals were about 1.0 inch in diameter. Sample lengths varied from ½ inch to 4 inches. Very light pressure was used to seat the crystal on the sample. Actually increasing the pressure made no detectable difference in the measurements. For x-cut crystals each crystal was coupled to the sample with an oil film; for shear crystals the aluminum foil was omitted, and the sample rested directly on the crystal. With quartz samples the ends of the sample were painted with DuPont No. 4817 silver paint. Careful weighing showed the loading to be negligible.

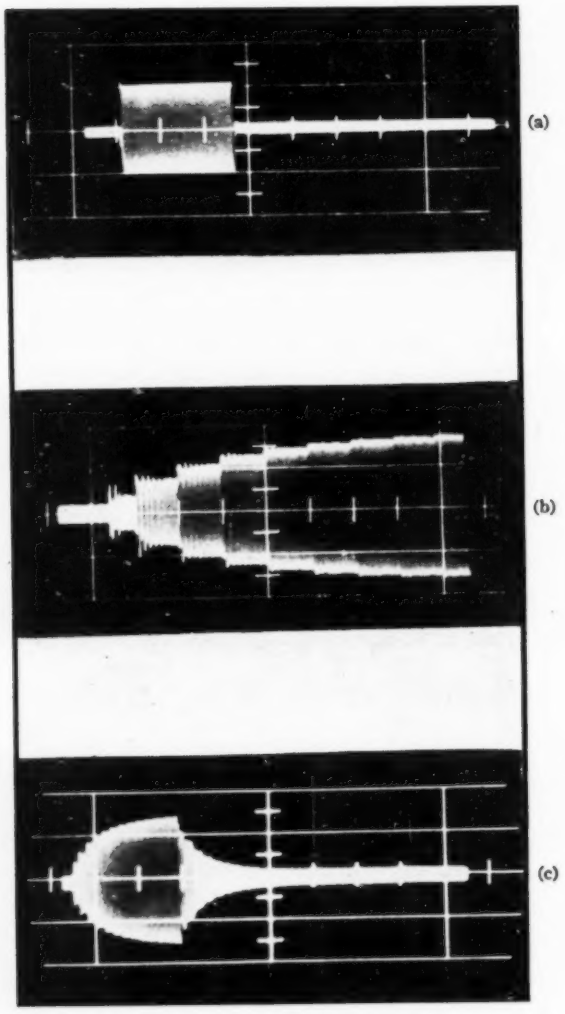

FIG. 2. Oscilloscope patterns of modulated pulses. (a) Input pulse sweep 36 μsec/cm. (b) Transmitted pulse, 1.0-in. Armco iron, sweep 8 μsec/cm. (c) Transmitted pulse, 1.0-in. Armco iron, 36 μsec/cm.

RESULTS

The only simple solutions for a cylindrical rod are those corresponding to torsional oscillations in which the displacement is parallel to the circumference of rod and perpendicular to the axis. These solutions satisfy the boundary conditions exactly.

No simple crystal generates these waves; however, by cutting y crystals into sectors and combining and orientating the sectors properly a very close approximation to this type of drive and detection can be achieved. We have used both four- and six-section assemblies with no apparent difference. The first data with these "torsional" crystals showed promise. Phenyl benzoate was used to seal the crystal to the sample. The effect of crystal loading was computed by considering the compound system of crystals and rods with rigid coupling and calculating the free resonance modes. On comparing these calculated modes with the observed it became apparent that the coupling between the rod and crystals was not rigid but varied erratically with frequency. Further computations showed that very loose viscous coupling would leave the rod free. Dow V-9 resin, viscosity 3000 poises, was tried with considerable improvement. Dow V-2 resin, viscosity 10 poises, was then used, and apparently this removes the crystal loading completely.

The data of Fig. 4 were obtained on two quartz rods. The mean deviation from the average of the points on these curves is ±1.0 m/sec. This is about the expected experimental error. The difference between the two is ascribed to the fact that they are not from the same stock. These data indicate that within these frequency limits the assumption of negligible crystal loading is valid.

Similar data on three samples of Armco iron are shown in Fig. 5. These three samples were cut from the same stock and machined to size. A complete set of data was taken, the samples thoroughly annealed, and the measurements repeated. The annealing gave an over-all decrease in velocity of about 0.1% but no other change. The data of Fig. 5 were taken after annealing. These data show the velocity to be practically independent of frequency for the range 0.5 to 1.5 Mc and to decrease by some 10 m/s in the range 1.5 to 3.5 Mc.

Dr. A. W. Nolle has pointed out, however, that if the

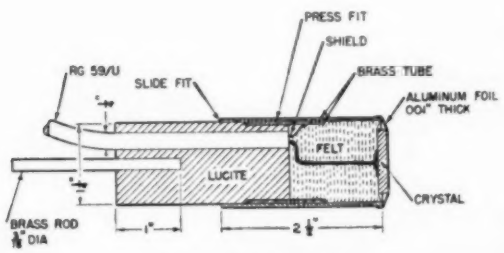

FIG. 3. Crystal holder.

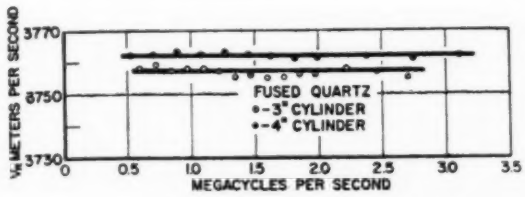

FIG. 4. Torsional wave velocity *vs* frequency in fused quartz.

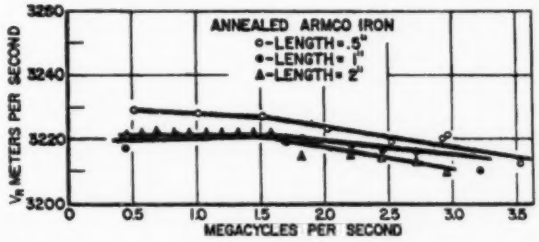

FIG. 5. Torsional wave velocity *vs* frequency in Armco iron.

viscosity of the coupling medium is complex there will be a small correction on the resonant frequency. This correction is essentially the ratio of the imaginary part of viscosity to the product of the mode number times the acoustic impedance of the sample.

If the imaginary part of the viscosity is proportional to frequency it gives a constant shift in the calculated velocity independent of frequency. Our results on fused quartz indicate that either the imaginary part of the viscosity is negligibly small, or it is proportional to the frequency. This may well explain the discrepancy between the velocity in the half-inch sample of Armco iron and that in the one- and two-inch samples.

JOURNAL OF APPLIED PHYSICS VOLUME 26, NUMBER 11 NOVEMBER, 1955

Ultrashort Light and Voltage Pulses Applied to Silver Halide Crystals by Turbine-Driven Mirror and Spark-Gap Switch*†

J. H. WEBB
Research Laboratories, Eastman Kodak Company, Rochester, New York
(Received May 20, 1955)

Studies of electron mobility in silver halide crystals have been carried out by Haynes and Shockley by means of ultrashort light and voltage pulses applied simultaneously to large, single crystals of these materials. Their apparatus made use of a radar-type, pulse-forming network discharged through mercury spark-gap tubes. An apparatus for carrying out this same type of experiment has been developed using an air-driven turbine with a mirror and a spark-gap switch. Repetitive light pulses of 3.33-microsecond duration and voltage pulses of 10 kv and about 20-microsecond duration can be applied to a crystal at a rate of 500 per second. The light and voltage pulses can be initiated simultaneously or at controlled time intervals. The simplicity and practicality of this type of apparatus for electron mobility and photolysis studies on the silver halides are illustrated by experimental results. Light pulses from a mercury arc release photoconduction electrons in the surface of a silver chloride crystal. The voltage pulse pulls the liberated electrons in a straight column for varying distances through the crystal, where they become trapped. This is shown by the direct photolysis along the column in the crystal. Also, print-out silver specks produced in large photographic grains are displaced to one side of the grains by the voltage pulses applied during exposure. The displacement is in the direction that electrons are pulled in the applied field. By separation of the light pulse and voltage pulse in time, the mean lifetime of the photoliberated electrons can be studied. The lifetime of the electrons was found to be approximately 10 microseconds, of the same order as that of electrons in large, well-annealed single crystals of silver chloride.

INTRODUCTION

TO study electron mobility in the silver halide crystals with direct-current electrical fields, it is necessary to work at very low temperatures in order to suppress the ionic conductivity that exceeds by many-fold the electronic conductivity in photoconductivity. To study electronic mobility at room temperature, which is the region of main interest in photographic processes, Haynes and Shockley[1] developed a technique using simultaneously applied pulses of light and voltage to crystals for a few microseconds' duration, repeated 500 to 1000 times per second. In this way, the silver ions, which give rise to the ionic conductivity, do not have a chance to move in the short times involved, whereas the electrons, which are highly mobile, can be moved several centimeters in these short times. Electrons released by light and trapped again in the crystal produce visible print-out silver which can be used as an indicator for the movement of the electrons in the crystal. By such techniques, Haynes and Shockley were able to measure the mobility of photoconduction electrons in crystals with considerable accuracy. These workers used for their experiments a radar-type, pulse-forming network, which was discharged by means of pulsed mercury spark-gap tubes, to obtain square-wave pulses of light and voltage of a few microseconds' duration.

The apparatus to be described here was developed

* Communication No. 1730 from the Kodak Research Laboratories.
† Presented at the meeting of the American Physical Society, Baltimore, Maryland, March 19, 1955.
[1] J. R. Haynes and W. Shockley, Phys. Rev. 82, 935 (1951).

for carrying out the same type of experiment as that performed by Haynes and Shockley in a different manner. Although it is impossible to obtain with this apparatus the square-wave pulses of voltage as obtained with the pulse-forming network, nevertheless, the apparatus can perform in a manner to give useful results. In addition, it has certain advantages over the radar-type equipment in simplicity, reduced power requirements, and versatility in allowing the time between light pulse and voltage pulse to be varied in a precise manner. The main purpose of the present paper is to describe this newly developed apparatus. A few results obtained with the apparatus in crystals of silver halides will be presented. These include columns of print-out silver produced by photoconduction electrons pulled through large single crystals of silver chloride and the displacement of photolytic silver in large silver bromide emulsion grains.

APPARATUS

Turbine

A schematic drawing of the apparatus is shown in Fig. 1. A small air-driven turbine (diameter, 3 cm) is shown in the center of the diagram with a mirror M and two electrical contacts S_1 and S_2 attached. The turbine is a copy of one kindly loaned to the author by Dr. J. W. Beams, in 1935, and described in a previous paper.[2] This turbine has a cone-shaped bottom that fits into a similarly shaped stator with several air jets projecting at appropriate angles along the inner surface of the stator cone. The air jets impinge upon minute blades in the form of shallow furrows cut at angles around the cone-shaped bottom of the rotor. The rotor is made of phosphor bronze and has a flat stellite mirror of high quality (8-×11-mm clear aperture) mounted vertically on its top. The rotor can be readily turned at a speed up to 1600 rps by application of about 80 lb/sq inch air pressure to the inlet hose attached to the stator of the turbine.

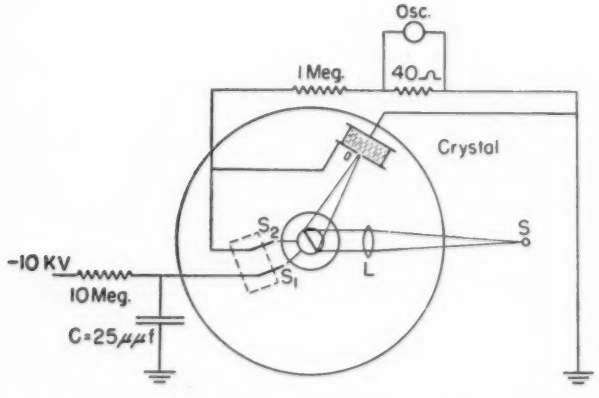

FIG. 1. Schematic drawing of air-driven turbine, optical system for illuminating crystal, and electrical circuit for applying voltage pulses.

[2] J. H. Webb, J. Opt. Soc. Am. 26, 347 (1936).

Light Source

The light source S is a General Electric Type H-3 mercury arc with its outer glass envelope removed. The arc consists of a vertical quartz tube about 0.5 inch high and 0.25 inch outside diameter. When the lamp is run with a dc current of 0.5 ampere, the hot column of mercury vapor comprising the vertical line source has a width of about 2 mm. Light from the source S is focused by the quartz lens L to form an image of 1-mm width. The light from the lens forming the image is reflected from the face of the stellite mirror placed so that the 1-mm image is focused at a distance of 5 cm from the mirror. As the mirror turns, the 1-mm-wide image is swept past a small aperture (1.5-mm diameter) in the front plate of the condenser holding the crystal. The rotor was turned at 500 rps in all experiments to be reported here. At this speed and with a separation distance of 5 cm between mirror and crystal, the 1-mm image of light passes a point on the crystal in 3.33 microseconds. The intensity of the combined radiations λ3650 and λ4047 A (the main wavelengths producing photolysis in the crystal) in the image from the H-3 mercury arc amounts to about 10^{10} quanta/cm²/flash.

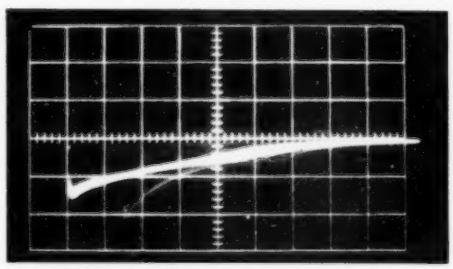

FIG. 2. Oscillogram of negative voltage pulse applied to crystal (10 microseconds equal to one large-scale division).

Voltage Pulses

The short-time voltage pulses are repetitively applied to the condenser containing the crystal through radial metal wires attached to the rotor, as shown in Fig. 1. The two projecting wires are mounted on one side of the rotor with an angular separation of 50°. Two stationary copper-wire electrodes are placed near the rotor in a position to almost make contact with the rotating electrodes on each revolution of the rotor. The two sets of electrodes have an air gap between them of about 1 mm at their closest approach. When sufficient voltage difference is applied to the stationary electrodes, the two sets of electrodes act as a rotary spark-gap switch to apply the voltage to the crystal condenser, as shown in Fig. 1. A low-power dc voltage supply (Beta Electric Corporation) is connected to one of the stationary electrodes, as shown. Between the voltage

supply and the rotary switch is placed a 10-megohm series resistor, followed by a 25-$\mu\mu$f condenser connected to ground. The 10-megohm resistor acts to drop the voltage to near zero on each discharge across the rotor electrodes, and the 25-$\mu\mu$f condenser acts as a small reservoir to supply sufficient charge to raise the voltage of the small crystal condenser to full value. The second stationary electrode is connected directly to the front plate of the crystal condenser, the back plate of the crystal condenser being connected to ground. Thus, on each revolution of the rotor, the spark-gap switch applies a pulse of voltage to the front plate of the crystal condenser. In order to bring the crystal condenser back to zero potential after each voltage pulse, a circuit containing a 1-megohm resistor is shunted around the crystal condenser. This resistance, together with the capacity of the crystal condenser, gives an *RC* product corresponding to a time constant of a few microseconds. The total duration of the voltage pulse on the crystal condenser, however, is determined by the entire circuit,

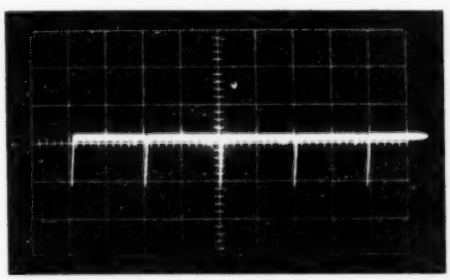

FIG. 3. Oscillogram of voltage pulses corresponding to revolution frequency of air-driven turbine (1 millisecond equal to one large-scale division).

including the 25-$\mu\mu$f condenser preceding the spark-gap switch, which must also discharge through the spark-gap switch and the 1-megohm resistor. The time constant of this circuit (time to decay to $1/e$ value) is theoretically 25 microseconds, and the measured value of the time decay of the voltage pulse on the oscilloscope is very close to this value, as shown in Fig. 2. It should be mentioned that the rotary spark-gap switch works very effectively at the speeds involved. The spark gap does not break down at the point of closest approach of the electrodes, but preceding this point. With 10-kv potential, the gap breaks down when the electrodes are about 3 mm apart. With the currents involved, the electrodes show no sign of burning off in continuous running periods of 20 hours.

The synchronization of the light pulses and the voltage pulses is achieved by placing the stationary electrodes of the spark-gap switch in the correct angular position relative to that of the mirror, so that the spark gap breaks down when the light image falls on the aperture in the front plate of the crystal condenser. It is possible to alter the separation time between the light and the voltage pulse by altering the position of

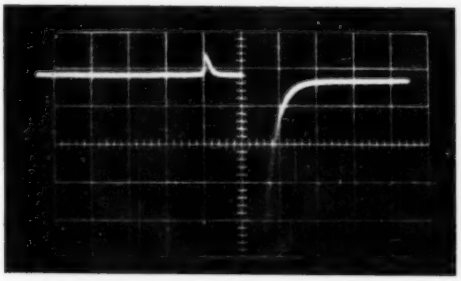

FIG. 4. Oscillogram showing light pulse and exponentially decaying voltage pulse on a single-sweep oscilloscope beam (40 microseconds equal to one large-scale division).

the stationary electrodes. With the rotor turning at a speed of 500 rps, a complete revolution corresponds to 2000 microseconds. Accordingly, a maximum separation time of this order of magnitude can be achieved between the light and the voltage pulse with either the light or the voltage pulse leading.

To observe the speed of the air turbine, an oscilloscope provided with a single sweep is connected across a 40-ohm resistor at the low-voltage end of the circuit shunting the crystal condenser. The trigger-sweep circuit is set so that one voltage pulse triggers the sweep and, providing the sweep time is sufficiently long, a number of succeeding pulses will be recorded on a single trace. This is illustrated in Fig. 3, in which the sweep velocity of the oscilloscope beam corresponds to one large-scale division per millisecond. The negative pulses along the trace occur at 2-millisecond intervals, indicating a rotor speed of 500 rps.

The synchronization of the light and voltage pulses is observed by picking up an electrical signal from both the light pulse and the voltage pulse on a single sweep of the oscilloscope beam. To obtain a signal from the light pulse, a Lucite probe optically connected to a photomultiplier tube is placed at the position of the aperture in the front plate of the crystal condenser. This signal was arranged to give a positive voltage pulse to the oscilloscope. A sufficiently strong signal was obtained, in this case from one of the voltage pulses, by direct radiation from the spark-gap switch, to trip the single-sweep beam of the oscilloscope. With a sufficiently long sweep, subsequent light and voltage pulses are registered on the same trace. This is shown in Fig. 4, where the positive light pulse appears just preceding the negative voltage pulse. By arranging the relative positions of the spark-gap electrodes and the mirror, it is possible to fix the time separation between light and voltage pulses in any desired manner. In Fig. 4 the horizontal time scale is 40 microseconds per large-scale division.

In Fig. 5 is shown a photograph of the complete apparatus. The rotor is in operation with the spark-gap switch arcing. The apertures in the crystal condenser are plainly in view, as well as the Lucite probe attached to the photomultiplier tube. It is obvious how the

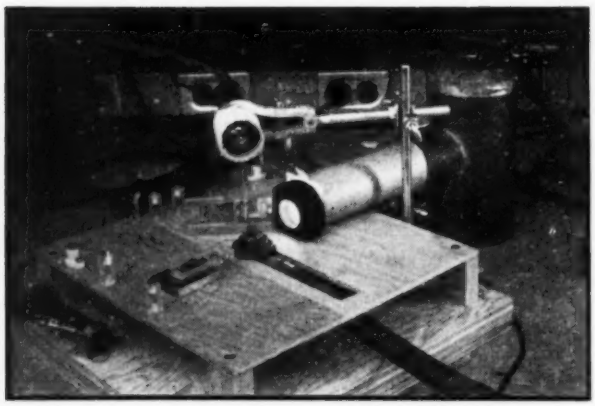

FIG. 5. Photograph of complete apparatus, showing light source, turbine, crystal holder, electric circuits, and photomultiplier pickup tube.

stationary spark-gap electrodes can be shifted in angular position in order to change the time separation between light and voltage pulses.

ILLUSTRATIVE RESULTS

In Fig. 6 is shown a photograph of a silver chloride crystal (3×7×10 mm) that received an 18-hour exposure to pulses of light and voltage initiated simultaneously. The light was applied to the crystal in the 3-mm direction through two circular holes (1.5-mm diameter) in the front plate of the crystal condenser. The crystal used here was unannealed. The rotor was run at 500 rps. The crystal condenser was placed at 5-cm distance from the center of the rotor. With a light image of 1-mm width rotating in a circle of 5-cm radius, and a rotor speed of 500 rps, the time of each light pulse amounts to 3.33 microseconds. The radiation in the image incident on the crystal that is absorbed by silver chloride, consisted of the mercury lines given in Table I. The condenser plates were separated from the crystal surface on each side by a thin sheet of mica to avoid electrical breakdown and direct current flow into the crystal from the electrodes. The voltage pulse in this experiment amounted to −8 kv applied to the condenser plate containing the aperture for the light exposure. The voltage pulse was applied instantaneously at time t_0 and decayed exponentially to zero with time. The time required for the voltage to fall to $1/e$ of its initial value was measured on the oscilloscope as 20 microseconds. The light pulses were applied simultaneously with the beginning of the voltage pulses.

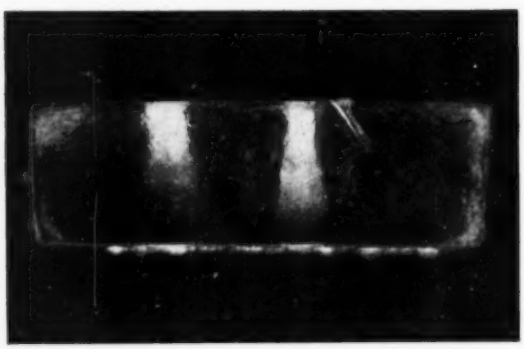

FIG. 6. Photomicrograph (10 times) of silver chloride crystal, showing two faint columns of photolytic silver through crystal.

As may be seen in Fig. 6, there are two columns of photolytic silver extending throughout the depth of the crystal. As explained by Haynes and Shockley, the photolytic silver results from the photoconduction electrons being trapped at various points throughout the crystal depth. The drift mobility, μ_D, of the electrons in well-annealed silver chloride crystals, is about 50 cm/sec per volt/cm, and the mean free lifetime is about 10 μsec. Therefore, the distance d traveled by an electron in a well-annealed crystal, under conditions of the present experiment should be

$$d=\mu E t=\mu\frac{V}{L}t \text{ cm}=50\frac{8\times10^3}{0.3}\times10\times10^{-6}=13 \text{ cm},$$

where V is the total voltage across the crystal of length L cm. Since the crystal of silver chloride used in this experiment was not annealed and therefore not free of traps, the mobility was reduced and the mean lifetime of the electrons was less than in a perfect crystal. Therefore, electrons were trapped on passage through the crystal. The trapped electrons were subsequently neutralized by migration of silver ions to form internal specks of photolytic silver. Some photolytic silver was also formed on the rear surface of the crystal, owing to some electrons being drawn completely through the crystal and trapped there to form silver.

TABLE I.

λ(a.u.)	Relative intensity	Quanta/cm²/flash
2650	0.02	
2967	0.05	
3022	0.16	6.6×10^9
3124	0.50	
3341	0.06	
3654	1.00	9.0×10^9
4078	0.28	2.5×10^9
Total	2.07	18.1×10^9

To illustrate the free migration of electrons completely through the crystal, a well-annealed silver chloride crystal was subjected to light and voltage pulses, as shown in Fig. 7. In this case, the apertures in the front condenser plate were in the form of letters. In Fig. 7(a) is shown the print-out silver on the front face of the crystal where considerable surface silver was formed, owing to the trapping of electrons in surface states. This crystal was subjected to simultaneous pulses of light and voltage for 40 hours, the voltage being 9 kv across the crystal. As may be seen, the silver

images are sharp in this case. In Fig. 7(b) are the images of the same letters as they appeared on the back surface of the crystal (crystal 3 mm thick). Here it will be noticed that the images of the letters are more diffuse. The letters *G* and *M* were chosen as appropriate reminders of the names of Gurney and Mott, who were the first to elucidate the mechanism of formation of photolytic silver in the silver halides.

A more useful application of the present apparatus is in connection with the simultaneous light- and voltage-pulse experiments with emulsion grains. In this case, a small strip of film (3 mm×13 cm) with emulsion grains of silver bromide in a single layer is placed in a Lucite holder, as shown in Fig. 8. The Lucite holder is placed between the plates of a condenser, with the film lying in the arc of a circle centered about the rotating mirror *M*. The light image *I* travels from right to left along the face of the film, which stands vertically in the applied pulsed electric field *E*. With the mirror turning at 500 rps, each point on the film receives a 3.33-microsecond light pulse 500 times per second. If the

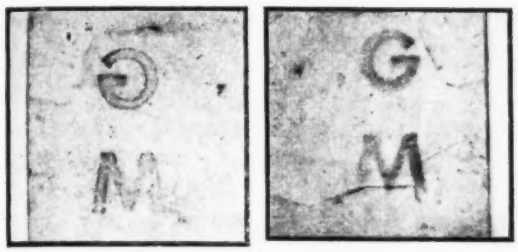

(a) (b)

FIG. 7. Photomicrographs of two faces of silver chloride crystal with images printed on two opposite faces: (a) print-out silver on front face of crystal; (b) blurred image produced on back face by electrons pulled through crystal by electric field.

light flash is made simultaneous with the voltage pulse at the left end of the film strip, then the light pulse will lead the voltage pulse by 44 microseconds at the right-hand end of the film strip. In this way, a variable-time separation between light pulse and voltage pulse, up to 44 microseconds, can be achieved for a single piece of film in one experiment. Accordingly, emulsion grains subjected to this variable treatment can be studied along the strip of film.

In order to show the results obtainable with this apparatus on individual photographic grains, the photomicrographs of Fig. 9 are presented. These pictures represent microscopic fields taken at random on the emulsion. The emulsion grains shown here received 20 hours of pulsed exposures, for which the repetition rate was 500 per second, the duration was 3.33 microseconds per pulse, and the intensity was about 2×10^{10} quanta/cm²/flash. The grains shown in these figures were very large, being of the order of 10μ in diameter for the largest grains. The voltage pulse across the condenser plates was 8 kv and the separation between the plates was 3 mm, giving a maximum field strength of 26.6 kv/cm. The actual field in the silver bromide grains is less than this, depending on the

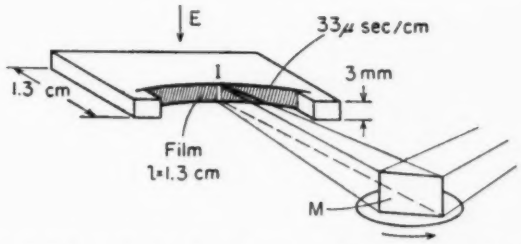

FIG. 8. Schematic drawing illustrating holder for film, in which light and voltage pulses can be applied along strip with variable time separation.

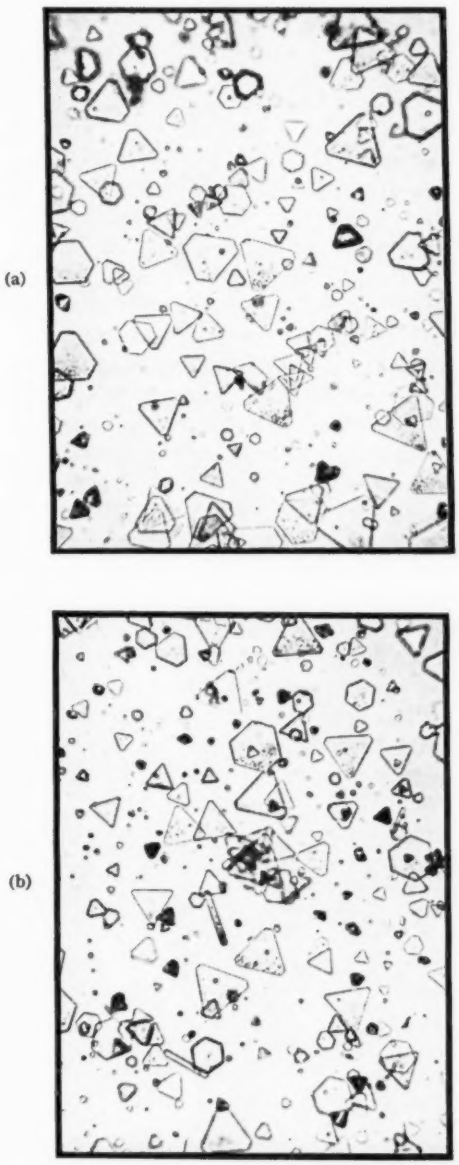

(a)

(b)

FIG. 9. Photomicrographs showing large, single crystal grains of silver bromide with displaced photolytic silver.

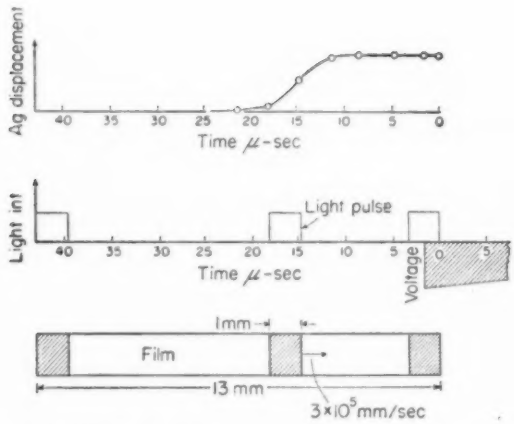

FIG. 10. Diagram to illustrate exposure conditions and results of displacement of photolytic silver on photographic grains receiving pulsed exposures with variable delay time between light and voltage pulses.

geometrical spacing of the grains in the gelatin and the relative dielectric constant of the two media. Assuming equal spacing for grains and gelatin and dielectric constants of silver bromide and gelatin to be 12 and 5, respectively, the field in the grain would be about 11 kv/cm. The initiation of the voltage pulse was simultaneous with the light pulse (see Fig. 4), and the duration of the voltage pulse was of exponential shape with time, decaying to $1/e$ of its maximum value in 20 microseconds. In making the photomicrographs, the microscope was focused on a single grain near the center of the field. However, various other grains in each field are also more or less in focus. It will be seen that most of the grains in focus exhibit a marked displacement of the silver specks in one direction. The direction of displacement corresponds to the direction in which electrons would move in the applied electric field. It is to be realized that the photolytic silver specks shown here consist of direct print-out silver with no development. Especially to be noticed are the needle-shaped grains showing silver displaced toward one end.

In Fig. 10 are shown results obtained by a study of silver displacement in emulsion grains exposed in the manner illustrated in Fig. 8, where the separation time between light and voltage pulse varies continuously along the strip of film. In the lower part of the figure is shown the strip of film with light images at different locations. In the middle line of the figure are shown the light pulses and voltage pulses placed on a time scale in microseconds for different points along the film. At the extreme right end of the figure, the light pulse and the beginning of the voltage pulse are simultaneous. At other points along the film, the light pulse leads the voltage pulse by varying times from zero to about 43 microseconds. The results observed on displaced silver in the grains are depicted qualitatively in the graph at the top of the figure. As this curve shows, if the light pulse precedes the voltage pulse by 20 microseconds or more, there is no displacement of photolytic silver in the grains. However, beginning at a separation time of about 15 microseconds, there is considerable displacement, about half the grains being affected. At a point 10 microseconds before the voltage pulse, the displacement has reached a strong value that changes little with reduced separation time. The curve shown was arrived at by viewing the displaced silver under a light microscope. At 1-mm intervals along the strip of film, the grains were scanned across the strip and the percentage number of grains in which displacement occurred, as well as the gradient of displaced silver, was noted. Both factors influenced the drawing of the curve. The chief point, however, is that the displacement of silver had reached its maximum value at a separation time of at least 10 microseconds between the light and the voltage pulse. This seems to afford evidence that the electrons liberated by the light pulse have a free lifetime of the order of 10 microseconds. This result indicates that the silver bromide crystalline grains of this emulsion were as free of electron traps as well-annealed, large, single crystals of silver chloride. The emulsion grains used here were pure silver bromide of the so-called primitive type, that is, no deliberate chemical sensitizing material was used in their preparation.

The experimental results given here are mainly for the purpose of illustrating what can be accomplished with this simplified apparatus. It is believed that its simplicity, low power requirements, and versatility in allowing variation in separation time between light and voltage pulses afford real advantages for this type of research.

Deformation of an Explosively Loaded Aluminum Single Crystal*

JOHN S. RINEHART†
Michelson Laboratory, U. S. Naval Ordnance Test Station, China Lake, California
(Received May 31, 1955)

A hollow cylindrical single crystal of pure aluminum was deformed by detonating an explosive charge that had been placed axially within the crystal. The approximate strain rate achieved was 10^5 sec^{-1}. The object of the test was to relate the pattern of deformation to the stresses set up by the explosive and the crystallographic axes of the crystal. The reaction of the cylinder was markedly different from the reaction which would be exhibited by a similarly shaped cylinder of polycrystalline material. The deformation was nonuniform with both the fracturing and the plastic flow exhibiting a twofold symmetry that could be unambiguously related to the orientation of stress with respect to the crystallographic axes and their associated slip systems.

INTRODUCTION

IT is well known that under identical stressing a metal single crystal does not deform in the same way as a polycrystal specimen of the same metal.[1–4] The deformation of the crystal is usually anisotropic and takes place along well-defined slip systems. The systems that will be operative in a particular case depend, among other factors, upon the structure of the crystal that is being stressed, the temperature, the rate of straining, and the angles made between the stress fields and the crystallographic directions and planes of the crystal.

The object of the present test was to see whether the pattern of deformation of a single crystal would be similarly governed by crystallographic directions and planes when stressed at the very high rates of strain and exceedingly high pressures that are reached when an explosive charge is detonated in intimate contact with the crystal.

EXPERIMENTAL

A hollow cylindrical single crystal of pure aluminum was used for the test specimen. The crystal, shown in longitudinal cross section in Fig. 1, was one which had been previously prepared in a form suitable for tensile testing.[5] It was grown by the strain-annealing process. The section between the point A and the point B is single; the threads themselves, since they were not subjected to strain during annealing, remained polycrystalline. Between the points A and B, the specimen had been machined straight to a diameter of 13 mm. A hole 5 mm in diameter had been bored through the specimen before the crystal was grown. Thus in cross section the specimen was essentially a thick-walled right circular cylinder with a 4-mm thick wall. Eight circumferentially evenly spaced lines had been ruled parallel to the axis on the outside surface of the cylinder. These were numbered consecutively from 1 to 8 for reference purposes.

The specimen was partially filled with a charge of explosive, the charge detonated, and the fragments then recovered.[6] The explosive loading is also illustrated in Fig. 1. Only half of the cavity was filled so that an undistorted portion of the specimen could be compared with the distorted portion. Granulated PETN was used; a small plug of plasticine wax was used to hold the PETN in place. The specimen was suspended centrally by wires at the center of a 10-in. diameter, 18-in. long thin cardboard tube which was surrounded by a large amount of dry sawdust.

The orientation of the crystal was determined by means of back reflection Laue x-ray photographs.[7] The axis of the cylinder had very nearly a ⟨102⟩ direction. Its orientation is shown stereographically in the right

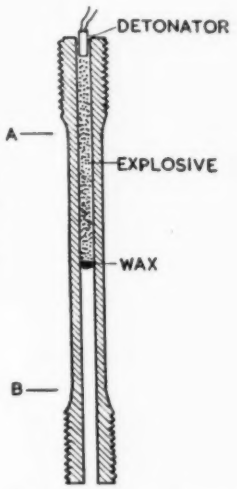

FIG. 1. The metal-explosive system. Section of specimen between points, A and B, is aluminum single crystal. Threaded portions are polycrystalline.

* The work reported herein was performed while the author was temporarily in residence in Cambridge, England.

† Present address: Smithsonian Astrophysical Observatory, 60 Garden Street, Cambridge 38, Massachusetts.

[1] E. Schmid and W. Boas, *Plasticity of Crystals* (F. A. Hughes, London, 1950). Translation of "Kristallplastizität," published in 1935.

[2] C. F. Elam, *The Distortion of Metal Crystals* (Oxford University Press, New York, 1935).

[3] E. O. Hall, *Twinning* (Butterworths Publication Ltd., London, 1954).

[4] C. S. Barrett, *Structure of Metals* (McGraw-Hill Book Company, Inc., New York, 1952), second edition.

[5] The author is greatly indebted to Mrs. C. F. Tipper, Engineering Laboratory, Cambridge University, who kindly provided the crystal from her collection and suggested that it be used in the present study.

[6] Dr. W. E. Soper of the Armament Research Establishment was good enough to provide facilities for detonating the charge and recovering the pieces.

[7] Dr. P. B. Hirsch of the Cavendish Laboratory kindly arranged to have the photographs taken.

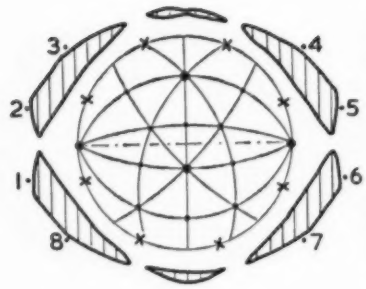

FIG. 2. Cross-sectional view of fragments. Diagram also illustrates the relationship between circumferential tensile stress, deformation pattern, and orientation of specimen with respect to crystallographic axes. Each cross indicates the direction of the tensile stress at a ruled line. The axis of the specimen passes through the center of reference circle of stereogram.

hand side of Fig. 2. The axis of the crystal has been put through the center of the stereogram. The locations of the ruled lines are shown by black dots on the circle in the reference plane.

DEFORMATION AND FRACTURING

On the recovery of the fragments it was found (1) that the loaded portion of the specimen had broken into four major pieces and two minor ones, and (2) that the plastic deformation which took place within the wall of the specimen before it broke up was nonuniform to a remarkable degree. The respective cross sections of fragments were traced and are assembled in Fig. 2. The numbers indicate the locations of the ruled lines. The unloaded portion of the cylinder remained intact but suffered considerable deformation in the region close to where the fragments broke off from it. The deformation was quite uniform in the threaded polycrystalline portion of the cylinder.

Both the fracturing and the plastic deformation seem to exhibit a strong twofold symmetry. Between rulings 1 and 2, and between rulings 5 and 6, the crystal was drawn down abruptly to a knife-edge. Between rulings 3 and 4, and rulings 7 and 8, the section was reduced much more gradually. On the other hand, the extension was much greater. Each section is nearly uniform between the two rulings preserved on each of the major fragments. The thickness of the section was reduced from 4.0 mm to 2.5 mm, a 40% reduction. The distance between the two ruled lines on any piece was about 7 mm, a percentage increase also of about 40% over the original separation of 5.1 mm, about equal to the reduction in thickness.

The two minor fragments are of interest for two reasons: first, because they exist at all, and second, because they are dissimilar. The fragment between ruling 3 and ruling 4 is seen to be nearly broken in two, while that between 7 and 8 is not.

One aspect of the deformation suffered by the unloaded end of the specimen as a consequence of the fragments being pulled off of the end of the stump is illustrated in Fig. 3. The left-hand outline in this figure is a plan view traced from a photograph. The locations of the ruled lines are indicated by lines and numbers. As a fragment left the stump, each presumably by its own momentum, the end of the fragment and the corresponding section of the stump were drawn to sharp knife-edges.

THE STRESSES

The stress field generated by a detonating explosive charge is usually a complex and rapidly changing one.[8] In the particular expolosive-metal system investigated here, the detonation proceeds, upon initiation, down the cylinder of the explosive with a velocity of approximately 26 000 ft/sec. At the front of the detonation the maximum pressure reached will be about 3×10^6 psi. The charge initiates a sharp-fronted high-intensity stress wave within the wall of the cylinder. The induced stress wave moves both outward and downward though the cylinder. As the stress wave propagates through the cylinder wall, there exist simultaneously a very high tensile stress in the circumferential direction, a compressive stress in the radial direction, and a compressive stress parallel to the longitudinal axis of the cylinder. In an isotropic homogeneous material, the stress field and the strains which accompany its application will be axially symmetrical except for certain end effects. A cylinder composed of a single crystal will not, in general, be elastically isotropic. The anisotropy in aluminum is small, however, and it probably does not need to be considered further here.

A circular cross section of the cylinder would show the vector component of the stress wave in that plane as a circularly expanding wave. The material immediately behind the wave front will be moving radially outward. Its particle velocity will depend upon the level of stress within the wave. The highest particle velocity will be attained at the inner surface: there its value will be in the neighborhood of 4000 ft/sec. The particle velocity just behind the wave front will decrease fairly rapidly as the wave progresses radially outward in the plane of the cross section. If it is assumed that the decrease is not so rapid as to influence greatly the deformation of the cylinder, and thus that the cylinder can be thought of as beginning to expand substantially as an integral hoop, then the rate of strain is between 10^5 sec^{-1} and 10^6 sec^{-1}.

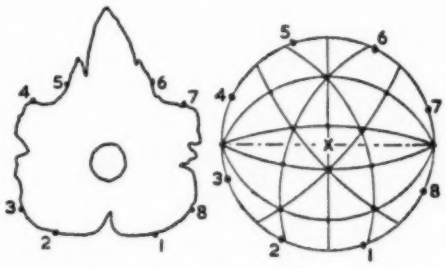

FIG. 3. Comparisons between shape of end of stump and orientation of specimen with respect to crystallographic axes. Each heavy black dot indicates the location of a ruled line. Cross on stereogram indicates direction of axis of the specimen.

[8] J. S. Rinehart and J. Pearson, *Behavior of Metals Under Impulsive Loads* (American Society for Metals, Cleveland, 1954).

The stresses in the plane are, for purposes of analysis, best resolved into two components: a radially directed compressive stress and a tangentially directed tensile stress.

A further stress that comes into play in the present instance is the tensile stress that is set up because the fragments are pulled away, by their own momentums, from the unloaded portion of the cylinder. This stress can, to a first approximation, be considered as acting parallel to the axis of the cylinder.

ALUMINUM SLIP SYSTEM

The deformation of single metal crystals under gradually applied uniaxial tension and compression has been studied extensively. In most cases the deformation can be ascribed to slip which consists of the displacement of one part of the crystal relative to another along a definite crystallographic plane (slip plane) and in a crystallographic direction (slip direction). The behavior of crystals under biaxial stress conditions, however, does not seem to have received much attention.

There are 12 equivalent glide systems available in an aluminum single crystal[9]: four octahedral planes each with three face diagonals. The choice of system in the case of extension depends upon the direction of the tensile stress in relation to the crystallographic axes. Glide always occurs along the system subjected to maximum shear stress. Multiple slip can occur in several special directions. A uniaxial tension can produce multiple slip if it lies along a ⟨100⟩, ⟨110⟩, or ⟨111⟩ direction for which there are respectively eight, four, and six equally favorable slip systems.

In general, as a specimen is pulled in tension, the slip planes will rotate in such a way that they tend to align themselves with the axis of the specimen. As the deformation continues, the resolved shear stress may increase along a second system and finally may equal that along the first system. Glide will then take place along both systems and crystal axes will rotate so that the axis of tension is held in a plane symmetrical to the two acting systems. The end point of deformation will be reached when the axis has moved to the point that is symmetrically located between the two operative slip directions.

RELATIONSHIP BETWEEN STRESSES, SLIP SYSTEMS, AND DEFORMATIONS

The orientation relationships that exist between stresses, slip systems, and deformations are perhaps best seen by superimposing two or more diagrams. For example, the relationship between the tangential circumferential stress, the slip systems of the cylinder, and the deformation which took place in a plane perpendicular to the axis of the cylinder is evident in Fig. 2. In this figure the stresses all lie on the periphery of the reference circle of the stereographic projection. Each cross indicates the direction of the circumferential tensile stress at one of the ruled lines. The stereogram has been so oriented with respect to the deformation pattern that there is a one-to-one correspondence between the locations of the crosses and the locations of the ruled lines on the pattern of the deformed crystal. The contour of the end of the stump is shown beside a properly oriented stereogram in Fig. 3. In this case the tensile stress passes through the axis of the cylinder. The heavy black dots on the periphery of the stereographic projection indicate the location of the ruled lines.

The most significant fact evident from these diagrams is that the pattern of deformation is closely controlled by the orientation of stresses with respect to the crystallographic axes and their associated slip systems. Viewed purely qualitatively the relationships are most striking. For example, in Fig. 2 the portion of the specimen that contains rulings 2, 3, 4, and 5 is almost, but not quite, a mirror image of the portion that contains rulings 6, 7, 8, and 1. The slight departure from true symmetry is readily relatable to a corresponding asymmetry in the orientation of the stresses with respect to the crystallographic axes. The secondary asymmetries in Fig. 3 are equally as striking in this respect.

Fracturing, which is preceded by extensive but highly localized slip, seems to occur at a region in the crystal where the tensile stress lies along a direction that is most favorable for multiple slip. The sharp knife-edge fractures that lie between ruling 1 and ruling 2 and between ruling 5 and ruling 6 and the sharp edge on the end of the stump are examples of such fractures. The fracturing between the ruling 7 and ruling 8 and between ruling 3 and ruling 4 is somewhat modified as a consequence of the fact that the axis of the specimen is slightly inclined to the [001] direction in the crystal. Had the axis been parallel to a ⟨100⟩ direction, the deformation pattern of the crystal would most likely have exhibited fourfold symmetry.

It has not been possible to determine the exact number of slip systems that were operative or to measure the amount of slip which took place along any one system. One difficulty is that the slip system for aluminum is most complex; a second, that no data seem to have been published concerning the deformation of single face centered crystals under biaxial stressing; and a third, that the stress situation generated by an explosive charge is a very complicated one.

[9] G. I. Taylor and C. F. Elam, Proc. Roy. Soc. (London) **102**, 643 (1923); **108**, 28 (1925).

Influence of Pulsed Magnetic Fields on the Reversal of Magnetization in Square-Loop Metallic Tapes

D. S. RODBELL AND C. P. BEAN
General Electric Research Laboratory, Schenectady, New York
(Received July 7, 1955)

Reversal of magnetization in square-loop metallic tapes is described in terms of the domain geometry and the dependence of this geometry upon the applied magnetic field wave shape. For a steady field whose amplitude is slightly greater than the coercive force, the reversal is accomplished by growth of a single axial domain originating at the thin tape edge. For steady fields of much greater amplitude, the reversal domain grows in from all tape surfaces. Because of the finite nucleation time required to establish the reversal domain, short duration, high amplitude field pulses can be used to investigate the mechanism of nucleation of the high field reversal domain configuration. A model which accounts for the nucleation process is suggested. The compatability of this model with various experimental results is presented. From these results an understanding of the high field reversal-domain configurations and the kinetics of the nucleation and growth of these domains in lamellar materials is obtained. An auxiliary result obtained is the value of the "intrinsic mobility" of a domain wall which for a 65 Permalloy specimen is determined to be about 100 cm/sec oe.

INTRODUCTION

WHEN a change is made in the state of magnetization of a ferromagnetic metal, eddy currents of appreciable magnitude are generated. In many cases the magnetic fields from these currents determine the geometry of the domain walls whose motion gives rise to the changing magnetization. Conversely, the amount and distribution of the eddy currents is determined by the geometry of the domain walls and their motion. For materials thicker than several thousandths of an inch, the eddy currents account for the major part of the energy loss during rapid magnetization.

We present experiments to confirm the domain wall geometries previously postulated[1,2] and to illuminate the process by which these domains are formed.

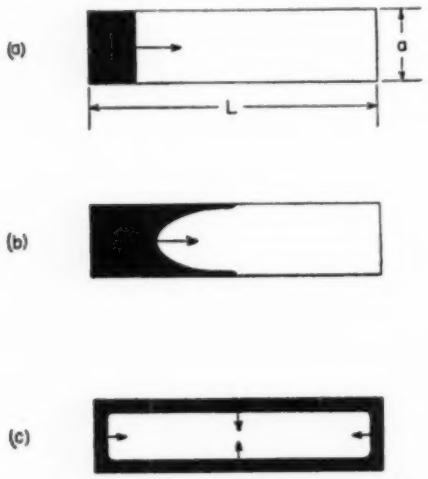

FIG. 1. Cross sections through a long rectangular tape of width L and thickness a, illustrating the eddy current controlled domain wall motion for (a) low fields, (b) intermediate fields, and (c) high fields ($H_a \gg H_c$). The magnetization has been reversed in the dark regions by passage of the domain walls indicated.

[1] C. P. Bean and D. S. Rodbell, J. Appl. Phys. **26**, 124–125 (1955).
[2] Williams, Shockley, and Kittel, Phys. Rev. **80**, 1090 (1950).

EDDY CURRENT MODEL

In this section we assume the only inhibition to wall motion, in addition to the coercive force, arises from eddy currents. The domain configuration assumed is illustrated in Fig. 1, which represents a cross section through a very long tape of width L and thickness a. The tape initially was magnetized to saturation and an opposing field than applied. For an opposing field only slightly larger than the coercive force, it is assumed that a single axial domain wall moves across the width of the specimen, as in Fig. 1(a). Surrounding this wall are the eddy currents that act upon the wall through the magnetic field they produce.

As the opposing field is increased, the wall moves faster, generating larger eddy currents. At the center of the wall the net field is $-0.37\ H_a$ in the approximation of zero coercive force. At the surface of the tape, however, the local field is equal to the applied field, H_a, and the domain wall curves until it reaches equilibrium with respect to its surface tension. In the region of low applied fields where the wall is nearly planar, it moves with a velocity proportional to the applied field (in excess of the coercive force) and the time it takes to move across the width of the tape is given accurately[2] (for $L \gg a$) by

$$T = 33.6 B_s a L / \pi^2 \rho c^2 (H_a - H_c) \text{ seconds}, \qquad (1)$$

where B_s is the saturation flux density, a and L are the thickness and width of the tape and ρ is the specific resistance. The units are Gaussian.

For higher fields the surface tension is insufficient to maintain even an approximately plane domain wall, and the wall bends over, the edges moving ahead of the center, as in Fig. 1(b). In addition, other nuclei of the reversed domains will grow at the surface, as discussed in a later section. At sufficiently high fields the domain wall will have completely formed along the perimeter of the tape before the center of the wall has moved very far. For fields of this size the magnetization reverses by

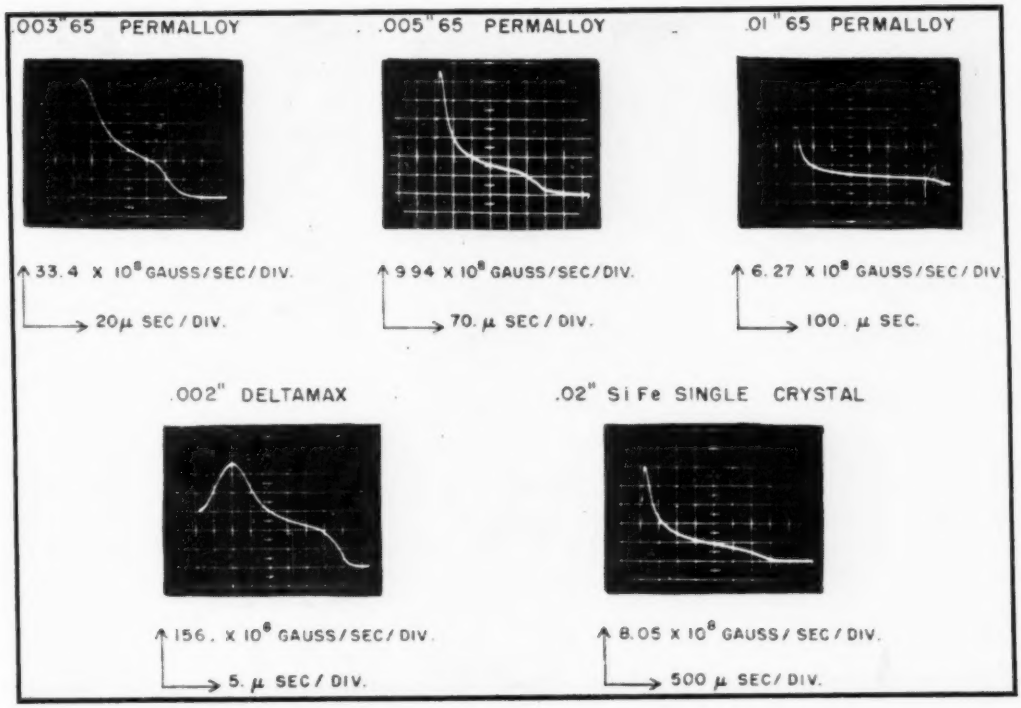

FIG. 2. Some typical high field reversals for the specimens indicated. The shape after the initial peak is characteristic of eddy current controlled motion. The value (H_a-H_c) is about 1 oersted for each.

walls moving in from all surfaces, as in Fig. 1(c), the center of the tape being shielded by the eddy currents which circulate in the space between the domain walls and the tape surface. In this high field region, with the assumption that the cylindrical domain configuration is established instantly on application of the field, the time to reverse the magnetization is given by[3]

$$T=\pi a^2 B_s/c^2\rho(H_a-H_c) \text{ seconds.} \quad (2)$$

There are thus two distinct linear regions in the relation between reversal time and reciprocal excess field, with a time scale ratio approximately equal to L/a. The reversal time is determined by which domain configuration is established, domain walls as in Fig. 1(a) requiring long times and those in Fig. 1(c) requiring only short times.

EXPERIMENTAL OBSERVATIONS AND DISCUSSION

The rate of change of magnetization was measured as a function of time and driving field. Specimens in the form of long tapes wound into toroids, or single crystals cut in the proper fashion, make the demagnetizing end effects negligible. Windings suitable for the driving and setting fields are then applied. A voltage proportional to dB/dt is observed with an auxiliary winding and displayed on an oscilloscope.

Only the data for the 0.005-in. magnetically annealed 65 Permalloy (65% nickel-iron alloy) are presented here in detail; however, 0.003-in. and 0.01-in. tapes of the same material as well as a picture frame single crystal of 3.25% silicon-iron (0.02 in. thick) yield equally confirmative evidence.

In low fields, the domain wall will move with a constant velocity, except when it is near the thin edge of the specimen, since the eddy current distribution is confined to a small region near the wall of width approximately equal to the specimen thickness. From Eq. (1) the magnetization changes at the constant rate

$$dB/dt=\pi^2 c^2\rho(H_a-H_c)/16.8aL \text{ [gauss/second]}. \quad (3)$$

The rate of magnetization is not constant at high fields because, when the closed domain configuration sketched in Fig. 1(c) is formed, the eddy currents, which occupy the space between the domain walls and the surface of the sheet, move in a path of lower resistance as the walls move in toward the center. As the resistance of the eddy current path decreases, the eddy currents increase and the domain wall slows down. For high fields, then, the magnetization reversal rate, dB/dT, should increase during the short time required to grow the configuration, reach a peak corresponding to completion of the growth process, and then decay in a fashion described by the expression

$$(dB/dt)^{-2}=\pi a^2 t/\rho c^2 B_s(H_a-H_c)[\text{gauss/sec}]^{-2}. \quad (4)$$

This form of the relationship is useful for comparison with the experimental data.

Some typical high field reversals are shown in Fig. 2. Low field reversals and the verification of Eqs. (1) and (2) have been described elsewhere.[1]

Experimental confirmation of Eq. (4) is shown in Fig. 3 for the 65 Permalloy tape specimen. The plot of $(dB/dT)^{-2}$ *versus* time in Fig. 3(a) was obtained from

[3] P. F. Dorey, *Soft Magnetic Materials for Telecommunication*, C. E. Richards and A. C. Lunch, editors (Pergamon Press, London, 1953), p. 286.

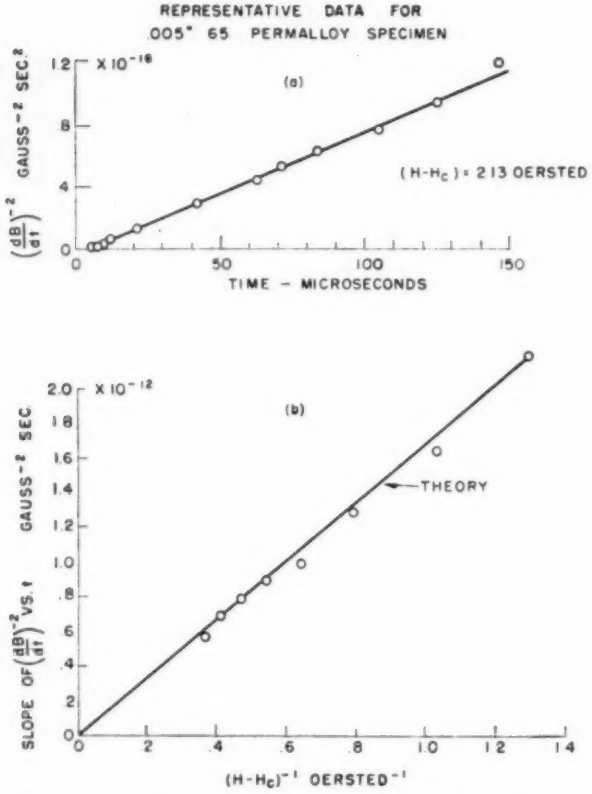

FIG. 3. Analysis of the high field reversal wave shape, (a) $(dB/dT)^{-2}$ *versus* time, whose slope as a function of $(H_a-H_c)^{-1}$ is compared in (b) to the prediction of the high field theory.

an oscilloscope record of a reversal wave similar to those shown in Fig. 2. The curve is a straight line as required by Eq. (4). There are two reasons why the straight line in Fig. 3(a) does not pass through the origin. The first, is that dissipation of energy to the spin system can shift the line to the left, and the second is that a finite time is required to achieve the cylindrical domain configuration, which can shift the line to the right. Neither of these causes should change the slope of the line. The lower plot in Fig. 3 gives the slopes of curves similar to Fig. 3(a) as a function of reciprocal excess field, $(H_a-H_c)^{-1}$. The proportionality is in agreement with theory, and confirms the domain configuration assumed.

Ekstein[4] treats the rate of magnetization with the assumption of a finite mobility for the domain wall in the absence of eddy currents. The result is similar to Eq. (4) with the modification that t is replaced by $(t+t_0)$ where

$$t_0 \equiv \rho c^2/16\pi B_s \alpha^2 (H_a-H_c) \text{ seconds.} \quad (5)$$

The constant α is the domain wall mobility in the absence of the eddy currents and has the units of cm/sec oersted.[5]

Evaluation of the intrinsic mobility can be made using Eq. (17) of Ekstein.[4] The assumption is made that the time of formation of the cylindrical domain wall corresponds to the peak time of the dB/dt wave shape. This will be discussed later. The wall position immediately after formation is determined by integration of the dB/dt *versus* time wave shapes. This may be done since the ratio of $\Delta A/A$ (where ΔA is the area up to the peak time and A is the total area of the wave shape) is a measure of the wall position at any time following the wall formation. An expression that may be solved for t_0 is obtained and from this and Eq. (5) solution is made for α.

The α extracted from data for the 65 Permalloy specimens is of the order of 100 cm/sec oersted. This value can be reconciled with the extremely high mobilities observed in the Sixtus-Tonks type experiments using the reasoning of Williams, Shockley, and Kittel.[2] As a domain wall passes a point in a ferromagnetic material, the magnetic moment at that point must reverse its direction in a time given by the thickness of the domain wall in the direction of its motion divided by the velocity of the domain wall. For glancing angles this time becomes long, the consequent losses low, and the velocity along the specimen large for a given driving field. To a first approximation, the velocity will be given by

$$v=A(H_a-H_c)=\alpha(H_a-H_c)/\cos\theta[\text{cm/sec}], \quad (6)$$

where θ is the angle between the normal to the domain wall and its direction of motion. In Sixtus-Tonks experiments on thin, magnetically annealed 60 Permalloy wires[6] values of A of 7.8×10^4 cm/sec oersted have been

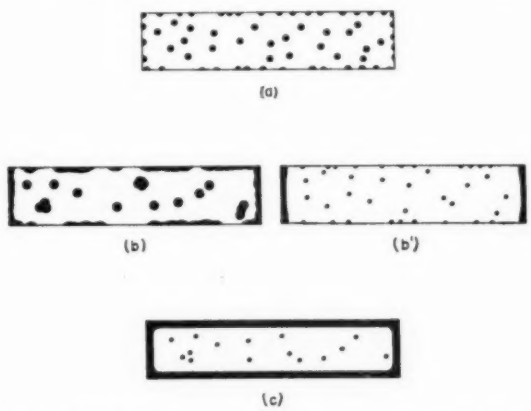

FIG. 4. A high field nucleation model. The cross section is normal to the magnetization in a long thin tape, the dark regions indicate reversed magnetization at various times after application of the reversing field. The growth is mainly eddy current controlled. (a) Immediately after application of the reversing field, nuclei throughout the volume have begun to grow. (b) The growing nuclei have met and joined at many places. (c) The surface is surrounded by the reversal domain, and interior regions of reversal stop growing and collapse. This situation would correspond to the maximum value of dB/dT. Further reversal follows Eq. (4). (b') If the field is removed at the time corresponding to (b), the growth of reversal domains stops and the domain walls retract because of their surface tension.

[4] H. Ekstein, J. Appl. Phys. **26**, 1342 (1955).
[5] L. Landau and E. Lifshitz, Physik z. Sowjetunion **8**, 153 (1935).
[6] L. J. Dijkstra and J. L. Snoek, Philips Research Rept. **4**, 334-356 (1949).

observed while $\cos\theta$ was measured to be 4.3×10^{-4}. Equation (6) predicts α to be 34 cm/sec oersted, which is of the same order of magnitude as that reported above.

The wave shapes of Fig. 2 and the previous discussion concerning Fig. 3 indicate that the time at which the major peak occurs in the *dB/dt versus* time behavior corresponds to the completed formation of the cylindrical reversal domain configuration. We believe this formation to be the result of growth and impingement of small regions of reversed magnetization[7] which occur about inclusions and surface irregularities and which are not completely removed on application of a magnetizing field. The process of Fig. 1 which assumes but one nucleus is discarded since the distance one nucleus can move is, at a maximum, with neglect of the work done against surface energy, on the order of $(A\cdot t_p)$ where A is the Sixtus-Tonks mobility mentioned earlier and t_p is the time for formation of the cylindrical domain wall. This distance is approximately 0.3 cm for a field of two oersteds while the width of the tape is 1.27 cm. Evidently several nuclei were active.

If many nuclei are present, and a field is applied, only those nuclei that are large enough will grow. Considering the nuclei to be long circular cylinders, Appendix 1 shows that those nuclei that have a radius greater than $\gamma/2(H_a-H_c)I_s$ will grow. For two oersteds this critical radius is about 1 micron. The growing nuclei will impinge as shown in Fig. 4. When a cylindrical domain wall surrounds the specimen, eddy currents induced by its motion will shield the nuclei in the interior of the specimen from the applied field, and may even allow them to shrink by contraction of their domain walls.

It is of interest to note that for very thin metallic tapes or for ferrites, where eddy currents play only a minor role, the shielding behavior described above does not hold. In addition, for applied fields greater than the anisotropy field, $2K/I_s$ (where K is the appropriate anisotropy constant), one may expect to find coherent rotation of the magnetization which, from another viewpoint, corresponds to the homogeneous nucleation of an infinitely thick domain wall.

Consider what happens when the driving field is limited to a time shorter than that required to complete a high field reversal but long enough that the cylindrical domain wall configuration of Fig. 4(c) is obtained. When the driving field is removed, the domain wall cannot move outward, for to do so would increase its surface energy. It cannot move inward either, except at the tape edges, for the radius of curvature of the walls that parallel the tape surfaces is much greater than the critical radius for wall collapse.* For this reason the walls† that parallel the broad tape surfaces will remain in place. The radius of curvature of the walls at the edges of the tape, on the other hand, will be less than the critical radius for collapse, and they will move inward slowly. Additional pulses, applied rapidly enough so that only a small amount of inward motion at the edge domain walls can occur will find the domain configuration essentially unchanged between pulses, hence the magnetization as a function of time will be that obtained by segmenting, in time, the steady field reversal. This situation is shown in Fig. 5 wherein the reversal has been completed within three successive pulses, each of 80 microseconds duration. This pulse amplitude, applied as a steady field, would require 200 microseconds to accomplish reversal.

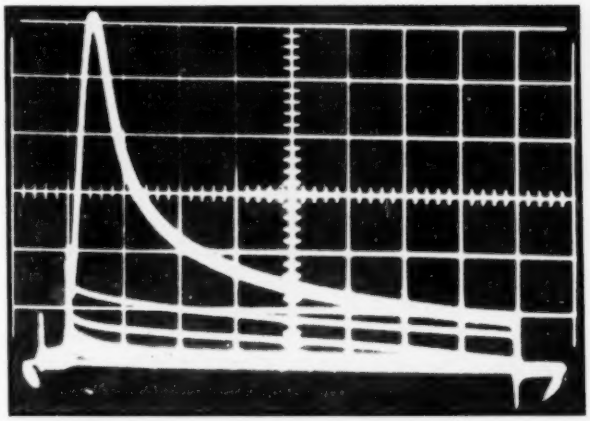

FIG. 5. A high field pulsed reversal for the 0.005-in. 65 Permalloy specimen. The pulse duration is much greater than the peak time with a repetition rate of 60 pps. Successive pulses are superimposed. The pulse amplitude is 2 oersteds. The scales are 10 microsec/div and 33.7×10^3 gauss/sec div.

Consider now a pulse whose duration is just too short to establish a complete cylindrical domain wall. The domain configuration is that shown in Fig. 4(b) where the small nuclei have, in the main, impinged on one another but some breaks exist. If the field is removed at this point, the high curvature at the breaks will cause the domain wall to retreat from these points until, as is shown in Fig. 4(b′), two approximately straight end walls are formed. A second similar pulse will nudge the two walls toward each other, and succeeding pulses will accomplish magnetization by the motion of two edge walls toward the center of the tape. The result is a reversal that depends upon magnetic field and time of application of the field just as though a steady low field were applied [Fig. 1(a)], except that it takes half as long to accomplish because two domain walls are moving. An experimental demonstration of this behavior is

[7] L. J. Dijkstra, "A nucleation problem in ferromagnetism," *Thermodynamics in Physiacl Metallurgy* (A. S. M., 1949), p. 271.

* The critical radius for wall collapse, 0.02_3 cm, is obtained from Eq. (2) of Appendix 1, using $\gamma=0.5$ erg/cm² (an estimate from unpublished experiments), $I_s=1.0_4\times10^3$ cgs and $H_c=0.011$ oersted.

† *Note added in proof.*—We now believe the wall energy appropriate to the Permalloy tape to be more nearly 0.1 erg/cm² than 0.5 erg/cm²; the higher value being obtained from measurements on 65 Permalloy wires of different heat treatment than the tape specimens. In addition, the appropriate value of the coercive force measured on walls unattached to the tape surface is 0.0045 oersteds. These new values decrease the estimate of the critical radius by a factor of about 1/3. This change does not affect the conclusions stated in the text. (The foregoing values are from measurements in this Laboratory, to be published.)

shown in Fig. 6 for a series of driving pulses whose duration is nearly equal to the peak time, and whose repetition rate is 60 pulses per second. The curve of dB/dT as a function of time is shown for every 30th pulse. Each curve of dB/dT is similar to the preceding one, but smaller in amplitude since, in successive pulses, a decreasing volume of material is magnetized in opposition to the field. Quantitatively, the volume available for transient growth and retraction of nuclei with each pulse should decrease linearly with time, and hence the peak height should decrease linearly with time. Figure 6 shows this to be approximately true. In addition, Fig. 6 shows, through the reverse voltage spike following the termination of each field pulse, the collapse of the nuclei when the field is removed.

The preceding discussion and the assumption of nuclei of uniform size and distribution would predict that for pulses of longer duration than that required to establish a cylindrical domain wall, i.e., longer than the peak time, the total time of magnetization (neglecting time between pulses) would be equal to that for a steady field. For pulse durations less than the peak time the cylindrical domain wall will not be formed, and the growth of nuclei accomplished during a driving pulse will completely regress during the time interval between pulses. Complete reversal can never be accomplished with pulses of this duration. These predictions of reversal time as a function of pulse duration are shown as the dashed curve in Fig. 7. The experimental curve is given by the longest solid line in Fig. 7. The lack of agreement in detail is taken as a measure of the degree of nonuniformity in the initial distribution and size of nuclei. Because nuclei of different initial sizes grow at different rates, it may be that in some regions edge walls are formed for pulse durations less than the peak time, allowing the reversal of magnetization to take place for these short pulses. In other regions, a complete cylindrical wall may not be formed in three times the peak time, making the time for reversal in those regions greater than that predicted for pulses of longer duration than the peak time. Furthermore, the lack of a uniform distribution of nuclei throughout the material makes the probability of having a continuous region of reversed magnetization along the edge walls greater than having a similar continuity along the wide faces of the tape (the ratio L/a is about 100). At the peak time, therefore, the chance of having the double edge wall picture of Fig. 4(b′) is good. For a pair of edge walls formed and moving inwards in a stepwise fashion as previously described the time to accomplish reversal is just one half that predicted by Eq. (1). This value is plotted as the open circle in Fig. 7 for the pulse duration just equal to the peak time.

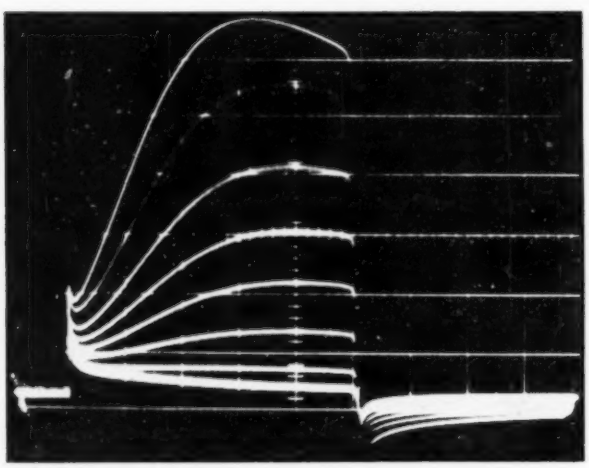

FIG. 6. A high field reversal for the 0.005-in. 65 Permalloy specimen. The pulse duration is about equal to the peak time and the repetition rate is 60 pps. Every 30th pulse is presented. The pulse amplitude is 1 oersted. The scales are 20 μsec/div and 3.3×10^8 gauss/sec div.

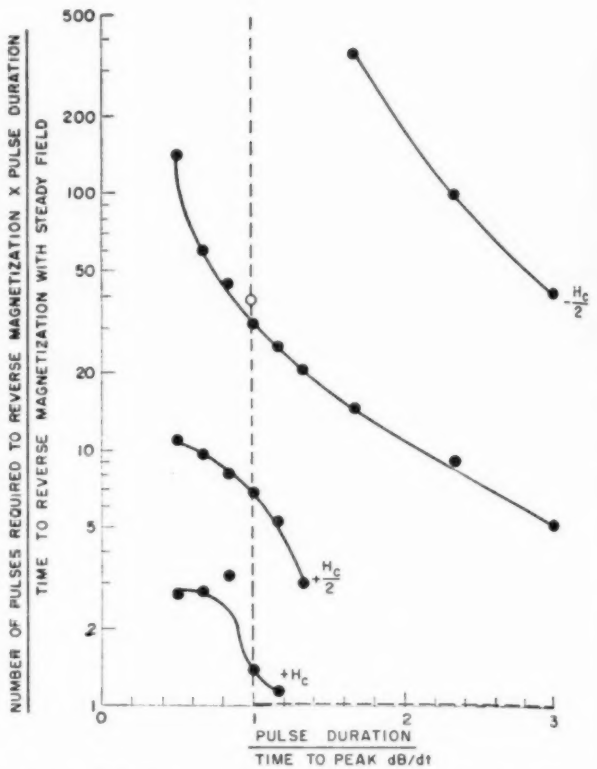

FIG. 7. Pulsed reversal time as a function of pulse duration and background field. Pulse amplitude 2.9 oersteds. The coercive force, H_c, is 0.011 oersted for this tape specimen of 0.005-in. 65 Permalloy. Added fields + are in the direction of the pulse, − are opposite. The dashed curve represents the prediction for completely uniform size and distribution of the nuclei of reversed magnetization.

The other curves in Fig. 7 show the influence of small background fields on the reversal times. As might be expected, background fields in opposition to the driving field increase the reversal time, while those that reinforce the driving field decrease it. The main effect arises from the influence of the background field upon the relaxation of the curved walls of Fig. 4(b′) after the pulse. For instance, background fields in the direction of the pulse cause the curved walls to relax in such a way

that they accomplish more magnetization in the direction of the pulse. If the background field is in the direction opposite to the driving pulse, then in the time between pulses the edge walls of Fig. 4(b′) will relax almost entirely by retracting their advanced ends.

A final point illustrating the influence of domain geometry upon reversal time is given in Fig. 8, which shows two reversal wave shapes (dB/dt *vs* time). The lower of the two traces is a steady field reversal for a field in the transition region between low and high field behavior, where the domain is neither an essentially plane edge wall nor a closed cylindrical domain of high field type. The upper trace was caused by the same steady field, which was, however, preceded by a pulse of 3.6 oersteds and 10 microseconds duration. By the application of the 10 microsecond nucleating pulse, the reversal time was decreased to less than half its value for the steady field alone. The idea here is that the nucleating pulse creates the high field cylindrical domain wall, which then is moved inward by the small steady field that could not itself have established the high-field domain configuration. For still lower background fields, in the low field range, the ratio of reversal times with and without a nucleating pulse should be of the order of L/a, which for this specimen is about 100. Time ratios of this value have been observed and lend support to the concept of reversal domain nucleation presented here.

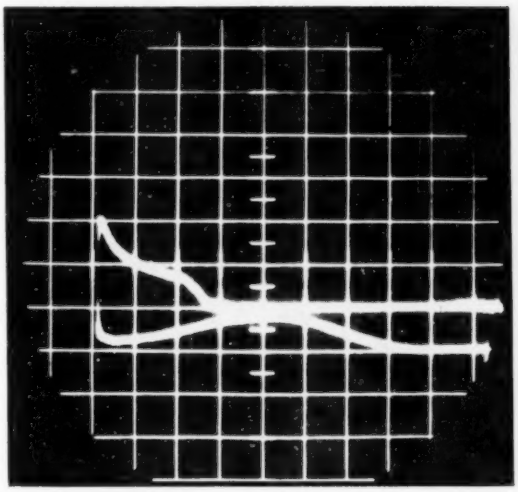

FIG. 8. Demonstrating the effect on total behavior by a nucleating pulse. The steady field is 0.12 oersted for both traces. The upper reversal is preceded by a pulse of 3.6 oersteds 10 microseconds duration. The scales are 1200 microseconds/div and 1.98×10^8 gauss/sec div. The base line has been shifted 1 division.

CONCLUSION

For magnetization accomplished by domain wall motion, the rate of magnetization is determined by the number of domains, their geometry, and the velocity of the domain walls which separate them. For a material with a given distribution of inhomogeneities, the applied magnetic field controls both the domain geometry and the domain wall velocity.

APPENDIX 1

A circularly cylindrical domain wall of radius r will tend in zero field to collapse because of its surface tension. In a material with zero coercive force, the energy per unit length of a domain wall in a field H_a opposing its collapse is (neglecting terms independent of r)

$$F=2\pi\gamma r-2H_aI_s\pi r^2,$$

where γ is the wall energy per unit area, and I_s is the saturation magnetization. To calculate the radius which is in equilibrium with this field, we differentiate the free energy with respect to the radius and equate this derivature to zero, obtaining

$$r_{\text{critical}}=\gamma/2H_aI_s. \tag{A1}$$

Introduction of the coercive force gives the result that for a radius

$$r_{\min}<\gamma/2(H_a+H_c)I_s \tag{A2}$$

the cylinder will collapse. For radius $r_{\max}$ such that

$$r_{\max}>\gamma/2(H_a-H_c)I_s \tag{A3}$$

the cylinder will expand. These results may be generalized to noncircular cylinders by substituting for the radius, the radius of curvature of the cylinder at any point.

JOURNAL OF APPLIED PHYSICS VOLUME 26, NUMBER 11 NOVEMBER, 1955

Spin Echo Serial Storage Memory

A. G. ANDERSON, R. L. GARWIN, E. L. HAHN,* J. W. HORTON, G. L. TUCKER,† AND R. M. WALKER
Watson Scientific Computing Laboratory, Columbia University, New York, New York
(Received July 26, 1955)

By utilizing the method of pulsed nuclear magnetic resonance, radio-frequency energy in the form of pulses can be stored serially in a sample of nuclear spins and recalled at an arbitrary later time within the memory or relaxation time of the spin sample. Weak pulses of radio-frequency energy condition the nuclear spins to start precessing in phase. After they become completely out of phase, a strong recollection pulse brings about a phase reversal of precession and produces a series of spin echoes in a sequence corresponding to direct or reverse order of input pulses. The echo amplitudes in such a series are given as a function of the number and strength of the input pulses and the conditions for maximum storage capacity in a spin ensemble are determined. The maximum specific storage capacity in liquids is expressed in terms of the thermal noise of the detecting apparatus, the effect of self-diffusion of the molecules, and the relaxation times. The origin of undesired spin echoes arising from the interaction of input pulses is discussed, and means for eliminating these echoes by frequency and magnetic field modulation are discussed and applied. Extensive use is made of a magnetic field modulation technique to destroy undesired echoes, and to permit novel types of recall of serially stored groups of pulses. Whereas Fernbach and Proctor [J. Appl. Phys. 26, 170 (1955)] have demonstrated multiple pulse storage under conditions which reproduce the input pulse shape, the present investigation is concerned with the storage of a maximum number of pulses whose shape is ideally determined by the nuclear spin band width. In practice, the order of 1000 rf pulses can be stored and recalled by this method in a proton sample several cc in volume within a memory time of 10 to 50 milliseconds. Large specific storage capacities expected for existing long relaxation time liquids are not realized because of excessive self-diffusion.

INTRODUCTION

A VARIETY of techniques in nuclear magnetic resonance[1,2] have been applied in recent years to the study of nuclear moments, molecular structure, and the solid state. Although these techniques were originally devised for measurements of nuclear magnetism, they also appear to be useful for applying nuclear induction phenomena in the development of elements for electronic devices. The very narrow nuclear resonance lines which can be obtained, and the long times during which coherent spin precession is maintained, indicate that a nuclear spin system can serve as a very narrow band filter and as a medium in which information may be stored. The phenomenon of spin echoes[3,4] is illustrative of the latter possibility. In this paper methods are presented for the storage of information in a nuclear spin system by use of the free induction spin echo technique. A critical discussion and analysis is given of the advantages and limitations of spin echo storage.

The memory storage in a nuclear spin system is based upon principles of free nuclear precession. According to the standard arrangement in nuclear resonance experiments, a sample of nuclear magnetic moments placed in a tuned inductance becomes polarized in a large magnetic field $\bar{H}_0$,‡ and presents an average magnetic moment $\bar{M}_0$. The inductive coil with its axis perpendicular to $\bar{H}_0$ is excited, for example, by a pulse of alternating magnetic field for a short time t_w at an angular frequency $\omega=\omega_0=\gamma H_0$, where γ is the nuclear gyromagnetic ratio and ω_0 is the nuclear Larmor precession frequency. The moment vector $\bar{M}_0$ is then tipped from its alignment along $\bar{H}_0$, precesses about $\bar{H}_0$ at the natural frequency ω_0 after the pulse is removed, and induces a voltage in the coil. This new orientation of $\bar{M}_0$ is obtained in a short time t_w, which includes many cycles of Larmor precession, but is very much less than the nuclear relaxation times. In practice we deal with the average moment $\bar{M}_0$ in liquids. Here $\bar{M}_0$ is made up of component moment vectors, with long relaxation times, distributed over a range of precessional frequencies because of external $\bar{H}_0$ field inhomogeneities over the sample volume. During the short pulse these component moments do not lose precessional coherence about the $z(\bar{H}_0)$ axis. During the long relaxation time following the pulse, however, each component vector precesses about the z-axis at its particular Larmor frequency ω_0, and induces a voltage in the coil. The net voltage lasts only as long as the component moments precess in phase. This can be visualized by first transforming to a frame of reference (x',y',z') which is chosen to rotate at frequency ω'. In this frame each vector precesses at a frequency $\Delta\omega=\omega_0-\omega'$, where ω' is the average frequency at which the entire nuclear ensemble induces a free inductive voltage in the coil. The integrated signal then lasts for a time $1/(\gamma\Delta H_M)$ (assuming a relaxation time $\gg 1/(\gamma\Delta H_M)$, where ΔH_M is the average H_0 field inhomogeneity over the sample.

If a second pulse is applied at time $\tau<T'$, where T' represents the observed relaxation time of the nuclei, the spin vectors can be conditioned to add in phase and produce a free induction spin echo signal at $t=2\tau$. Such a signal comprises the simplest type of nuclear storage

* Now at Physics Department, University of California, Berkeley, California.
† Now at IBM Engineering Research Laboratory, Poughkeepsie, New York.
[1] F. Bloch, Phys. Rev. **70**, 460 (1946).
[2] Bloembergen, Pound, and Purcell, Phys. Rev. **73**, 679 (1948).
[3] E. L. Hahn, Phys. Rev. **80**, 580 (1950).
[4] E. L. Hahn, Phys. Today **6**, No. 4, 4 (1953).
‡ Vector quantities are to be denoted by bars.

[see Figs. 1(a) and 1(b)]. The first rf pulse is to be taken as the information pulse, the second pulse the recollection pulse, and the echo is to be called the output echo or stored pulse. The output echo pulse may be arbitrarily delayed by applying the recollection pulse at any time within the relaxation time of the spin sample. In principle, maximum delays of the order of a second from nuclei in liquids are possible. The fixed delay of information, inherent in the mercury delay line or magnetic tape, is not imposed by nuclear spin storage, and the delay time is temperature independent. The present investigation extends the study of such nuclear echoes to cases where a series of weak information pulses is applied to the inductive coil, and then received later by the coil in the form of echoes after a strong recollection pulse is applied. For cases in which several successive echoes appear, Fernbach and Proctor were the first to show[5] that weak input information pulses of square and trapezoidal shape are reproduced in shape by the echo if the nuclear spin band pass is broad enough to store faithfully all of the frequency components contained by the information pulses. They apply a weak information signal of amplitude H_1 gauss under the conditions $H_1 \ll \Delta H_{Av}$ and $\gamma \Delta H_{Av} t_w \gg 1$, followed by a strong recollection pulse to obtain the echo. The storage of information pulses may also be considered under the conditions: $\gamma H_1 t_w \ll 1$ and $\gamma \Delta H_{Av} t_w \ll 1$. With these conditions the echo output pulse lasts for a time $1/(\gamma \Delta H_{Av})$, as shown in earlier work,[3] so that the echo now displays the Fourier integral of the spin spectrum rather than the pulse shape obtained by Fernbach and Proctor. Application of pulses according to the first inequality in this case results in a small nutation or tipping angle $\theta = \gamma H_1 t_w$ of $\bar{M}_0$ away from the z axis, as seen in the rotating frame of reference, so that a proportional amount of magnetization $\bar{M}_0\theta$ is projected onto the xy-plane. The $\bar{M}_0\theta$ component can be stored for later display in the form of a delayed echo, as shown in Fig. 1(b). The second inequality insures that nearly all of the moment vectors in the spectrum are tipped through the same angle by the pulse, and that the echo will have a short lifetime given by $t_e \sim 1/(\gamma \Delta H_{Av})$ if ΔH_{Av} is made large over the sample volume. The condition above is not achieved in our work here; rather, the condition $\gamma \Delta H_{Av} t_w \sim 1$ applies in our experiments. It can be shown, however, that our results do not differ significantly from the results obtained assuming $\gamma \Delta H_{Av} t_w \ll 1$.

The appearence in time of echoes in the two cases introduced above is the same. In the case given by Fernbach and Proctor, echo shape reproduction is obtained at the sacrifice of optimum output signal amplitude because only a small fraction of the spins are excited due to the necessary condition that $\gamma \Delta H_{Av} t_w \gg 1$. For our case, where most of the spin spectrum is excited due to condition $\gamma \Delta H_{Av} t_w \sim 1$, a larger signal-to-noise

[5] S. Fernbach and W. Proctor, J. Appl. Phys. **26**, 170 (1955).

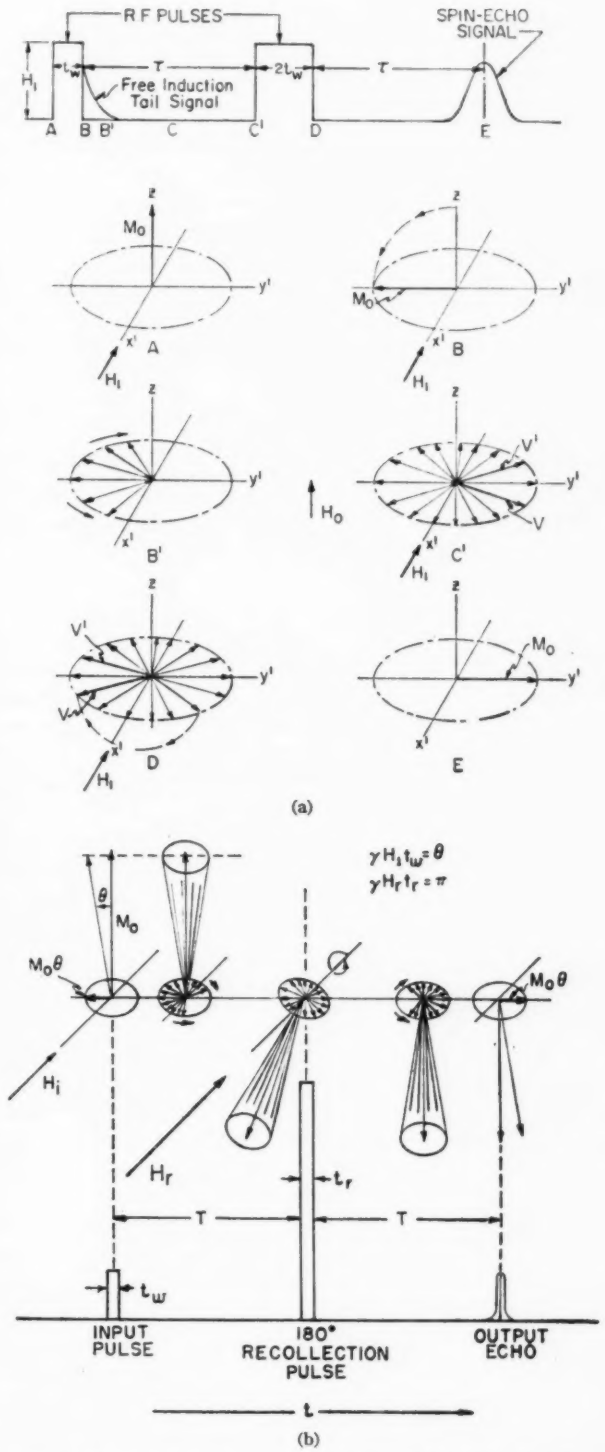

FIG. 1(a). Spin echo formation in the special case where a 90° and 180° pulse sequence is applied. From B to C' vectors V and V', which are symmetrically off resonance with respect to ω, precess through equal but opposite angles about the z-axis in time τ. From C' to D they are rotated in a time $2t_w \ll \tau$ by 180°, and again precess through the same angles in time τ to coincide at $E(t=2\tau)$ where the echo maximum is formed. This realignment holds for all moment vectors in the spectrum. 1(b). Echo formation due to a weak input pulse and strong 180° recollection pulse. The mechanism of echo formation is the same as in Fig. 1(a) except that the small magnetization $M_0\theta$ provides the signal.

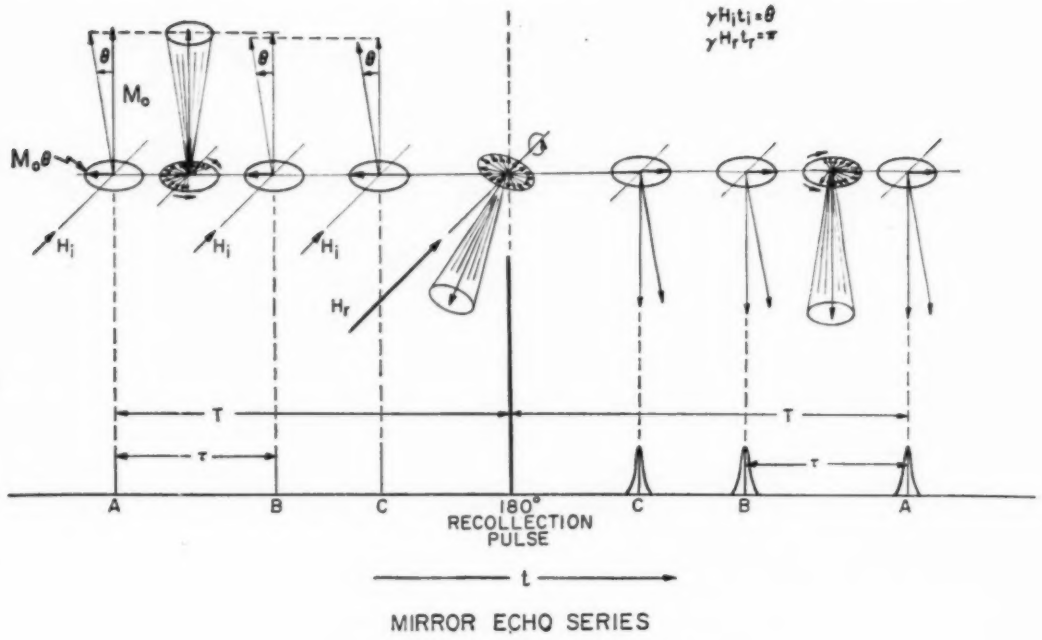

FIG. 2. Multiple mirror echo formation.

ratio of output echoes is obtained along with a higher echo resolution. An appreciable storage capacity is then available in which a large number of radio-frequency pulses can be stored and recalled as a series of sharp echoes.

Inverse Order Mirror Echoes

A qualitative vector model of the formation of a series of spin echoes is shown in Fig. 2. After the first information pulse has depleted the z magnetic moment component by the small amount $M_0\theta^2/2$, the magnitude $M_z=M_0(1-\theta^2/2)$ remains along the z-axis to be tipped by a second information pulse at τ. To a first approximation a second pancake is formed independently, but superimposed upon the first one, and produces an echo at $t=2T-\tau$ with magnitude $\sim\bar{M}_0\theta$. A series of such information pulses applied in the order 1, 2, 3, $\cdots$, n, $\cdots$, N will then be returned after the 180° recollection pulse in the order N, $\cdots$, n, $\cdots$, 3, 2, 1 as inverted or "mirror" echoes.

Stimulated Normal Order Echoes

A more useful type of echo momory is obtained from a series of normal order echoes, rather than from the inverted series described above. The storage outlined above takes place in the $x'y'$ plane, whereas the stimulated echo type storage takes place along the z-axis. The stimulated or normal order echo for memory storage is obtained as follows (see Fig. 3). At $t=0$ a strong 90° pre-pulse is applied to the sample at the pulse condition $\gamma H_p t_p=\pi/2$. At $t=t_p$ the total moment M_0 is rotated into the y' axis and $v=M_0$, where the x', y', z' components of $\bar{M}$ are to be denoted by u, v, M_z. After a time $t\gg 1/(\gamma\Delta H_M)$ (at 0′ in Fig. 3) all of the component moment vectors are spread out in the $x'y'$ plane, and the average total moment is zero. It is instructive to follow the motion of a particular vector precessing at frequency $\Delta\omega$ in the absence of pulses. Let one information pulse be applied at time τ. This vector, denoted by $\bar{M}_{\Delta\omega}$, is at the angular position $\Delta\omega\tau$ at time τ, and provides $v=M_{\Delta\omega}\cos\Delta\omega\tau$. Other component vectors will superimpose upon $\bar{M}_{\Delta\omega}$ at $t=\tau$ which have precessed through a total angle $\varphi=\Delta\omega\tau+2\pi n$, where n is an integer. For the present we shall only follow the motion of $\bar{M}_{\Delta\omega}$. During the information pulse the z component is tipped through a small angle $\theta=\gamma H_i t_i$ about $\bar{H}_i$, and provides the z component $(\bar{M}_{\Delta\omega})_z=M_{\Delta\omega}\theta\cos_{\Delta\omega}\tau$. While $\bar{M}_{\Delta\omega}$ undergoes such a motion, there will be a vector $\bar{M}_{\Delta\omega+\pi/\tau}$ with frequency $\Delta\omega+\pi/\tau$ which carries out a similar motion with opposite phase. This must follow since the condition $\gamma H_M\tau\gg 1$ implies that all of the vectors are completely spread in the $x'y'$ plane at $t=\tau$, and there must be a vector $\bar{M}_{\Delta\omega+\pi/\tau}$ antiparallel to $\bar{M}_{\Delta\omega}$ at this time with angular position $\varphi=\Delta\omega\tau+\pi$. For $t>\tau$ these components are antiparallel along the z-axis until a 90° recollection pulse ($\gamma H_r t_r=\pi/2$) is applied at $t=T$. Such a distribution along z constitutes the z-axis storage. At $t=T+t_r$, $(\bar{M}_{\Delta\omega})_z$ and $(\bar{M}_{\Delta\omega+\pi/\tau})_z$ are then opposed along the y' axis, and precession begins for each at frequencies $\Delta\omega$ and $\Delta\omega+\pi/\tau$ respectively. The stimulated echo v_s will be seen to occur at $t=T+\tau$, where both these particular vectors superpose at an angle $\Delta\omega\tau$ with the y' axis. The echo will be due to the contribution of all vector pairs $(\bar{M}_{\Delta\omega+[2\pi n/\tau]})_z$ and $(\bar{M}_{\Delta\omega+[(2n+1)\pi/\tau]})_z$, where $n=0$ for the pair discussed above.

There appear to be three chief advantages in using stimulated echo memory in preference to the inverted type echo. First, of course, the output echoes are in normal order. Second, it has been shown[3] that the lifetime for spin vector storage along the z-axis is primarily determined only by T_1 for information closely following the recollection pulse. With this condition the echo is not seriously affected by the self-diffusion attenuation. For information which does not follow closely after the recollection pulse, the attenuation effects of both self-diffusion and T_2 become serious. A third virtue of the stimulated echo lies in the fact that its mode of storage allows it to be distinguished from mirror echo storage. While the stimulated echo vectors are stored along the z-axis before the recollection pulse, it is possible to apply along the z-axis, momentarily, an arbitrary inhomogeneous magnetic field pulse H_c, so that the phase memory of any $x'y'$ plane echo storage may be completely erased. Yet the z memory is returned when H_c returns to zero, and the z-axis stimulated echo storage remains undisturbed and independent of the phase loss in the $x'y'$ plane. Later it will be shown how this technique serves to eliminate undesired interpulse $x'y'$ plane echoes which would otherwise interfere with the desired stimulated z-axis storage echoes.

Maximum Echo Amplitude

It can be shown that the ideal amplitude of the echo of the nth information pulse in a train of N echoes, under

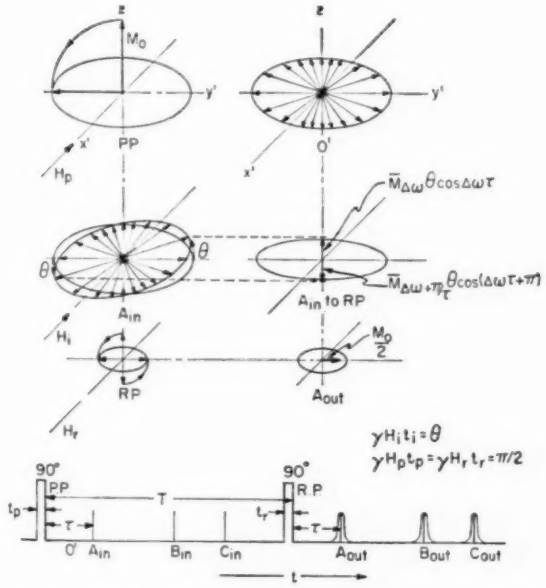

FIG. 3. Normal order echo formation. A pre-pulse (PP) and recollection pulse (RP) of 90° are applied. At 0′ all vectors have completely spread in the $x'y'$ plane. The first input pulse at A_{in} tips the pancake of moments by angle θ, and stores the z components of magnetization as shown from A_{in} to RP. At RP the stored z component is rotated by a 90° recollection pulse into the $x'y'$ plane. At A_{out} the stimulated or normal order echo occurs with a peak value of $M_0\theta/2$. Other input pulses at B_{in} and C_{in} produce independent echoes in the same manner.

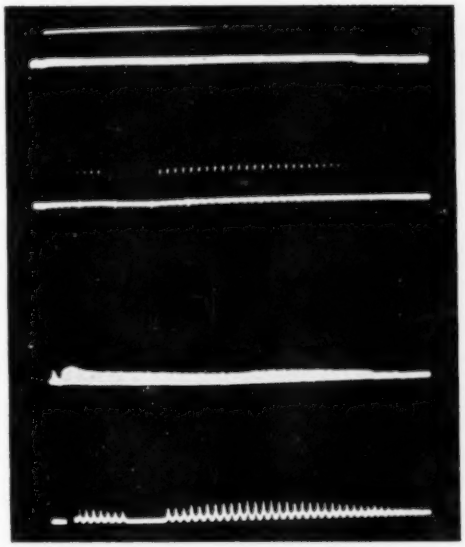

FIG. 4. 450 normal order echoes. Top to bottom: input envelope, input envelope expanded 5×, output envelope, output envelope expanded 5×. Total time of input 1/60 sec.

the condition of equal $\theta=\gamma H_i t_i$ for each information pulse, is given by

$$a_n(N)=\sin\theta(\cos\theta)^{n-1}\left(\cos^2\frac{\theta}{2}\right)^{N-n} \tag{1}$$

for mirror echoes. These functions represent the fraction of M_0, the initial magnetization, which appears at the time of the echo maximum. The ideal amplitude is given by

$$b_n(N)=\tfrac{1}{2}\sin\theta(\cos\theta)^{N-n}\left(\cos^2\frac{\theta}{2}\right)^{n-1} \tag{2}$$

for normal order echoes.

Maximizing with respect to θ, we find that if $\hat{E}_1$ is the maximum voltage echo signal which can be obtained in the detecting coil with a single information pulse, the maximum voltage signal of the first of N echoes for both the mirror and stimulated echo case is

$$\max E_1(N)=\hat{E}_1/(eN)^{\frac{1}{2}}. \tag{3a}$$

When the first pulse is maximum, the last echo will be given by

$$E_N(N)=\hat{E}_1/(e^{\frac{1}{2}}N)^{\frac{1}{2}}, \tag{3b}$$

so that $E_N(N)>\max E_1(N)$. Equation (3a) is the fundamental equation which limits the number of pulses which can be stored by the spin echo method, since N can only be increased until $\max E_1(N)$ becomes of the order of the thermal noise generated by the detecting system.

Signal Limitations on Memory Storage

The maximum number of echo pulses obtained in this investigation is of the order of 1000 normal order echoes. Figure 4 shows a case in which 450 normal order proton echoes are being read out. A glycerine-water mixture of

2 cc volume was used having a $T_1=70$ milliseconds. The information pulse width is 7 microseconds, and there is a 1 millisecond delay before read out. Cycle repetition rate of the entire pattern is 3.75 sec^{-1} and the signal to noise ratio is estimated to be 8 to 1.

The natural spin relaxation parameters involved in the choice of sample materials are given by T_1 and T_2, where T_1 is the time for recovery of M_z toward thermal equilibrium, and T_2 is the time for retention of phase coherence of spin precession in the $x'y'$ plane. In mirror echo memory the storage time is limited by T_2, while in normal order echo memory the storage time is limited by both T_1 and T_2. In both cases the cycle repetition rate is limited by T_1.

For storage times of longer duration than a few milliseconds the echoes suffer also an attenuation due to the loss of phase memory caused by the self-diffusion of molecules in liquids. The formulas for the attenuation due to self-diffusion and natural relaxation can be applied to determine storage times which are realized in practice. It is found for normal order echoes with a total useful memory time, T, between entry of pre-pulse and entry of recollection pulse, that the last observable echo, relative to the echo obtained in the absence of T_1, T_2, and diffusion, is attenuated by the factor[5]

$$A=\exp\left\{-\left[\frac{2T}{T_2}+\tfrac{2}{3}k_1T^3\right]\right\}. \tag{4}$$

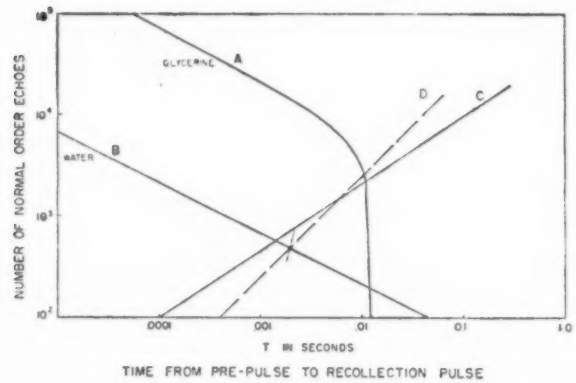

FIG. 5. Plot of maximum number of pulses, N, which can be serially entered into a spin echo store in a period of time T, under the conditions that relaxation and diffusion attenuation be limited to a loss in echo strength of $1/e$. Sample volume $V=1$ cm³, nuclear band width is determined by a magnetic field gradient over $l_0=1$ cm [see Eq. (13)], external field $H_0=7450$ gauss, resonance frequency $32M$ cps. Curves A and B are plots of N *vs* T from Eq. (14) which considers diffusion and T_2-relaxation. Curve A represents glycerine with parameters in Eq. (14) of $D=2\times10^{-5}$ cm²/sec, $T_2=24\times10^{-3}$ sec.; curve B is for water with $D=2\times10^{-5}$ cm²/sec and $T_2=2$ sec. Curve C is the signal to noise limit alone from Eq. (12) and curve D represents a practical limit on N *vs* T, assuming a pulse power limit of 500 watts [see Eq. (18) with $t_p=t_s/4=T/4N$]. An approximate maximum number of echoes is determined for glycerine, for example, by noting that diffusion- and T_2-attenuation limit the values of N and T to those under curve A, while a signal-to-noise ratio of 10 to 1 limits N and T to the values under the curve C. The intersection of A and C determines the approximate maximum number of echoes under the conditions given.

The symbol $k_1=\gamma^2(dH_0/dl)^2D$ where dH_0/dl is the average field gradient and D is the self-diffusion coefficient. Since the last echo is the most severely attenuated of all echoes in the entire train, it will suffice to consider the limitations on this echo to be the limitations upon the multiple pulse storage capabilities of the system.

A calculation of the signal to noise ratio of the nuclear system follows along lines similar to the calculations of Bloembergen, Purcell, Pound,[2] and Torrey,[6] with the modification that the total available nuclear signal power is divided among N information echoes. First we consider the unattenuated echo signal E_0 which results across the tuned solenoid for the case of 90° information pulse, pre-pulse and recollection pulse

$$E_0=\tfrac{1}{2}(Qnl_0B_sA_1\omega)10^{-8}\text{ volt}, \tag{5}$$

where n is the number of solenoid turns per cm, A_1 is the cross-sectional area of the coil, l_0 is the length of the coil, and the flux of nuclear induction is given by $B_s=4\pi M_0$. In general

$$M_0=\frac{\gamma^2\hbar^2I(I+1)NH_0}{3kT}.$$

N is the number of nuclear moments per cc having spin I, T is the absolute temperature, and k is the Boltzmann constant. Formula (5) assumes an ideal sample filling factor, namely that the nuclear sample completely fills the solenoid, and the rf field is uniform in the solenoid volume. For the tuned RLC circuit the rms thermal noise voltage at the terminals of the inductance is taken to be[7]

$$E_T=\left(\frac{kT}{C}\right)^{\frac{1}{2}}=\frac{63.5\omega\sqrt{L}}{10^{12}} \tag{6}$$

where $T=293$°K, and C is the capacitance in farads. Assuming $L=4\pi n^2V\cdot10^{-9}$hy for an infinite solenoid, where the solenoid volume $V=l_0A_1$, the maximum signal-to-noise ratio is given by

$$R=\frac{E_0}{E_T}=\frac{(QnV^{\frac{1}{2}}B_s)10^8}{(142.6)n}=(0.7QB_sV^{\frac{1}{2}})10^6. \tag{7}$$

For a set of N noncoherent information pulses, completely free of interference from interpulse effects, and optimized according to (3a), the echo amplitude E_n will be in the range given by

$$\frac{E_0}{(Ne)^{\frac{1}{2}}}\leq E_n\leq\frac{E_0}{(Ne^{\frac{1}{2}})^{\frac{1}{2}}}. \tag{8}$$

The corresponding range in signal-to-noise ratio is given by

$$\frac{(0.42QB_sV^{\frac{1}{2}})10^6}{\sqrt{N}}\leq R_n\leq\frac{(0.55QB_sV^{\frac{1}{2}})10^6}{\sqrt{N}}. \tag{9}$$

[6] H. C. Torrey, Phys. Rev. **76**, 1059 (1949).
[7] Valley and Wallman, Radiation Laboratory Series **18**, (1948).

For protons, taking $H_0=7600$ gauss as used in our experiments, then $B_e=3.2\times10^{-5}$ gauss at echo time for our particular glycerine sample. It is useful to generalize the expression for R_n in terms of other parameters in the memory system. If the pulse-to-pulse spacing in the information train is τ, then the echo width t_e cannot be greater than τ. Taking $t_e\leq\tau$, and requiring that all pulse widths t_p,§ t_r and $t_i\leq\tau/4$, it follows that the necessary circuit Q is given by the condition that

$$\tau/4\geq1.4Q\left(\frac{2\pi}{\omega}\right)=\frac{1.4Q}{32\times10^6}, \tag{10}$$

hence

$$Q\leq(5.7\tau)10^6.$$

Since $N=T/\tau$, and substituting for Q from (10) into (9) we obtain for the last echo

$$R\leq10^8V^{\frac{1}{2}}TN^{-\frac{1}{2}}. \tag{11}$$

A signal-to-noise level of 10:1 would give

$$N\leq(4.6V^{\frac{1}{2}}T^{\frac{1}{2}})10^4. \tag{12}$$

(We note that for $T=1$ sec, $V=1$ cc, $N\simeq50\,000$; diffusion effects considerably reduce this value, however.) By combining (10) and (4), the resultant signal to noise ratio which also takes into account diffusion and relaxation is given for the Nth echo as

$$R_N\leq\frac{10^8TV^{\frac{1}{2}}}{N^{\frac{1}{2}}}\exp-\left[\frac{2T}{T_2}+\frac{2}{3}\left(\frac{4\pi}{l_0}\right)^2N^2DT\right]. \tag{13}$$

The relationship $\gamma(dH/dl)_nT=N\cdot4\pi/l_0$ has been used. Formula (13) is then conveniently expressed in terms of the physical parameters T, D, V, l_0, and T_2.

Figure 5 shows the effect these limitations have on the number of echoes which can be obtained. In this figure N is plotted in terms of T under the assumption that diffusion attenuation is limited to e^{-1}, $l_0=1$ cm, giving

$$N\leq\left(\frac{T_2-2T}{TT_2}\right)^{\frac{1}{2}}\left(\frac{1}{\frac{2}{3}(4\pi)^2D}\right)^{\frac{1}{2}}. \tag{14}$$

Equation (12) is also plotted in the figure for the last echo with $V=1$ cc. The intersection of these two curves sets an approximate limit to the maximum number of normal order echoes available from the materials indicated under reasonable conditions of signal to noise and sample size. The dashed line indicates the limit (without H_c variations) to the number of echoes set by a maximum rf power of 500 watts/cc (i.e., an echo width of 4 μsec).

For the case of mirror echo, the formulas above must be slightly modified but the same conclusions hold.

ELIMINATION OF INTERPULSE ECHOES

Each pulse in a train of information pulses acts as a pre-pulse for succeeding pulses and as a "recollection pulse" for preceding pulses to generate spurious echoes which will be called "interpulse echoes." Figure 6 shows how four types of interpulse echoes, which occur when information is stored in mirror echo form, are generated within a train of ten pulses to effect the desired echo of pulse number 8. Echoes of type 1 are produced by all pairs of pulses which precede pulse number 8 and give an echo at the time of entry of pulse number 8. Echoes of type 2 consist of all those echoes produced by three pulses to give a stimulated echo at pulse entry time number 8. Echoes of type 3 occur when a type 2 echo is recalled by a 180° pulse. As shown in Fig. 6, two identical echoes occur separated by an interval which is twice that between the first two generating pulses. The second echo to appear is called a "type 3" echo. Type 4 echoes arise because the 180° recollection pulse is imperfect and recalls some z-axis storage of interpulse z-components. Adding pulses in the manner of Fig. 6, we find for $N>10$ the following expressions for

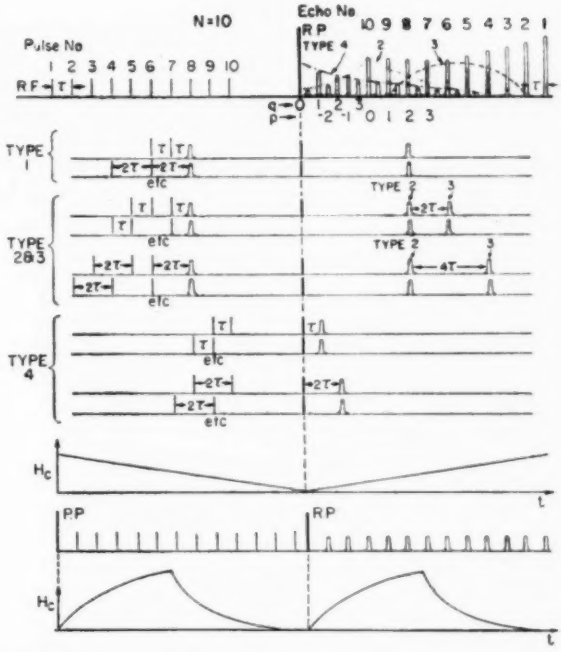

FIG. 6. Formation of several important types of interpulse echoes in a coherent rf system. Input pulses preceding pulse no. 8 produce echoes at the time of entry of pulse no. 8. The magnetization of these echoes in the $x'y'$ plane subtracts from that delivered into the $x'y'$ plane by pulse no. 8. The reduced magnetization is recalled by the 180° pulse. Echoes of type 1 are "eight ball" echoes.[3] Type 2 echoes are stimulated echoes[3] produced by three equal generating pulses acting as "pre-pulse," "information pulse," and "recollection pulse." When a stimulated echo (type 2) is recalled in mirror fashion *two* identical echoes appear. The second is called a "type 3" echo. Type 4 echoes occur because the 180° pulse is imperfect and acts like a stimulated-echo recollection pulse. Theoretical amplitude functions for the echoes of types 2 and 3 [see Eq. (15)] are shown for a value of nutation angle $\theta=\gamma H_i t_i$ for which the accumulated interpulse echo amplitude of type 2 echoes at echo time no. 10 is $\frac{1}{2}$ the desired echo amplitude at that time. Echoes of type 1 are much smaller for this value of θ and are not shown. Echoes of type 4 are shown as observed experimentally under the conditions described.

§ Subscripts p, r, i refer to pre-pulse, recollection pulse, and information pulse.

TABLE I.

rf method	θ	Max. amp Type 1	Type 2	Type 3	Type 4	Type n $n=5, 7, 9$	Amp desired echo	Signal amp / Interpulse amp
Coherent	θ	$\left(\frac{1}{2}N\right)\frac{\theta^2}{4}$	$\left(\frac{1}{4}N^2\right)\frac{\theta^3}{2}$	$\left(\frac{1}{4}N^2\right)\frac{\theta^3}{2}$	$(N)\theta^2\sin\theta'$	$\left(a(n)\frac{N^{n-1}}{(n-1)!}\right)\theta^n$	θ	
Coherent	$\frac{1}{N}$	$\frac{1}{8N^2}$	$\frac{1}{8}\ \frac{1}{N}$	$\frac{1}{8N}$	$\frac{\sin\theta'}{2N}$	$\frac{a(n)}{n-1!N}$	$\frac{1}{N}$	$\frac{8}{1}$
Coherent	$\frac{1}{\sqrt{N}}$	$\frac{1}{8\sqrt{N}}$	$\frac{\sqrt{N}}{8}$	$\frac{\sqrt{N}}{8}$	$\frac{\sin\theta'}{2}$	$\frac{a(n)N^{n/2-1}}{(n-1)!}$	$\frac{1}{\sqrt{N}}$	$<\frac{8}{N}$
Incoherent or freq. mod.	$\frac{1}{\sqrt{N}}$	$\frac{1}{4\sqrt{2N}}$	$\frac{1}{4\sqrt{N}}$	$\frac{1}{4\sqrt{N}}$	$\frac{\sin\theta'}{2\sqrt{N}}$	$\frac{a'(n)}{[(n-1)!N]^{\frac{1}{2}}}$	$\frac{1}{\sqrt{N}}$	$\frac{4}{1}$
Field pulsing	$\frac{1}{\sqrt{N}}$	~ 0	~ 0	~ 0	~ 0	~ 0	$\frac{1}{\sqrt{N}}$	$\sim\infty$

the amplitudes of the four types of interpulse echoes under discussion‖:

Type 1: $(\frac{1}{2})(N-p)\cdot\sin\theta(\sin\theta/2)^2$, $p=0,\ \pm1,\ \pm2,\ \cdots\pm(N-1)$

Type 2: $(\frac{1}{4})[(N-p)^2-(N-p)]\cdot(\frac{1}{2})(\sin\theta)^3$, $p\pm0,\ \pm1,\ \pm2,\ \cdots,\ \pm(N-1)$

Type 3: $(N-p)(p-1)\cdot(\frac{1}{2})(\sin\theta)^3$, $p=1, 2, \cdots N$

Type 4: $(N-q)\cdot(\frac{1}{2})(\sin\theta)^2\cdot\sin\theta'$, $q=1, 2, \cdots N$ (15)

where p and q are the integral variables shown in Fig. 6, θ is the tipping angle of each information pulse. The existence of these four types of echoes was confirmed experimentally by applying magnetic field pulses in the pulse and echo train at several places, and by observing when the storage was in the xy plane or along the z-axis. Experimentally, when a coherent rf oscillator was employed, the observed echo pattern resembled the pattern predicted by Eq. (6) in a satisfactory way for values of θ up to $\sim 1/N$.

For larger values of $\theta\sim(1/N)^{\frac{1}{2}}$, there are important interpulse echo amplitudes which should be considered in addition to those given in Eq. (15). These are found upon considering the sum of all interpulse echoes occurring at a given time which were generated by all possible combinations of five, seven, nine, etc. pulses, and which were stored along the z-axis between successive pairs of the generating set of pulses. These will be referred to as "type n" echoes. The largest sum amplitude is an expression of the form $a(n)N^{(n-1)}/(n-1)!\times(\sin\theta)^n$, where $n=5, 6, \cdots N$(odd), and $a(n)$ is some function of n which is much less than unity, and decreases as n increases. It can be shown that $a(5)=\frac{1}{8}$.

Two different methods have been employed to eliminate the effects of interpulse echoes. The first method recognized that interpulse echoes add up in proportion to N^2 and higher powers of N because the train of rf pulses is derived from a stable, coherent oscillator, and that consequently interpulse echoes are in phase with each other. If this fixed phase relationship is destroyed so as to introduce a randomization of phase, the interpulse echoes should add not arithmetically but as vectors which make random angles with one another. According to two-dimensional random-walk theory the root-mean-square length of the resultant vector of N^2 vectors each of length λ is $N\lambda$, apart from a factor ≈ 2. In the first line of Table I, the factor in parentheses is the number of vectors which are adding up; the second factor in θ (radians) is the length of each vector. Taking the square root of the first factor, and setting $\theta=1/\sqrt{N}$ in the second, the fourth line of that table is obtained for the condition of optimum θ. The signal to rms interpulse amplitude is now predicted to be 4/1 which approaches a desired value of 10/1. Two systems were constructed to achieve this. In the one, the frequency of the rf was varied linearly during the input period at a rate of at most 4 kc/millisecond. After empirical adjustment of the rate of frequency variation, the interpulse echoes were largely eliminated. The signal to interpulse echo ratio, was approximately the 4 to 1 figure calculated for random cancellation. There was little fluctuation about this value because the cancellation was systematic. In the second system, the primary rf oscillator was turned on and off for each rf pulse. This system behaved as well as the first, but the fluctuation of the interpulse echo amplitudes about the rms value was clearly noticeable. With both systems, the interpulse echoes increased so rapidly as the desired echoes approached maximum that it was impossible to ascertain that a maximum in the desired echo amplitude did exist and had been reached. The reason for this is evident from the formulas of Table I which show that the interpulse echoes vary with high powers of θ.

The second method for eliminating interpulse effects makes use of the ability of a time-dependent inhomogeneous magnetic field ΔH_c to destroy echoes. [See Eq. (22), Eq. (24).] Suppose the field ΔH_c has an rms value over the sample of $(\Delta H_c)_{av}$. In Fig. 6 the value of

‖ Except for type 4 echoes, the amplitudes of a single echo of the other three types can be taken from reference 3.

$(\Delta H_c)_{Av}$ is shown decreasing linearly to zero at the recollection pulse and then increasing at the same linear rate after the recollection pulse. It is clear that such a wave form having mirror symmetry about the recollection pulse preserves the desired echoes without attenuation and attenuates all the types of interpulse echoes described above. Since it is difficult to produce electronically an H_c-field having mirror symmetry about the recollection pulse, a system was constructed to produce the time varying ΔH_c-field shown at the bottom of Fig. 6. This wave shape, composed of exponentially rising and falling segments, has only translational symmetry in time, and so destroys interpulse echoes in a train of normal order echoes in a manner which is analogous to that just considered for the mirror echo case. It was found that the interpulse echoes were completely eliminated from a coherent rf train of 800 pulses spaced 20 μsec apart by having a peak value of $(\Delta H_c)_{Av}$ of from 3 to 5 gauss. Although a theoretical treatment of this method was carried out for the elimination of type 2 echoes in the mirror echo case, the details will not be reproduced here. It is worth noting, however, that type 2 echoes are substantially eliminated in a coherent rf system when the maximum value of $(\Delta H_c)_{Av}$ is $150/\tau$ gauss-microseconds $(100 \leq N \leq 1000)$. For $\tau = 20$ μsec, $\max(\Delta H_c)_{Av} = 7$ gauss and this compares favorably with the value measured for the normal echo case.

The ΔH_c-field variation method is fundamentally better than frequency or phase modulation of the input pulses alone, because it completely removes the problem of interpulse echoes in spin-echo systems. However, it is simpler to instrument one of the phase or frequency modulation methods, and by sacrificing some loss in echo strength, the signal to interpulse echo ratio may be increased from 4 to 1 to a safe, higher value.

Spin Memory Peak Power Requirements for Recollection and Pre-pulses

Consider a toroidal coil of volume V_c which is the inductive element in a parallel resonant circuit with figure of merit Q. The power dissipated in this circuit when a magnetic field of strength $2H_1 \sin\omega t$ is produced within the coil is given in watts by

$$P = 10^{-7}\omega H_1^2 V_c (2\pi Q)^{-1}. \tag{16}$$

It is sufficiently accurate here to apply this formula to a long, thin solenoid taking V_c as the interior volume of the coil, and to assume that H_1 is uniform throughout the volume V_c. A 90° pre-pulse or recollection pulse requires that $\gamma H_1 t_{p,r} = \pi/2$. For protons, $\gamma = 2.68 \times 10^4$, and therefore $H_1 = 58.7/t_{p,r}$ where $t_{p,r}$ is expressed in microseconds. With $\omega = \gamma H_0$ radians/sec corresponding to the nuclear resonance frequency expressed in radians per sec, Eq. (16) then becomes

$$P = \frac{55.3 V_c \omega \times 10^{-6}}{Q t_{p,r}^2} \text{watt}. \tag{17}$$

Since the desired echo widths are of the order of $t_e \sim 1/(\gamma \Delta H_{Av})$, where ΔH_{Av} is the width in gauss of the nuclear bandpass, the application of 90° and 180° pulses must not seriously impair the desired echo widths (increase them) by conditioning only a portion of the nuclear band for constructive interference. This is avoided if $t_{p,r} \ll 1/(\gamma \Delta H_{Av})$ or $t_{p,r} \ll t_e$. Formula (17) then indicates that the required power rises rapidly as the desired echo width decreases. For example, with $t_e = 4$ μsec, a 1 μsec recollection pulse, and a $Q = 23$ (which is necessarily low in order to obtain a 1 μsec recollection pulse), the pulse power required is about 500 watts/cc. Within the range of realizable Q, according to the relation $Q = (\omega t_{p,r})/(2\pi \cdot 1.4 \times 10^6)$, Eq. (17) becomes for protons

$$P = 480 V_c t_{p,r}^{-3} \text{ watt}, \tag{18}$$

independently of ω. Here $t_{p,r}$ is expressed in microseconds. The fact that the pulse shape is not rectangular has been ignored.

Variable Nuclear Band Width

The high peak power requirement pointed out in the foregoing can be circumvented by providing a means for varying the total nuclear band width $(\gamma \Delta H_{total})_{Av}$. Let $(\gamma \Delta H)_{Av}$ be the width of the spin spectrum due to fixed inhomogeneity of the magnet. In addition surround the sample by a set of small air core coils through which a direct current is pulsed in order to superimpose upon the sample an additional field inhomogeneity given by ΔH_c. The time during which H_c is turned on or off is always large compared to a Larmor period so that the Larmor frequency adiabatically follows the actual field at the sample. Now fixing the condition that $(\gamma \Delta H_c)_{Av} > (\gamma \Delta H)_{Av}$, H_c is turned on and remains on while information pulses are injected and received. The nuclear band pass will be shown to be determined by $\delta_{Av} = \gamma[(\Delta H)_{Av}^2 + (\Delta H_c)_{Av}^2]^{\frac{1}{2}}$. During recollection and pre-pulse times, however, H_c is turned off, and the nuclear band width shrinks to the value $(\gamma \Delta H)_{Av}$. The pulse power now required is less for a given t_e because the condition $t_{p,r} \ll 1/(\gamma \Delta H)_{Av}$ only need apply, whereas the relation $t_e \sim 1/\delta_{Av}$ still holds for the echoes if $t_r \ll 1/\delta_{Av}$. Formula (18) is still applicable for the peak power which is necessary, but is now a function of ΔH_{Av} only and not a function of echo width. With a ratio of 10 to 1 between ΔH_c and ΔH_{Av} the peak power required is reduced by a factor of 100.

The fraction of nuclei at a given frequency $\Delta\omega$ due to magnet inhomogeneity is assumed to be given by

$$P(\Delta\omega) = \left(\frac{1}{2\pi(\Delta\omega)_{Av}^2}\right)^{\frac{1}{2}} \exp\left[-\frac{\Delta\omega^2}{2(\Delta\omega)_{Av}^2}\right] \tag{19}$$

where

$$\int_{-\infty}^{\infty} P(\Delta\omega)d(\Delta\omega)=1.$$

When ΔH_c is turned on the spin vector $\bar{M}_{\Delta\omega}$ is assumed, in practice, to divide into many small vectors which are randomly distributed throughout a spectrum $\delta=\Delta\omega+\Delta\omega_c$ according to the distribution function

$$P(\delta)=\left(\frac{1}{(2\pi\delta_{Av}{}^2)}\right)^{\frac{1}{2}}\int_{-\infty}^{\infty}\times\exp-\left[\frac{(\Delta\omega_c-\delta)^2}{2(\Delta\omega)_{Av}{}^2}+\frac{\Delta\omega_c{}^2}{2(\Delta\omega_c)_{Av}{}^2}\right]d(\Delta\omega_c) \quad (20)$$

$$=\left(\frac{1}{2\pi\delta_{Av}{}^2}\right)^{\frac{1}{2}}\exp\left(\frac{-\delta^2}{2\delta_{Av}{}^2}\right),$$

where

$$\delta_{Av}=[(\Delta\omega)_{Av}{}^2+(\Delta\omega_c)_{Av}{}^2]^{\frac{1}{2}},\quad \delta=\Delta\omega+\Delta\omega_c,$$

$$\int_{-\infty}^{\infty} P(\delta)d(\delta)=1.$$

The applied H_c field is thus assumed to spread the original Gaussian distribution into a new Gaussian distribution. The variable band width effect can now be explained in the simple case where an echo at $t=2T$ is produced by a 90° pulse at $t=0$ followed by a 180° pulse at $t=T$. Let the field H_c be applied as shown in Fig. 7, where $H_c=0$ for intervals t_1 before and t_2 after the 180° pulse, so that the 90° pulse represents the information pulse. In general, for given initial values $u(t_i)$ and $v(t_i)$ of magnetization components in the rotating frame following a pulse, free precession in an effective field H gives[3]

$$F(t)=F(t_i)\exp[iH\gamma(t-t_i)], \quad (21)$$

where $F=u+iv$. Initial conditions are applied in steps as required. Note is taken of the fact that the 180° pulse at $t=T$ transforms $F(T)$ to $F(T+t_r)$ where $F(T+t_r)=F^*(T)$ and $F^*(T)$ is the complex conjugate of $F(T)$. The final expression for the echo is obtained by integrating $F(t)$ with (20) to give,

$$F(t)_{Av}=-iM_0\exp\left[\frac{-(t-2T)^2(\Delta\omega)_{Av}{}^2}{2}\right]\times\exp\left[\frac{-(t-2T+t_1-t_2)^2(\Delta\omega_c)_{Av}{}^2}{2}\right] \quad (22)$$

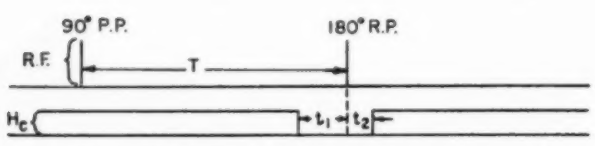

FIG. 7. Band width variation[3] by means of an additional magnetic field. The additional field is provided by a set of coils which produce the field H_c and a gradient across the nuclear sample of ΔH_c. If the static and coil fields add randomly the band width is $\gamma[(\Delta H_c)_{Av}{}^2+(\Delta H)_{Av}{}^2]^{\frac{1}{2}}$ except during the interval t_1 before and t_2 after the recollection pulse where the band width is $\gamma(\Delta H)_{Av}$.

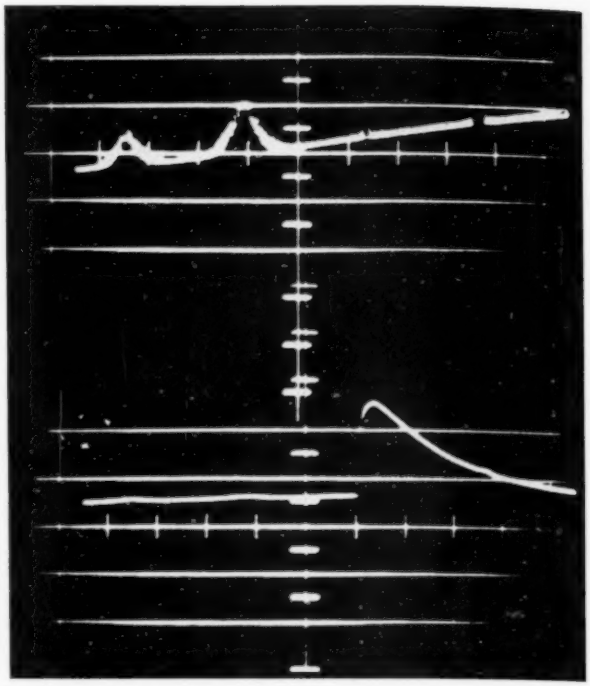

FIG. 8. Band width variation. The top line shows the normal order echo output while the bottom line shows the current to the H_c coils which were used to produce the variable band width. The increased band width during the H_c pulse produces the narrower echoes visible as two breaks in the base line on the right-hand side of the upper trace. The H_c pulse was also present (translationally symmetric) during the corresponding information input time. The total sweep is one millisecond.

where $t\geq T$. $F(t)_{Av}$ provides a maximum echo at a time

$$t=2T+\frac{(t_2-t_1)(\Delta\omega_c)_{Av}{}^2}{\delta_{Av}{}^2}$$

and has an amplitude

$$(F(t)_{Av})_{\max}=-iM_0\times\exp-\left(\frac{(\Delta\omega_c)_{Av}{}^2(\Delta\omega)_{Av}{}^2(t_2-t_1)^2}{\delta_{Av}{}^2}\right). \quad (23)$$

The echo is shifted in time ahead or behind $t=2T$ depending on the sign of (t_2-t_1), but such a shift is at best observable only within a time $\sim\delta_{Av}/(\Delta\omega_c)_{Av}(\Delta\omega)_{Av}$ according to (23). The field has mirror symmetry in time about the recollection pulse when $t_1=t_2$, and the echo is unattenuated, unshifted, and lasts for a time $t_e\sim1/\delta_{Av}$. Also (23) indicates how it is possible to erase echo memory completely with asymmetric field pulses under the condition

$$(t_2-t_1)^2\frac{(\Delta\omega_c)_{Av}{}^2(\Delta\omega)_{Av}{}^2}{(\Delta\omega_c)_{Av}{}^2+(\Delta\omega)_{Av}{}^2}\gg1.$$

A similar time shift and band width variation is obtained by applying H_c in stimulated echo formation. Here the time duration (t_1) of H_c between the pre-pulse

and the input pulse has to be the same as the duration (t_2) of the same H_c between recollection pulse and echo. Any shape of field pulse may be applied between the input pulse and the recollection pulse because the z-axis storage in this interval is not altered by changes in Larmor precessional frequencies. It is required, only, that the z-axis storage return to its original frequency distribution after the recollection pulse is applied. The photo in Fig. 8 shows the use of an H_c field pulse for band width variation of several of a series of normal order echoes.

If the field inhomogeneity $\Delta\omega_c$ were completely controllable such that an entire spin vector $\bar{M}_{\Delta\omega}$ was translated, unattenuated, into a new precessional field $K\Delta\omega$, where K is a constant, the echo time could be shifted arbitrarily without attenuation. Assuming no correlation between $\Delta\omega$ of the magnet and $\Delta\omega_c$, a fixed magnetic field homogeneity of about a milligauss over the sample would be necessary in order to shift the echo time through a range of about 0.1 second by varying K. The complete control of $\Delta\omega$ would be possible in obtaining electron spin resonance echoes. Here the H_0 required is about 11 gauss for a Larmor frequency of 30 mc, and could be entirely derived from a set of current coils.

Symmetry Properties of H_c Field Pulses

Equation (22) has already indicated how a mirror symmetry of square field pulses about the recollection pulse leaves the mirror echo unmodified at $t=2T$. By applying the method of rotation transformations to the Bloch[1] equations, neglecting attenuating terms, it is possible to show that the mirror echo envelope for a train of N equal information pulses is given by

$$\bar{a}(t)=-\bar{j}M_0\sum_{n=1}^{N}\left\{a_n\exp\left[\frac{-\left(\int_T^t g(t)dt-\int_{t_n}^{T}g(t)dt\right)^2(\Delta\omega_{c0})_{Av}^2}{2}\right]\exp\left[\frac{-(t-2T+t_n)^2(\Delta\omega)_{Av}^2}{2}\right]\right\}. \tag{24a}$$

In this formula, $\Delta\omega_c=g(t)\Delta\omega_{c0}$; $a_n=\sin\theta_n\cos\theta^{n-1}\times(\cos^2\theta/2)^{N-n}$; t_n = time of entry of information pulse n; T = time of entry of recollection pulse which is assumed to be 180°, and $\bar{j}$ is the unit vector along the rotating y' axis.

In order to assure that no pulses will be attenuated it is sufficient to make the function $g(t)$ mirror symmetrical about the recollection pulse, while in the limit of large $\Delta\omega_{c0}$ and dense pulse spacing this is a necessary condition.

For the case of normal order echoes, the equivalent of Eq. (24a) is,

$$\bar{a}(t)=\frac{-\bar{j}}{2}M_0\sum_{n=1}^{N}\left\{b_n\exp\left[\frac{-\left(\int_T^t g(t)dt-\int_0^{t_n}g(t)dt\right)^2(\Delta\omega_{c0})^2_{Av}}{2}\right]\exp\left[\frac{-(t-T-t_n)^2(\Delta\omega)_{Av}^2}{2}\right]\right\}, \tag{24b}$$

where,

$$b_n=\sin\theta_n(\cos\theta)^{N-n}\left(\cos^2\frac{\theta}{2}\right)^{n-1}.$$

In this case the field condition for nondestruction of echoes is that $g(t)$ be translationally symmetrical with respect to the times 0 to t_N and T to $T+t_N$. Since information entered before t_N is stored along the z-axis during the period t_N to T, $g(t)$ may assume any value during this period without distortion of the information.

Erasure of Memory; Information Selection

First an illustration is given in which the field H_c may be used for the erasure of echoes. Figure 9(a) shows a sequence in which the H_c field pulse is applied for a short time Δt_a following the recollection pulse in either type of echo. The effect of such an H_c field pulse is found in the manner of Eq. (24). A train of mirror echoes is described by the expression,

$$\bar{a}(t)=-\bar{j}M_0\exp\left[\frac{-(\Delta t_a)^2(\Delta\omega_c)_{Av}^2}{2}\right]\sum_{n=1}^{N}a_n\times\exp\left\{\frac{-[t-(2T-t_n)]^2(\Delta\omega)_{Av}^2}{2}\right\}. \tag{25}$$

Similarly, a train of stimulated echoes would be described by the expression

$$\bar{a}(t)=\frac{-\bar{j}M_0}{2}\exp\left[\frac{-(\Delta t_a)^2(\Delta\omega_c)_{Av}^2}{2}\right]\sum_{n=1}^{N}b_n\times\exp\left\{\frac{-[t-(T+t_n)]^2(\Delta\omega)_{Av}^2}{2}\right\}. \tag{26}$$

The echo terms above are completely attenuated if the condition $(\Delta t_a)^2(\Delta\omega_c)^2_{Av}/2\gg 5$ applies.

The erasure method indicated in Fig. 9(a) may be generalized to the case where H_c pulses are introduced for durations Δt_b and Δt_a before and after the recollection pulse, respectively. Assume for generality that the

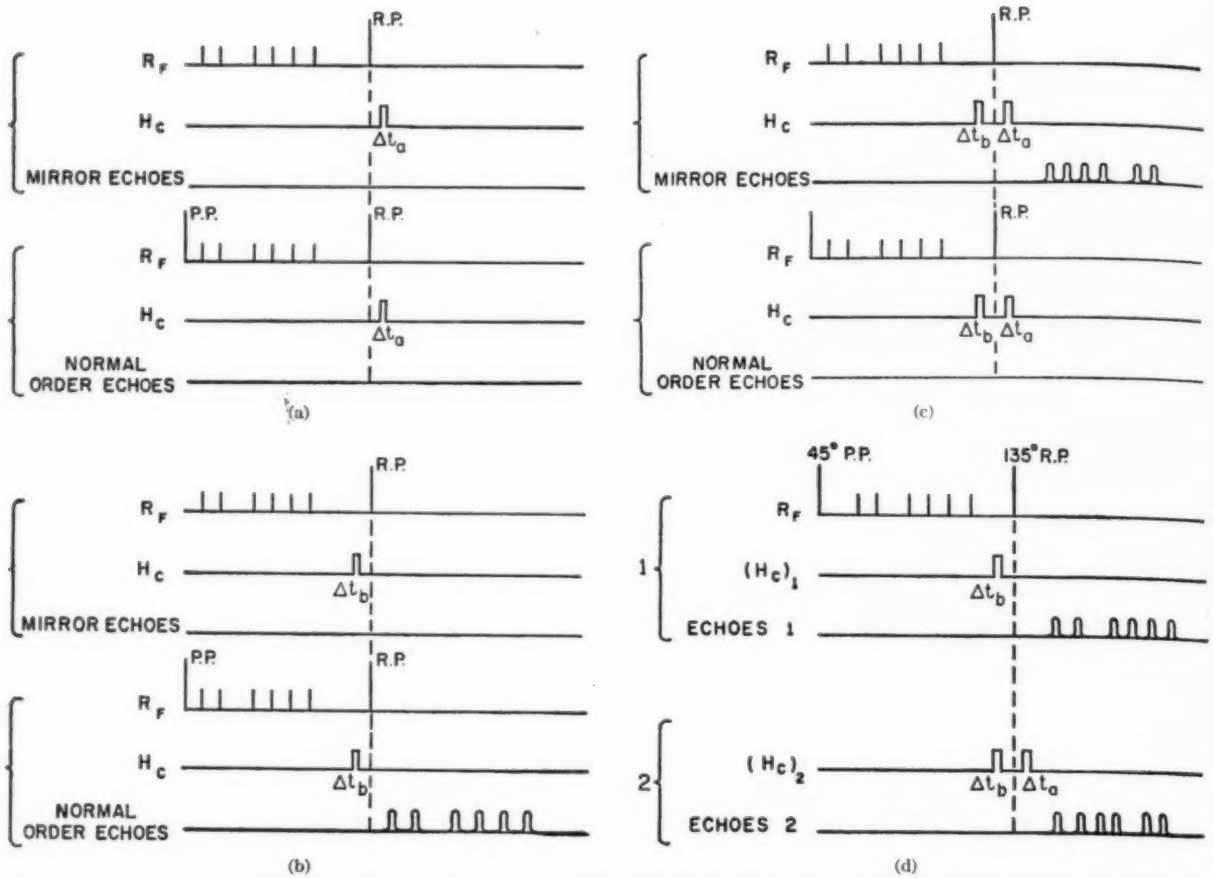

FIG. 9(a). Effect of H_c variation for erasure of information. The H_c field, produced by a set of air coils has an associated gradient ΔH_c and band width $\gamma(\Delta H_c)_{Av}$. If this field and the static field are randomly additive the introduction of an H_c pulse, as shown in Eqs. (25), (26), can be used to destroy the echo sequence. (b). Destruction of mirror echo and preservation of normal order echo by means of H_c pulses. The inhomogeneity, $\gamma\Delta H_c$, acts upon the mirror echo components which are precessing in the xy plane but does not affect the normal order echo components which are in z-axis storage. See Eq. (27). (c). Destruction of normal order echo and preservation of mirror by means of H_c pulses. The inhomogeneity, $\gamma\Delta H_c$, has effect on the normal order echoes only during the second pulse and destroys them, while in the mirror echo case the effect of equal ($\Delta t_b = \Delta t_a$) area pulses on either side of the recollection pulse cancels. See Eq. (27). (d). Use of H_c pulses to select echo type to be read out. In case 1 the mirror echoes are destroyed while normal order echoes are unaffected. In case 2 the mirror echoes are unaffected, for $\Delta t_b = \Delta t_a$, while normal order echoes are destroyed. This is shown for example in Eq. (27).

pre-pulse is θ_1 degrees and that the recollection pulse is θ_2 degrees. The output is given by,

$$\bar{a}(t) = -\bar{j}M_0 \cos\theta_1 \sin^2\frac{\theta_2}{2} \times\left(\sum_{n=1}^{N} a_n \exp\left\{\frac{-[t-(2T-t_n)]^2(\Delta\omega)_{Av}^2}{2}\right\}\right) \times\exp\left[\frac{-(\Delta t_a-\Delta t_b)^2(\Delta\omega_c)_{Av}^2}{2}\right] -\frac{\bar{j}M_0}{2}\sin\theta_1\sin^2\frac{\theta_2}{2} \times\left(\sum_{n=1}^{N} b_n \exp\left\{\frac{-[t-(T+t_n)]^2(\Delta\omega)_{Av}^2}{2}\right\}\right) \times\exp\left[\frac{-(\Delta t_a)^2(\Delta\omega_c)_{Av}^2}{2}\right]. \quad (27)$$

The first summation in (27) provides mirror echo terms while the second summation provides normal order echoes. The preservation of normal order echoes requires that $\Delta t_a = 0$ [Fig. 9(b)], and the preservation of mirror echoes requires that $\Delta t_c = \Delta t_b$ [Fig. 9(c)]. Destruction of all echoes results if $\Delta t_a \gg \Delta t_b$. Selection of either type and destruction of the other requires that $\Delta t_b(\Delta\omega_c)_{Av}^2 \gg 1$ and $\Delta t_a = \Delta t_b$ or $\Delta t_a = 0$ [Fig. 9(d)]. If the H_c pulses are to be entirely effective they must be applied at times when neither information pulses nor echoes are present.

Selective and Repeated Recall

The spin-echo system has several features which provide versatility as a memory device. If, for example, groups of pulses A, B, and C are properly introduced into the spin memory it is possible to recall the groups in arbitrary sequence, as $ABBAC$. The photographs in Fig. 10 display two basic methods for recalling mirror echoes or normal order echoes. In Fig. 10(a), a group of

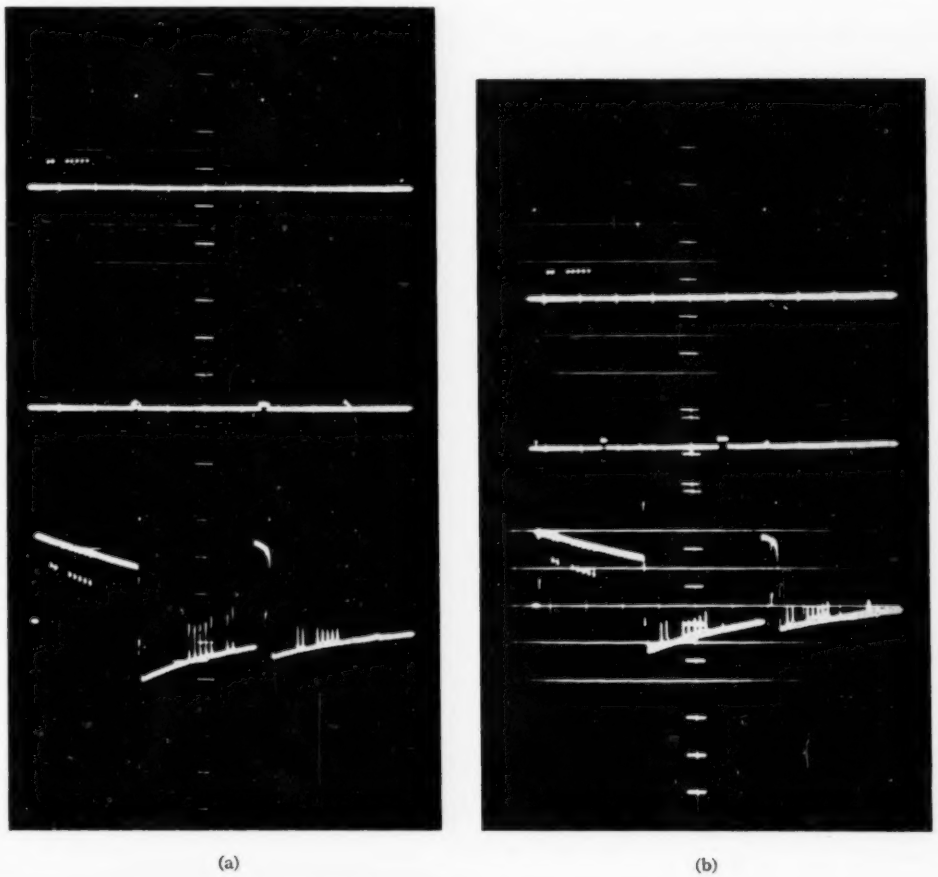

(a) (b)

FIG. 10(a). Mirror echo repeated recall. The lines, top to bottom show rf input envelope, H_c variation, and output envelope. Variation of the H_c field is used to eliminate undesired echoes. (b). Normal order echo repeated recall. The lines, top to bottom, show the rf input envelope, the H_c variation, and the output envelope. In this case, each recollection pulse but the last must be kept $<90°$.

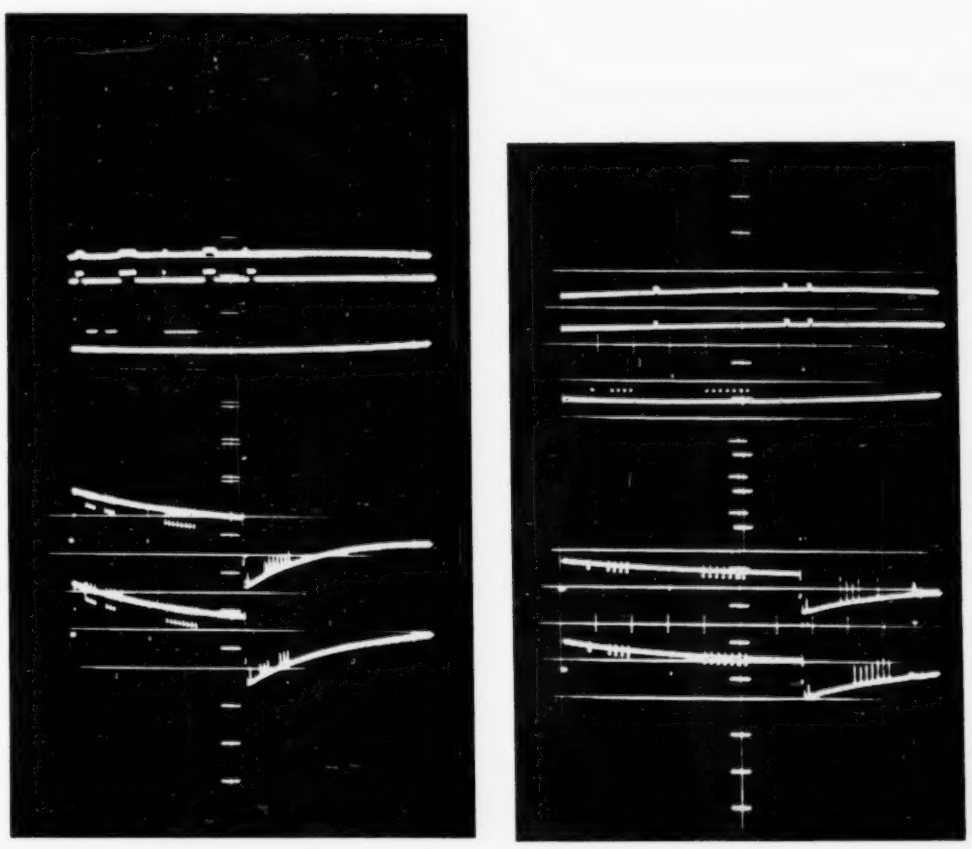

(a) (b)

FIG. 11(a). Selective recall of either of two normal order groups. The top line shows the H_c variation used to produce the output shown in 2nd line from the bottom, while the 2nd line down shows the H_c variation used to produce the output shown in the bottom line. The center line shows the rf input envelope. Sweep speed 800 μsec/cm. (b). Selective recall of either of two groups in reverse order. The top line is the H_c variation used to produce the output shown on the 4th line down, while the 2nd line is the H_c variation used to produce the output shown on the bottom line. The envelope of the input rf is shown on the middle line. Sweep speed 800 μsec/cm.

mirror echoes, whose time sequence is distinguished by the absence of the third input pulse, is recalled for the second time by a second 180° pulse. Note that the echoes are in input order after the second recall, and that H_c field pulses are applied symmetrically about each recollection pulse. This means that only mirror echoes will appear, according to the argument given before. Additional recollection and H_c-pulses may be applied until the echoes are finally destroyed by diffusion and relaxation effects. Since normal order echoes are stored along the z'-axis, the basic method of repeated recall for echoes of this type is to recall partially the storage with recollection pulses which are less than 90°. This is done in order to retain a balance of z'-axis spin storage for a later recall. At each recall echoes appear in input order. This method is shown in Fig. 10(b) where a group of normal order echoes is first recalled by a 45°-pulse and again by a subsequent 90°-pulse. H_c-field pulses are introduced before each recollection pulse to destroy any storage which may exist in the $x'y'$-plane.

An example of the selective recall of either of two serially stored normal order groups of pulses is illustrated in Fig. 11(a). The first group A is distinguished from the second group B by the absence of two input pulses in the middle of A. Reference to the two lower lines in the oscillograph shows in the lowest trace the appearance of group A alone, beginning just after the recollection pulse. In the second trace from the bottom only B appears. This performance is achieved in the following way: an information group, such as A, is given its own pre-pulse $(PP)_A(<90°)$ and H_c-field pulse of duration Δt_A. This H_c-pulse occurs between $(PP)_A$ and the beginning of A. Consequently if this pulse is reproduced following the recollection pulse the necessary and sufficient conditions have been established for the occurrence of normal order echoes of A. If the dissimilarity of the H_c-pulse labelling the B group is sufficiently great, the necessary condition for the occurrence of B is violated and only A appears. The H_c-pulses are shown in the top traces of Fig. 11(a). In addition to the labelling pulses just described, two additional pulses are introduced after each group is put into z'-axis storage in order to destroy any storage which may exist in the $x'y'$-plane. In this case, if the H_c pulses are labelled a, b, c, d, e, in order of appearance and if $(PP)_A$ occurs at $t=0$, $(PP)_B$ at $t=t_m$, the echo output is given by:

$$\bar{a}(t)=-\frac{jM_0}{2}\left\{\begin{aligned}
&\exp\left[\frac{-(\Delta t_e-\Delta t_a)^2(\Delta\omega_c)_{Av}^2}{2}\right]\sum_{n=1}^{m-1}\left(b_n\exp\left[\frac{-(t-T-t_n)^2(\Delta\omega)_{Av}^2}{2}\right]\right)\sin\theta_{pp_A}\cos\theta_{pp_B}\\
&+\exp\left[\frac{-(\Delta t_e-\Delta t_c)^2(\Delta\omega_c)_{Av}^2}{2}\right]\sum_{n=m+1}^{N}\left(b_n\exp\left[\frac{-(t-T-t_n+t_m)^2(\Delta\omega)_{Av}^2}{2}\right]\right)\cos\theta_{pp_A}\sin\theta_{pp_B}\\
&+\exp\left[\frac{-(\Delta t_e-\Delta t_a-\Delta t_b-\Delta t_c)^2(\Delta\omega_c)_{Av}^2}{2}\right]\sum_{n=m+1}^{N}\left(c_n\exp\left[\frac{-(t-t_n)^2(\Delta\omega)_{Av}^2}{2}\right]\right)\sin\theta_{pp_A}\cos^2\frac{\theta_{pp_B}}{2}\\
&+\exp\left[\frac{-(\Delta t_e-\Delta t_b)^2(\Delta\omega_c)_{Av}^2}{2}\right]\sum_{n=1}^{m-1}\left(d_n\exp\left[\frac{-(t-T-t_m+t_n)^2(\Delta\omega)_{Av}^2}{2}\right]\right)\cos\theta_{pp_A}\sin\theta_{pp_B}
\end{aligned}\right.$$

$$+\text{mirror echo terms,} \quad (28)$$

where $b_n\simeq c_n\simeq d_n$ for optimum echo amplitude conditions, and equal θ_i.

Two or more groups of pulses may also be stored in reverse order and recalled in arbitrary group sequence. Figure 11(b) illustrates this for a case where the first group is stored in reverse order z axis storage, achieved by following the group with a "post pulse" which acts as an "information pulse" upon the preceding group of small "pre-pulses." The second group is in mirror echo storage. Field pulses are applied with either translational or mirror symmetry to select the desired group. The recollection pulse must be between 90° and 180° in this particular case.

Information in H_c

Since the nature of the output echo train is strongly dependent upon the nature of the H_c-field pulsing, this field may be used as a second channel for entering information into the system. Figure 12 shows an rf input in the form of a uniform series of pulses whose amplitudes and durations are such as to produce an echo train of optimum amplitude. If an H_c pulse of width Δt_a is entered at t_a seconds after the rf pre-pulse and an identical H_c pulse is entered at t_b seconds after the rf recollection pulse, the echo envelope is given (from formula 24) by

$$\bar{a}(t)=\frac{-j}{2}M_0\left(\sum_{n=1}^{N}b_n\exp\left[\frac{-(t-T-t_n)^2(\Delta\omega)_{Av}^2}{2}\right]\right)$$

$$\times\exp\left\{\frac{-[\Delta t_a\cdot G(T+t_a)-\Delta t_b\cdot G(T+t_b]^2(\Delta\omega_c)_{Av}^2}{2}\right\}$$

where

$$G(T+t_x)=0, \quad t<T+t_x$$
$$=\frac{(t-T-t_x)}{\Delta t_x}, \quad T+t_x\leq t\leq T+t_x+\Delta t_x \quad (29)$$
$$=1, \quad t>T+t_x+\Delta t_x.$$

For $t_a=t_b$ [Fig. 12(a)] the echo train is uneffected, while for $t_a<t_b$ [Fig. 12(b)] echoes in the interval $T+t_a$ to $T+t_b$ will be attenuated. The presence or absence of a gap in the echo train is therefore a sensitive indication of the equality of the time intervals t_a and t_b. This method may be used for the comparison of integrals of the form $\int_0^{t_i} g(t)dt$ and $\int_T^{T+t_i} g(t)dt$ or of the form $\int_{t_i}^{T} g(t)dt$ and $\int_T^{2T-t_i} g(t)dt$ by means of normal order echo or mirror echo, respectively, where $g(t)$ represents the variation of H_c.

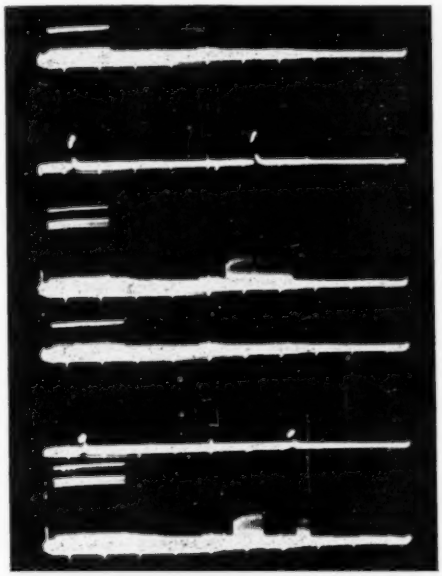

FIG. 12. Information storage in H_c field. The upper three traces, Fig. 12(a), show, (reading from top to bottom), the envelope of a train of rf input pulses, the H_c field variation, and the envelope of receiver output for the case where the two H_c pulses are equal in area and come at the same time following pre-pulse and recollection pulse, respectively. (The input pulses in the receiver output appear also because of feed-through). The lower three traces, Fig. 12(b), show corresponding patterns for the case where the H_c pulses are still equal in area, but differ in timing with respect to pre-pulse and recollection pulse respectively. The hole in the output echo train indicates the time difference of the H_c pulses with respect to these two references. Sweep speed $\sim 1\times 10^{-3}$ sec/cm.

APPARATUS

Most of the apparatus (Fig. 13) used in this experiment is typical of nuclear spin echo work, consisting of a magnet, radio-frequency head and generator, receiver, viewing oscilloscope and pulse equipment. The permanent magnet used was a 350 pound, 7600 gauss

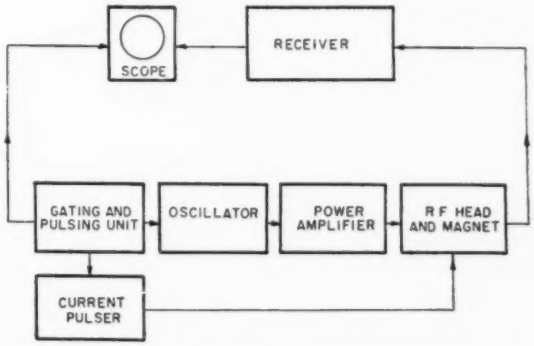

FIG. 13. Block diagram of spin echo memory apparatus.

magnet with a 1 inch gap, $3\frac{1}{2}$ inch diameter pole pieces and a ΔH at the center of 5 gauss/cm. Several types of rf head circuit configurations were used, these being of the crossed-coil type, the balanced bridge type, and types of the form shown in Fig. 15. In this latter arrangement a TR circuit is used to decouple the receiver from the high power rf pulses. Figure 14 shows the location of the H_c coils with respect to the sample. These coils are arranged to have bucking fields and are driven from a current supply of 3 ampere capacity which uses type 807 tubes.

Most of the experiments herein reported were carried out using an oscillator-amplifier type transmitter. The transmitter consisted of a stable 4 megacycle oscillator, followed by three doublers, a buffer amplifier, and a grid modulated 300 watt power amplifier using a pair of 813's in push-pull. The oscillator was gated so that it operated only during the information input interval and had provision for reactance-tube frequency modulation during this interval. A simple type of pulse

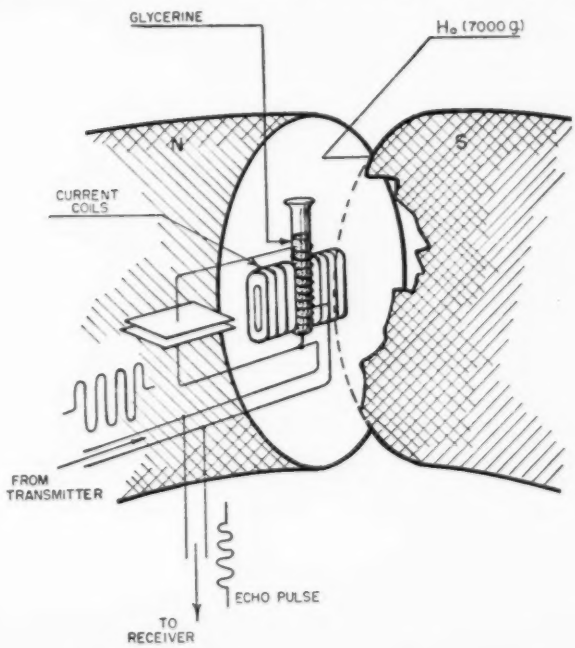

FIG. 14. Storage unit of the spin echo apparatus.

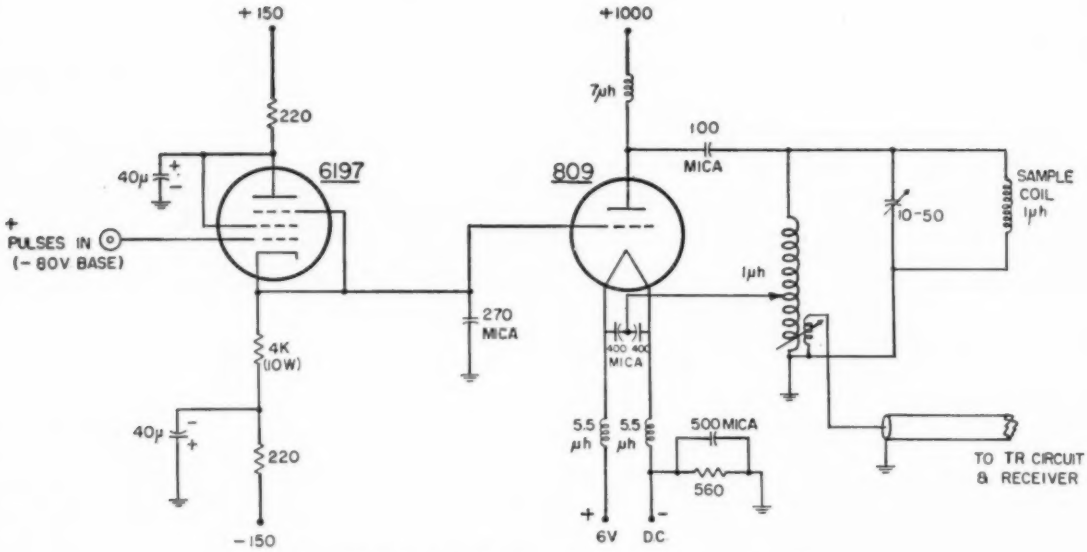

FIG. 15. Pulsed oscillator used in spin echo experiments.

transmitter which was used in the final stages of the experiment is shown in Fig. 15. This arrangement was capable of providing a 90°, 5 microsecond, pre-pulse or recollection pulse and needed no frequency molduation provision because of its basic incoherence.

For the receiver section, a cascode-type[7] of preamplifier using two 6AK5's followed the *TR* circuit. This was followed in turn by a six stage carrier-frequency amplifier, a diode detector and a one stage video amplifier. Gain control was provided by adjusting screen voltage of the tubes, while the band width was set by one or more high Q interstage circuits.

The electronic circuitry for providing the various pulses and other wave forms in their desired time sequence is of conventional design consisting of scale-of-two circuits, diode switching matrices, delay multivibrators, etc. The output pulses are obtained from adjustable width single-shot miltivibrators.

CONCLUDING REMARKS

Spin echo storage in liquids such as glycerine and solutions of paramagnetic ions in water which have given the best performance thus far, provide memory times in the range of 10 to 50 milliseconds with a storage capacity of the order of 1000 echoes. A severe limitation against greater series storage capacity is imposed by the fact that a large field inhomogeneity ΔH_{Av} over the sample volume to produce short echoes accentuates a loss of spin phase coherence due to the self-diffusion of molecules in liquids.[3] Although the natural spin relaxatime T_2 for precessional phase coherence can be of the order of seconds in liquids, the loss of phase due to the diffusion transport of precessing nuclei from one local ΔH value to another reduces the useful storage time to values generally much less than T_2. No concentrated effort has been made to remove this limitation in the present work. Although certain approaches would be expected to reduce self-diffusion, such as confinement of the liquid within small cells, the natural relaxation times themselves then appear to shorten considerably. Most of the problems associated with spin echo storage have been solved to a considerable extent. In particular, the requirements of high power for the recollection pulse can be reduced, and interference with the desired output echoes by unwanted echoes can be eliminated. In addition it has been found possible to provide methods of information selection and destruction by means of a magnetic field modulation technique.

An interesting alternative to the use of nuclear magnetic moments and a magnetic field H_0 is the use of nuclear quadrupole moments and crystalline electric field gradients.[8] Since a magnetic moment is also present in this case, the methods of information modification by an external field could be applied.

ACKNOWLEDGMENTS

The authors wish to express their thanks to Mr. J. E. Applequist who did much of the early apparatus design and test work, and to Mr. R. Heyman for his work in the construction and testing of the apparatus.

[8] M. Bloom and R. Norberg, Phys. Rev. **93**, 639 (1954); E. L. Hahn and B. Herzog, Phys. Rev. **93**, 639 (1954); Bloom, Hahn, and Herzog, Phys. Rev. **97**, 1699 (1955).

JOURNAL OF APPLIED PHYSICS VOLUME 26, NUMBER 11 NOVEMBER, 1955

Improved Wave Diagram Procedure for Shock Reflection from an Open End of a Duct*

GEORGE RUDINGER
Cornell Aeronautical Laboratory, Incorporated, Buffalo, New York
(Received July 1, 1955)

Recently derived improved boundary conditions for the reflection of weak shock waves from an open end of a duct can be well approximated by a centered expansion wave if the center of the later is located on the leading characteristic of the reflected wave and some distance e outside the duct. A relation is derived between e/D (D is the duct diameter), the shock pressure ratio p_1/p_0, and γ (the ratio of specific heats). This relationship is represented with sufficient accuracy by the empirical formula

$$\frac{e}{D}=\left(0.90+\frac{0.677}{(p_1/p_0)-1}\right)(\gamma+1.08)-3.8.$$

This result makes it possible to apply the improved boundary conditions without losing the convenience of of the customarily used wave diagram procedure.

WHEN a shock wave propagating into a gas at rest reaches an open end of the duct, an expansion wave of such strength is reflected that the exit pressure is adjusted to the level required by the steady-flow boundary contitions.[1,2] Customarily, this pressure adjustment is assumed to take place instantaneously and the reflected wave then becomes a centered expansion wave. It has been shown[3,4] that, for weak shock waves, the adjustment times may occasionally not be negligible. Improved boundary conditions were obtained, and these are shown as the heavy line in Fig. 1 where the variation of the exit pressure p in the form of the ratio

$$I=(p-p_0)/(p_1-p_0), \tag{1}$$

is plotted as a function of the nondimensional time

$$\tau=a_0t/D. \tag{2}$$

The time t is here measured from the instant at which the shock wave reaches the duct exit; subscripts 0 and 1 indicate the conditions immediately before and after the passage of the shock wave, respectively; the speed of sound is denoted by a, and the duct diameter by D. By comparison, the conventional boundary conditions for which the adjustment time is neglected appear in the same figure as the instantaneous change of I from one to zero.

The improved boundary conditions could be used directly in the construction of a wave diagram. The resultant computing procedures, however, become rather inconvenient; while the velocity of any characteristic of the reflected expansion wave is easily computed, the determination of its location in the wave diagram is rather tedious. It is a great advantage of the conventional procedure that the reflected expansion wave is centered and that, therefore, no work is involved in locating the characteristics. It was found that the reflected wave resulting from the improved boundary conditions could be approximated by a centered expansion wave and the location of its center will be determined in the following.

The leading characteristic of the reflected expansion wave is not affected by the improved boundary conditions but all later characteristics are delayed. If they

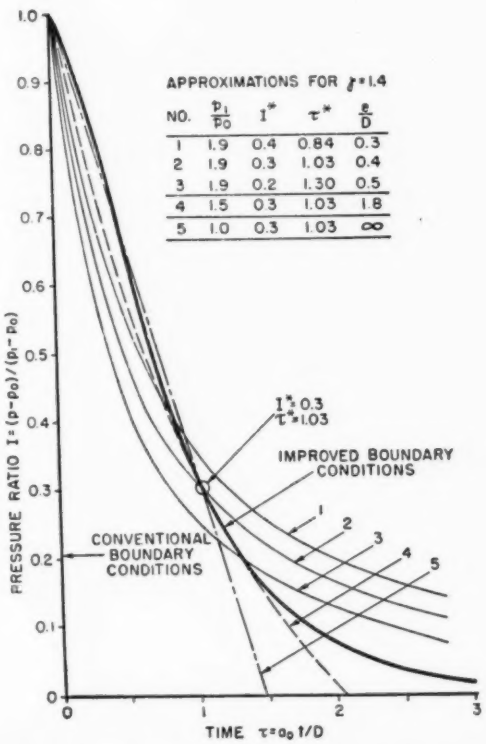

FIG. 1. Approximation of the improved boundary conditions by a centered reflected expansion wave.

* This research was conducted under the auspices of Project SQUID, jointly sponsored by the Office of Naval Research, Department of the Navy, the Office of Scientific Research, Department of the Air Force, and the Office of Ordnance Research, Department of the Army.

[1] G. Rudinger, *Wave Diagrams for Nonsteady in Flow in Ducts* (D. Van Nostrand Company, Inc., New York, 1955), pp. 59 and 147.

[2] A. H. Shapiro, *The Dynamics and Thermodynamics of Compressible Fluid Flow* (The Ronald Press Company, New York, 1954), Vol. II, pp. 960 and 1021.

[3] G. Rudinger, J. Appl. Phys. **26**, 981 (1955). (See also Project SQUID Technical Report No. CAL-61-P, August, 1954, ASTIA No. AD52851, Microcard.)

[4] Reference 1, p. 148.

are to form a centered expansion wave, their extensions must all pass through a point located on the leading characteristic and a distance e from the exit of the duct (Fig. 2). The manner in which the exit pressure varies with time depends on e which must be selected to yield the best possible approximation of the required boundary conditions.

Since the leading characteristic of the reflected wave propagates with the velocity u_1-a_1 where u denotes the flow velocity, the time coordinate of the center is given by $-e/(a_1-u_1)$. (Note that u_1-a_1 is negative.) For a general point of the wave diagram within the expansion wave and located on the line representing the duct exit (for instance, point A in Fig. 2), the characteristic relation

$$2(\gamma-1)^{-1}a+u=2(\gamma-1)^{-1}a_1+u_1, \tag{3}$$

applies where γ is the ratio of the specific heats. It is also seen from Fig. 2 that

$$t=e[(a-u)^{-1}-(a_1-u_1)^{-1}]. \tag{4}$$

If u is eliminated from Eqs. (3) and (4), one obtains

$$\frac{a}{a_0}=\frac{\gamma-1}{\gamma+1}\left[\frac{2}{\gamma-1}\frac{a_1}{a_0}+\frac{u_1}{a_0}+\left(\frac{D}{e}\tau+\frac{a_0}{a_1-u_1}\right)^{-1}\right] \tag{5}$$

where the nondimensional time has been introduced from Eq. (2). Since only weak shock waves are of interest here, changes of state can be considered as isentropic without significant loss of accuracy; and one may, therefore, use the relations

$$a_1/a_0=(p_1/p_0)^{(\gamma-1)/2\gamma}, \tag{6}$$

and

$$u_1=2(\gamma-1)^{-1}(a_1-a_0). \tag{7}$$

Equation (1) may then be expressed as

$$I=[(a/a_0)^{2\gamma/(\gamma-1)}-1][(p_1/p_0)-1]^{-1}, \tag{8}$$

where the first factor is given by Eqs. (5), (6), and (7). Thus, once a value of e/D has been selected, I can be computed as a function of τ for any value of γ and the shock pressure ratio p_1/p_0. This relation between I and τ should approximate the heavy line in Fig. 1. It already yields the correct value $I=1.0$ for $\tau=0$, and one may choose e/D so that agreement is also reached for some other point given by I^* (and τ^*). For this point, Eqs. (5) and (8) can be solved for e/D and one obtains

$$\frac{e}{D}=\tau^*\left(\frac{1}{\psi}-\frac{a_0}{a_1-u_1}\right)^{-1}, \tag{9}$$

where the abbreviation

$$\psi=\frac{\gamma+1}{\gamma-1}\left[1+I^*\left(\frac{p_1}{p_0}-1\right)\right]^{(\gamma-1)/2\gamma}-\frac{2}{\gamma-1}\frac{a_1}{a_0}-\frac{u_1}{a_0}, \tag{10}$$

has been used.

The results of the foregoing procedure depend on both γ and p_1/p_0. The influence of these variables must be investigated since the boundary conditions do not depend on them.[3] Various values of I^* were tried to find the one which yields the best possible approximation of the boundary conditions. Some of the results for $\gamma=1.4$ are included in Fig. 1. It is seen that, for $p_1/p_0=1.9$, the best possible approximation of the boundary conditions is obtained if one chooses $I^*=0.3(\tau^*=1.03)$ although this value is not critical. The same value of I^* also leads to good agreement for shock pressure ratios of 1.5 and 1.0. In the latter case, the approximate curve becomes a straight line.

The residual disagreement indicates that the reflected expansion wave derived from the improved boundary conditions is not centered. The approximation is good for weak shock waves, at least over the most important part of the curve. The lack of agreement in the region where I is less than 0.1 is not considered important since the pressure adjustment at the duct exit is then already over 90% completed. Even for stronger shock waves, the approximation should be considered adequate because the flow phenomena inside the duct are then rather insensitive to inaccuracies of the boundary conditions.[3] Furthermore, if one compares the customarily used boundary conditions with the proposed approximations, it is seen that the latter represent a considerable improvement and that they should be satisfactory in practically all cases. When other values of γ were investigated, it was found that the same choice of $I^*=0.3$ and $\tau^*=1.03$ led to similarly good results.

The computational labor involved in finding e/D in every case from Eqs. (9) and (10) is considerable, but it was found that these relations can be expressed by the convenient empirical formula,

$$\frac{e}{D}=\left[0.90+\frac{0.677}{(p_1/p_0)-1}\right](\gamma+1.08)-3.8, \tag{11}$$

which holds for any value of γ between 1.0 and 5/3, and for all shock pressure ratios up to the limit that yields

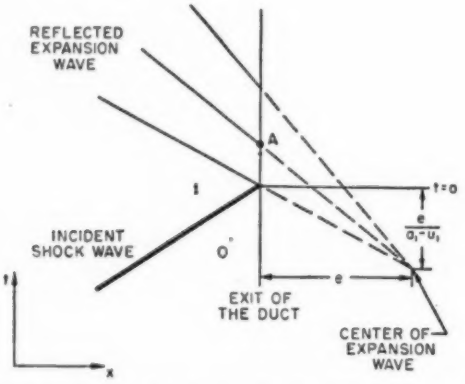

FIG. 2. Wave diagram for shock reflection from an open end with the improved boundary conditions approximated by a centered reflected expansion wave.

$e/D=0$. This limit follows from the consideration that the center of the expansion wave cannot be located inside the duct and that e, therefore, cannot be negative. The outflow from the duct has then, practically, become sonic so that there is no longer any advantage to be derived from the use of the improved boundary conditions. Near this upper limit, the errors of e/D that are introduced by Eq. (11), generally, amount to less than 0.1. The effect of such errors is the same as if I^* had been changed by about 0.1 which is quite tolerable (see Fig. 1). For weaker shock waves, for which the procedure is more important, the errors remain within a few percent of e/D.

Equation (11) makes the application of the improved boundary conditions quite convenient. The magnitude of the end correction can be seen in Fig. 3 where e/D is plotted as a function of p_1/p_0 for three values of γ. For actual applications, one would have to prepare a larger chart or use Eq. (11) directly.† Wave diagrams are usually prepared in terms of the nondimensional distance and time coordinates x/L_0 and a_0t/L_0, respectively, where the reference length L_0 represents some

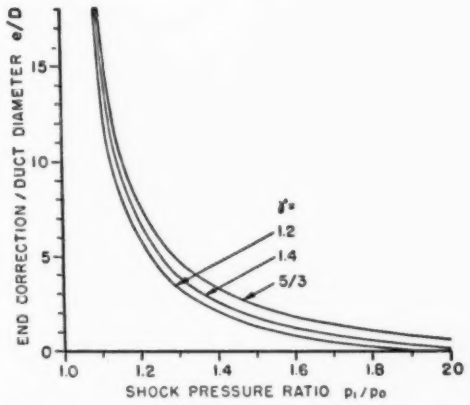

FIG. 3. End correction as calculated from Eq. (11).

significant dimension—often the total length—of the system under investigation. Thus, the quantity which must be determined in every case is not e/D but $e/L_0=(e/D)(D/L_0)$. Once the center of the reflected expansion wave has been located on the wave diagram, the graphical and numerical computations remain the same as those customarily used. In addition, the magnitude of e/L_0 gives a good indication of the modifications that result from using the improved rather than the conventional boundary conditions.

† Equation (11) may also be represented by a nomographic alignment chart. Copies of such a nomogram may be obtained from the author.

Theory of Remagnetization of Thin Tapes

H. EKSTEIN
Armour Research Foundation, Chicago, Illinois
(Received July 7, 1955)

It is assumed that the velocity of the domain wall is proportional to the difference between the magnetic field intensity at the wall and the coercive force. The local magnetic field, which is not equal to the external field, is calculated from the eddy-current equations. The rate of change of the magnetic flux as a function of time is determined. The total switching time is expressed in terms of two phenomenological constants: the retardation constant α mentioned above, and a delay time τ, the duration of the formative phase during which the plane walls are formed.

THE subject of this paper is the reversal of the magnetization of thin ferromagnetic tapes with rectangular hysteresis loops, under the influence of an external field parallel to the tape surface.[1] The tape is considered to be long and wide enough so that demagnetizing surface effects can be disregarded, as long as the magnetization is parallel to the tape surface. If the tape is initially totally magnetized in a direction parallel to the surface (the x direction) then the application of an external field in the $(-x)$ direction will reverse the magnetization. It is reasonable to assume that the first nuclei of reversed magnetization occur at the surface and that they grow laterally at first to form, after a very short time, a domain-wall boundary approximately parallel to the surface (Figs. 1 and 2).

After this initial formative phase, which will not be further discussed, the domain walls progress in the direction z normal to the surface. If the external field H is, as we shall assume, a monotonically increasing function of time, the domain walls will finally meet in the center.

The following assumptions are made concerning the velocity of propagation in the walls: (1) The effective field driving the walls is $H-H_c$ where H_c is the coercive force. (2) The velocity of propagation is proportional to the effective driving field, i.e.,

$$\dot{w}=\alpha(H-H_c). \tag{1}$$

(3) The domain wall may be considered as infinitely thin. The quantity H in Eq. (1) is not the external field H_a, but the internal field which must be determined by solving the eddy-current equations.

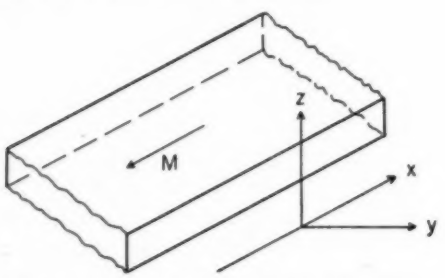

FIG. 1. Thin tape with coordinate directions.

[1] A preliminary report was given by H. Ekstein and J. Kelly, Phys. Rev. 94, 1440 (1954).

From the symmetry of the problem, it is clear that

$$\partial/\partial x=\partial/\partial y=0 \tag{2}$$

and

$$H_y=H_z=E_x=E_z=0, \tag{3}$$

where E is the electric field.

One obtains easily from the electromagnetic equations

$$\frac{\rho c^2}{4\pi}\frac{\partial^2 H}{\partial z^2}=\frac{\partial H}{\partial t}+4\pi\frac{\partial M}{\partial t}, \tag{4}$$

where ρ is the resistivity in Gaussian units and M the magnetization.

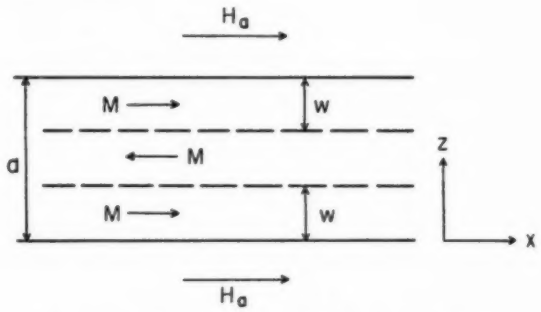

FIG. 2. Cross section through the tape (xz plane). The dashed lines are domain boundaries.

The magnetization M as a function of z at a particular time is shown in Fig. 3. If S is the usual step function, equal to -1 for negative and to $+1$ for positive arguments, one sees from Fig. 3 that

$$M=m-mS(z-w)+mS(z-a+w), \tag{5}$$

where m is the absolute value of the magnetization.

From Eq. (5) we obtain

$$\frac{\partial M}{\partial t}=\frac{\partial M}{\partial w}\dot{w}=2m\dot{w}[\delta(w-z)+\delta(z-a+w)], \tag{6}$$

where δ is Dirac's delta function. Eq. (4) becomes

$$\frac{\rho c^2}{4\pi}\frac{\partial^2 H}{\partial z^2}=\frac{\partial H}{\partial t}+8\pi m\dot{w}[\delta(w-z)+\delta(z-a+w)]. \tag{7}$$

The first term on the right-hand side, the rate of change of the field, is usually negligible in comparison to the second term which represents the rate of change of the magnetization, so that we drop the former. We shall justify this approximation later.

If this is done, Eq. (7) states that H as a function of z is linear, with discontinuities of the derivatives at the points $z=w$ and $z=a-w$ (Fig. 4). From Eq. (7) and Fig. 4 it is clear that

$$\frac{H(w)-H_a}{w}=\frac{32\pi^2 m}{\rho c^2}\dot{w} \tag{8}$$

and, eliminating $H(w)$ by Eq. (1)

$$\dot{w}\left(1+\frac{32\pi^2 m}{\rho c^2}w\alpha\right)=(H_a-H_c)\alpha. \tag{9}$$

If the external field H_a is constant in time, which is the simplest experimental condition, Eq. (9) yields by integration:

$$w=\frac{\rho c^2}{32\pi^2 m\alpha}\left[1+\frac{64\alpha^2\pi^2 m(H_a-H_c)}{\rho c^2}t+A\right]^{\frac{1}{2}}-1, \tag{10}$$

where A is a constant, to be determined from the initial conditions. If the "formative phase" is very short, the initial condition is $w(0)=0$, and hence $A=0$.

In this case, one obtains from Eq. (10) by differentiation

$$\dot{w}=\frac{\alpha(H_a-H_c)}{\left(1+\frac{64\alpha^2\pi^2 m(H_a-H_c)}{\rho c^2}t\right)^{\frac{1}{2}}} \tag{11}$$

or

$$\frac{1}{\dot{w}^2}=\frac{64\pi^2 m}{\rho c^2(H_a-H_c)}\left(t+\frac{\rho c^2}{64\pi^2\alpha^2 m(H_a-H_c)}\right). \tag{12}$$

If the tape has width L, the magnetic flux ϕ is

$$\phi=L\cdot 4\pi m(4w-a), \tag{13}$$

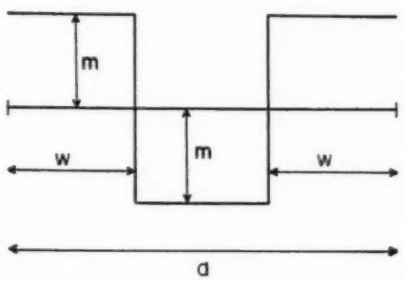

FIG. 3. The magnetization M as a function of z (thickness direction).

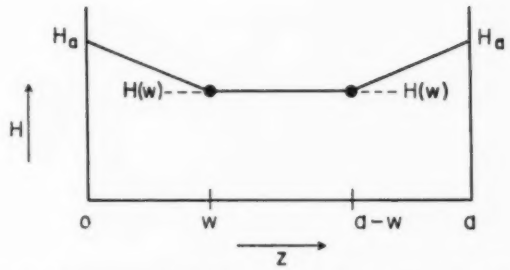

FIG. 4. The magnetic field intensity $H=H_z$ as a function of z at an arbitrary time t when the walls are at $z=w$ and $z=a-w$, respectively.

disregarding again the small contribution of the magnetic field to the total flux. Within the same approximation, we may set

$$4\pi m=B_s, \tag{14}$$

where B_s is the saturation induction. Equation (12) becomes

$$(\dot{\phi})^{-2}=\frac{4\pi(t+t_0)}{\rho c^2 L^2 B_s(H_a-H_c)} \tag{15}$$

$$t_0=\frac{\rho c^2}{\pi 16 B_s\alpha^2(H_a-H_c)}. \tag{16}$$

This equation is valid for the period after the formation of the domain wall. By integration of Eq. (9), one obtains for the time

$$(H_a-H_c)\alpha(t+\tau)=w+\frac{4\pi B_s}{\rho c^2}\alpha w^2, \tag{17}$$

where τ is a constant which depends on the length of the formative phase. If this time is considered as very short, one obtains for the total switching time T (by setting $w=a/2$)

$$T=\frac{\pi B_s a^2}{\rho c^2(H_a-H_c)}+\frac{a}{2\alpha(H_a-H_c)}. \tag{18}$$

The first term is the contribution of eddy-current retardation, and agrees with previous calculations by Ganz.[2] The second term is the contribution of the "anomalous retardation" of the domain walls.

In order to verify the validity of the approximation made in omitting the first term of the right-hand side of Eq. (7), one can substitute the value of $H(z,t)$ obtained in first approximation into the small term of Eq. (7) and re-solve it. One finds that the correction term is of the order of

$$H_a/B_s,$$

which is very small under usual conditions.

[2] A. G. Ganz, Trans. Am. Inst. Elec. Engrs. **65**, 177 (1946).

Reflection of a Compression Wave from a Symmetrical Wedge

R. W. SKULSKI, *Farnsworth Electronics Company, Fort Wayne, Indiana*

AND

D. WEIMER, *American Machine and Foundry Company, Chicago, Illinois*

(Received June 10, 1955)

Compression waves generated by paper pistons accelerated by shock waves in a shock tube have been reflected from a symmetrical wedge. Studies of the density fields in the interaction region have been made with an interferometer, and the parameters, "wave age," distance up the wedge, and angle of incidence have been investigated over a range of incidence angles from 25° to 80° and "effective shock strengths" from $\xi=1.1$ to $\xi=2.0$. The limit of regular reflection for this type of wave is shown to exist theoretically, and this limit has been verified experimentally. Beyond this limit a type of Mach reflection occurs.

I. INTRODUCTION

Reflection of Waves

IT is well known that a wave propagating in a gaseous medium will be reflected at a solid boundary or at an interface where there is a variation in the properties of the medium.

Figure 1 schematically shows a shock wave obliquely reflecting from a plane surface. Because the phenomenon is nonlinear, the angle of incidence is not equal to the angle of reflection. Referring to Fig. 1, the incident wave is traveling with a velocity U into an undisturbed medium. Particle velocity directions in the different regions of flow are represented by the small arrows. In the triangular region the compressed gas flows perpendicular to and with a velocity u toward the incident wave front. In the region beyond the incident wave, the reflected wave must be of such a strength and at such an angle that the flow is turned parallel to the surface.

A limit exists for the regular reflection of shock waves. It was first reported by E. Mach[1] that a new type of reflection occurred after the incidence angle exceeded a critical value. The analytical determination of this angle, found in the works of J. von Neumann[2] and Polachek and Seeger,[3] showed that this critical angle depended only on the incident wave strength. A survey of the Mach reflection of shock waves can be found in the thesis of D. R. White.[4]

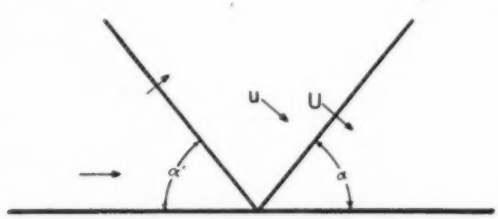

FIG. 1. Schematic of regular reflection.

Investigations concerning compression waves are less plentiful. K. O. Friedrichs[5] and A. F. Pillow[6] have recently presented theoretical treatments on shock growth, and A. B. Laponsky[7] offers experimental evidence on this subject. One other work by T. Schiffman[8] treats the head-on reflection of a compression wave using the numerical method of S. Chandrasekhar.[9]

Objectives

Essentially the objectives of this investigation were: (1) to provide a method for generating compression waves suitable for reflection studies; (2) to ascertain the general behavior of compression waves in oblique reflection; (3) to determine if a limit of regular reflection exists; (4) to determine what type of reflection occurs beyond such a limit.

II. EXPERIMENTAL APPARATUS

The experimental study to be described was conducted in the Armour Research Foundation shock tube using a Mach-Zehnder interferometer to observe the shock field. This 8-in.×8-in. tube as arranged for the study consisted of a 3-foot long chamber, a 20-foot channel, and was operated as a compressed air shock tube with a cellulose acetate diaphragm between the chamber and the channel. Because of the large fringe shifts involved, the channel was reduced to a width of 2 inches by splitter plates in the test section. Figure 2 illustrates the test setup.

In order to study compression waves, it was necessary to use a method by which the discontinuous change in medium properties across a shock wave could be modi-

[1] E. Mach, Vienna Acad. Sitzber. **78**, 819 (1878); other papers, **72–92**, (1875–1889).

[2] J. von Neumann, "Oblique reflection of shocks," Explosive Research Report, No. 12, Navy Dept. Bureau of Ordnance Re2c, Washington, D. C. (1943).

[3] H. Polachek and R. Seeger, "Regular reflection of shocks in ideal gases," Explosive Research Report, No. 13, Navy Dept. Bureau of Ordnance Re2c, Washington, D. C. (1943).

[4] D. R. White, "An experimental survey of the Mach reflection of shock waves," Tech. Report II–10, Princeton University (1951).

[5] K. O. Friedrichs, Commun. Appl. Math. **1**, 211 (1948).

[6] A. F. Pillow, Proc. Cambridge Phil. Soc. **45**, 558 (1949).

[7] A. B. Laponsky, "Observation of shock formation and growth," Technical Report No. 1 ONR, Lehigh University (1951).

[8] T. Schiffman, "Numerical solutions for the reflection of a compression wave from a rigid wall," Unpublished Report Appendix, Armour Research Foundation (1951).

[9] S. Chandrasekhar, "The normal reflection of a blast wave," BRL Report 439 (1943).

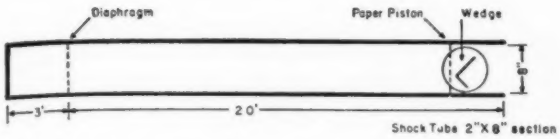

FIG. 2. Shock tube arrangement for compression wave study.

Piston

fied into a smooth isentropic compression. The method devised by White and Weimer[10] was used to modify the pressure profile of a shock wave into that of a compression wave. This consisted of a paper curtain hung across the shock tube and struck by a shock wave. The accelerated sheet of paper acted like a piston to produce the desired wave.

In the present study, various weights of paper were used in combination with several shock strengths[11] to produce compression waves of various strengths. Two serious difficulties, leakage around the edges and secondary waves, were encountered in attempting to produce a compression wave of the desired shape. By bending $\frac{1}{2}$-inch flaps on the edges of the piston and placing them on the downstream side, the motion of the paper tended to seal the edges against the tube walls and satisfactory compression waves were formed if the piston was parallel to the incident shock wave.

The character of a compression wave depends upon the piston acceleration, which is equal to the ratio of the pressure difference across it to its mass per unit area. A strong shock and/or a light piston will produce a steep wave which will transform quickly into a shock; a weak shock and/or a heavy piston will produce a gradual pressure rise of longer duration. Placing the piston at various positions in front of the observation point will give pictures of the wave at various stages of its development into a shock (see Fig. 3).

A particular stage of development will be defined as the age of the compression wave in subsequent discussions and is defined as the time interval between the start of piston acceleration and the photograph time.

Wedge

The reflection surface for this study was a symmetrical wedge. It was made from a piece of ground two-inch channel iron, pivoted on two trunnions mounted on a base plate. A worm and worm gear set were used to vary the wedge agle. The whole assembly was attached to the floor of the tube.

III. EXPERIMENTAL DATA

All of the experimental data for this study are in the form of monochromatic and white light interferograms of the various wave configurations and the undisturbed field. Enlarged prints were made of the disturbed monochromatic fields and in cases where there was some doubt as to the path of a fringe through the wave front a large print also was made of the white light field. After positive fringe identification was made, the monochromatic prints were placed on the enlarger table. The negative of the monochromatic undisturbed field was inserted into the enlarger and projected onto the print. With proper alignment and a small allowance for print shrinkage, the superimposed fields yielded the lines of constant fringe shift.

For all experiments, pistons were constructed of paper 0.004-inch thick and weighed 1.29 grams. A shock of strength 1.88 (as previously defined) generated in the shock tube was used to accelerate the pistons. The undisturbed medium was in all cases at 14.7 psia and 70°–75°F.

Compression Wave Series

Initially a set of photographs of the compression wave in various stages of its development were obtained. The piston was set at increasing distance from the point of observation in order to catch the wave at increasing ages, proceeding on to shock development. One of the photographs is included as Fig. 4. The approximate position of the lines of constant fringe shift may be found by using a straight edge to extend the fringe lines in the undisturbed regions before the wave.

Variable Angle Series

The first reflection studies were made by photographing a compression wave reflecting from a plane surface set at various angles of incidence. The piston was always set at the same distance from the point of observation in order to produce an identical wave of

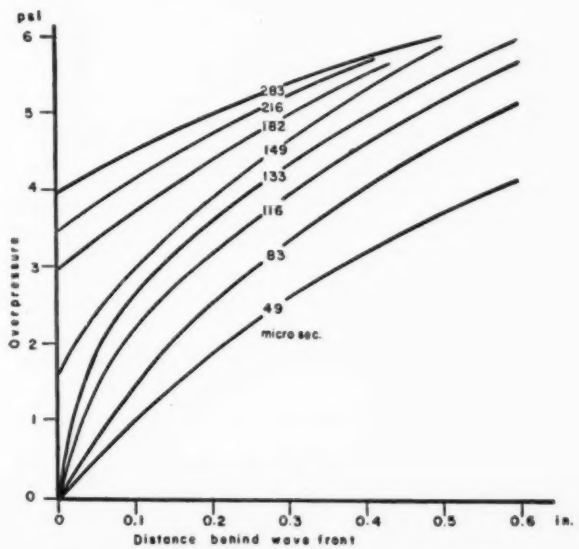

FIG. 3. Wave profiles at successively greater ages.

[10] D. R. White and D. K. Weimer, "A method for modification of the pressure profile in a shock tube," Tech. Report II-12, Princeton University (1952).

[11] The strength of a wave is defined as the ratio of the absolute pressure behind the wave to that ahead of the wave.

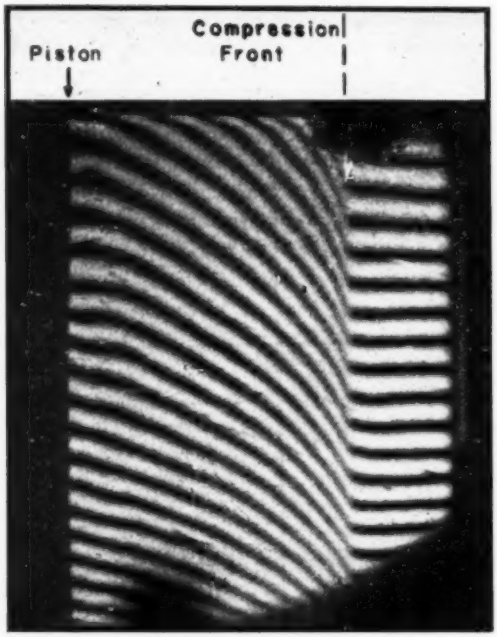

FIG. 4. Typical interferogram of compression wave of duration time $t=83$ microseconds.

same age for each incidence angle. The purpose of this series was to ascertain whether a limit of regular reflection exists, and if so, what type of reflection occurred above this limit. In addition, information concerning reflection angles and compression wave strengths was desired in order to determine proper parameters for the next set of photographs.

Mach Reflection Series

In the third series of photographs, a set of pictures was taken at a 65° incidence angle in order to separate, for study, the effects of the wave age and distance traveled up the wedge on the development of Mach reflection of a compression wave.

IV. DISCUSSION AND RESULTS

Compression Waves

The manner in which the isentropic variation of medium properties occurs in a compression wave is not fixed but depends on the type of forcing function accelerating the piston. The compression waves employed in the present investigation were generated by a pressure difference across the piston commencing at the value of the reflected shock overpressure. As soon as the piston began to accelerate, the compression wave starting from the front of the piston raised the pressure there above atmospheric, while a rarefaction wave leaving the rear of the piston decreased the reflected overpressure. The net effect was a monotonically decreasing force on the piston. Observations for various combinations of shock strength and piston mass showed that the compression wave front always turned into a shock before the piston ceased to accelerate (see Fig. 3). Hence, in order to observe a compression wave without a shocked front, it was necessary to photograph the wave before any maximum pressure was attained. It is obvious that if the acceleration could be made zero before the shock formed, a compression wave of finite width followed by a region of uniform state would occur. Indeed, White and Weimer[10] caught the piston with a wire grid, resulting in a rarefaction wave overtaking the compression wave producing a peaked wave.

The piston method of generating compression waves is limited in that it is difficult to produce a steep wave profile because very large piston accelerations are required. In addition, the wave must be observed very early before it transforms into a shock. In the reflection series of photographs, this was difficult due to interference between the piston and the wedge point.

The well-known interferometer Eq. (1), written below, illustrates that lines of constant fringe shift are lines of constant density if ρ_0 is taken as the density of the uniform region into which the wave is traveling:

$$\Delta N=\rho_0 M[1-(\rho/\rho_0)]. \tag{1}$$

For isentropic compression,

$$p/p_0=(\rho/\rho_0)^{\gamma}. \tag{2}$$

Using Eq. (2) in Eq. (1) gives

$$\Delta N=\rho_0 M[1-(p/p_0)^{1/\gamma}], \tag{3}$$

which shows that constant fringe shift lines are lines of constant pressure. Similarly, on these constant fringe shift lines, temperature is also constant. As the sound velocity is a function of temperature only, it is also constant along these lines.

The above statements hold for the interaction region of the reflected wave also, so long as every part of the region has experienced only isentropic changes of state. In the case of a one-dimensional wave Courant and Friedrichs[12] have integrated the equation of compressible flow using Eq. (2) to obtain a relation between the flow velocity and the pressure:

$$u-u_0=\frac{2c_0}{\gamma-1}\left[\left(\frac{p}{p_0}\right)^{(\gamma-1)/(2\gamma-1)}\right]. \tag{4}$$

If we take $\gamma=7/5$ and assume an undisturbed region at a pressure of $p_0=14.7$ psia and a temperature of $T_0=530°R$, then Eq. (4) reduces to

$$u=5640\left(\frac{p^{1/7}}{1.47}-1\right). \tag{5}$$

This equation combined with Eq. (3) gives an equation in u and ΔN.

[12] R. Courant and K. O. Friedrichs, *Supersonic Flow and Shock Waves* (Interscience Publishers, Inc., New York, 1948).

Wave Profiles

Because the flow and sound velocity are both constant on the fringe shift lines of a one-dimensional wave, they are also lines of constant wave disturbance velocity $(u+c)$, and hence the record of their progress on a time-distance plane gives a characteristic plot. The equation of the "plus" characteristics of a forward-facing simple wave is a straight line[13]:

$$\Delta x/\Delta t=(u+c). \tag{6}$$

The x and t coordinates are found from the compression wave photographs. The zero time coordinate of each wave photograph is taken relative to the start of piston motion. The x coordinate for each fringe shift line is obtained by measuring its distance from a hairline in the picture in front of the wave and subtracting this distance from the measured distance between the hairline and the piston.

Reflection of Compression Waves

Regular Reflection

Before reflection is discussed, it is well to include an illustration giving the nomenclature of reflection. This illustration is Fig. 5.

The most outstanding feature of the regular reflection photographs in the variable angle series is that the reflected wave front is curved between the inflection and reflection points. Above $\alpha=35°$, the front is concave in the direction of motion while below this angle the front is convex. At $\alpha=35°$ no curvature is discernible.

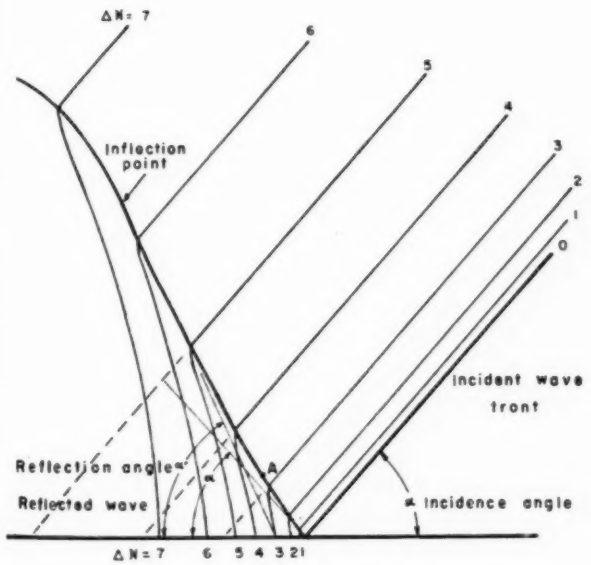

FIG. 5. Typical compression reflection with isodensity lines. $\Delta N=-26.2[1-(P/P_0)^{1/\gamma}]$.

[13] Geiger and Mautz, "The shock tube as an instrument for the investigation of transonic and supersonic flow patterns," Engineering Research Institute, University of Michigan, (1949).

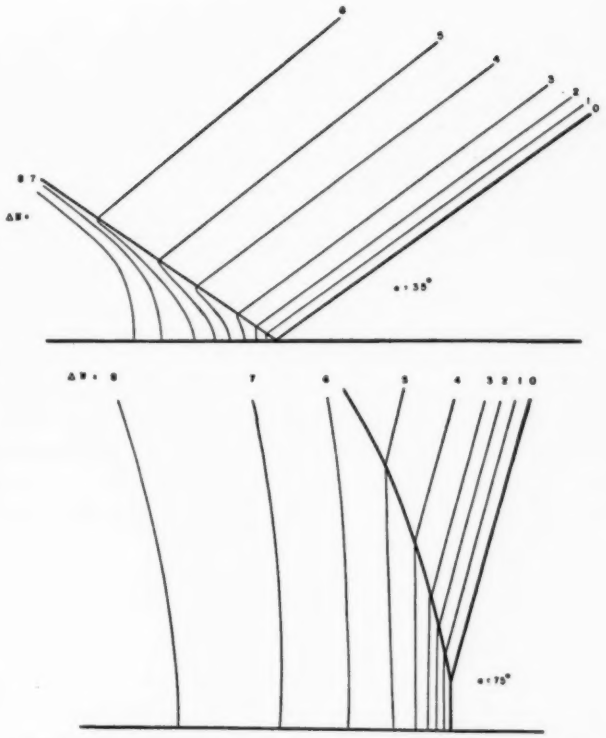

FIG. 6. Reflection of compression wave with age $t=133$ microseconds and angle of incidence 35° to 75°.

Referring to Fig. 5, consider a point, A, on the reflected wave near the reflection point. As A moves along the reflected front toward the reflection point, it travels into a region only slightly different in state from the undisturbed region. In the limit then, the infinitesimal portion of the reflected wave adjacent to the reflection point moves into an undisturbed region. In addition, the incident and reflected wave fronts may be considered equivalent to sound waves because the pressure gradient is infinitely small across these fronts; thus, optical reflection must occur at the point of reflection. In more precise terms, if a tangent is drawn to the reflected wave front at A, the angle between this tangent and the reflecting surface approaches the angle of incidence as point A approaches the point of reflection as a limit. Since optical reflection occurs only at the reflection point and not along the entire wave front, it is concluded that the reflection of a compression wave is nonlinear in character as in the case of shock wave reflection.

In order to explain the curvature, it is convenient to replace the smooth profiles of Fig. 3 by a series of step functions. We then have approximately equal jumps in the medium properties at the fringe shift lines with uniform regions between these lines. The reflected wave front will then appear as a series of line segments showing a discontinuity in slope at each fringe shift line. The velocity of the reflected wave front with respect to the wedge surface is the sum of the sound velocity of the medium into which the front is traveling

and the component of the flow velocity perpendicular to the front. For $\alpha' > 45°$, both of these velocities act to increase the front velocity as one proceeds away from the reflection point across successive discontinuities. Thus, the wave front increases its slope as it crosses a discontinuity. At $\alpha' = 45°$, the flow velocity has no perpendicular component; however, the increase in sound velocity is enough to bend the front slightly forward. At some angle less than forty-five degrees the increase in the sound velocity is counteracted by the increase in flow velocity whose component still acts perpendicular to the wave front but in the opposite direction so that the wave appears straight. This apparently is the case in Fig. 6 for $\alpha = 35°$. Below this angle the flow velocity change predominates, thus bending the front to cause a decrease in slope. If the step functions postulated above are made finer so that the smooth wave profile is approached as a limit, the straight line segments become smaller and more numerous approaching the smooth curved front given in the variable angle series of photographs.

The angle of reflection is defined as the angle that a tangent to the reflected wave front makes with the wedge at the point where the rarefaction wave from the wedge tip becomes tangent to the curved, reflected wave front. (Above $\alpha = 35°$, this point is the inflection point.)

If a compression wave of finite width could be produced wherein no rarefaction wave was present to alter the reflected wave, the slope of the reflected wave should continue to change to that final value associated

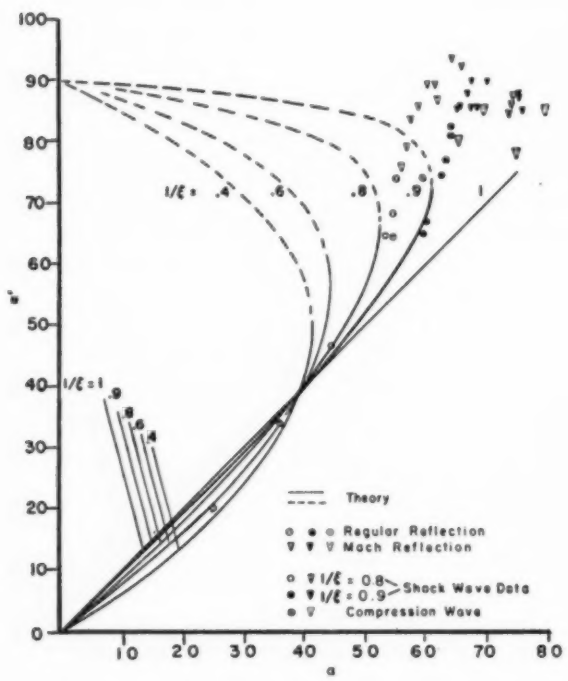

FIG. 7. Incident *vs* reflected angle for theoretical and experimental results.

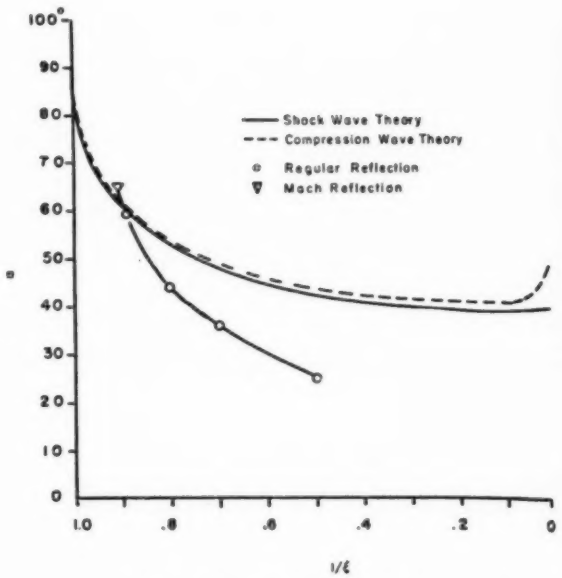

FIG. 8. Limit of regular reflection.

with reflection of a shock of the same strength as the finite compression wave. As the age of the wave increases, the incident and reflected waves begin to transform into shocks according to Fig. 3. As the rear of the incident wave of finite width passes down the reflected wave front, the reflected front becomes straight and takes on the final value of the reflection angle.

If the wave is infinite in width, as it was in this investigation, then for incidence angles of less than about 39° (see Fig. 7) the slope of the reflected wave should approach the angle for an infinitely strong shock[3] $(1/\xi = 0)$. Above 39° the regular reflection wave front steepens (here we are forced to reinstate the rarefaction wave in the configuration) up to the inflection point. As the age of the wave increases, the slope at the inflection point will increase, bringing the point nearer to the reflection point. After the points are superimposed, as will be seen later, the reflection point separates from the wedge.

Compression Wave Strength

If a compression wave has finite width, then its strength is the ratio of the absolute pressures in the uniform regions after and before the wave. For the infinite wave, the strength at each point increases indefinitely with increasing distance from the wave front; therefore, this wave has no absolute strength defined.

Upon observation of the reflection configuration, it is evident that not all of the compression wave is effective in producing the observed reflection configuration. Hence, the notion of effective strength must be defined. The natural definition arising from these considerations is to compare this reflection to that of a shock wave producing the same angle of reflection for the same in-

cidence angle. The incident and reflected angles for the variable angle series (Fig. 6) were plotted in Fig. 7. The angles are measured from a line parallel to the wedge in the cases where the reflection point leaves the wedge surface. The solid lines were obtained by using the two-shock theory of Polachek and Seeger.[3] The experimental data for shock waves plotted in Fig. 7 was obtained by L. G. Smith.[14] Smith measured his angles in the case of Mach reflection with respect to the path of the triple point; they have therefore been changed by the magnitude of the angle between the path of the triple point and the wedge.

Two points are noted from Fig. 7. The first is that the effective strength is seen to decrease with increasing incidence angles, even though compression waves of identical age were used. A plot of this variation is seen in Fig. 8 along with the curves giving the limit of regular reflection for shock waves and compression waves to be discussed in the next section. The second is that the effective strength for a given incidence angle increases with the age of the incident wave. From Fig. 3 it is seen that the fringe shift lines are more widely spaced for the younger waves of the series. For infinitely wide spacing, a sound signal results which must reflect optically. As the spacing is decreased by increasing the age, the reflected angle changes and likewise the effective strength, according to Fig. 7. It is inferred that observing the reflection of a compression wave at increasing age is equivalent to observing the reflection of waves of increasing effective strengths.

Limit of Regular Reflection

The variable angle series of photographs also yielded information concerning a limit of regular reflection of a compression wave. Fig. 9 illustrates that a limit of regular reflection does exist, just as in the case of shock waves. In order to obtain Fig. 9, the fringe shift lines of the incident wave were extended downward until they intersected the wedge as shown in Fig. 5. The distance between the wave front and the wedge, measured along these lines, was plotted against the corresponding fringe shift line. Note that the curves beginning with the one for a 65° incidence angle have ordinate intercepts. This means that the reflected wave front meets the incident wave front at the reflection point which has separated from the wedge. The curves are not evenly spaced because of slight errors in the time interval and because of unequal enlargement of the photographs. An attempt to predict the limit theoretically is presented in the Appendix. The procedure of von Neumann[2] was used, substituting isentropic equations describing the change across the waves for the Rankine-Hugoniot relations. The assumption of regions of uniform flow between the incident and reflected wave and following the reflected wave, of course, does not hold for the present study. Equation (A18) was solved by iteration using an IBM Card Program Calculator. The equation was broken down into the fundamental mathematical operations and programmed by properly punching the IBM cards. Running these cards through the machine performs one iteration. Sufficient accuracy was obtained by five iterations per point. The results of this computation and the curve applying for shock waves are shown in Fig. 8. The curves approach each other as the strength decreases (the reciprocal strength $1/\xi$ increases toward one) because the entropy loss in shock waves decreases as the strength decreases. The effective strengths of the waves used in the variable angle series were determined from Fig. 7 and plotted *versus* the corresponding incidence angle in Fig. 8. This curve is seen to intersect the limiting curve for compression waves at about $\alpha=62°$. The plotted point for $\alpha=65°$ as seen from Fig. 9 has an ordinate intercept, thus classifying it as a new type of reflection, which is discussed in the next section. The agreement between theory and experiment for weak waves is good, despite the erroneous uniform region assumption.

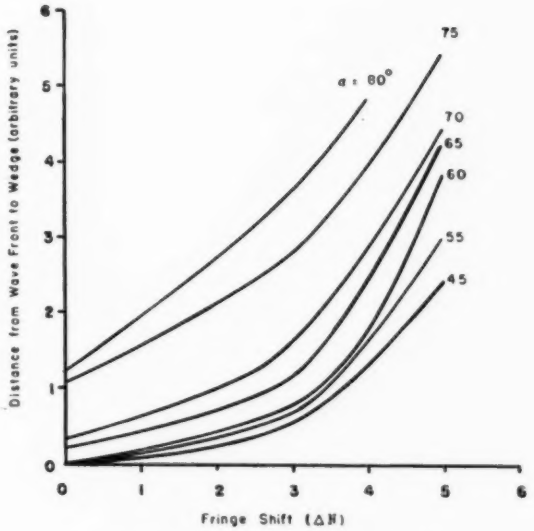

FIG. 9. Wave front-wedge distance *vs* fringe shift for various incidence angles.

Mach Reflection

Above the limit of regular reflection, another type of reflection for compression waves occurs. The reflection point moves away from the wedge surface, causing a third compression wave to form between this point and the wedge surface (see Fig. 6). This wave front is perpendicular to the wedge at the surface. As this configuration is very similar to Mach reflection observed for shock waves, this name will also be used to denote this compression wave reflection form.

As already described, a series of photographs was taken at $\alpha=65°$ of this type of reflection called the

[14] L. G. Smith, "Photographic investigation of the reflection of plane shocks in air," NDRC Report No. A-350, OSRD Report No. 6271, Princeton University (1945).

Mach reflection series. The same method of measurement used to produce Fig. 9 was used to obtain Figs. 10 and 11.

Figure 10 shows the effect of increasing the age of

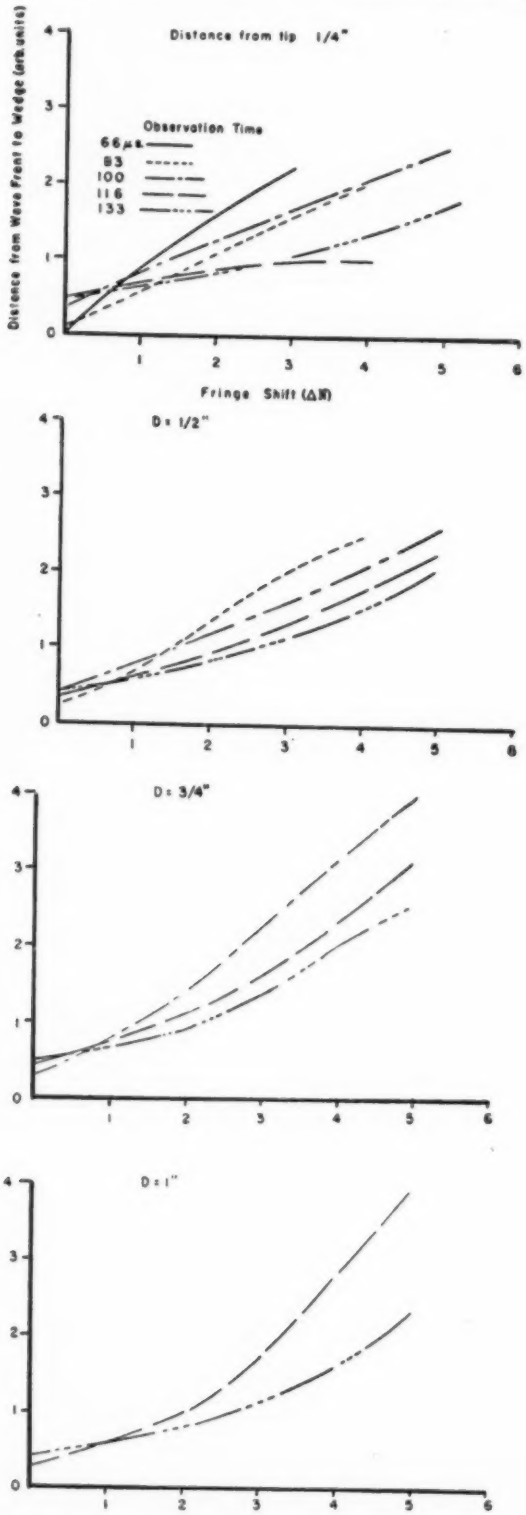

FIG. 10. Wave front-wedge distance *vs* fringe shift for various observation times at given wedge positions.

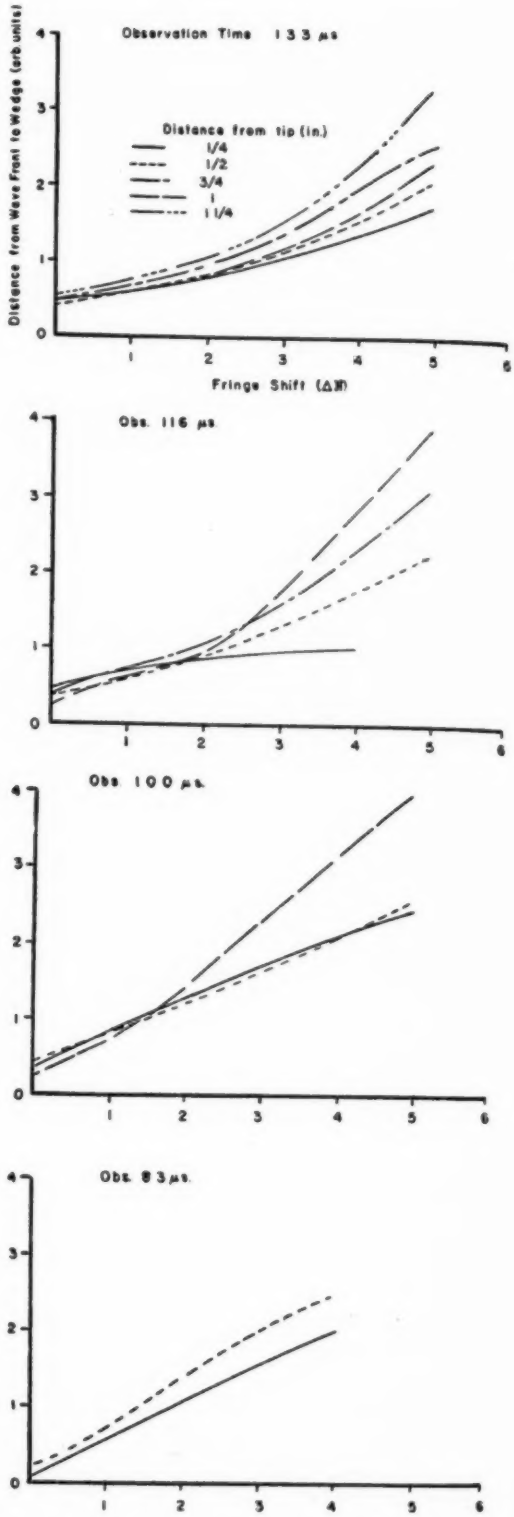

FIG. 11. Wave front-wedge distance *vs* fringe shift for various wedge positions at given observation times.

the wave at the given wedge positions. The reflection point height increases with increasing wave age. As mentioned previously, this increase in age is equivalent to an increase in the effective strength. For the $\frac{1}{4}$ in.

wedge position, the reflection begins regularly and transforms to Mach reflection as the effective strength increases. This is in accordance with Fig. 8. Apparently, the first observation lies on the 65° line to the left of the limit curve. This point then moves horizontally to the right, crossing the curve, in later observations.

Figure 11 gives the effect of increasing distance from the wedge tip for given wave ages. No discernible trend is evident. The reflection point heights are very nearly the same, the small scatter being due to experimental errors. This observation differs from the results concerning the Mach reflection of shock waves. Here, the triple point is observed to rise linearly with distance traveled up the wedge.

On an interferogram, the slipstream in a Mach shock wave configuration appears as a small discontinuous fringe shift beginning at the triple point and trailing out behind until it intersects the reflection surface. Its appearance is that of a weak shock. However, it is a discontinuity in density, entropy, and temperature, but not pressure. Its cause is unequal entropy change in the medium, depending upon whether the flow passes through the incident and reflected shocks or through the single Mach stem. A physical explanation of the Mach stem growth with distance traveled up the wedge is afforded by considering the triangular region bounded by the slipstream, the wedge surface and the Mach stem. There is a medium flow across the Mach stem but no flow across the slipstream or the wedge surface. The triangular region acts as a sink and must grow in order to accommodate the flow entering through the Mach stem. In the case of Mach reflection of compression waves, no slipstream has been observed, and indeed does not exist, because the entire reflection region has been subjected only to isentropic changes. Since there is no slipstream, there is no sink region and hence, no necessity for the reflection point to change its height above the wedge surface.

V. ERRORS

In the Mach reflection series, the nominal wedge observation positions were 0.25, 0.50, 0.75, 1.0, and 1.25 inches, measured horizontally from the wedge tip. The average observed positions of the compression waves were 0.26, 0.41, 0.75, and 0.92 inches. (The last position could not be measured because the wedge tip was not visible in the photographs.) The mean deviation from these average positions was 0.04 inch, or the equivalent of about three microseconds assuming standard sound velocity. This deviation could easily be accounted for by slight wedge misplacements or interval generator deviations.

For angular measurements, it is estimated that all angles are accurate to one degree.

VI. SUMMARY AND CONCLUSIONS

1. Compression waves suitable for reflection studies may be produced in a shock tube by placing a properly designed paper piston across the tube and accelerating it with a shock wave.

2. The reflected wave is curved because it is traveling into a region where the flow velocity and the sound velocity are continuously changing.

3. If the incident and reflected angles are matched with an equivalent shock, an effective compression wave strength is defined which increases with increasing incidence angle for identical incident waves.

4. The effective strength increases with increasing observation time of a given compression wave at constant incidence angle.

5. A theoretical and experimental limit of regular reflection exists for compression waves.

6. Above this limit, the reflection point leaves the wedge surface. Due to the similarity of this configuration with the Mach reflection of a shock wave, it is also called Mach reflection.

7. For a given wedge position, the Mach stem grows with increasing observation time, hence increasing effective strength.

8. For a given observation time, and hence effective strength, no definite growth in Mach stem with distance up the wedge was observed. It was concluded that no growth was necessary because of the isentropic reflection region.

APPENDIX. DERIVATION OF THE LIMIT OF REGULAR REFLECTION FOR COMPRESSION WAVES

Referring to Fig. 1, it is assumed that the compression wave is of finite width and that uniform regions exist in front of the incident wave, between the incident and reflected wave and after the reflected wave. The wave is represented schematically by a single line.

The fact that the vertical component of the flow velocity u is cancelled by the reflected wave may be expressed by

$$u\cos\alpha = u'\cos\alpha'. \tag{A1}$$

The velocity of the reflected wave relative to the boundary is its velocity, U', relative to the flow in front of it plus the normal component of the flow

$$u\cos(\alpha+\alpha'). \tag{A2}$$

The condition that the reflection point be the intersection of the incident and reflected waves is given as

$$\frac{U'-u\cos(\alpha+\alpha')}{\sin\alpha'} = \frac{U}{\sin\alpha}. \tag{A3}$$

The change in the flow velocity across a compression wave is given by Courant and Friedrichs.[12] If we use $\gamma=7/5$ for air and postulate that the incident wave is moving into an undisturbed medium

$$u = 5c_0(\xi^{1/7}-1) = 5c_0 y, \tag{A4}$$

where c_0 = sound velocity of the undisturbed medium, $\xi = p_1/p_0$, and $y=\xi^{1/7}-1$. The wave velocity is defined

as the average of its front and rear velocities

$$U=\frac{c_0+(u+c_1)}{2}=c_0(3\xi^{1/7}-2)=c_0(3y+1), \quad \text{(A5)}$$

where

$$c_1=c_0\xi^{1/7}=c_0(y+1) \quad \text{(A6)}$$

is the sound velocity of the region between the incident and reflected waves.

For the reflected wave, we may write similar equations using (A6) for c_1.

$$u'=5c_1(\xi'^{1/7}-1)=5c_0y'(y+1), \quad \text{(A7)}$$

$$U'=\frac{c_1+(u'+c_2)}{2}=c_0(y+1)(3y'+1), \quad \text{(A8)}$$

where $\xi'=p_2/p_1$ and $y'=\xi'^{1/7}-1$. c_2=sound velocity of the medium behind the reflected wave. From Eq. (A7) and Eq. (A8), y' is eliminated to obtain

$$u'=5/3(U'-c_0(y+1)). \quad \text{(A9)}$$

Using Eq. (A1), u' is removed, giving

$$U'=c_0(y+1)-\tfrac{3}{5}u\frac{\cos\alpha}{\cos\alpha'}=0. \quad \text{(A10)}$$

Substituting for U' from Eq. (A3), we have

$$\left(\frac{U}{\sin\alpha}-u\sin\alpha\right)\sin\alpha'+u\cos\alpha\cos\alpha' -c_0(y+1)-\tfrac{3}{5}u\frac{\cos\alpha}{\cos\alpha'}=0. \quad \text{(A11)}$$

Letting $X=\cos\alpha'$, Eq. (A11) becomes

$$\left(\frac{U}{\sin\alpha}-u\sin\alpha\right)X(1-X^2)^{\frac{1}{2}}=-u\cos\alpha X^2 +c_0(y+1)X+\tfrac{3}{5}u\cos\alpha. \quad \text{(A12)}$$

On squaring, a quartic in X is obtained

$$\left[u^2\cos^2\alpha+\left(\frac{U}{\sin\alpha}-u\sin\alpha\right)^2\right] \times X^4-[2uc_0(y+1)\cos\alpha]X^3 +\left[c_0^2(y+1)^2-\frac{6}{5}u^2\cos^2\alpha-\left(\frac{U}{\sin\alpha}-u\sin\alpha\right)^2\right]X^2 +\left[\frac{6}{5}c_0(y+1)u\cos\alpha\right]X+\frac{9}{25}u^2\cos^2\alpha=0. \quad \text{(A13)}$$

It was found that a meaningless root of this equation is

$$X=\cos\alpha'=\cos\alpha \quad \text{(A14)}$$

Factoring out this root by means of synthetic division and using Eq. (A4), Eq. (A5) and

$$\cos\alpha=Z \quad \text{(A15)}$$

the resulting cubic is

$$[(5y^2+10y)Z^2+(4y^2-4y+1)]X^3 +[-5y^2Z^3+(14y^2+6y+1)Z]X^2 +[(3y^2-6y)Z^2+(-3y^2+6y)]X +[9y^2Z^3-9y^2Z]=0. \quad \text{(A16)}$$

From the theory of the reflection of a shock wave, similar considerations indicate that there is another meaningless root in Eq. (A16) which would reduce it to a quadratic. For a given wave strength and incidence angle, y and Z two values of the reflection angle X are obtained. For certain values of y and Z, a double root is obtained and for still others no real values of X are possible. The values of y and Z which give this double root describe the limit of regular reflection. The condition for any two of the roots of a cubic to be equal was applied to Eq. (A16). It is necessary that

$$p^2q^2+4q^3+27r^2-18pqr+4p^3r=0 \quad \text{(A17)}$$

where p, q and r are the coefficients of Eq. (A16) after normalization. A double quintic in Z is obtained with y as a parameter

$$AW^5+BW^4+CW^3+DW^2+EW+F=0, \quad \text{(A18)}$$

where

$$W=Z^2, \quad \text{(A19)}$$

$$A=(-500y^6), \quad \text{(A20)}$$

$$B=(11600y^6+26200y^5+19100y^4), \quad \text{(A21)}$$

$$C=(-11940y^6-30360y^5-22400y^4+11200y^3+100y^2), \quad \text{(A22)}$$

$$D=(4412y^6+10512y^5+11236y^4-14200y^3+2124y^2+40y), \quad \text{(A23)}$$

$$E=(-704y^6-184y^5-4276y^4+6152y^3-2152y^2+128y+4), \quad \text{(A24)}$$

$$F=(48y^6-366y^5+876y^4-1032y^3+528y^2-96y). \quad \text{(A25)}$$

Theoretical Basis for Measuring the Saturation Emission of Highly Emitting Cathodes under Space-Charge-Limited Conditions

C. R. CROWELL
Radio and Electrical Engineering Division, National Research Council, Ottawa, Canada
(Received June 22, 1955)

The second derivative of the current-voltage relationship of an ideal plane diode is calculated from the Epstein-Fry-Langmuir analysis. From this analysis it is shown that for the large saturation emissions characteristic of oxide-coated cathodes at normal operating temperatures, the current at the inflection point (i.e., the zero of the second derivative) is a sensitive measure of the saturation emission and is unaffected by the existence of a linear interface impedance. It is also shown that the general features of the results apply to cylindrical diodes.

INTRODUCTION

MEASUREMENT of the saturation emission of an oxide-coated cathode offers considerable difficulty. Static measurements of saturation emission at normal heater voltages require that large currents be drawn from the cathode. The power dissipated in the tube then overheats both the anode and the cathode. This has two effects on conditions at the cathode: the operating temperature of the emitter is raised and overheating of the tube parts usually results in outgassing and subsequent poisoning of the cathode. If the emitting properties are measured at a reduced heater voltage, the cathode is more susceptible to poisoning from residual gas in the tube and the change in equilibrium of the diffusion processes occurring in the cathode can result in a different cathode composition.

Measurement of pulsed emission at operating temperatures eliminates many of the above difficulties. When pulsed emission is measured in the temperature limited region, however, the effect of the accelerating field at the cathode surface is difficult to assess if the emitter is a semiconductor. This difficulty could be surmounted if a measurement indicative of saturation emission were possible in the space-charge-limited region.

The foregoing condition is satisfied if the current at the inflection point in the current-voltage characteristic of a diode can be used as a measure of the saturation emission. The inflection point current has been stated to be an approximate measure of the saturation emission in the definition of terms provided by the 1950 I.R.E. Standards on Electron Tubes.[1] Hopkins and Shrivastava[2] have recently developed a method of measuring this current and found that for the rectifier tube types they tested, the inflection-point current appeared to be a good indication of cathode quality. This conclusion is reinforced and the relationship between saturation emission and the inflection-point current is established theoretically by the analysis which follows, since it will be shown that the second derivative undergoes a rapid transition as it passes through zero and the current at the zero point is very sensitive to changes in saturation emission.

THEORETICAL ANALYSIS

The situation to be examined is that existing when a potential minimum occurs betwen the emitter and collector of a plane diode. The notation and results of the Epstein-Fry-Langmuir[3] analysis are summarized in the following paragraphs.

Using the normalized coordinates η and ξ for voltage and distance,

$$\eta=(V+V_m)/V_T \tag{1}$$

and

$$\xi^{\pm}=\pm(x-d_m)\xi_\infty(I_a/I_\infty)^{\frac{1}{2}}/s, \tag{2}$$

where V is the voltage at a distance x from the cathode; $-V_m$ is the voltage at the potential minimum, and d_m the distance of the potential minimum from the cathode. V_T is the voltage equivalent of the temperature and s the anode-cathode spacing. ξ^+ is the value of ξ in the region between the potential minimum and the anode, and ξ^- that between the cathode and the potential minimum. I_a is the anode current density and I_∞ the current density when the saturation current density I_s is infinite and the potential minimum occurs at the anode. $\xi_\infty(=2.5539)$ is the value of ξ^- at the cathode when $I_a/I_s\to 0$. When I, s, and T are measured in MKS units,

$$I_\infty=0.2451\times 10^{-6}(T/1000)^{\frac{1}{2}}s^{-2}. \tag{3}$$

The $\xi-\eta$ relationships are determined by the equation,

$$\xi^{\pm}=\int_0^{\eta}[\phi^{\pm}(u)]^{-\frac{1}{2}}du \tag{4}$$

where

$$\phi^{\pm}(u)=e^u-1\mp 2e^u\left(\int_0^{u^{\frac{1}{2}}}\exp(-x^2)dx-u^{\frac{1}{2}}\right)\pi^{-\frac{1}{2}}. \tag{5}$$

At the anode and cathode the values of ξ, η, and ϕ will be designated by the subscripts a and k, respectively. The anode current is determined by the saturation

[1] Standards on Electron Tubes, Proc. Inst. Radio Engrs. 38, 426 (1950).
[2] E. S. Hopkins and K. K. Shrivastava, Proc. Inst. Radio Engrs. 43, 707 (1955).
[3] H. F. Ivey, *Advances in Electronics and Electron Physics* (Academic Press, Inc., New York, 1954), Vol. VI, p. 137.

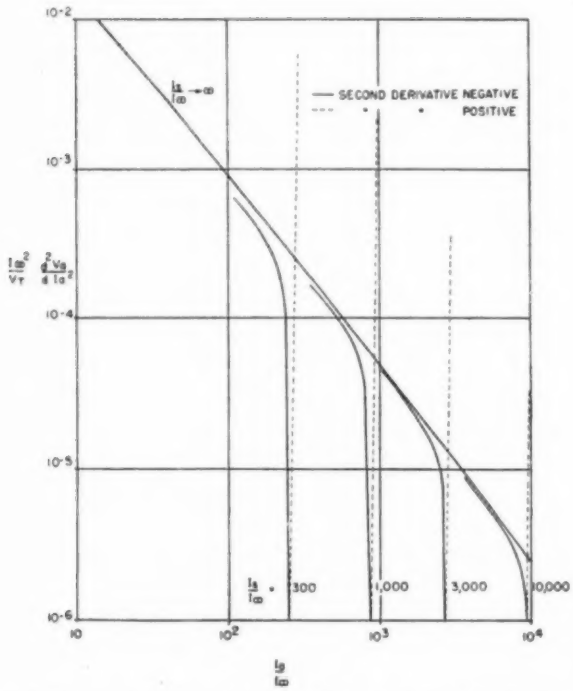

FIG. 1. The second derivative of the I–V characteristic of an ideal plane diode as a function of the anode current.

emission and the depth of the potential minimum:

$$I_a = I_s \exp(-\eta_k). \tag{6}$$

The six equations thus far listed contain the essential information available in the Epstein-Fry-Langmuir solution for the current-voltage characteristic. The second derivative can therefore be calculated from these equations. Since

$$V_a/V_T = \eta_a - \eta_k, \tag{7}$$

and Eq. (6) determines the relationship between I_a and η_k,

$$\frac{I_\infty}{V_T}\frac{dV_a}{dI_a} = -\frac{I_\infty}{I_a}\left(\frac{d\eta_a}{d\eta_k} - 1\right) \tag{8}$$

and

$$\frac{I_\infty^2}{V_T}\frac{d^2V_a}{dI_a^2} = \left(\frac{I_\infty}{I_a}\right)^2\left(\frac{d^2\eta_a}{d\eta_k^2} + \frac{d\eta_a}{d\eta_k} - 1\right). \tag{9}$$

The relationship between η_a and η_k is determined by Eq. (4) and Eq. (2) which requires that

$$\xi_a + \xi_k = \xi_\infty (I_a/I_\infty)^{\frac{1}{2}}. \tag{10}$$

Thus,

$$\int_0^{\eta_a} [\phi^+(u)]^{-\frac{1}{2}} du = \xi_\infty (I_s/I_\infty)^{\frac{1}{2}} \times \exp(-\eta_k/2) - \int_0^{\eta_k} \phi^-(u)^{-\frac{1}{2}} du. \tag{11}$$

Evaluating $d\eta_a/d\eta_k$ and $d^2\eta_a/d\eta^2_k$ from Eq. (11) and utilizing the fact that

$$d\phi^\pm/d\eta = \phi^\pm + 1 \mp 2(\eta/\pi)^{\frac{1}{2}}, \tag{12}$$

from Eq. (8) it follows that

$$\frac{I_\infty}{V_T}\frac{dV_a}{dI_a} = \frac{I_\infty}{I_a}\{1 + \phi_a^{\frac{1}{2}}[\phi_k^{-\frac{1}{2}} + \xi_\infty (I_a/I_\infty)^{\frac{1}{2}}/2]\} \tag{13}$$

and from Eq. (9),

$$\frac{I_\infty^2}{V_T}\frac{d^2V_a}{dI_a^2} = \left(\frac{I_\infty}{I_a}\right)^2\left\{\frac{\phi_a^{\frac{1}{2}}}{2} \times\left[(1+2(\eta_k/\pi)^{\frac{1}{2}})\phi_k^{-\frac{1}{2}} - \phi_k^{-\frac{1}{2}} - \xi_\infty\frac{(I_a/I_\infty)^{\frac{1}{2}}}{2}\right] + \frac{d\phi_a}{2d\eta_a}\left[\phi_k^{-\frac{1}{2}} + \xi_\infty\frac{(I_a/I_\infty)^{\frac{1}{2}}}{2}\right]^2 - 1\right\}. \tag{14}$$

Figure 1 shows the normalized second derivative as a function of I_a/I_∞ for various values of I_s/I_∞, and Fig. 2 shows the behavior of the second derivative as a function of I_a/I_s. It is apparent that the transition at the inflection point becomes sharper as the ratio I_s/I_∞ increases, but the value of the second derivative decreases. Figure 3 shows the ratio of the current at the inflection point (I_i) to the saturation current as a function of the ratio I_s/I_∞. Outlines of the calculations involved are presented in the Appendix.

COMPARISON OF CURRENT AND VOLTAGE SECOND DERIVATIVES

The second derivative with respect to the voltage can be obtained in terms of derivatives with respect to the current since

$$\frac{d^2I_a}{dV_a^2} = \frac{d}{dI_a}\left(\frac{dV_a}{dI_a}\right)^{-1}\frac{dI_a}{dV_a} = -\left(\frac{dV_a}{dI_a}\right)^{-3}\frac{d^2V_a}{dI_a^2}. \tag{15}$$

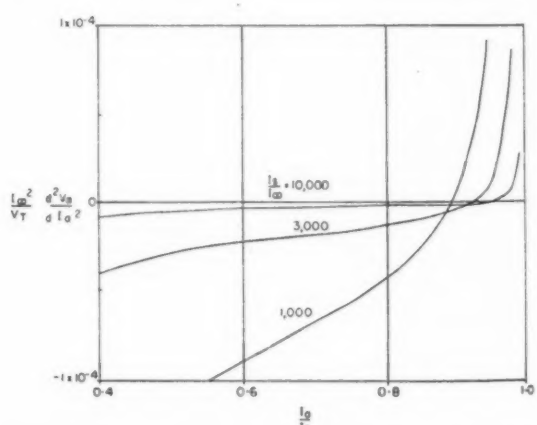

FIG. 2. The second derivative of the I–V characteristic of an ideal plane diode as the anode current approaches the saturation emission.

The variation of the second derivative with respect to voltage is not as sensitive a measure of the saturation emission as the variation of the second derivative with respect to current because the transition near the inflection point is not as sharp. The term involving $\phi_k^{-\frac{1}{2}}$ in Eq. (14) is largely responsible for the sharp transition shown in Fig. 2. The effect of this term is virtually cancelled by a $\phi_k^{\frac{1}{2}}$ term inside the cubed expression in Eq. (15)$\cdots$[see Eq. (13)].

The current second derivative has another practical advantage over that with respect to voltage. If in practice a linear impedance z exists in series with the ideal diode, a term $I_a z/V_T$ must be added to the right hand side of Eq. (7). Thus the I–V characteristic and the first derivative of that characteristic are not the same as for an ideal diode. Since

$$d^2(I_a z)/dI_a^2=0 \tag{16}$$

however, the second derivative with respect to current remains unaltered. This is not true of the second derivative with respect to voltage [see Eq. (15)] although the inflection point remains unaffected.

CYLINDRICAL CASE

A rigorous analysis in the cylindrical case is much more complex than in the plane case. It is known, however, that the effect of initial velocities of the electrons on the I–V characteristic is reduced[3] since both radial and tangential emission velocities assist in the escape of an electron over the potential minimum and a larger collecting field exists near the cathode. Thus the space charge limited emission should follow the three-halves power law more closely in the cylindrical case than in the plane case, since the requirements for rigid adherence to the three-halves power law are that the current must be space charge limited and the initial emission velocities of the electrons must be completely negligible. If these conditions were to be satisfied, then the following I–V characteristic would result:

$$I_a=KV_a^{\frac{3}{2}} \tag{17}$$

and

$$d^2V_a/dI_a^2=-(2/9)I_a^{-4/3}K^{-2/3} \tag{18}$$

(K is the perveance). The zero of the second derivative would then occur at the transition from the space charge limited region to the Schottky region since the second derivative has the opposite sign in the Schottky region. Thus in the cylindrical case the inflection point must occur closer to the saturation emission than in the plane case. The difference between the plane and cylindrical case is then small, since for may applications in the plane case, the current at the inflection point is sufficiently close to the saturation current to be considered a good approximation to the saturation current.

SUMMARY

At high current densities the current at the inflection point in the I–V characteristic of a plane or cylindrical diode has been shown to occur very near saturation emission. Thus measurement of the current at the inflection point constitutes a measurement of saturation emission from a surface which is not subject to a strong electric field. The current at the inflection point is also independent of the magnitude of the interface impedance.

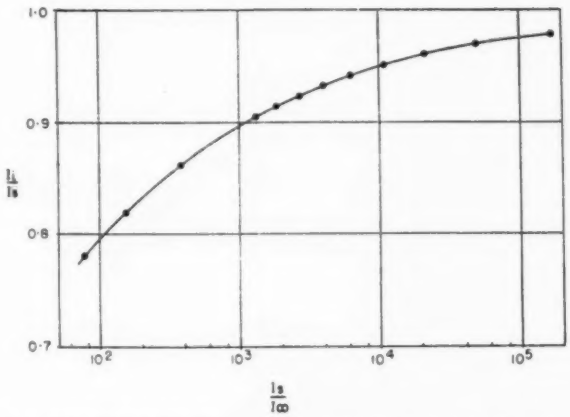

FIG. 3. The ratio of the current at the inflection point to the saturation emission as a function of the saturation emission.

APPENDIX

In calculating the second derivative it was found simplest for any given ratio I_a/I_∞ to assume values of η_k for which ϕ_k and ξ_k were tabulated by Ferris[4] and to calculate η_a and its associated functions. Equation (14) was rearranged in the following form:

$$\frac{I_\infty^2}{V_T}\frac{d^2V_a}{dI_a^2}=\left(\frac{I_\infty}{I_a}\right)^2\frac{\phi_a^{\frac{1}{2}}}{2}$$
$$\times\left[-\left(\frac{2-\chi}{4}\right)\xi_a+\chi f(1+f/\xi_a)-2\phi_a^{-\frac{1}{2}}+g\right] \tag{19}$$

where

$$f=\phi_k^{-\frac{1}{2}}+\xi_k/2 \tag{20}$$

$$g=(1+2(\eta_k/\pi)^{\frac{1}{2}})\phi_k^{-\frac{1}{2}}-f \tag{21}$$

and

$$\chi=\phi_a^{-\frac{1}{2}}\frac{d\phi_a}{d\eta_a}\xi a. \tag{22}$$

χ is a slowly varying function of η_a:

$$\chi\to\tfrac{2}{3} \quad \text{as} \quad \eta_a\to\infty. \tag{23}$$

When

$$\eta_k\to\infty, f\to\xi_\infty/2 \quad \text{and} \quad g\to-\xi_\infty/2. \tag{24}$$

When

$$\eta_k\to 0, \quad \phi_k\to 0. \tag{25}$$

Thus the dominant term in the square bracket in Eq. (19) is $(2-\chi)\xi_a/4$ for large η_a and η_k. When η_k is sufficiently small, g is the dominant term. For any η_k the value of ξ_a for which the second derivative is zero can be found by equating the square bracket in Eq. (19)

[4] W. R. Ferris, RCA Rev. **X**, 134 (1949).

to zero; i.e., by finding the ξ_a which satisfies the condition

$$\xi_a=[\chi f(1+f/\xi_a)-2\phi_a{}^{-\frac{1}{2}}+g]\frac{4}{2-\chi}. \quad (26)$$

This equation can be solved for ξ_a by the method of successive approximations and is rapidly convergent because the right-hand side is only slowly varying with η_a.

In the case of the ideal diode with infinite saturation emission ($I_s/I_\infty\to\infty$, in Fig. 1),

$$\frac{I_\infty{}^2}{V_T}\frac{d^2V_a}{dI_a{}^2}=-\left(\frac{I_\infty}{I_a}\right)^2 \left[1+\phi_a{}^{\frac{1}{2}}\xi_\infty\frac{(I_a/I_\infty)^{\frac{1}{2}}}{4}+\frac{d\phi_a}{d\eta_a}\xi_\infty{}^2\frac{(I_a/I_\infty)}{8}\right]. \quad (27)$$

In calculating the above results, the values of ϕ_t tabulated by Ferris[4] and the $\xi-\eta$ tables of Kleijnen[5] and Ferris were used. Values of $d\phi_a/d\eta_a$ were calculated using the series[6]

$$\frac{d\phi_a}{d\eta_a}=(\pi\eta_a)^{-\frac{1}{2}}\left(1-\frac{1}{2\eta_a}+\frac{1}{4\eta_a{}^2}-\frac{15}{8\eta_a{}^3}+\cdots\right). \quad (28)$$

ϕ_a was calculated from Eqs. (12) and (28). When values of η_a fell outside the range tabulated by Kleijnen, ξ_a was calculated from the equation[3]

$$\xi_a=\frac{2^{\frac{1}{2}}\pi^{\frac{1}{2}}}{3}\eta_a{}^{\frac{3}{2}}+\frac{\pi^{\frac{1}{2}}}{2^{\frac{1}{2}}}\eta_a{}^{\frac{1}{2}}+\cdots \quad (29)$$

[5] P. H. J. A. Kleijnen, Philips Research Repts. **1**, 81, (1945).
[6] D. O. North, RCA Rev. **V**, 106 (1940).

JOURNAL OF APPLIED PHYSICS VOLUME 26, NUMBER 11 NOVEMBER, 1955

On the Transient Behavior of Semiconductor Rectifiers*

B. R. Gossick
Purdue University, Lafayette, Indiana
(Received June 20, 1955)

If the forward current through a p–n junction suddenly ceases, an emf appears due to nonequilibrium carrier concentrations at the junction barrier. Measurements of the barrier emf have been made with a wide range of injection currents and yield current *vs* barrier voltage characteristic curves. The open circuit case of voltage decay across a p–n junction in the range $V\gg kT/q$ is discussed. The voltage decay is observed to be linear with time with a slope $kT/q\tau$. It follows from an analysis based on a simple model that the excess minority carrier concentrations decrease exponentially with the time constant τ. The floating emitter and collector voltages, $V_E(t)$ and $V_C(t)$, of p–n–p transistors are observed to decay like the open circuit voltage across a p–n junction, and it is noted that $V_E(t)\approx V_C(t)$ in the range $V\gg kT/q$. The transient response of a semiconductor rectifier connected in parallel with a large external capacitance is analyzed. The response calculated for large negative excursions of voltage gives a simple relation by which the saturation current may be determined. Measurements are presented and discussed.

I. POST-INJECTION BARRIER EMF OF p-n JUNCTIONS

Introduction

THE current-voltage characteristic curve of any nonlinear circuit element is essential for understanding its behavior. A pulse method of obtaining the characteristic curve of a p–n junction barrier is described herein. As this characteristic curve does not follow directly from dc measurements made across the exterior terminals, the pulse measurements are of interest.

A method of observing the equilibrium barrier height directly with an oscilloscope is treated. This technique is of practical interest, because a rapid measurement of the equilibrium barrier height can be conveniently used in production for quality control testing.

* This investigation was supported by the U. S. Signal Corps, and the paper consists of excerpts from a Ph.D. thesis submitted to the faculty of Purdue University, May 30, 1954, and issued as a Signal Corps Report.

Description of the p-n Junction

For the purpose of clarifying the remarks to be made later, the theory of p–n junctions is summarized as follows: The p–n junction consists of a semiconductor with a boundary (the barrier) separating two regions one which is p-type, from the other, which is n-type. [Fig. 1(a)]. The holes are the "majority" carriers on the p-side and "minority" carriers on the n-side, and therefore the concentration of holes on the p-side is much greater than on the n-side [Fig. 1(b)]. A similar argument applies to the electron concentrations on the two sides of the barrier, so that the electron concentration may be schematically depicted as shown in Fig. 1(c). When there is no current flow, the equilibrium potential difference across the barrier [Fig. 1(d)] maintains the carrier concentration gradients shown in Fig. 1(b) and Fig. 1(c). Injection of current in the direction of easy flow requires the potential of the p-side

to increase relative to the n-side as shown in Fig. 2 where the barrier height has been reduced from the equilibrium value φ by the amount V. Hereafter, the term *applied barrier voltage* always refers to V as signified by Fig. 2.

When the forward current through a p–n junction is interrupted, a transient voltage is observed across the terminals. It is this voltage which we call the post-injection barrier emf.[1] Following a description of the experimental procedure used to measure this voltage, and a presentation of the observations made with the equipment, the physical significance of this transient voltage will be discussed.

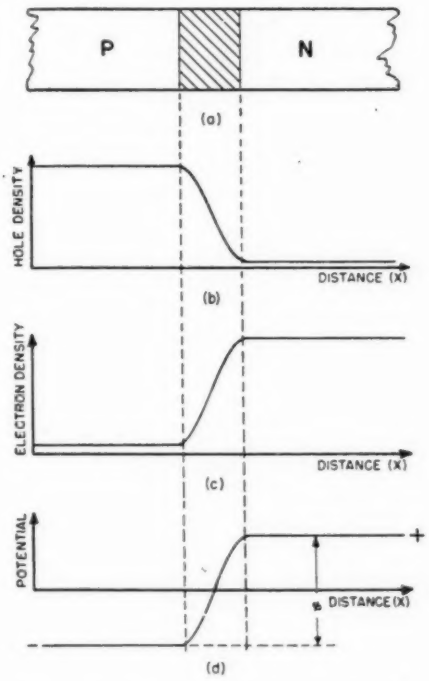

FIG. 1. Schematic diagrams related to a p–n junction. (a) Schematic sketch of p–n barrier. (b) Equilibrium hole density *vs* distance. (c) Equilibrium electron density *vs* distance. (d) Equilibrium electric potential *vs* distance.

Details of the Experiments

The circuits used to measure the post-injection voltage are shown in Fig. 3. The pulser used to inject current is shown in the upper drawing [Fig. 3(a)], and the test circuit is shown in the lower drawing [Fig. 3(b)].† Resistors of different values were substituted for the one labeled 13 000 ohms in Fig. 3(b), in order to study the effect of series resistance on the post-injection voltage. Measurements were also made with the series resistor replaced by a high back voltage (hbv) germanium point contact diode. The back resistance of such a point contact diode may be as low as 100 ohms for around 0.02 microsecond after drawing forward current, a time which is quite short compared with the post-injection transient of the p–n junction. Thus, the point contact diode provides a low resistance during injection and a very high resistance for approximately the remainder of the time.

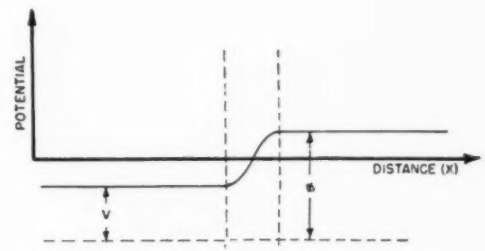

FIG. 2. Nonequilibrium electric potential *vs* distance.

The post-injection voltage of hbv germanium point contact diodes was also observed. The circuit was as shown in Fig. 3(b) except that the p–n junction was replaced by the point contact diode and different values of series resistance replaced the resistor marked 13 000 ohms.

All measurements discussed here were made with germanium rectifiers at room temperature.

A typical series of oscilloscope traces of the voltage across the sample ($V \gg kT/q$) against time,‡ observed with different series resistors, is shown in Fig. 4. It is to be noted that the voltage drops almost instantaneously to V_2 at the end of the applied current pulse, after which the voltage decays slowly to zero. We are interested in the significance of the magnitude of V_2, and in the decay rate of the post-injection voltage. With a given voltage V applied across the barrier, a voltage V_2 appears across the external terminals, according to the relation

$$V_2 = R_x V/(R_x + R_g), \tag{1.1}$$

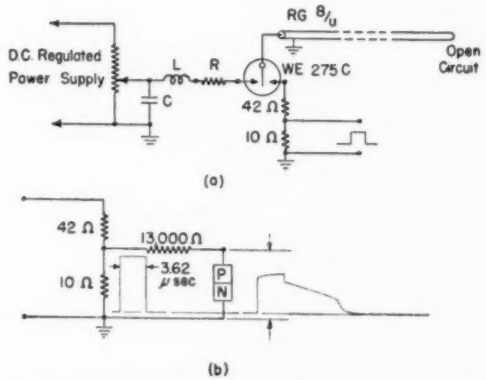

FIG. 3. Test circuits. (a) Pulser circuit. (b) Test circuit for measuring transient behavior of rectifiers.

[1] B. R. Gossick, Phys. Rev. **91**, 1012–1013 (1953).

† The pulser [Fig. 2(a)] was used to calibrate oscilloscope (Tektronix 517) deflection in terms of voltage and time. The pulse height was calibrated by comparing the voltage to which the cable charged with a standard cell. The pulse width was determined by resonating the cable with a rf signal generator. Full scale deflection was 15 mm, and the trace width was less than ½ mm.

‡ Symbols k, T, and q denote, respectively, Boltzmann's constant, temperature in °K, and the electronic charge.

FIG. 4. Terminal voltage across a p–n junction against time. The curves are drawn from a multiple-exposure photograph of oscilloscope patterns taken with the p–n junction rectifier connected in series with a Raytheon CK 708 point contact diode (curve with maximum decay time), and resistors with the following values: 3300Ω, 1500Ω, 560Ω, and 180Ω (the decay time decreasing with decreasing series resistance). V_1 represents the voltage drop across the germanium in series with the junction, and V_2 denotes the applied barrier voltage.

where R_x is the external series resistance and R_g is the resistance of the germanium in series with the junction. This relation was verified in the experiments. As the condition $R_x \gg R_g$ was satisfied in all measurements recorded in Fig. 4, the voltage V_2 was the same as V in each case. However, the duration of the post-injection voltage was different and increased with increasing series resistance. The longest pulse with approximately linear decay, was observed with a hbv point contact germanium diode connected in series with the p–n junction.

Fig. 5 shows the post-injection voltage with different amounts of injected current, observed with a hbv point contact germanium diode connected in series with the p–n junction. The upper curves (a) show voltage against time with the small amplitude current pulses. The voltage V_1 (refer to Fig. 4) is very small in the curve with the smallest amplitude, and with increasing amplitude both V_1 and V_2 (refer to Fig. 4) increase. The lower curves (b) show voltage against time with large amplitude current pulses. Here voltage V_1 increases appreciably with increasing amplitude, but V_2 slowly approaches a saturation value.

Characteristic curves of forward current *vs* voltage, measured with p–n junctions, are shown in Figs. 6 and 7. In each case curve A refers to the voltage V_1+V_2 (Fig. 4) observed at the end of a 3.62 microsecond pulse, and curve B refers to the voltage V_2 observed immediately after the pulse. The relation $R_x \gg R_g$, referred to in the foregoing, was satisfied throughout the measurements recorded in Figs. 6 and 7. The current plotted in both A and B is the current measured just before the end of the injection pulse. Similar characteristic curves were measured with hbv germanium point contact diodes, an example being shown in Fig. 8. Curve A refers to voltage V_1+V_2 observed at 0.007 microsecond after the beginning of a current injection pulse of 0.347 microsecond duration. Curve B refers to voltage V_1+V_2 just prior to the end of the pulse, and curve C refers to the voltage V_2 immediately after the pulse.

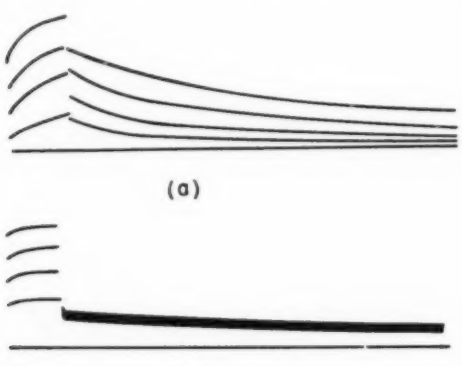

FIG. 5. Terminal voltage across a p–n junction against time with varying amounts of current injection. The p–n junction rectifier was connected in series with a Raytheon CK 708 point contact diode. An injection pulse of 3.62 μsec duration was used. (a) Curves obtained with small current pulses. (b) Curves showing the saturation of the post-injection emf obtained with large current pulses.

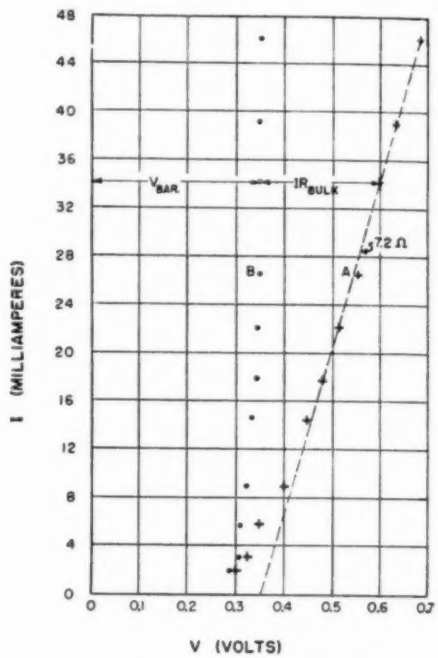

FIG. 6. Current-voltage curve for germanium p–n junction (sample 394). Curve A refers to terminal voltage observed during a 3.62 μsec pulse. Curve B refers to terminal voltage observed immediately after the pulse. The barrier voltage calculated from A coincides with B, $T=300°K$.

Conclusions

(A) The first conclusion to be drawn is that with $R_x \gg R_g$, the post-injection voltage can be only the applied barrier voltage, because the only voltages in the circuit are the IR drops across R_x and R_g, and the applied barrier voltage.

(B) In connection with Fig. 5 it was noted that V_2 saturates with large values of final injection current. As the potential difference V (Fig. 2) cannot exceed a saturation value equal to the equilibrium barrier height φ, because the barrier is entirely removed when $V=\varphi$, we conclude that the observed saturation value of V_2 equals φ.

(C) It was also mentioned in the discussion of Fig. 5 that the voltage, shown as V_1 in Fig. 4, increases with increasing injected current. Prior to the end of the

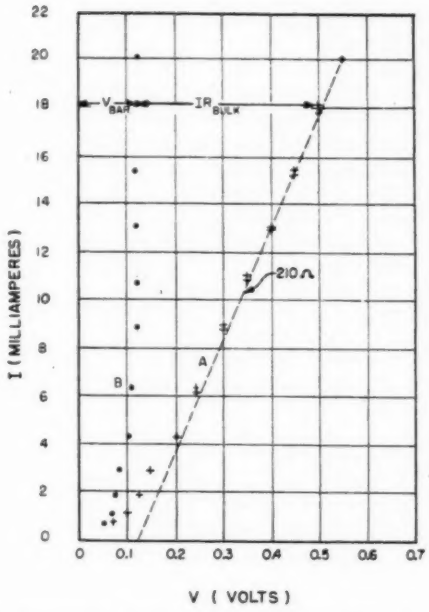

FIG. 7. Current-voltage curve for germanium p–n junction (sample 2). Curve A refers to terminal voltage observed during a 3.62 μsec pulse. Curve B refers to terminal voltage observed immediately after the pulse. The barrier voltage calculated from A coincides with B, $T=300°K$.

current pulse, the terminal voltage is the sum of the IR drop across R_g and the voltage across the barrier, and the terminal voltage is also the sum V_1+V_2. After the current pulse vanishes, the IR drop across R_g must therefore vanish, leaving only the voltage applied across the barrier V_2. It follows then that V_1 is the voltage drop across R_g.

(D) The applied barrier voltage depends on the excess minority carrier concentrations which, with a closed circuit, can decay by flow across the barrier (as well as by recombination). Therefore, we conclude that the duration of the post-injection applied voltage is decreased by decreasing the external series resistance because this increases the flow.

(E) It may be seen (Figs. 6 and 7) that the points of curve A (measured just before the end of the injection pulse) approach a linear region asymptotically with large values of applied voltage. With large forward current, the barrier is virtually removed, and the current is limited almost completely by the resistance R_g. Therefore, from the linearity of large forward current with voltage, we conclude that the resistance R_g remained constant at its equilibrium value with both samples during measurements.§

(F) Since R_g remains constant during the measurement, it follows that the increase of voltage during an injection pulse with time (Figs. 4 and 5) is produced by the barrier admittance.

Although the remaining conclusions to be drawn from Figs. 6 and 7 duplicate some that have already been drawn from Figs. 4 and 5, they are worth including because the experimental evidence is shown here in more detail. For example, after evaluating R_g from the slope of the linear region, the voltage drop across it was calculated and subtracted from the terminal voltage to yield the drop across the barrier. In each case the points, calculated in this manner, coincided with the points of curve B. Thus the voltage V_2, measured immediately after injection, is the voltage which was applied across the barrier just before [see (A) in the foregoing]. Furthermore, the voltage V_1 is therefore the voltage drop across R_g as was concluded before (C) on the basis of Fig. 5. It may be seen that curve B approaches a vertical asymptote with increasing applied voltage. Thus V_2 saturates with large injection currents as noted in Fig. 5. The vertical asymptote of curve B and the asymptote of curve A (the slope of which gave R_g) intersect the voltage axis at the same value. In other words, the saturation value of V_2 and the barrier height φ obtained from curve A are equal, as stated under (B).

One cannot draw definite conclusions[2] from Fig. 8, which refers to a hbv point contact diode. Neither curve A at 0.007 microsecond nor curve B at 3.6 microsecond, after the beginning of the pulse, shows a con-

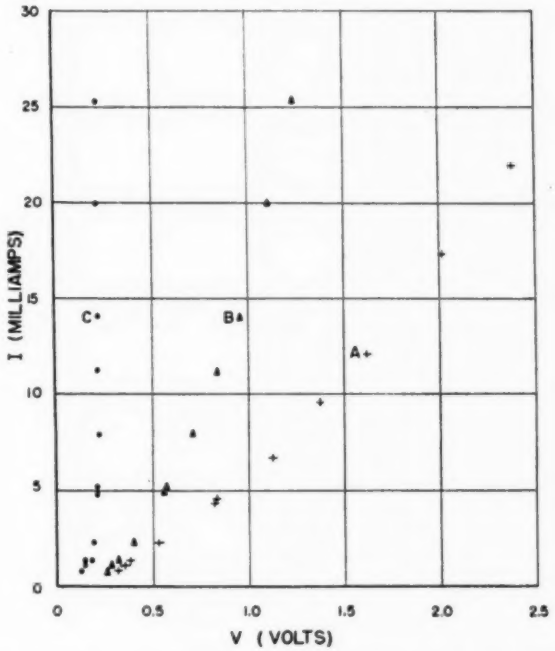

FIG. 8. Current-voltage curve for 1N56A Sylvania diode. Curve A refers to terminal voltage 0.007 μsec after a 0.347 μsec pulse was applied. Curve B refers to terminal voltage at the end of the pulse. Curve C refers to terminal voltage immediately after the pulse. $T=300°K$.

§ Given sufficient time for penetration of minority carriers into the bulk of the semiconducting material outside the junction, the value of R_g decreases with increasing forward current. In other words, with dc or sufficiently slow pulses, R_g is not constant but a function of current. Thus, the characteristic curve of the junction itself cannot be readily determined from dc measurements made across the exterior terminals, making the success of the pulse technique important.

[2] R. Bray and B. R. Gossick, Phys. Rev. **91**, 1011–1012 (1953).

stant spreading resistance indicating that the spreading resistance is decreasing with injected minority carriers. The observed current increased markedly during injection, and this would indicate that even at 0.007 microsecond the spreading resistance cannot be obtained from the curves (Fig. 8). On the other hand, the terminal voltage observed immediately after injection decayed slowly when the external series resistance was large, as in the case of the p–n junctions. Therefore we conclude that it is the applied barrier voltage (Fig. 8, curve C), relying on the argument already given under (A).

II. OPEN CIRCUIT VOLTAGE ACROSS A p-n JUNCTION FOLLOWING A CURRENT INJECTION

Introduction

The following discussion is concerned with experiments approximating open circuit conditions, for example, those in which a hbv germanium point contact diode is connected in series with the p–n junction. The observations are compared with the behavior predicted from a simple model. It is found that the open circuit behavior depends almost entirely on the recombination of minority carriers and provides a simple measurement of the effective recombination time.

Description of the Experiments

The barrier voltage response to rectangular pulses of forward current was investigated. These experiments were also carried out on the *emitter-base* junction of a p–n–p transistor with the collector left floating and the base grounded. Following a current pulse, in the forward direction through the emitter base junction, both emitter and collector voltages were measured as functions of time by means of a high impedance probe (cathode follower) connected to an oscilloscope.

All measurements were made at room temperature.

The pertinent observation is the linear decrease of the voltage across a p–n junction with time following a current pulse of 3.62-microseconds duration.‖ The linear decay occurs when the initial voltage is large compared with kT/q. Twelve germanium p–n junctions were tested, and the linearity was observed in each case, but the slope differed depending on the sample. Two samples were tested in the low voltage range $V \ll kT/q$, and the voltage was observed to decay exponentially with time.

Tests were made on nine p–n–p junction transistors, and in each case the observed time dependence of the open circuit emitter voltage V_E and collector voltage V_C was essentially the same as with a single p–n junction. Immediately following injection, V_C was slightly less than V_E, both decreasing linearly with time. At a quarter of the maximum value, V_E and V_C were still approximately equal.

‖ See the curve in Fig. 4 measured with a point contact diode in series with the junction.

Simple Model for the Transient Behavior

An explanation of the time dependence of the post-injection voltage will now be given in terms of a simple model suggested by Fan.[3,1]

The following two assumptions will be made:

(a) The semiconductor regions outside the barrier are electrically neutral.

(b) The carrier concentrations at the boundaries of the p–n barrier, and the potential difference across the barrier, always bear the relationship to each other which holds at equilibrium.

(c) The concentration of majority carriers is large compared with the concentration of minority carriers on either side of the barrier.

(d) The recombination lifetime of minority carriers is constant throughout the sample.

Assumptions (a), (b), and (c) have been commonly employed in treating p–n junctions.

As it has been shown elsewhere[4–6] (see Appendix) that the transient behavior can be expressed in terms of average lifetimes, the use of assumption (d) may not severely limit the generality of the treatment.

Following a current injection pulse, the gradient of charge outside the barrier is zero by assumption (a). Therefore, on open circuit, the terminal voltage equals the difference between the barrier potential and its equilibrium value, which is indicated by V in Fig. 2.

It follows from assumptions (b) and (c) that the concentration of holes p_n in the N region just outside the barrier is related to the applied barrier voltage by the equation

$$p_n = p_{no} \exp(qV/kT) \tag{2.1}$$

$$= p_{no} + (\Delta p)_n, \tag{2.2}$$

where p_{no} is the equilibrium concentration. Solving Eq. (2.2) for $(\Delta p)_n$ gives the relation

$$(\Delta p)_n = p_{no}(e^{qV/kT} - 1). \tag{2.3}$$

By assumption (d), the excess minority carrier concentration $(\Delta p)_n$ may be expressed by the exponential decay law.

$$(\Delta p)_n = (\Delta p)_{n\,\max} e^{-t/\tau}. \tag{2.4}$$

By combining Eqs. (2.3) and (2.4) we have

$$\frac{(\Delta p)_{n\,\max} e^{-t/\tau}}{p_{no}} = (e^{qV/kT} - 1). \tag{2.5}$$

We next take the derivative of Eq. (2.5) with respect to time

$$-\frac{1}{\tau}\frac{(\Delta p)_{n\,\max}}{p_{no}} e^{-t/\tau} = \frac{qe^{qV/kT}}{kT}\frac{dV}{dt}. \tag{2.6}$$

Substituting Eq. (2.6) into Eq. (2.5) yields the dif-

[3] H. Y. Fan, Phys. Rev. **75**, 1631 (1949).
[4] B. R. Gossick, Ph.D. thesis, Purdue University, May 30, 1954.
[5] B. R. Gossick, Phys. Rev. **94**, 1427 (1954).
[6] B. R. Gossick, Proc. Natl. Electronics Conf. **11**, (1955).

ferential equation

$$\frac{dV}{dt}=\frac{kT}{q\tau}(e^{-qV/kT}-1). \tag{2.7}$$

As is well known, a nonlinear equation of the type Eq. (2.7) reduces to the following linear equation.

$$\frac{de^{qV/kT}}{dt}+\frac{e^{qV/kT}}{\tau}=\frac{1}{\tau}. \tag{2.8}$$

The solution of Eq. (2.8) with the boundary condition, V equals $V(0)$ at time $t=0$, is given by

$$(e^{qV/kT}-1)=(e^{qV(0)/kT}-1)e^{-t/\tau}. \tag{2.9}$$

Equation (2.9)¶ predicts a voltage monotonically decreasing with time, which in the range $V(t)\gg kT/q$ may be expressed as

$$V=V(0)-kTt/q\tau, \tag{2.10}$$

and in the range $V(t)\ll kT/q$ reduces to

$$V=\frac{kT}{q}(e^{qV(0)/kT}-1)e^{-t/\tau}. \tag{2.11}$$

The relation (2.10) was given earlier[1,4] and was more recently reported by Lederhandler and Giacoletto.[7]

As has been remarked earlier, experiments carried out in the voltage range $V\gg kT/q$, show that $V_E(t)\approx V_C(t)$ with p–n–p transistors. This relation is explained below in terms of the model of the p–n junction which was used to obtain Eq. (2.9). It follows from Eq. (2.1) that the open circuit emitter and collector voltages are given by

$$V_E=\frac{kT}{q}\ln(P_E/P_{EO}), \tag{2.12}$$

and

$$V_C=\frac{kT}{q}\ln(P_C/P_{CO}), \tag{2.13}$$

in which the nonequilibrium hole concentrations at the emitter and collector surfaces of the base are denoted, respectively, by p_E and p_C, and the corresponding equilibrium concentrations by p_{EO} and p_{CO}.

Let β represent the fraction of holes injected by the emitter into the base which arrive at the collector.**,[8] Recognizing that $p_{EO}=p_{CO}$, it follows that the nonequilibrium hole concentrations at the emitter and collector surfaces within the base may be expressed as

$$p_E=p_{EO}+\Delta p_E \tag{2.14}$$

$$p_C=p_{EO}+\beta\Delta p_E. \tag{2.15}$$

Substituting Eqs. (2.14) and (2.15) into the difference between Eqs. (2.12) and (2.13) yields

$$V_C=V_E-\frac{kT}{q}\ln\left\{\frac{1+(\Delta p_E/p_{GO})}{1+(\beta\Delta p_E/p_{GO})}\right\}. \tag{2.16}$$

With a good transistor $\beta\approx 1$, and hence $V_E(t)\approx V_C(t)$.

Comparison of the Model and Experimental Results

Equation (2.9) has been derived from the simple model suggested by Fan. We are interested in the degree to which this relation is fulfilled by experiments. The conditions under which Eqs. (2.10) and (2.11) apply are widely separated. For example, in the measurements which are described later, the amplitude of the current pulse varied by over 10^4 to one. Therefore, a comparison of the values of τ, obtained with the two measurements, tests the validity of Eq. (2.9) over widely separated conditions.

As was remarked earlier, twelve junctions were tested, and each exhibited a linear decay of voltage with time in the range $V(t)\gg kT/q$. Thus, the linearity of Eq. (2.10) agrees with observations. With ten of the junctions, the low voltage behavior was not examined in detail, but it was observed to resemble Eq. (2.9). Four junctions were tested in both the high- and low-voltage ranges, and the results are tabulated in Table I. In view of the simplicity of the model used to obtain Eq. (2.9), there is justification for regarding the discrepancies as reasonably small. We conclude that Eq. (2.9) gives an approximation of the open circuit response of a p–n junction to an input current pulse. Our conclusion is supported by the recent report[7] of RCA workers who have checked lifetime measurements of this kind with independent measurements utilizing the decay of photoconductivity.

We have discussed elsewhere[4] how a deep penetration of minority carriers into the bulk material beyond the barrier (long input current pulse) will make the mean lifetime $\bar{\tau}$ dominate the output voltage, even if the barrier RC time constant is much greater than $\bar{\tau}$. As Fan's model is based entirely on injection of minority carriers, it becomes somewhat obvious that it holds only with current pulses in the forward direction (see Sec.

TABLE I.[a]

Sample	τ (μsec) $V\gg kT/q$ data analyzed by Eq. (2.10)	τ (μsec) $V\ll kT/q$ data analyzed by Eq. (2.11)
PN–394	2.9—3.0	2.5—2.7
PN–1	18—19	14—15
PN–M1	2.6	2.5
PN–M3	3.6	3.6

[a] Measurements of τ made on four germanium p–n junctions.

¶ We are interested here especially in the case where $V\gg kT/q$, and only in the case where $V>0$. Otherwise the barrier capacitance, which is ignored here, plays an important role as discussed in Sec. III.

[7] S. R. Lederhandler and L. J. Giacoletto, Proc. Inst. Radio Engrs. **43**, 477–483 (1955).

** The quantity β as defined here is a standard quantity used in evaluating the performance of transistors. The definition of β here corresponds to the definition given by Shockley, Sparks, and Teal.[8]

[8] Shockley, Sparks, and Teal, Phys. Rev. **83**, 151–162 (1951).

III), and with current pulse duration which is not negligible compared with $\bar{\tau}$, or with τ which must be of the same order as $\bar{\tau}$.

The applicability of Fan's model was demonstrated by showing that it predicts the observed behavior of the p–n–p transistor with floating emitter and collector potentials. We conclude from the behavior of both the p–n junction and the p–n–p transistor, that Fan's model is approximately correct. Let us then inquire as to the justification for treating the junction in terms of a single lifetime.

Time Decay of the Post-Injection Barrier emf

It follows from assumption (b) and Eq. (2.1) that the applied barrier voltage must simultaneously equal $kT/q \ln n_p/n_{po}$ and $kT/q \ln p_n/p_{no}$. Consequently, n_p and p_n cannot return to their equilibrium values independently by the relations

$$(\Delta p)_n = (\Delta p)_{n\ \max} e^{-t/\tau_p} \tag{2.17}$$

$$(\Delta n)_p = (\Delta n)_{p\ \max} e^{-t/\tau_n} \tag{2.18}$$

with $\tau_p \neq \tau_n$. Instead, it is essential that the concentrations n_p and p_n be coupled so as to make the ratios p_n/p_{no} and n_p/n_{po} equal. Without at first attempting to describe the mechanism by which it is brought about, let us see if the existence of such a coupling can account for the behavior observed with the p–n–p junction transistors.

Suppose there is a coupling between the hole concentration p_E and the electron concentration n_E at the emitter-base junction. As the base is thin compared with the diffusion length of holes, the concentration p_E is practically equal to the concentration p_C. At the same time p_C must be coupled to the electron concentration n_C in the collector next to the collector-base junction. Therefore, concentrations n_E and n_C are coupled, or in other words, both barriers are coupled. The same conclusion follows directly from the experimental observation that $V_E(t) \approx V_C(t)$ with the emitter and collector floating. Thus the existence of a coupling between the minority concentrations on opposite sides of a barrier leads to the behavior which is observed with p–n–p junction transistors.

In what way can the concentrations n_p and p_n on opposing sides of a p–n junction be coupled? This can occur in only one way, by hole and electron current flow across the barrier such as to make the combined decay rate due to flow and recombination correspond to Eq. (2.4). The tendency of the junction to behave according to either a single lifetime τ, or average values of the lifetime[4–6] requires such a flow of carriers coupling n_p to p_n. Thus, the fact that the saturation currents serve as the weighting factors for averaging the lifetime is physically plausible.††

†† The argument that the single lifetime arises because of the dominance of one type of carrier is not inconsistent with our picture, because in this case the mean lifetime is taken over by the dominant carrier (Appendix).

To summarize, it was observed with p–n junctions that the open circuit voltage (in the range $V \gg kT/q$) decays linearly with time, following a current pulse. In the low-voltage range ($V \ll kT/q$), the voltage was observed to decay exponentially with time. It was also observed with p–n–p junction transistors that the floating emitter and collector voltages (in the range V_E, $V_C \gg kT/q$) decay linearly with time, following a pulse of emitter current; and at the same time V_E was observed to be approximately equal to V_C. These results were compared with the calculated behavior based on a model suggested by Fan, and the calculations were found to approximately agree with the observations.

III. TRANSIENT BEHAVIOR OF A SEMICONDUCTOR RECTIFIER CONNECTED TO A CAPACITANCE

Analysis of Behavior by a Circuit Model

The transient response of a rectifying barrier in parallel with a capacitance will be analyzed. Such an analysis at the same time accounts for the behavior of a rectifying barrier in series with a capacitance, by a well-known circuit transformation. In this analysis,‡‡ the conduction current is considered to be given at all times by the well-known Wagner[9] equation

$$I(t) = I_s(e^{\alpha V(t)} - 1), \tag{3.1}$$

where α varies only with temperature and should equal q/kT according to theory.

The displacement current is assumed to have the following form

$$I(t) = C dV(t)/dt, \tag{3.2}$$

where the capacitance C across the barrier is assumed to be constant.

We are interested only in the case where C is determined by a large external capacitance C which is very large compared with the barrier capacitance C_b. An upper limit on $V(t)$ is also imposed to make the barrier resistance dV/dI large compared with the resistance in series with the barrier which is neglected. Furthermore, the product $C(dV)/(dI)$ must be large compared with τ (Sec. II), as the transient conduction current term which depends on recombination lifetimes is neglected.

Consider the current as the input function $I(t)$, and the voltage across the barrier and capacitance in parallel as the output function $V(t)$. One always has

$$I(t) = C\frac{dV}{dt} + I_s(e^{\alpha V} - 1). \tag{3.3}$$

It is well known that Eq. (3.3) may be rearranged to

‡‡ The argument is given here in terms of a p–n junction, but it should apply to any rectifying barrier that obeys Eq. (3.1).

[9] C. Wagner, Physik. Z. 32, 641 (1931).

give the following linear equation in $e^{-\alpha V}$.

$$\frac{de^{-\alpha V}}{dt}+\frac{\alpha}{C}(I(t)+I_s)e^{-\alpha V}=\frac{\alpha I_s}{C}. \tag{3.4}$$

Consider the weighting function[10] of this nonlinear circuit, i.e., the output voltage for a delta-function input current. We have as the solution of Eq. (3.4)

$$(e^{-\alpha V}-1)=(e^{-\alpha V(0)}-1)e^{-\alpha I_s t/C}, \tag{3.5}$$

where the delta function consists of a charge $Q=CV(0)$ injected at time $t=0$.

Equation (3.5) might be appropriately called a sweep circuit function. With negative pulses of large amplitude ($|V(0)|\gg\alpha^{-1}$) one gets an almost ideal approximation of the sawtooth function.

$$\begin{aligned} V(t)&=V(0)-(I_s t/C), \quad 0<t<CV(0)/I_s \\ &=0, \quad t<0, \\ &\quad t\geq CV(0)/I_s. \end{aligned} \tag{3.6}$$

However, if the voltage scale is greatly magnified, and one examines (3.5) in the range $|V(0)|\ll\alpha^{-1}$, then one finds that the voltage follows the exponential decay law

$$V(t)=\left[\frac{1-e^{-\alpha V(0)}}{\alpha}\right]e^{-\alpha I_s t/C}. \tag{3.7}$$

A comparison between Eq. (3.5) and (2.9) provides additional support for Fan's model (Sec. II). Equation (3.5) can be converted to an equation of the form of Eq. (2.9) by substituting $-V(t)$ for $V(t)$ in Eq. (3.5). As the behavior of Eq. (3.5) is quite different for negative and positive values of $V(t)$, it is quite clear that the linear behavior observed with large positive values of $V(t)$, (Sec. II) could not be ascribed to a discharge of the barrier capacitance.

Discussion of Experiments

The measurements of the transient voltage across a germanium rectifier and capacitance connected in parallel will be described. The saturation current was determined from these measurements using the relation (3.6). The circuit arrangement is shown in Fig. 9. The capacitor is charged by the diode with current in the direction of easy flow, but the capacitor discharges through the diode in the back direction. After the charging pulse, the resistance in series with the rectifier is negligible compared to its back resistance, and therefore the voltage observed with the high impedance cathode follower probe is the voltage across the capacitance and rectifier connected in parallel. Voltage was measured against time with a Tektronix type 511 cathode-ray oscilloscope, using voltage and time calibrations of the oscilloscope. The value of the capacitance C (Fig. 9) was measured with a B.E.C.O. impedance bridge Model 250–C.

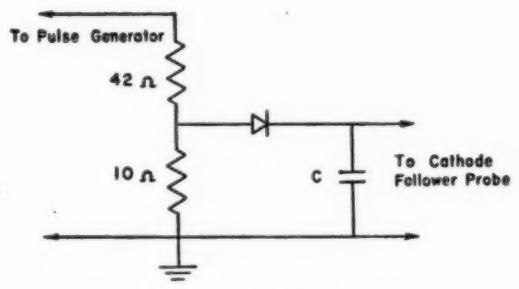

FIG. 9. Test circuit.

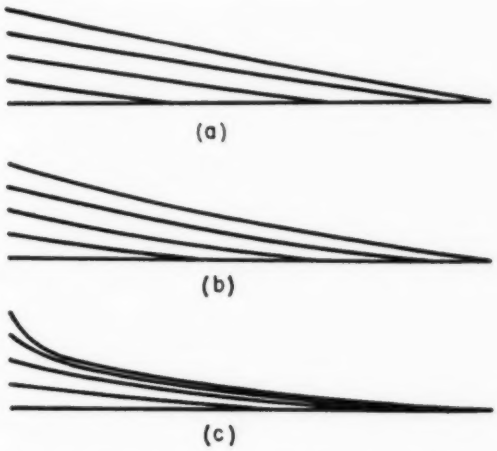

FIG. 10. Oscilloscope patterns of voltage against time measured across a capacitor (241 $\mu\mu$f) and 1N34A diode in parallel. (a) $V(0)=1,2,3$, and 4 volts. Sweep time=300 μsec. (b) $V(0)=2,4,6$, and 8 volts. Sweep time=450 μsec. (c) $V(0)=4,8,12$, and 16 volts. Sweep time=600 μsec.

Tracings of oscilloscope patterns of voltage measured against time are shown in Fig. 10. The test sample was a Sylvania type 1N34A germanium hbv point contact diode. It may be seen that measurements carried out with initial voltage $V(0)$ less than 8 volts give a family of curves which are approximately parallel straight lines. With $V(0)$ equal to -8 volts the slope at first shows a small curvature and later becomes constant. This curvature which appears as capacitor C commences to discharge is seen to increase as $V(0)$ is increased. Therefore, we conclude that with these samples, the reverse current commences to markedly depart from the saturation value at around -8 volts.

Measurements of this kind were made with four germanium hbv point contact diodes. The following measured quantities: initial voltage $V(0)$, pulse length $CV(0)/I_s$ by Eq. (3.6), capacitance C, and the calculated saturation current I_s are listed in Table II. It may be seen that the variation of saturation current is small with fairly wide variations of initial voltage and external capacitance. For example, with sample 10,

[10] H. M. James and P. R. Weiss, *Theory of Servomechanisms*, edited by James, Nichols, and Phillips, (McGraw-Hill Book Company, Inc., 1947), Chap. 2.

TABLE II.[a]

Initial voltage $V(0)$ volts	Pulse-length $CV(0)/I_s$ μsec	Capacitance C μμf	Saturation current I_s μamp	Sample Sylvania
−0.71	63	241	2.7	1N56A–180
−1.4	120	241	2.9	1N56A–180
−1.3	460	1000	2.9	1N56A–180
−1.9	690	1000	2.8	1N56A–180
−0.71	92	241	1.9	1N56A–22
−1.4	190	241	1.8	1N56A–22
−2.6	310	241	2.1	1N56A–22
−1.3	640	1000	2.1	1N56A–22
−1.9	980	1000	2.0	1N56A–22
−2.7	1400	1000	1.9	1N56A–22
−1.2	5.5	8.4	1.9	1N56A–22
−1.8	8.4	8.4	1.8	1N56A–22
−2.5	9.6	8.4	2.2	1N56A–22
−0.71	60	241	2.9	1N34A–10
−1.4	117	241	2.9	1N34A–10
−1.3	480	1000	2.7	1N34A–10
−1.9	700	1000	2.7	1N34A–10
−2.7	890	1000	3.0	1N34A–10
−1.2	3.7	8.4	2.7	1N34A–10
−1.8	5.2	8.4	2.8	1N34A–10
−2.4	6.4	8.4	3.1	1N34A–10
−0.72	100	241	1.7	1N34A–330
−1.4	180	241	1.8	1N34A–330
−2.6	310	241	2.0	1N34A–330
−1.3	750	1000	1.7	1N34A–330
−1.9	1100	1000	1.8	1N34A–330
−2.6	1300	1000	2.0	1N34A–330
−1.4	6.8	8.4	1.7	1N34A–330
−1.9	9.3	8.4	1.7	1N34A–330

[a] Tabulation of initial voltage $V(0)$, pulse length $CV(0)/I_s$ [see Eq. (3.6)], capacitance C, and the calculated saturation current I_s. The types of Sylvania commercial diodes used in the measurements are listed.

the voltage varied by 3.7 to 1, the capacitance by 120 to 1, while the saturation current varied by only 1.13 to 1.

It is well known that the dc reverse characteristics of germanium hbv point contact diodes often display no evidence of a saturation current. This is the case with the dc characteristic curves of two typical samples shown in Fig. 11. Both samples were used to obtain data listed in Table II, and one sample (1N34A–330) was used to obtain the curves shown in Fig. 10. Yearian[11] made a detailed comparison of the dc characteristics of

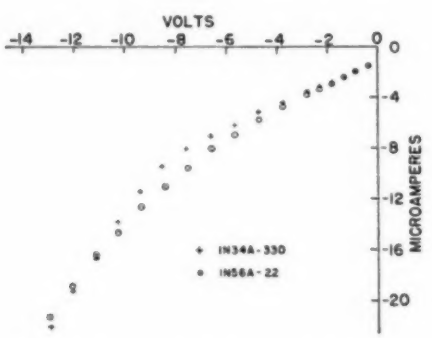

FIG. 11. Reverse I–V characteristics of two hbv point contact Ge diodes.

[11] H. J. Yearian, J. Appl. Phys. **21**, 214–221 (1950).

silicon and germanium low-voltage point contact rectifiers, and observed that the reverse current did not saturate. Benzer[12] also found this to be the case with germanium hbv point contact diodes. More recently Simpson and Armstrong[13] measured the reverse characteristic of germanium hbv point contact diodes, using pulses of 2 to 10 microseconds duration with a slow repetition rate to minimize contact heating. They observed that with some diodes the reverse current saturated over a range of reverse voltage down to about −10 volts, while a linear term was superimposed on the saturation current in the range $-50 < V < -10$ volts. With other samples which rectified about as well, the range of the linear contribution was either shorter or missing entirely. The conclusion is that with the point-contact rectifiers, Eq. (3.6) holds only for pulses which (a) are short compared to the thermal response time, and (b) have a voltage amplitude always more positive than a lower limit at which the reverse current commences to exceed the saturated value. Our results merely confirm the observations of Simpson and Armstrong.[13] However, our method of measuring the saturation current is different.

Measurements of reverse voltage against time were also made with p–n junctions using the circuit shown in Fig. 9. The observed behavior did not follow Eq. (3.6) in quite the ideal manner of the point contact diodes. Within the duration of the post-injection emf (during the time that there is a large excess concentration of minority carriers in the bulk material on either side of the barrier) the external capacitance discharges rapidly until the minority carriers are swept back across the barrier. Then the voltage decays slowly in the manner indicated by Eq. (3.6). The transition between the two modes of decay is abrupt and quite easily observed. However, in order to make the second mode of decay large and convenient to measure, it is necessary to select a large external capacitance which will still retain a substantial amount of original charge once the voltage commences to obey Eq. (3.6). The need for a sufficiently large external capacitance to minimize the post-injection effect was stated earlier in a more formal manner following the discussion of Eq. (3.2).

The post-injection effect exists with germanium hbv point contact rectifiers, but its duration is quite small compared with that of the p–n junction. With the input capacitance of the cathode follower probe (8.4 μμf) alone supplying the external capacitance, the initial voltage was observed to drop about 10% before the slow linear decay began.

Relation (3.7) permits measuring α by transients. As the transient measurements of the saturation current give considerably better agreement with theory than dc measurements, it is interesting to see whether or not a similar situation exists between the transient and dc

[12] S. Benzer, J. Appl. Phys. **20**, 804–815 (1949).

[13] J. H. Simpson and H. L. Armstrong, J. Appl. Phys. **24**, 25–34 (1953).

TABLE III.

Samples	α(volt^{-1}) Pulse	dc
1N34A–180	25	24
1N56A–22	25	26
PN–394	33	33
PN–M3	40	39

measurements of α. This is of particular interest with point contact diodes, because of the well-known discrepancy between the theoretical value of α and the values obtained from dc measurements. The conclusion based on the comparison of dc and pulse measurements of α is that when the dc behavior of the diode can be described by Eq. (3.1) (which by no means is always the case), then both pulse and dc determinations of α lead to approximately the same result. Values of α obtained by both dc and pulse measurements are listed in Table III.

ACKNOWLEDGMENTS

The author wishes to express his appreciation to K. Lark-Horovitz for suggesting this work and for helpful suggestions, and to H. Y. Fan, R. Bray, H. M. James, and V. A. Johnson for their counsel.

APPENDIX

The following summarizes the argument that the behavior of a p–n junction does not depend explicitly on the individual lifetimes τ_n and τ_p, but rather on average lifetimes of the form

$$\langle \tau^r \rangle_{Av} = \frac{I_{ps}\tau_p{}^r + I_{ns}\tau_n{}^r}{I_{ps}+I_{ns}} \tag{A.1}$$

where I_{ps} and I_{ns} are the saturation currents for holes and electrons, respectively.

In treating the small amplitude response of p–n junctions, the author found[4–6] that the dependence of the solutions on τ_n and τ_p could be eliminated by substitutions of the form (A.1) with r taking on values $\frac{1}{2}$, 1, and 2. Obviously, the next step was to see whether or not the further generalization

$$\langle W(\tau) \rangle_{Av} = \frac{I_{ps}W(\tau_p)+I_{ns}W(\tau_n)}{I_{ps}+I_{ns}} \tag{A.2}$$

plays a role in p–n junction behavior. Equation (A.2) was tested and found to apply to the two most general results at hand, the first by Shockley,[14] and the second by Lehman[15]:

The small amplitude ac admittance of a junction[14] may be written in terms of (A.2) as follows

$$Y(j\omega) = G_b\langle (1+j\omega\tau)^{\frac{1}{2}} \rangle_{Av} + j\omega C_b \tag{A.3}$$

in which the conductance G_b is the slope of the dc characteristic curve, C_b is the capacitance of the barrier, ω is the circular frequency of ac, and $j=(-1)^{\frac{1}{2}}$.

Lehman has treated the transient response of the p–n junction, in which $V(t)$ is restricted to the range over which Eq. (3.1) is valid. His result may be written as follows:

$$I(t) = I_s(e^{qV(t)/kT}-1) + I_s\langle F(\tau) \rangle_{Av} + \frac{d}{dt}C_bV(t), \tag{A.4}$$

in which

$$F(\tau_n) = \int_0^t dt_1 \left(\frac{d}{dt_1} e^{qV(t_1)/kT} \right) \times \left[\left(\frac{\tau_n}{\pi(t-t_1)} \right)^{\frac{1}{2}} e^{-(t-t_1)/\tau_n} - \operatorname{erfc}\left(\frac{t-t_1}{\tau_n} \right)^{\frac{1}{2}} \right] \tag{A.5}$$

and $F(\tau_p)$ is the same as (A.5) except that τ_p replaces τ_n. The first term on the right of (A.4) is the steady-state solution, the second term is the transient conduction current, and the third term is the displacement current.

[14] W. Shockley, Bell System Tech. J. **28**, 435–489 (1949).
[15] G. Lehman, (private communication).

Photoelectric Yields in the Vacuum Ultraviolet

W. C. WALKER,* N. WAINFAN, AND G. L. WEISSLER
Department of Physics, University of Southern California, Los Angeles, California
(Received May 17, 1955)

Absolute photoelectric yields of Ni, Cu, Pt, Au, W, Mo, Ag, and Pd are presented for the spectral region from 1400 to 473 A. Measurements were obtained for commercially pure polycrystalline surfaces which were treated in various ways including heat treatment *in vacuo* and in various gas atmospheres at reduced pressures. Surfaces, heat treated *in vacuo*, gave reproducible yields ranging from 10^{-3} electrons per photon at 1400 A to 10^{-1} electrons per photon at 500 A. Although untreated samples exhibited a maximum in the region studied, this maximum disappeared after heat treatment resulting in most cases in a broad plateau extending from 1000 A to 500 A. At wavelengths longer than 1000 A a decrease in yield was observed. Representative experiments with a Ni cathode, heat treated *in vacuo* then exposed to O_2 at reduced pressures, indicated that the maxima for untreated surfaces were caused by adsorbed gases and metallic oxide formation. The absolute error in the values of the photoyields was estimated to be within ±15%.

I. INTRODUCTION

IT has been established that the production of photoelectrons at the cathode of certain gas discharge tubes by ultraviolet photons generated in the discharge itself is an important mechanism in the maintenance of the discharge.[1–3] An analysis of the role played by this effect in such a discharge shows a dependence primarily on the number and spectral distribution of the ultraviolet photons produced and the number of electrons emitted by the cathode per incident photon, that is, the photoelectric yield of the cathode. The emission properties of many substances are known for visible and near ultraviolet radiation; however, for the vacuum ultraviolet region, that is, for wavelengths shorter than 1800 A only a limited amount of data is available.

The photoyields of degassed Ni, W, and Mg were obtained by Kenty[4] in 1933 for radiation of 1060 A, 740 A, and 584 A. Baker,[5] in 1938, presented results for Cd in the region from 3130 A to 1000 A, and Ni, Pt, and W were investigated in an untreated state by Hinteregger[6] for the region from 2500 to 850 A. Preliminary data for Pt and Ta in the spectral range from 1000–473 A both in the untreated state and after heating in vacuo were reported by Wainfan, Walker, and Weissler.[7] In addition to these results Hinteregger[8] recently obtained the yields of Be for radiation between 1600 A and 600 A.

The aforementioned investigations represent the total amount of direct information available on the photoelectric yields of metals for wavelengths between 1800 and 400 A. It therefore seemed desirable to investigate this field more completely with emphasis on those metals which are most commonly used as electrodes in gas discharges.

II. EXPERIMENTAL EQUIPMENT AND PROCEDURE

In the present investigation the photoelectric yields of commercially pure polycrystalline cathodes of Ni, Cu, Pt, and Au were studied in detail, and in addition, reproducible preliminary data were obtained for W, Mo, Pd, and Ag. Absolute measurements of the yields of a given sample were made with a monochromatic beam of radiation by measuring its intensity and determining the number of photoelectrons per second it released from the photocathode. A normal incidence concave grating vacuum spectrograph, which was altered to serve as a monochromator by fitting a motor driven screw to the grating to rotate it about its own vertical axis, was used to obtain a 10 A band of radiation in the region from 1400 A to 473 A. The light sources used were a 14-kilovolt, pulsed (90 pulses per second), condensed discharge in argon and air, and an 800-volt, 0.4 amp dc glow discharge in hydrogen. It was observed that the pulsed nature of the argon light source produced no serious effects in the measurement of either the photocurrent or the light intensity. This was ascertained by comparing the results for the dc hydrogen source and the pulsed source in the overlapping spectral region between 900 and 1000 A. Light scattered from the diffraction grating was prevented from striking the external electrical leads by the use of copper sheet shielding while the fact that the light intensity and photocurrent were zero between light source emission lines indicated that scattered light reaching the detectors was negligible. Further details of the light sources, radiation measuring equipment and monochromator calibrating technique have been described previously.[7,9]

The metal to be investigated was mounted as the cathode of a photocell which is shown schematically in Fig. 1. Photocathodes in the form of 0.0005 inch to 0.002 inch thick sheets were supported on two copper rods which were electrically insulated from the brass

* Now at the University of California, Santa Barbara College.
[1] L. B. Loeb, *Fundamental Processes of Electrical Discharges in Gases* (John Wiley and Sons, Inc., New York, 1939), pp. 402.
[2] P. F. Little and A. von Engel, Proc. Roy Soc. (London) **A224**, 209 (1954).
[3] L. Colli, Phys. Rev. **95**, 892 (1954).
[4] C. Kenty, Phys. Rev. **44**, 891 (1933).
[5] R. Baker, J. Opt. Soc. Am. **28**, 55 (1938).
[6] H. Hinteregger and K. Watanabe, J. Opt. Soc. Am. **43**, 604 (1952).
[7] Wainfan, Walker, and Weissler, J. Appl. Phys. **24**, 1318 (1953).
[8] H. Hinteregger, Phys. Rev. **96**, 538(L) (1954).
[9] Wainfan, Walker, and Weissler, Phys. Rev. **99**, 542 (1955).

base plate in order that the cathode could be heated by conduction. A flat sheet of Ni with a one centimeter diameter hole through its center was placed about 6 mm in front of the cathode and maintained at a potential of ten volts positive with respect to the cathode to serve as an electron collector. In order to allow gases at known pressures to be admitted to the photocell, it was fitted with a gas inlet and a thermocouple pressure gauge. The photocell was mounted behind the exit slit in a brass chamber. With this geometry, the dark current and photoemission from the copper support rods due to scattered light were found to be negligible. The photocurrent was found to exhibit good saturation properties, becoming essentially constant for collector voltages larger than three volts.

During the experiment emission currents from the photocathode in the range from 10^{-10} to 10^{-13} amp were measured with a Beckman micro-microammeter coupled to a Leeds and Northrup, type G, recorder. By measuring the emission rather than the saturated collection current, such disturbing effects as incomplete saturation and the possibility of picking up stray photoelectrons from the slits were eliminated. Pressures between 10^{-4} and 10^{-5} mm Hg were maintained in the photocell during the measurements.

In order to simulate the various conditions prevailing at the cathode of a discharge tube the photocathodes were treated in several ways. Since it was observed that these treatments had an appreciable effect on the magnitude as well as the spectral distribution of the photoyields, they will be described below.

All the metals named were first studied after only superficial cleaning in which thick layers of dirt and grease were removed by cleaning with organic solvents. The condition of the surface after this treatment and subsequent evacuation of the chamber was designated as the untreated state. Measurements were also made on each photocathode after it had been heated in a vacuum of about 5×10^{-5} mm Hg for a period of time sufficient to insure reproducibility of the photoelectric yields when determined, after cooling, at room temperature. A few of the metals were also tested after exposure to O_2, H_2 and air at various pressures, both at room temperature and after being heated in these gases for varying periods of time. In addition to these treatments, it was possible to obtain the yields of several metals while they were maintained at temperatures between 500°C and 1000°C. A steady electrical current was used to heat the photocathode continuously and with very little fluctuation. For this purpose a six-volt storage battery and a series resistor bank were mounted in an electrically shielded box, insulated from ground by bakelite standoff insulators, and provided with external controls for the heating current. With this system it was possible to keep the leakage resistance to ground high enough and the electrical noise level from the heating unit sufficiently low to carry out the measurements at elevated temperatures. Under these conditions, the thermionic emission

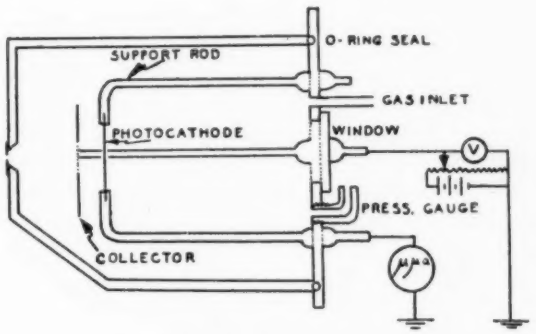

FIG. 1 The experimental photocell.

from the photocathode was at least one-hundred times less than the smallest photocurrent measured. It was also observed in auxiliary experiments that the magnetic field produced by the heating current had no effect on the emission from the cathode.

The procedure followed in obtaining the photoelectric yields of a given metal was to sweep, by means of the grating drive, a portion of the spectrum of interest past the slits of the photocell chamber and the radiation detector so that almost simultaneous measurements of the light intensity and the photoelectric current were obtained. Several such runs were made on each cathode in order to average fluctuations from the light source.

III. RESULTS AND DISCUSSION

For the purpose of this investigation the photoelectric yield $\gamma(\lambda)$ of a given material was defined as the ratio of the number of photoelectrons per second emitted, by the action of light of a given wavelength, to the incident radiation flux in photons per second. A more satisfactory definition from a theoretical point of view would involve the actual number of photons per second absorbed by the cathode. However, the experimental data of Sabine[10] on metallic reflectivities at normal incidence for vacuum ultraviolet radiation show that for wavelengths less than 1200 A the fraction of the light reflected is less than about 10% for all metals tested. Since the experimental error in the present work also amounted to about 10%, it is evident that for the present purpose the two definitions of $\gamma(\lambda)$ are equivalent.

The photoelectric yields were calculated from the data using the relation

$$\gamma(\lambda)=\frac{I(\lambda)\times6.24\times10^{18}}{N_i}\text{ electrons per photon,}$$

where N_i is the incident photon flux and $I(\lambda)$ the total photoelectric emission current in amperes. The accuracy of the values of $\gamma(\lambda)$ obtained was estimated to be within $\pm15\%$. Since, however, most of the error in the absolute value was introduced by the photon flux determination, the relative values of $\gamma(\lambda)$ for a given metal under the

[10] G. Sabine, Phys. Rev. **55**, 1064 (1939).

various conditions studied were felt to be correct to within ±5%.

Nickel

The absolute photoelectric yields of Ni are presented in Fig. 2, where the yield $\gamma(\lambda)$ in percent or electrons per 100 photons is plotted against the wavelength of the incident radiation. Results for an untreated sample are indicated by circles. The solid curve drawn through these points in this instance, as well as in all subsequent cases, represents only the general trend of the data and has no theoretical basis. A comparison of these yields to those given by Hinteregger and Watanabe[6] for untreated Ni shows good agreement in the spectral range common to both investigations. Since the metal surface in the untreated state was covered with layers of organic materials, metallic oxides and adsorbed gases, the yields in this case cannot be considered as characteristic of a

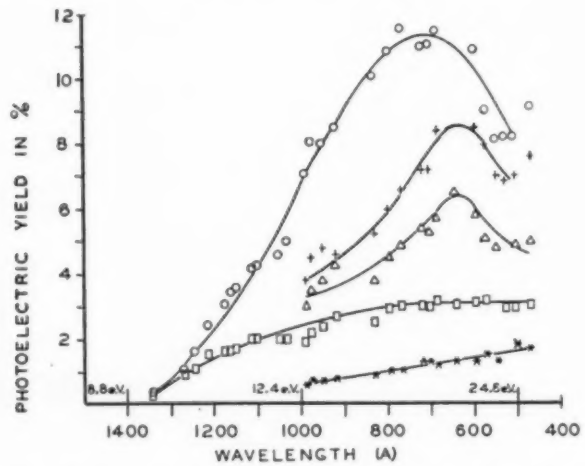

FIG. 2. Photoelectric yield of Ni. ○ Untreated cathode. □ Heat treated cathode in equilibrium with residual gases at about 10^{-5} mm Hg. * Cathode maintained at 900°C in a vacuum of 10^{-5} mm Hg. △ Heat treated cathode at room temperature after exposure to O_2 at 0.1 mm Hg for one-half hour. + Heat treated cathode, heated in 0.05 mm Hg of O_2 at 800°C for one minute.

pure metallic surface. It should be mentioned, however, that the untreated state is likely to correspond to the condition of the electrodes in many discharge tubes.

The photoelectric yields obtained for a cathode which had been heated to a temperature in excess of 1000°C in a vacuum of the order of 5×10^{-5} mm Hg are shown by the squares in Fig. 2. During this measurement, the heating, cooling, and testing cycle was repeated until no further change in the yields occourred. It was found that a single ten minute heating period at a temperature above 1000°C was sufficient to stabilize the emission. Under these conditions the large maximum of the curve for untreated Ni disappeared and the yields decreased to approximately 0.03 electrons per photon in the region from 800 A to 473 A. Since it was found on removing the sample after the heat treatment that some evaporation had occurred, it was assumed that the heating process produced initially a clean surface. As it was not possible, however, to test the cathode until several minutes after heating it, the formation of adsorbed gas films must be considered. At a pressure of about 10^{-5} mm Hg a monomolecular layer of adsorbed gas forms on an initially clean metallic surface in less than one second.[11] Thus in the present case it must be assumed that the yields obtained are characteristic of a gas covered surface; however, the decrease in yield and the disappearance of the maximum indicate that gross surface contaminations were removed by the heating process.

In order to obtain yields from as clean a surface as possible, measurements were made on a Ni sample which was maintained at a temperature of 900°C while being tested; the results are shown by the starred points in Fig. 2. It can be seen that in this case a decrease of about a factor of two occurred in the yields relative to those of a partially degassed cathode at room temperature and that the general shape of the curve was not seriously altered. Although no data were obtained at wavelengths longer than 1000 A because of the small size of the yields, it seems reasonable to expect a drop in yield similar to that obtained for the partially degassed surface. It was observed that for a previously degassed sample no change in yield occurred when measurements were made at temperatures between 500°C and 900°C. This result indicated that the decrease in emission was not primarily a temperature effect but instead was to be associated with a further cleaning of the surface. It seems likely that keeping the previously cleaned photocathode at elevated temperatures retarded the formation of gas and vapor layers hence giving a surface condition as close to that of a clean metallic surface as was possible with the present vacuum conditions. Thus for the spectral region from 473 A to 1000 A the photoelectric yields of a metallic Ni surface were found to be very nearly constant and of the order of 10^{-2} electrons per incident photon.

Photoelectric yields obtained for a Ni cathode which had been cleaned by heating in vacuum and then successively exposed to oxygen at a pressure of 0.1 mm Hg for one-half hour and heated to 700°C in oxygen at 0.05 mm Hg for one minute are shown in Fig. 2 by the triangles and crosses respectively. The observed increase in yield and the appearance of a maximum at 650 A were both assumed to be due to the formation of nickel oxide. This was supported by the observation of a heavy, grey-black oxide surface layer and the fact that the yields could be returned to those characteristic of the metal by heating the oxidized sample in a reducing atmosphere of hydrogen. It should be noted that for the untreated sample a maximum similar to that for the oxide coated one was observed, but that it was shifted

[11] Simple kinetic theory considerations, assuming a sticking coefficient of unity, show that at room temperature and at a pressure of 10^{-5} mm Hg a monomolecular layer forms on a surface in 0.04 second.

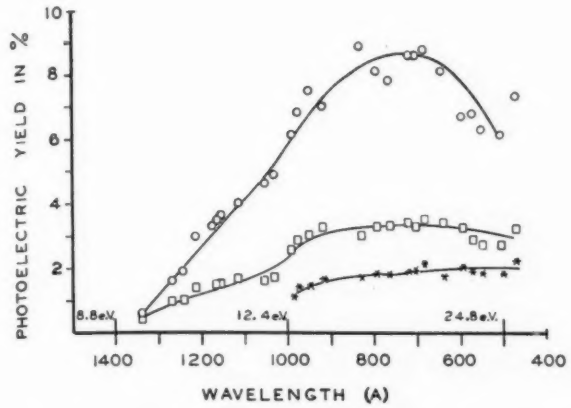

FIG. 3. Photoelectric yield of Cu. ○ Untreated cathode. □ Heat treated cathode in equilibrium with residual gases at about 10^{-5} mm Hg. * Cathode maintained at 500°C in a vacuum of 10^{-5} mm Hg.

slightly to longer wavelengths. Thus while the oxide layer was undoubtedly largely responsible for this maximum some other impurity, possibly organic material, must also be present on the untreated surface. An effect due to oxide formation similar to that observed in this work for Ni has been reported by Apker, Taft, and Dickey for BaO.[12] These investigators found that although the photoyield of BaO was much smaller than that of Ba for wavelengths longer than 2000 A, at wavelengths shorter than this the yields of BaO attained larger values than those of Ba. They concluded that the electrons liberated by photons of energy in excess of 5 ev must originate in the filled band of BaO. It seems likely that at higher photon energies a similar effect occurs for NiO.

Copper

In Fig. 3 the results for an untreated Cu cathode are represented by circles, and the yields for the same surface heated to 700°C in a vacuum of 5×10^{-5} mm Hg are shown by the squares. An interesting observation for this metal was that no change occurred in the yield after the surface had been exposed for eighteen hours following the initial heating to residual gases at a pressure of about 5×10^{-5} mm Hg.

Measurements made on a Cu sample maintained at a temperature of 500°C in vacuum are shown by the stars in Fig. 3. A general decrease in yield by about a factor of two compared to the results at room temperature was observed and attributed to a partial removal of the adsorbed gas layer. In an attempt to determine the effect of the formation of an oxide layer on the yields, the Cu sample was heated in 0.1 mm Hg of O_2 for periods up to one-half hour. Although at the end of the heating process a thick Cu_2O layer was present on the cathode, there was no difference in the yields when compared to the results for an initially clean sample heated in vacuum. In order to interpret this, it was assumed that a very tenacious copper oxide layer was present initially on the surface due to prolonged contact with air and that this layer was not removed by heating in a vacuum to temperatures just below the melting point of the metal. It thus seems clear that the photoyields measured for Cu, even at elevated temperatures, should be considered more characteristic of a cuprous oxide surface on a metallic backing rather than of metallic copper.

[12] Apker, Taft, and Dickey, Phys. Rev. **84**, 508 (1951).

Platinum

The results for a Pt photocathode are shown in Fig. 4. The general shape of the yield curve for the untreated surface agrees with that obtained by Hinteregger and Watanabe.[6] However, variations in the absolute value of the yield amounting to as much as thirty percent occurred and could be ascribed to differences in surface contaminations of the samples.

Photoyields for a Pt cathode partially degassed by heating at 1000°C in a vacuum of the order of 10^{-5} mm Hg are shown by the squares. It should be noted that the general shape of the curve was the same as for the untreated case but that the value of γ for the plateau was reduced to 3.5×10^{-2} electrons per photon. As was the case with many of the metals tested, the yields for a partially degassed cathode were remarkably reproducible. In the case of Pt, this fact together with the constancy of the yields in the region from 1000 A to 473 A suggests that a degassed Pt photocell may be useful as a linear photon counter for this region. The stability of such a counter to contamination by residual gases can be judged by making reference to the triangular points in Fig. 4, which give the yields for a partially degassed cathode exposed to air at atmospheric pressure for seventeen hours. Even under these extreme conditions the change in yield amounted to only thirty percent. Thus a Pt photon counter could be exposed to air without seriously affecting its calibration.

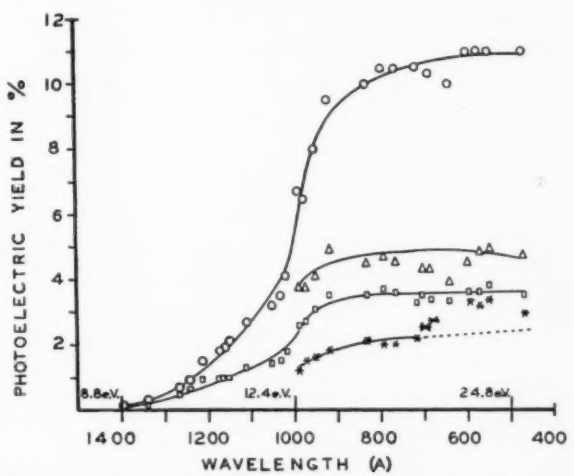

FIG. 4. Photoelectric yield of Pt. ○ Untreated cathode. □ Heat treated cathode in equilibrium with residual gases at about 10^{-5} mm Hg. * Cathode maintained at 900°C in a vacuum of 10^{-5} mm Hg. △ Heat treated cathode, at room temperature, exposed to air at atmospheric pressure for 17 hours.

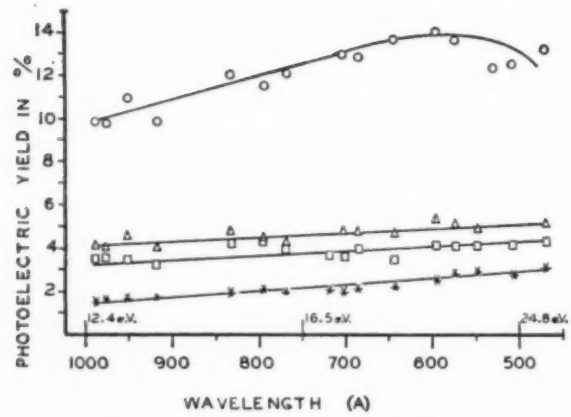

FIG. 5. Photoyield of Au. ○ Untreated cathode. △ Heat treated cathode. The cathode was heated for 40 seconds at 900°C in a vacuum of about 10^{-5} mm Hg. □ Heat treated cathode in equilibrium with residual gases at 10^{-5} mm Hg. The cathode was heated for several minutes at 900°C. * Cathode maintained at 800°C in a vacuum of 10^{-5} mm Hg.

The starred points in Fig. 4 give the yields for a Pt cathode which was maintained at a temperature of 900°C in a vacuum of about 5×10^{-5} mm Hg. In this case the yields at wavelengths below 650 A were found to remain about the same as those of a partially degassed sample. However, it was felt that this was due to the fact that insufficient time was allowed for the removal of surface contaminations before the measurements were taken. The dotted portion of the curve indicates the most probable trend of the yields in this region. Further work on Pt is needed in order to establish the accuracy of this extrapolation. The decrease in emission of the hot sample, between 1000 A and 700 A, relative to that of a degassed sample at room temperature again appeared to be due to a further cleaning of the Pt surface. Since it is known that the most likely surface impurities of Pt, namely PtO and PtO_2, have decomposition temperatures below 500°C, it can be assumed that the data for wavelengths longer than 700 A corresponded to a surface free from these substances, and the curve in Fig. 4 connecting the starred points should be representative of clean, metallic platinum.

Gold

Figure 5 presents the photoyields obtained for a Au cathode. The results for the untreated metal are marked by circles. After heating the cathode to 900°C for one minute, the yields were found to decrease to the values shown by triangles, and continued heating at the same temperature for five minutes resulted only in a slight further decrease as indicated by the squares. It should be noted that for Au, only mild heat treatment was necessary to remove much of the surface contamination, which was in accord with the fact that the expected surface impurities of Au, namely Au_2O_2, Au_2O_3, and Au_2O, all have decomposition temperatures less than 200°C.

The yields obtained from a Au cathode maintained at 800°C in vacuum during testing are shown in Fig. 5 by stars. For this hot sample the yields were found to be very nearly constant and equal to 2×10^{-2} electrons per photon over the region from 1000 A to 473 A. Since the surface contamination of Au was easily removed by heating, this value is probably characteristic of a metallic Au surface.

W, Mo, Ag, and Pd

In view of the few data available on the photoelectric properties of metals for vacuum ultraviolet radiation, it seemed important to survey several metals in a less detailed manner than that for the preceding ones. The photoelectric yields obtained for untreated and heat treated cathodes of W, Mo, Ag, and Pd are shown in Figs. 6–9, respectively. Untreated samples of the refractory metals W and Mo were found to have yields of the order of 0.15 electrons per photon at the maximum. These large values are probably related to the ability of these metals to adsorb large quantities of gas. The yields of heat treated samples of W and Mo exhibited a slight maximum in contrast to the plateau observed for Ni, Pt and Au. Since both W and Mo are difficult to outgas by heating, the yields for these metals can not be considered characteristic of a clean metallic state, but only of a surface partially covered with gas. In the case of W the yields of the untreated cathode were of the same order as those obtained by Hinteregger and Watanabe[6] for the same material. Agreement was also noted between the results for a heat treated W sample and those of Kenty[4] for outgassed tungsten.

For Ag, a maximum of about 0.12 electron per photon was observed at 800 A. Although the magnitude of the yields decreased after heating at 800°C for several minutes, the shape of the curve was not altered. Whether this maximum is characteristic of the metal or the surface contamination, can not be answered on the basis of the present data.

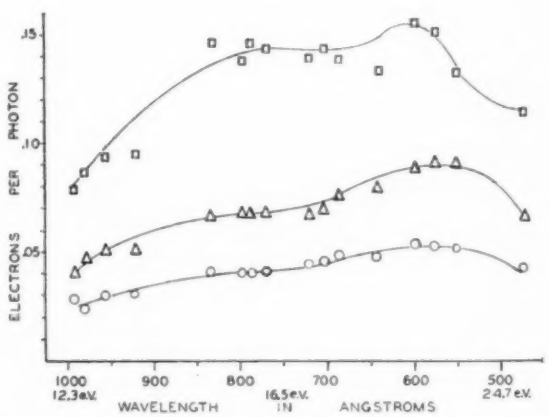

FIG. 6. Photoyield of W. □ Untreated cathode. △ Cathode heated for five minutes at a temperature above 1000°C in a vacuum of 10^{-5} mm Hg. ○ Cathode heated at a temperature above 1000°C until yield reproducibility was established.

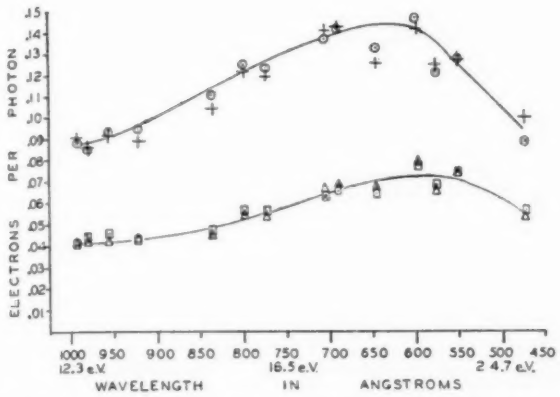

FIG. 7. Photoyield of Mo. ○, + Untreated cathode. □, △ Cathode heated at a temperature above 1000°C in a vacuum of about 10^{-5} mm Hg.

A remarkable similarity was noted between the yields of a heat treated Pd sample and the corresponding ones for Pt; in fact, the two curves were almost identical from 1000 A to 473 A. This is probably related to the fact that the electronic band structures of these metals are very similar.

IV. CONCLUSION

During the present investigation several interesting and unusual aspects of photoemission for vacuum ultraviolet radiation were observed, e.g., for all metals tested the yields were of the order of ten to one hundred times larger than those usually obtained for visible or near ultraviolet light. In addition, photoelectric currents produced by longer wavelength radiation have been found to change by factors of 50 to 500 for only minor variations in surface conditions, while in contrast the yields observed in this work decreased at most by only about a factor of ten from untreated to outgassed surfaces. This relative insensitivity to surface contamination is difficult to reconcile with an emission mechanism in which the electrons come from a thin surface layer of about 10^{-7} cm thick, as is usually assumed.

The unusual properties of photoemission at short wavelengths seem to be in general agreement with a *volume* effect, in which the electrons originate within the metal at depths of fifty to one hundred atomic diameters or greater. Large photoyields might be expected from such a process since most of the incident radiation is absorbed within the volume of the metal,[10] and hence if the internal photon-electron interaction cross section is not too small many electrons should be released. From x-ray photoelectric investigations for single atoms[13] this cross section appears to increase with the binding of the electrons. In analogy, the more tightly bound electrons within the metal should have a cross section larger than that for more loosely bound electrons in the surface field. Taken together, these considerations should lead to enhanced emission. In addition, since the electrons would not originate in a thin surface layer, the character of the surface should play a correspondingly smaller role. These conclusions are in accord with the present experimental data.

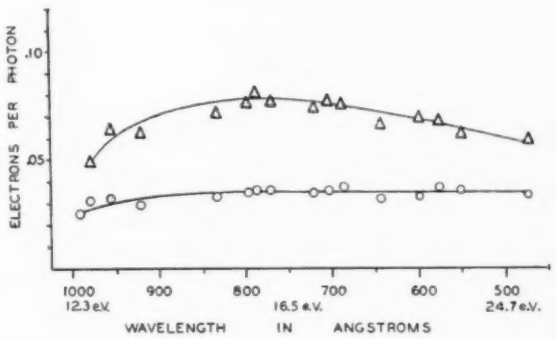

FIG. 9. Photoyield of Pd. △ Untreated cathode. ○ Cathode heated at a temperature above 1000°C for two minutes.

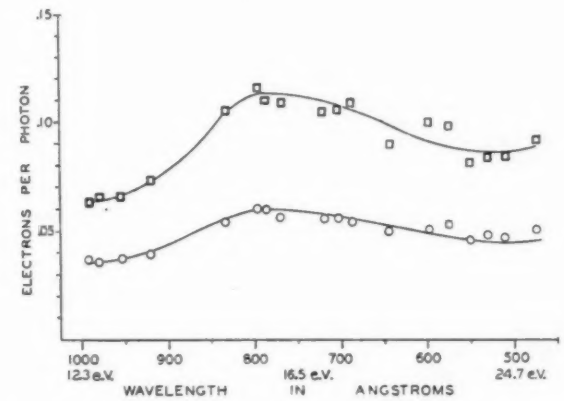

FIG. 8. Photoyield of Ag. □ Untreated cathode. ○ Cathode heat treated at 800°C for two minutes in a vacuum of 10^{-5} mm Hg.

No theoretical computations on the *volume* effect have been carried out for the metals treated in this investigation. Only the alkali metals Na and K have been considered theoretically.[14,15] Even for these only approximate methods have been used; however, they indicate that for far ultraviolet radiation a *volume* effect should be expected.

V. ACKNOWLEDGMENTS

Acknowledgments are due Mr. R. Schoen for many helpful discussions and to the Office of Ordnance Research, U. S. Army, for its continued support of this investigation.

[13] H. Hall, Revs. Modern Phys. **8**, 358 (1936).
[14] I. Tamn and S. Schubin, Z. Physik **68**, 97 (1931).
[15] H. Y. Fan, Phys. Rev. **68**, 43 (1945).

JOURNAL OF APPLIED PHYSICS VOLUME 26, NUMBER 11 NOVEMBER, 1955

Some Monte Carlo Calculations of Gamma-Ray Penetrations

J. F. PERKINS
Lockheed Aircraft Corporation, Marietta, Georgia
(Received June 16, 1955)

The transmission of gamma rays through slabs of various shielding materials has been calculated by a random sampling method in which the path lengths between interactions are deliberately chosen larger than those which occur naturally. Results for the case of normal incidence compare reasonably with values obtained by Goldstein and Wilkins for transmission in infinite media. The present results for the case of obliquely incident photons show the same general behavior as noted experimentally by Kirn, *et al.* In particular, the transmission plotted against slant path length shows a crossover, in the region of 1 or 2 mean free paths, of the curves corresponding to different incident angles. Angular and spectral distributions were obtained in the form of histograms, and it was found that the photons assume spatial equilibrium after one or two mean free paths, as evidenced by the constancy of the flux-to-current ratio. The relative contribution to the total penetration arising from the first, second, etc. scattering has been found to have the same general trend as noted earlier by Peebles. The biased sampling method which was used enables one to use the same set of photon case histories in treating a number of slab thicknesses.

THE penetration of gamma rays through shields has been calculated by several methods, but the only systematic calculations which have been done are those of Goldstein *et al.*,[1] who used the Spencer-Fano[2] method of moments. This method is limited to the case of infinite media, whereas the behavior of photons in realistic shields may be appreciably affected by the presence of boundaries. For this and other reasons a number of people are employing random sampling techniques for estimating gamma-ray penetration. The present calculations include cases of normal incidence which are directly comparable with the results of Goldstein *et al.* and cases of oblique incidence which apparently have not been treated before. They include values of over-all penetration and the angular and spectral distributions of the photons

These calculations were performed with the use of an IBM-701 computer using a modification of a program used earlier for calculating gamma-ray albedos.[3] Because the probability of transmission through a few mean free paths is much less than the probability of reflection, it was necessary to modify the sampling in such a way as to reduce the variance. In this connection the main guidance was taken from papers by Kahn,[4] the method being essentially what he calls importance sampling. Such a type of biased sampling has been used by Beach[5] and by Berger,[6] but in ways which seem specially adapted to the particular case considered, so that each shield thickness would have to be treated in a completely distinct calculation. It seems particularly desirable to modify the sampling in a manner that can be made to depend rather simply on at most a few parameters. One hopes to have a computer program which is of rather general usefulness, and would like to be able to use the same set of case histories for treatment of several different geometries.

In employing importance sampling one simply wishes to sample most heavily those portions of phase space which contribute strongly to the penetration. Expressions can be written for the optimum sampling distribution over a given number of the variables, but these will of course depend on a knowledge of the desired solution itself in anything but a trivial problem. In practice one merely uses intuition or results of previous calculations to devise trial variations in the sampling distribution, and chooses a fairly simple form of the distribution. In the case of photons penetrating fairly thick shields one expects that the photons which get through contain a large fraction of photons which have traversed long distances between scatterings, and which have scattered through fairly small angles. By simply choosing distances between scatterings which are just a constant multiple of those obtaining in nature one gets a very simple sampling method, and can use the same sample for a number of shield thicknesses, as will be shown. The scattering angles were not subjected to biased sampling in the present work, but were chosen from the true distributions.

To determine the proper weighting factors to compensate for the sampling bias one merely expresses the desired solution as an integral

$$I=\int g(x)f(x)dx,$$

where $f(x)$ is considered a sampling distribution, and hence must be normalized. One then estimates the value of I as the average value of a set of $g(x_i)$ which are chosen from the distribution $f(x)$. One can also express the integral as

$$I=\int g^*(x)f^*(x)dx.$$

[1] H. Goldstein and J. E. Wilkins, Jr., Nuclear Development Associates Report No. NYO-3075.
[2] L. V. Spencer and U. Fano, J. Research Natl. Bur. Standards **46**, 446 (1951).
[3] J. F. Perkins, J. Appl. Phys. **26**, 655 (1955).
[4] H. Kahn, Nucleonics **6**, 61 (1950).
[5] Beach, Theus, Plawchan, and Faust, Naval Research Laboratory Report No. NRL-4412.
[6] M. J. Berger (to be published).

The weighting factor to be used is thus $g^*(x)/g(x) = f(x)/f^*(x)$. Of course, $f^*(x)$ must also be normalized.

The only scattering process which need be considered in most problems of this sort is the Compton process, the cross section for which depends only on the electron density. On the other hand, the absorption processes, i.e., the photoelectric effect and pair production, depend also on the atomic number of the shield material. Thus, in cases where one would like to use the same set of case histories in treating different shielding materials, it is convenient to sample from a probability distribution for distance between successive scatterings. In this method one samples from

$$f(x)=\mu_s e^{-\mu_s x}$$

which gives

$$g(x)=h(\theta,E)e^{-\mu_a x}.$$

Here I represents the amount of radiation transmitted through a slab of shielding material. The dependence on the distance, x, traversed by the photon between the point of one particular interaction, say the ith, and the next one is written explicitly, while the dependence on all the other variables reposes in the function $h(\theta,E)$. The foregoing type of sampling requires the evaluation of an exponential, $e^{-\mu_a x}$, at each step in the calculation. In previous calculations[3] we have sampled instead from the distribution of total interactions, either scattering or absorption, i.e., from

$$f'(x)=Ce^{-(\mu_s+\mu_a)x}.$$

In the present sampling process we wish to choose x's which are J times as great as we would normally have. Hence we sample from

$$f^*(x)=C^*e^{-(\mu_s+\mu_a)x/J}.$$

We have also biased the samplings so as to force the photon to remain within the medium. Thus, the range of x is from 0 to $z/\cos\theta$ when $\theta<90°$, 0 to ∞ when $\theta\geq 90°$. The usual cylindrical coordinates are used, with the z-axis along the inward normal of the slab of shielding material. These conditions give for C^*

$$\frac{1}{C^*}=\int_0^{z/\cos\theta} e^{-(\mu_s+\mu_a)x/J}dx = \frac{-Je^{-(\mu_s+\mu_a)x/J}}{(\mu_s+\mu_a)}\Bigg|_0^{z/\cos\theta}=\frac{J(1-Q)}{(\mu_s+\mu_a)},$$

where

$$Q=e^{-(\mu_s+\mu_a)z/J\cos\theta} \quad \text{for} \quad \theta<90°$$
$$Q=0 \quad \text{for} \quad \theta\geq 90°.$$

Also, we put

$$P=Q^J.$$

For $g^*(x)$ we get

$$g^*(x)=h(\theta,E)\frac{\mu_s}{(\mu_s+\mu_a)}J(1-Q)e^{-(\mu_s+\mu_a)x(J-1)/J}$$

$$g^*(x)/h(\theta,E)=\frac{\mu_s}{(\mu_s+\mu_a)}J(1-Q)\psi^{(J-1)},$$

where $\psi=e^{-(\mu_s+\mu_a)z/J}$ is rather directly obtained from the sample. That is, one chooses x by choosing a random number N from the uniform distribution and puts

$$\int_0^x f^*(x')dx'=N.$$

This gives

$$x=\frac{-J}{(\mu_s+\mu_a)}\log[1-(1-Q)N]=\frac{-J}{(\mu_s+\mu_a)}\log\psi.$$

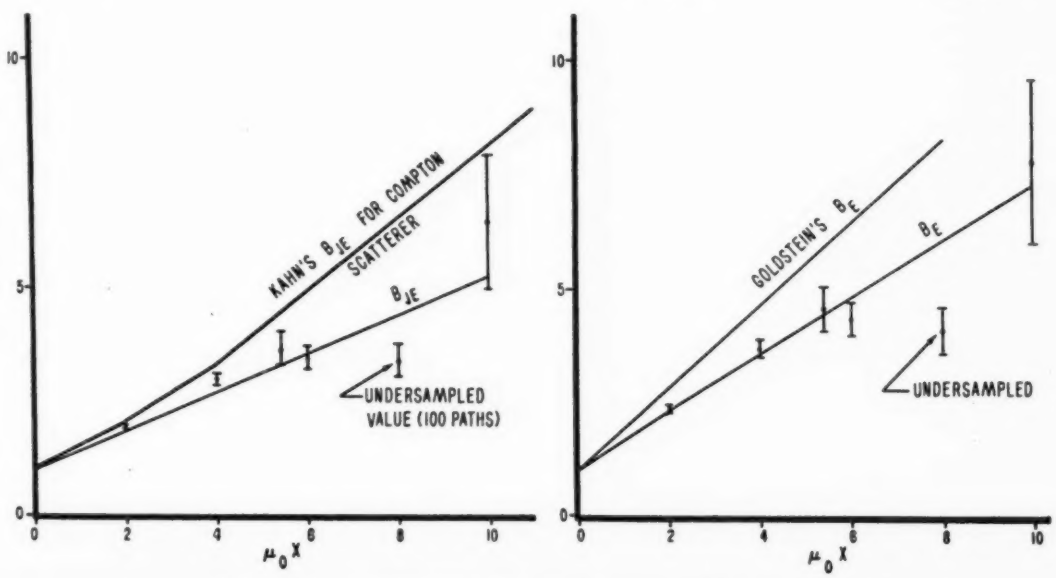

FIG. 1. Buildup factors for Co^{60} gamma rays normally incident on Al.

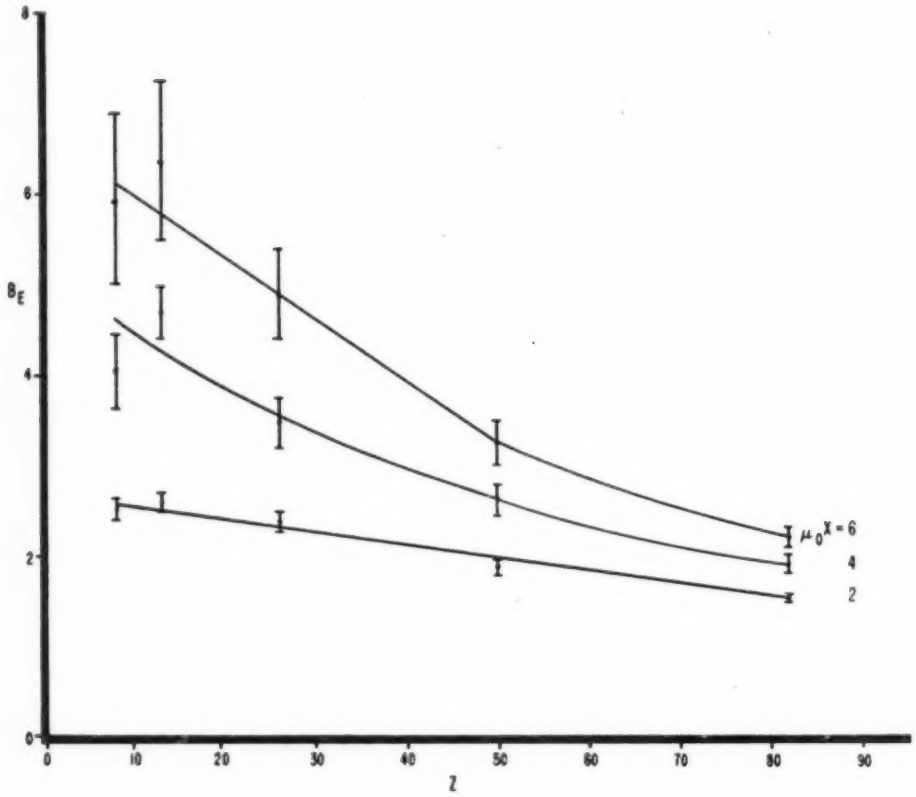

FIG. 2. Energy flux buildup factors for Cs^{137} gamma rays normally incident on slabs of various thicknesses as a function of atomic number.

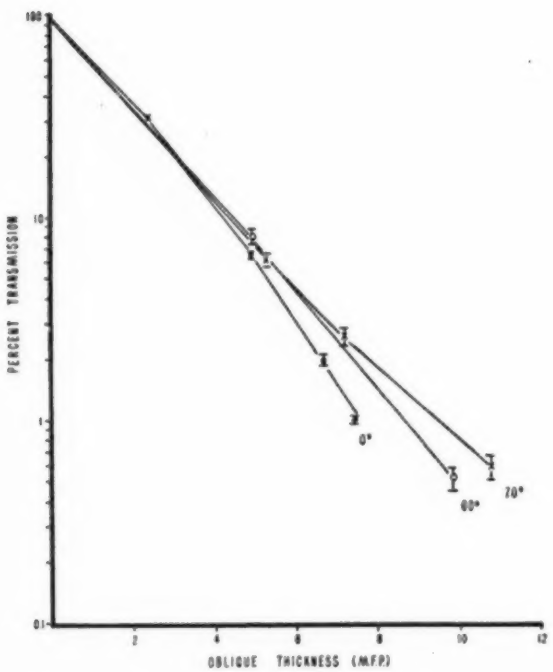

FIG. 3. Emergent energy flux as a function of oblique thickness (in mean free path of the incident radiation) for Cs^{137} gamma rays incident at various angles on slabs of H_2O.

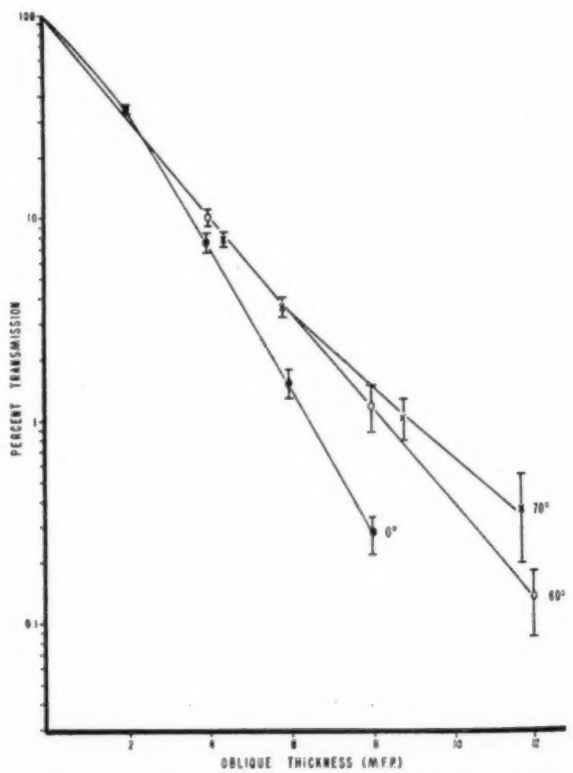

FIG. 4. Emergent energy flux as a function of oblique thickness (in mean free path of the incident radiation) for Cs^{137} gamma rays incident at various angles on slabs of Al.

If we put $x=JX$, we have

$$X=\frac{-1}{(\mu_s+\mu_a)}\log\psi$$

$$S_{i+1}=S_i\frac{\mu_s}{(\mu_s+\mu_a)}(1-Q_i)\psi_i{}^{J-1}$$

$$T_N=\sum P_iS_i.$$

In order to treat slabs of shielding material, as contrasted to semi-infinite media, we have set the survival factor equal to zero whenever the photon recrosses the entrance plane. That is, we have put $S_\kappa=0$ whenever

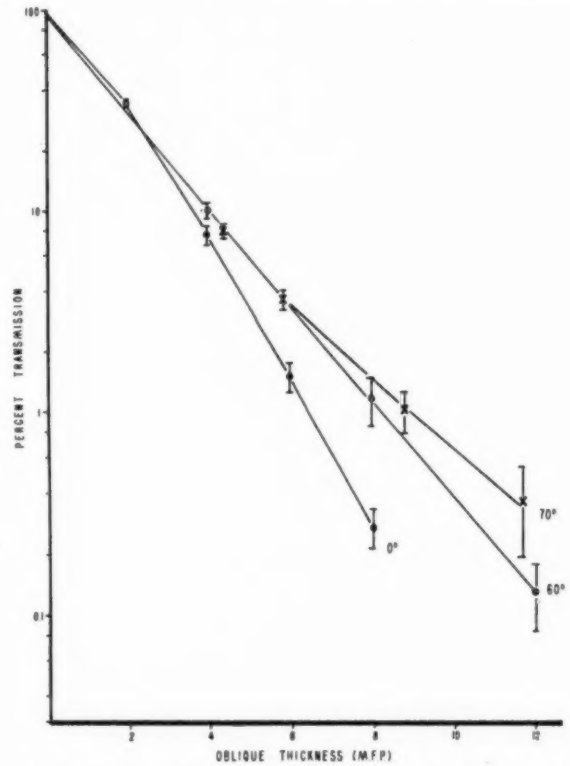

FIG. 5. Emergent energy flux as a function of oblique thickness (in mean free path of the incident radiation) for Co^{60} gamma rays incident at various angles on slabs of Al.

$\sum_1{}^k x_i\cos\theta_i<z_0$. The number and energy transmissions, T_N and T_E, have been directly calculated, while the number and energy flux were calculated by summing the calculated angular distributions of transmission, weighted with the factor $\sec\theta$.

To treat a slab of thickness $z=10$ mean free paths, we may put $Z=2$ mean free paths, $J=5$. For other thicknesses we may then keep this same value of Z but recalculate the survival factors, S, and the values of $P=Q^J$. Since J appears in these expressions as exponents as well as factors, we have chosen to limit the values of J to integers. The powers are obtained by repeated multiplication in iterative subprograms which treat J as a part of the input data.

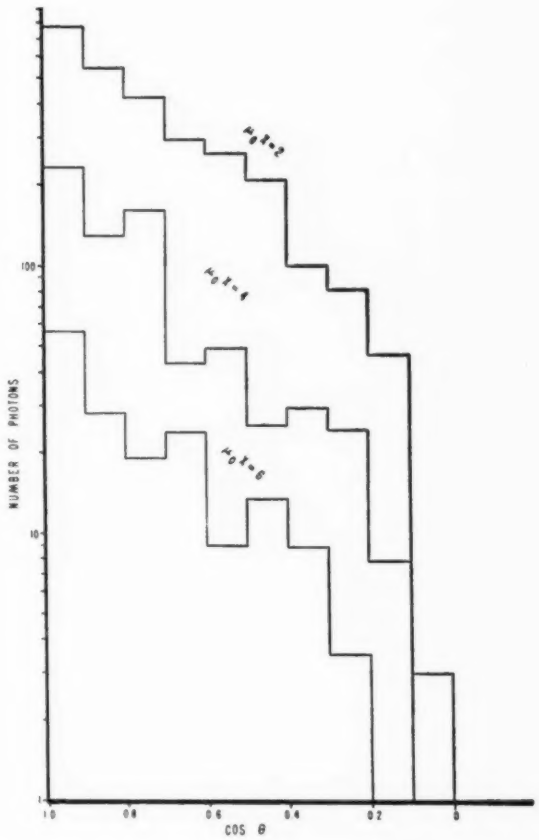

FIG. 6. Angular distribution of number of emergent photons. Co^{60} gamma rays normally incident on Al.

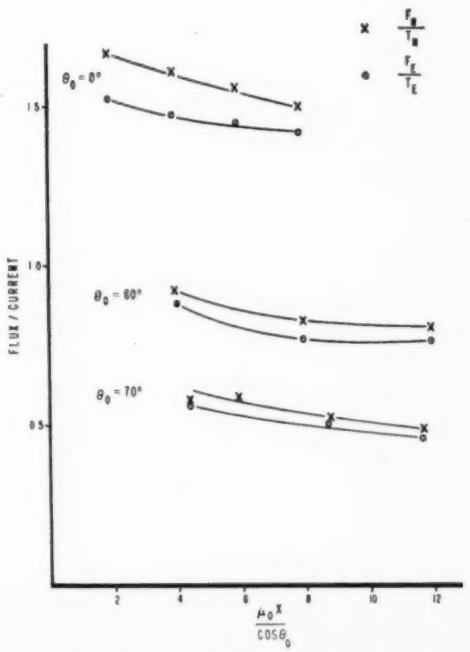

FIG. 7. Flux/current ratios for Cs^{137} gamma rays incident on H_2O.

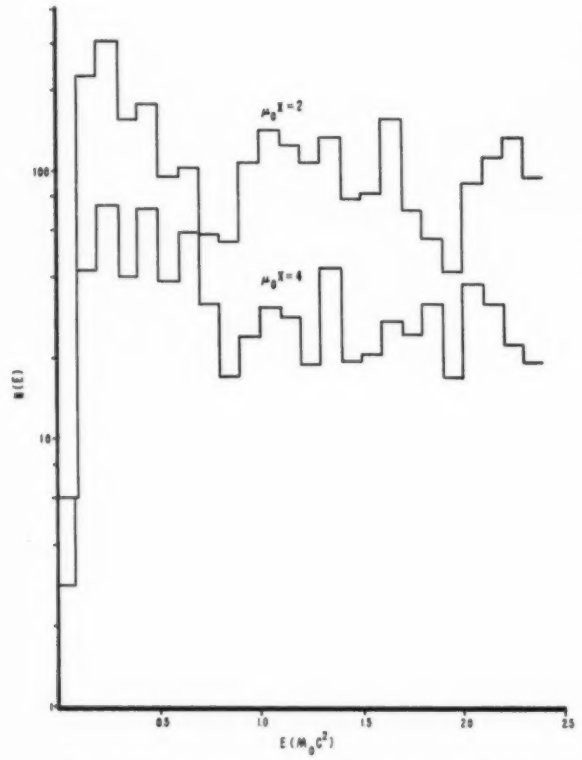

FIG. 8. Energy spectra for Co^{60} gamma rays in Al.

For slab thicknesses up to 8 or 10 mean free paths, the best choice of J seems to be that which corresponds to sampling from a pseudo-slab of thickness 1 or 2 mean free paths. By this sampling method the calculations required for a given accuracy were reduced by factors of from 5 to 100. Statistical tests in the form of χ^2 tests were performed to assure that the above sampling method did not introduce any bias into the result. Different combinations of Z and J corresponding to the same total thickness z were compared with the result that there was no suggestion of any bias in the calculated transmissions.

Some of the results of these calculations are presented in the accompanying figures. Figure 1 shows how the present results fall below the infinite media results of Goldstein *et al.*[1] resulting from boundary effects. The latter values were obtained by interpolation, which does not seem to be accurate to better than about 10% at this energy. Figure 1 was chosen for inclusion here because it shows the case of an underestimate of transmission coupled with an underestimate of the statistical uncertainty, such as was noted earlier by Kahn.[4] Such cases can be recognized both by the failure to fit the smooth trend of other values and by the unusually low value of the estimated standard deviation relative to sample size. This phenomenon arises from the use of too small a sample size. Most points in this figure resulted from sample sizes of 500 incident photons, whereas the one in question corresponds to a sample size of only 100.

Figure 2 shows buildup factors for energy flux as a function of atomic number. Figures 3 to 5 show energy flux as a function of oblique thickness for cases of oblique incidence. There do not appear to be previous calculations for such cases, but experimental data have been obtained by Kirn *et al.*,[7] who observed crossovers at 1 or 2 mean free paths, such as are shown here.

Figure 6 shows the angular distribution of emergent

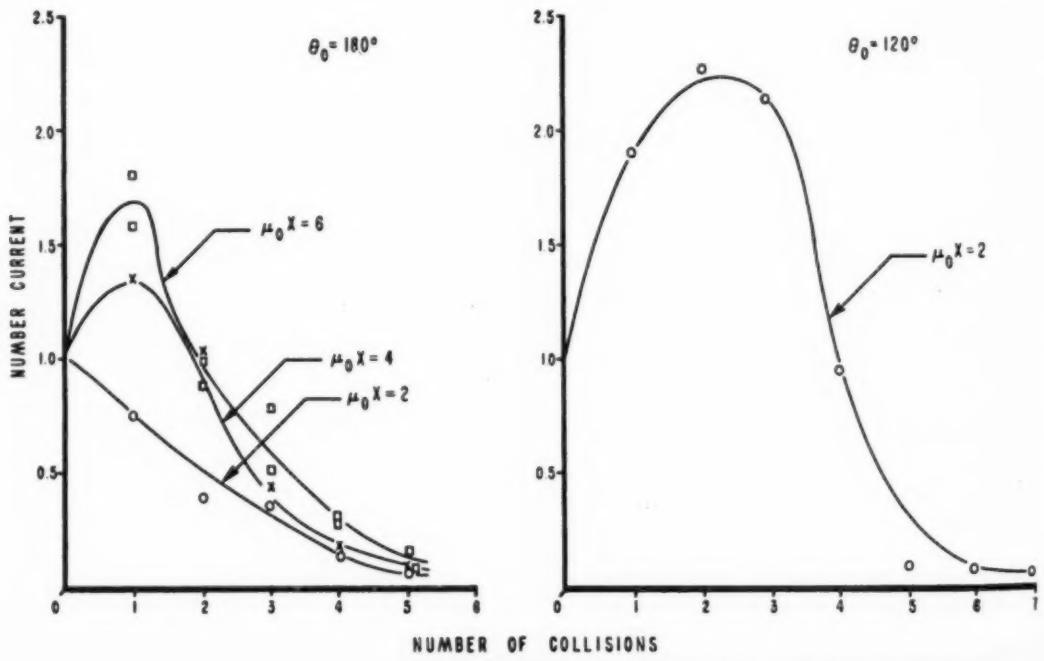

FIG. 9. Contributions to the number current from various orders of scatterings.

[7] Kirn, Kennedy, and Wyckoff, Radiology **63**, 94 (1954).

radiation. The ratio of flux to current is a measure of the sharpness of the angular distribution, and a typical case of this ratio is shown in Fig. 7. It is found in all cases that this ratio is rather constant beyond 2 mean free paths, indicating that the radiation rather quickly reaches angular equilibrium. In all cases the number flux is more strongly peaked in the forward direction than is the energy flux. Figure 8 shows spectral distributions in the form of histograms. The general shape is in agreement with the results of Goldstein *et al.*[1] Figure 9 shows the contribution to the transmission as a function of the number of scatterings. This may be compared with similar results of Peebles[8] for 5 m_0c^2 photons incident on Pb. The qualitative behavior is the same in the two cases, but the present results, which deal with a lower-Z material, peak at a higher number of scatterings.

[8] G. H. Peebles, J. Appl. Phys. **24**, 1272 (1953).

JOURNAL OF APPLIED PHYSICS VOLUME 26, NUMBER 11 NOVEMBER, 1955

Relative Influence of Majority and Minority Carriers on Excess Noise in Semiconductor Filaments*

LEON BESS†
Lincoln Laboratory, Massachusetts Institute of Technology, Lexington, Massachusetts

(Received June 24, 1955)

An experiment has been devised whereby excess noise is measured along various different directions in a germanium filament after the directions of current flow for the majority and minority carriers had been altered by a magnetic field. From this experiment it is possible to determine that whereas shot noise is caused by both majority and minority carrier fluctuation, $1/f$ noise is essentially produced only by majority carrier fluctuation.

I. INTRODUCTION

IF it is assumed, along with most current theories,[1–4] that excess noise in semiconductors is a result of a fluctuation of mobile carrier density with time, there is a very important question which suggests itself: What part of the total fluctuation is due to majority carrier fluctuation and what part to minority carriers? This paper will describe an experiment which attempts to answer this question both at low frequencies where $1/f$ noise predominates in the excess noise and at higher frequencies where shot noise predominates.

II. EXPERIMENTAL ARRANGEMENT

The arrangement of experimental apparatus is shown in Fig. 1. The sample, a square slab (1 cm by 1 cm) of n-type germanium 0.01-in. thick, was cut to the shape shown. A uniform magnetic field of about 8 kilogauss perpendicular to the plane of the paper could be applied in the area enclosed by the dotted line.

Current was passed through the central horizontal portion of the sample (whose surface was etched) from a large resistor R_L (about 15 kilo ohms) and a high voltage battery source (180 v).

The four wiring probes extending from the central portion of the sample are soldered to wires from the switches SW_1 and SW_2 as shown in Fig. 1. It is to be noted that the wing probes carry practically no current so that very little contact noise can be generated at their solder joints. The switches are then connected to the noise measuring apparatus consisting of an amplifier, wave analyzer, and a recorder.

The switching arrangement of SW_2 is very nearly equivalent to having a noiseless probe connected to the upper edge of the main central current-carrying body of

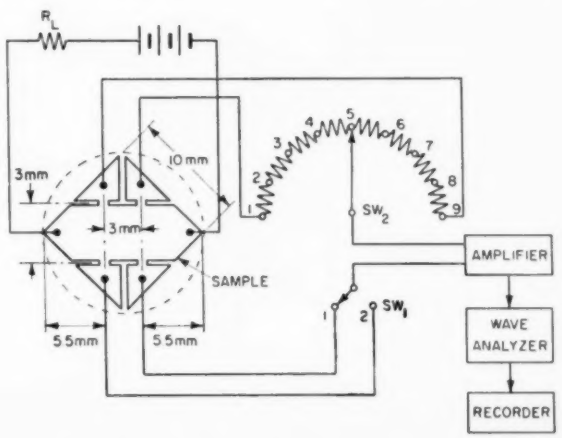

FIG. 1. Arrangement of experimental apparatus.

* The research in this document was supported in part by the U. S. Army, Navy, and Air Force under contract with the Massachusetts Institute of Technology, and in part by the Signal Corps, the Office of Scientific Research (Air Research and Development Command), and the Office of Naval Research.

† Staff Member.

[1] A. van der Ziel, Physica **16**, 359–372 (1950).
[2] M. Surdin, J. phys. radium **12**, 777–783 (1951).
[3] J. M. Richardson, Bell System Tech. J. **29**, 117–141 (1950).
[4] L. Bess, Phys. Rev. **91**, 1569 (1953).

the sample in any one of nine discrete equidistant positions (since the resistances on all the terminals of SW_2 are equal) varying from the position of the left upper-wing probe to that of the right upper-wing probe.

Thus with the switch, SW_1, in position 1, two noise measuring probes are effectively connected to the upper and lower edges of the central main body of the sample in such a way that the angle which the connecting line of these probes makes with the vertical can be varied from 0° to 45° by varying SW_2 from position 1 to position 9. Similarly, with SW_1 in position 2, the angle that the probe line makes with the vertical will be varied from −45° to 0° when SW_2 goes from position 1 to position 9.

Roughly speaking, the experiment to be described is based on the fact that, when noise at a given frequency is plotted against the angular position of the probe line, there will be a given position at which the noise will be minimum. This position will, in general, depend on the direction of flow of each type of carrier and the contribution to the total noise that each type of carrier makes. In the case of zero magnetic field through the sample, the direction of flow of both types of carriers will be horizontal, and a minimum noise output should occur when the probe line makes a zero angle with the vertical. This is found to be so experimentally.

However, when a large magnetic field is impressed on the sample, in the manner indicated in the foregoing, the Hall effect will occur, and the direction of flow of each type of carrier will be different. The noise minimum will occur when the probe line is at some other angle than zero degrees, and the analysis becomes complicated. However, it is possible to deduce the relative contributions to the noise of each type of carrier if the position of the minimum is known for a given value of magnetic field. The exact details of this analysis will be considered in Sec. IV.

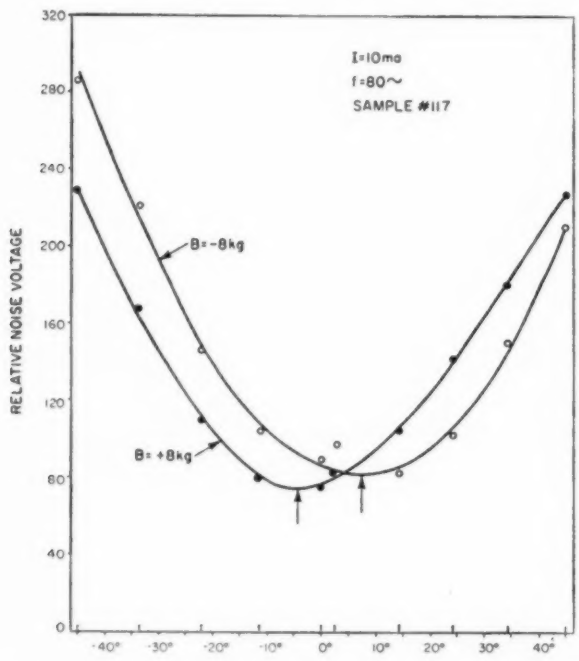

FIG. 2. Noise voltage *versus* probe line angular position at 80 cycles.

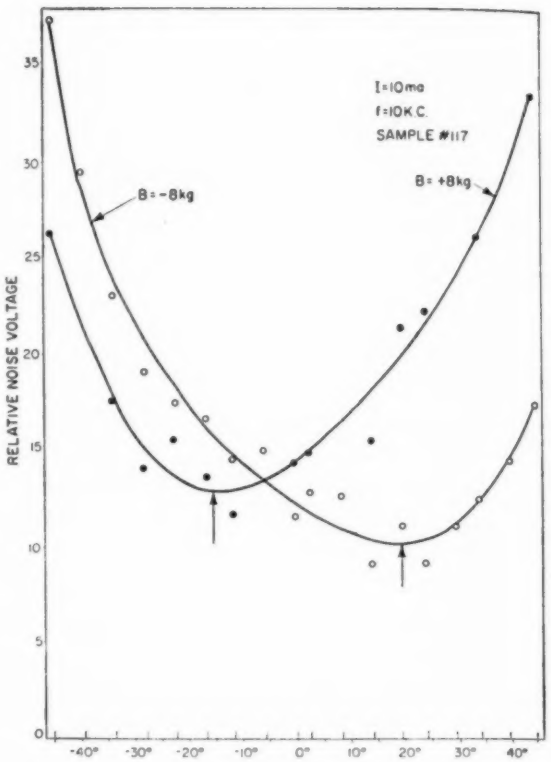

FIG. 3. Noise voltage *versus* probe line angular position at 10 kilocycles.

III. EXPERIMENTAL PROCEDURE AND RESULTS

The significant information in this experiment was obtained by plotting noise voltage against probe line angular position with both directions of magnetic field (of 8 kilogauss) and at frequencies of 80 cycles and 10 kilocycles. This was done for two samples, but the results were so nearly the same that the data from only one sample will be presented here.

By plotting the frequency spectrum for both samples, both with and without a magnetic field, it was found that at 80 cycles the $1/f$ component of noise exceeded the shot noise component by the order of 20 db.

At 10 kilocycles the shot noise component exceeded the $1/f$ noise component by the order of 12.5 db. Thus for all practical purposes, it could be said that at 80 cycles all of the noise was $1/f$ noise and at 10 kilocycles all of the noise was shot noise. Since the shape of the spectrum over the measured frequency range (from 80 cycles to 10 kilocycles) showed no significant change when the magnetic field was applied, it was inferred that the magnetic field would not change the basic character of the noise.

Figure 2 shows the results of the noise *vs* position plot at 80 cycles, and Fig. 3 shows the results at 10 kilocycles.

The fact that the scatter of points in Fig. 3 is greater than Fig. 2 is due to the relative background noise being greater. The arrows indicate the noise minimum positions. Figure 4 shows the results of the Hall data which was obtained by plotting the dc voltage between the arms of SW_1 and SW_2 for different probe line angular positions for the values of magnetic field indicated in the graph.

At this point it should be noted that at 80 cycles the position of the noise minimum is very nearly the same as that of zero voltage in Fig. 4 for the same magnetic field. (The tiny arrows in Fig. 4 correspond to the positions of the noise minimum.) Moreover, at 10 kilocycles there is a noticeable difference between the positions of noise minimum and zero dc voltage for the same magnetic field. The deviation of the noise minimum is always in the direction of minority carrier flow. These facts are very significant in the following analysis of results.

IV. THEORY AND ANALYSIS OF RESULTS

Before a meaningful analysis of results can be obtained, it is first necessary to consider the simplified theory of the processes involved here.

Figure 5 illustrates the ideal situation which will be treated. A very long horizontal thin ribbon of uniform n-type germanium has a total current density, J, with a horizontal direction flow and a strong magnetic field perpendicular to the face of the ribbon. The directions of current flow of each type of carrier and the direction of the resultant electric field will be as shown in Fig. 5.

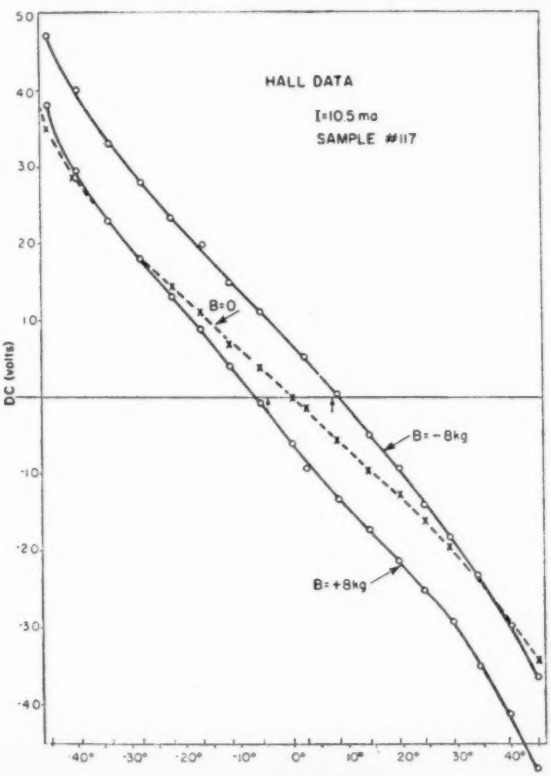

FIG. 4. Hall data.

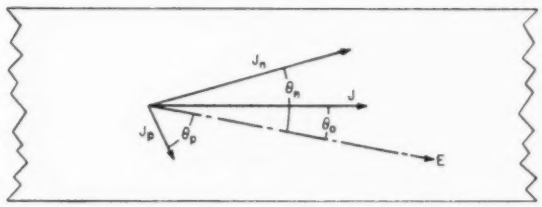

FIG. 5. The electric and current vectors for the idealized case.

From the simple Hall theory it can be established that E and θ_0 are related to the other parameters[5] in the following way:

$$E=\frac{J\cos\theta_0}{e(n\mu_n+p\mu_p)}, \tag{1}$$

$$\theta_0\cong\frac{n\mu_n\sin\theta_n-p\mu_p\sin\theta_p}{n\mu_n\cos\theta_n+p\mu_p\cos\theta_p}. \tag{2}$$

It will be assumed that the noise to be considered arises primarily from a fluctuation with time of n and p. From Eqs. (1) and (2) it can be expected that as a result the quantities E and θ_0 will fluctuate with time. (J is assumed not to fluctuate because the ribbon is being driven from a constant current generator.) If two noiseless probes were connected to the upper and lower edge of the ribbon, this would in general cause a fluctuating noise voltage to appear between them which is at each instant of time directly proportional to the component of E along the probe line.

To study this noise voltage it is, therefore, necessary to know how E and θ_0 vary with time. At this point, the plausible assumption will be made that whatever the relaxation time between an abrupt change in n or p and the attainment of a new equilibrium value, it will be small compared to the inverse frequency at which the noise is being measured.

In this case the time variation of E and θ_0 can be obtained from Eqs. (1) and (2) by substituting the time varying quantities n and p, which will be assumed to have the specific form

$$n=n_0[1+\epsilon_n(t)], \tag{3}$$

$$p=p_0[1+\epsilon_p(t)], \tag{4}$$

where the ϵ's are in general very small quantities. Then, θ_0 and E can be shown to have the form

$$\theta_0=\bar{\theta}_0+\alpha\beta[\epsilon_n(t)-\epsilon_p(t)], \tag{5}$$

$$E=\bar{E}[1+\epsilon_n(t)+\beta(1-\alpha\bar{\theta}_0)\epsilon_p(t)], \tag{6}$$

where

$$\alpha\equiv\frac{\sin(\theta_n+\theta_p)}{[\cos\theta_n+\beta\cos\theta_p]^2}, \tag{7}$$

and

$$\beta\equiv p_0\mu_p/n_0\mu_n. \tag{8}$$

[5] The table of symbols employed here is listed in Appendix A.

The $\bar{\theta}_0$ and $\bar{E}$ are the average values of θ_0 and E. It should be noted here that no assumption has been made as to whether $\epsilon_n(t)$ and $\epsilon_p(t)$ are correlated or not.

Let ϕ be the angle that the probe line makes with the perpendicular to the E direction. In the ideal case, for a given orientation of probe line, the voltage fluctuation, δE_T, would be measured is:

$$\delta E_T = \delta E_{\parallel} \sin\phi + \delta E_{\perp} \cos\phi \tag{9}$$

$$\delta E_{\parallel} = \bar{E}[\epsilon_n(t) + \beta(1-\alpha\bar{\theta}_0)\epsilon_p(t)], \tag{10}$$

$$\delta E_T = \bar{E}\beta\alpha[\epsilon_n(t) - \epsilon_p(t)]. \tag{11}$$

Equations (9), (10), and (11) can be combined to give the result

$$\delta E_T \cong \bar{E}\{\epsilon_n(t)[\sin\phi + \beta\alpha\cos\phi] + \epsilon_p(t)\beta[\sin\phi - \alpha\cos\phi]\}. \tag{12}$$

When $\epsilon_n(t)$ and $\epsilon_p(t)$ is known, Eq. (12) permits the analytical determination of the probe line orientation (i.e., the ϕ) for which the noise voltage (i.e., δE_T) will be a minimum. The operation of obtaining the minimum involves squaring both sides of Eq. (12), taking the time average, differentiating the right-hand side with respect to ϕ, setting the result equal to zero, and finally solving the resulting equation for ϕ. This produces the following relation:

$$\tan 2\phi_m = \frac{2\beta\alpha[\langle\epsilon_n^2(t)\rangle - \beta\langle\epsilon_p^2(t)\rangle - \langle\epsilon_n(t)\epsilon_p(t)\rangle]}{[\langle\epsilon_n^2(t)\rangle + 2\beta\langle\epsilon_n(t)\epsilon_p(t)\rangle + \beta^2(1-\alpha^2)\langle\epsilon_p^2(t)\rangle]}. \tag{13}$$

The angle for minimum noise is ϕ_m. In deriving Eq. (13), it was assumed that $\beta \ll |$ which, as can be seen from Eq. (8), is easily satisfied in practice with the doping ratios of most samples.

$\langle\epsilon_n^2(t)\rangle$, $\langle\epsilon_p^2(t)\rangle$, and $\langle\epsilon_n(t)\epsilon_p(t)\rangle$

denote time averages.

A study of Eq. (13) will reveal that, in general, ϕ_m will be in the order of β (i.e., ϕ_m will be small) until $\langle\epsilon_p^2(t)\rangle$ becomes of the order of $(1/\beta^2)\langle\epsilon_n^2(t)\rangle$ (i.e., until the magnitude of the hole fluctuations approaches that of electron fluctuations).

In what follows two special cases will be treated which are connected with the most probable physical process that can explain the result of Sec. II. The first case is where:

$$\epsilon_p(t) = \left(\frac{\mu_p}{\beta\mu_n}\right)\epsilon_n(t). \tag{14}$$

This is the relationship that would result between the ϵ's in van der Ziel's[6] theory of shot noise where the absolute fluctuation magnitudes of hole and electron densities are of the same order. Upon substituting Eq. (14) in Eq. (13), the result for ϕ_m is:

$$\tan 2\phi_m = -2\alpha[1 + b - \alpha^2/(1+b)]^{-1} \tag{15}$$

where $b \equiv \mu_n/\mu_p$.

Using the experimental Hall data in Eq. (7), α will be found to be about 0.7 at 8 kilogauss. With $b=1.5$, ϕ_m can be calculated from Eq. (15) to be about 15°. An experimental value of ϕ_m for shot noise can be found from Figs. 3 and 4. ϕ_m is the difference in angular position between a noise minimum and the position of the perpendicular to the E vector (which is where the dc voltage is zero in Fig. 4). The average experimental value for ϕ_m is about 10°. Considering the roughness of the measurement of Fig. 3, the agreement between experimental and calculated values of ϕ_m (an error of about 30%) is not too bad. It would appear, therefore, that the experimental data presented here tends to corroborate van der Ziel's theory.

The second case to be considered here is where

$$\epsilon_p(t) = -\epsilon_n(t). \tag{16}$$

Equation (16) describes the relationship between the ϵ's that would result from the $1/f$ noise theory of the author.[7] This theory postulates that $1/f$ noise is caused by a random shifting of the Fermi level with respect to the band edges.[8,9] This requires that for every change in majority carrier concentration there is an opposite change in minority concentration whose magnitude is the same percentage wise.

Upon substituting Eq. (16) in Eq. (13), the relation that results is

$$\tan 2\phi_m = 4\beta\alpha. \tag{17}$$

Since β is usually small compared to unity (in the sample here $\beta < .03$) ϕ_m as calculated from Eq. (17) will be small ($\phi_m < 2.5°$). The average experimental value of ϕ_m at 80 cycles as determined from Fig. 2, and Fig. 4 is about 1.7°. (The tiny arrows in Fig. 4 show the position of the noise minimum of Fig. 2.) The agreement here between the experimental and calculated values of ϕ_m is well within the experimental error (since at 80~ the minima cannot be measured to better than ±2°).

Thus it would appear from the data that a fluctuation of Fermi level can give rise to $1/f$ noise. At any rate, strong evidence is presented here that the fluctuation of majority carriers constitutes the major part of $1/f$ noise.

[6] A. van der Ziel, J. Appl. Phys. **24**, 1063 (1954).

[7] L. Bess, Research Laboratory of Electronics of Massachusetts Institute of Technology Progress Report, pp. 79–88 (January 15, 1955).

[8] W. Shockley, Electrons and Holes in Semiconductors (D. Van Nostrand Company, New York, 1950), pp. 342–346; H. C. Montgomery, Bell System Tech. J. **31**, 950 (1952).

[9] A. L. McWhorter, Massachusetts Institute of Technology Technical Memorandum No. 80 (1955).

V. SUMMARY

The data from the experiment described above would seem to warrant the following conclusions:

(1) Shot noise is generated by majority and minority carrier density fluctuations which are of the same order of magnitude. Within experimental error, the ratio of the magnitudes of these fluctuations seem to be those predicted by van der Ziel's theory of shot noise.[6]

(2) On the other hand, $1/f$ noise arises mostly from a fluctuation of majority carriers. In particular, the mechanism of a fluctuating Fermi level could explain the $1/f$ noise results.

VI. ACKNOWLEDGMENTS

Thanks are due to Professor J. B. Wiesner for extending the facilities of the Research Laboratory of Electronics, to Professor R. B. Adler for sponsoring the experiment, and to Professor H. Brooks for some very valuable discussions.

VII. APPENDIX A

The following is a table of symbols used throughout this paper:

n = electron carrier density
p = hole carrier density
μ_n = electron mobility
μ_p = hole mobility
J_n = electron current density
J_p = hole current density
J = total current density
θ_n = electron Hall angle
θ_p = hole Hall angle
θ_0 = total Hall angle
E = electric field strength
$b=\mu_n/\mu_p$
ϕ = the angle the probe line makes with the perpendicular to the E vector
ϕ_m = the ϕ corresponding to a noise minimum
n_0 = the time average electron carrier density
p_0 = the time average hole carrier density

JOURNAL OF APPLIED PHYSICS VOLUME 26, NUMBER 11 NOVEMBER, 1955

Hysteresis Loops of Mixtures of Ferromagnetic Micropowders

C. P. Bean
General Electric Research Laboratory, Schnectady, New York
(Received June 22, 1955)

A treatment is given of the hysteresis loops of dilute mixtures of various sizes of ferromagnetic particles. Three ranges of particle size are considered: very small particles called "super-paramagnetic" which are single domain and equilibrate resulting from thermal vibrations, single domain particles which are large enough that they do not equilibrate, and particles large enough to contain many domains in equilibrium. The results are compared to experiment.

IN experiments on the properties of fine particles of ferromagnetic materials, one deals always with a mixture of particles having differing magnetization curves. These differences arise from the various shapes, sizes, compositions, strains, and imperfections which characterize the components of the mixture. In addition, because of interactions between particles in a dense compact, the magnetization in a given field is not simply the sum of the magnetizations of isolated particles in that field. For this reason I shall treat only dilute compacts, where the volume fraction of ferromagnetic material is less than 1% and the magnetizations of isolated particles can be added, reserving the effects of interaction for a later paper.

The method of calculating the hysteresis loop of a dilute mixture is to add the magnetizations of the components for a given field, weighting them in proportion to their volume fraction of the total. Mathematically the magnetization I of a mixture of N types of particles in a field H is expressed by

$$I(H)=\sum_{n=1}^{N} I_n(H) f_n / \sum_{n=1}^{N} f_n, \qquad (1)$$

where f_n is the volume fraction of the nth constituent and $I_n(H)$ is the magnetization of this constituent in a field H. Because of hysteresis, the latter function is, in general, not single valued.

This paper analyzes in detail the magnetization of a mixture of particles of various sizes, composition, strain, and imperfections assumed constant. Wohlfarth[1,2] has recently treated the problem of shape variations using the same principle of superposition, but he arrived at a generalization that, as will be seen, has only limited application.

Ferromagnetic particles may be divided into three size catagories whose characteristic properties will be described. The first category consists of those particles that are so large that they contain many domains, and in which the initial stage of magnetization is accomplished by motion of domain walls that are relatively unimpeded by imperfections. The second category includes those particles that are so small that, in addition

[1] E. P. Wohlfarth, Research **7**, A1 (1954).
[2] E. P. Wohlfarth, *Soft Magnetic Materials for Telecommunications*, edited by C. E. Richards and A. C. Lynch (Pergamon Press, London, 1953), p. 13.

to containing but one domain, the thermal energy at the temperature of the experiment is sufficient to equilibrate the magnetization of an assembly in a time short compared with that of the experiment.[3] Although such particles are sometimes said to be paramagnetic,[4] the magnetization of individual particles possesses long range order. The particles, however act as paramagnetic particles of very large moment, and they will be designated "super-paramagnetic" particles. The third category contains particles that are single domain in all fields, and that accomplish their magnetization by coherent rotation of the magnetic moments against anisotropies present in the particles. This class of particle may not always exist, since the first two classes may overlap at some temperatures.

For the sake of simplicity, we shall consider a randomly oriented assembly of spherical particles with uniaxial magnetocrystalline anisotropy, characterized by a first order constant, K_1. Further, K_1 is assumed to be less than I_s^2, the square of the saturation magnetization of the material. The extension to other shapes and parameters is obvious and gives, in the main, the same qualitative results. The magnetization of a multidomain particle is

$$I=3H/4\pi \quad -4\pi I_s/3\leq H\leq 4\pi I_s/3 \qquad (2)$$
$$I=-I_s \quad H<-4\pi I_s/3$$
$$I=I_s \qquad H>4\pi Is/3$$

if we assume that the magnetization in the internal field (the sum of external and demagnetizing fields) is perfectly easy. There is, of course, a slight rounding near saturation caused by the magnetocrystalline anisotropy. The magnetization curve is sketched as curve *a* of Fig. 1. The magnetization of the "super-paramagnetic" particles is shown as curve *b* of Fig. 1. The initial slope is

$$I/H=4\pi I_s^2 r^3/9kT \qquad (3)$$

where r is the particle radius, as derived in Appendix I. The essential point (demonstrated in Appendix II) is that this magnetization can be extremely easy in the initial regions as compared to either the large particles, already treated, or the optimum single-domain particles. This behavior has been verified experimentally.[5] The magnetization of an aggregate of optimum single-domain particles has been treated by Stoner and Wohlfarth,[6] whose results are plotted in curve *c* of Fig. 1.

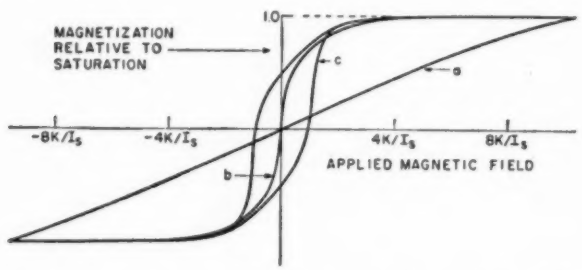

FIG. 1. Assumed magnetization curves in dilute samples of three sizes of ferromagnetic particles. *a*=large multidomain particles. *b*=small "super-paramagnetic" particles. *c*=optimum single-domain particles.

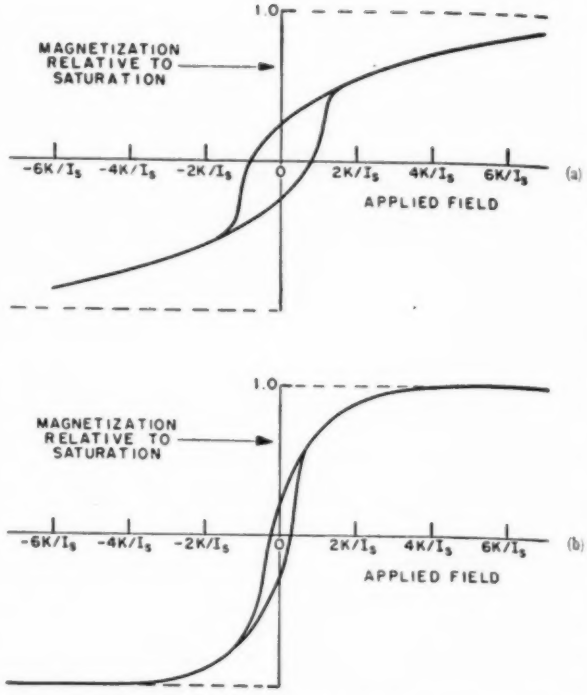

FIG. 2. (a) The hysteresis loop of a 50–50 mixture of optimum single-domain particles with multidomain particles. (b) The hysteresis loop of a 50–50 mixture of optimum single-domain particle with "super-paramagnetic" particles.

Figure 2 shows the results of combining equal amounts of optimum single-domain particles with large multidomain particles, and with small "super-paramagnetic" particles, respectively. Note that while the remanence is the same in the two cases, the coercive forces are very dissimilar. In Fig. 3(a), the coercive force is plotted as a function of relative volume fraction of the two types of low coercive materials. Figure 3(b) shows the experimental observations of Meiklejohn.[7] The points in curve I resulted from mixing iron or cobalt particles of optimum size, approximately 100 A, with very small iron particles whose size was not measured, but which by extrapolation is in the range from 20 A to 50 A. These very small particles exhibit the strongly temperature dependent coercive force that characterizes "super-paramagnetic" particles. Curve II shows the effect of mixing optimum size iron particles with oversize particles of about 1000 A.

The conclusion is, therefore, that the coercive force of a mixture may be primarily determined by either the

[3] L. Néel, Compt. rend. **228**, 664 (1949).
[4] E.g., Bate, Schofield, and Sucksmith, *Soft Magnetic Materials for Telecommunications*, edited by C. E. Richard and A. C. Lynch (Pergamon Press, London, 1953), p. 9.
[5] I. S. Jacobs and C. P. Bean (unpublished).
[6] E. C. Stoner and E. P. Wohlfarth, Trans. Roy Soc. (London) **A240**, 599 (1948).
[7] W. H. Meiklejohn, Revs. Modern Phys. **25**, 302 (1953).

large or the small coercive force constituent, depending upon their magnetization curves, and that Gerlach's observation,[8] recently restated,[1,2] that the small coercive force component always masks the large, has limited validity. It must be pointed out that this conclusion is valid only for relatively dilute solutions. In particular, packing will reduce the demagnetizing field that makes magnetization of multidomain particles so difficult. This in turn will make them more effective in diminishing the coercive force of a mixture.

I am indebted to I. S. Jacobs and W. H. Meiklejohn for helpful conversations.

APPENDIX I

To derive the magnetization curve of a random assembly of uniaxial "super-paramagnetic" particles, consider two limiting cases: first, when the applied field H is much smaller than the anisotropy field $2K_1/I_s$ and, secondly, when it is much larger. In the first case, each particle acts like a quantum moment of spin $\frac{1}{2}$ in that there are two stable positions parallel to the anisotropy axis. For a particle whose anisotropy axis makes an angle θ with the direction of the applied field, the component of the magnetization parallel to the field is given by

$$I = I_s \cos\theta \tanh(\mu H \cos\theta/kT). \tag{4}$$

In the limit of small magnetizations this becomes

$$I = I_s \mu H \cos^2\theta/kT. \tag{5}$$

Averaged over all orientations, and setting $\mu = 4\pi r^3 I_s/3$, this gives Eq. (3) of the paper. In the highest external fields, the anisotropy fields are overwhelmed by the external field, and the proper approximation is that of an infinite quantum number, for all orientations relative the crystal axes are equally probable. In no case, of course, does the magnetization curve rise above the demagnetization curve for pure rotation. It is worthy of note that Eq. (3) of the text also applies for the initial slope even if the applied field is much greater than the anisotropy field.

APPENDIX II

The expression derived by Néel[3] for the relaxation time τ_0 of an assembly of single-domain particles in zero field is

$$\begin{aligned} 1/\tau_0 &= f_0 \exp[-(\mu K_1/I_s kT)] \\ &= f_0 \exp[-(4\pi r^3 K_1/3kT)], \end{aligned} \tag{6}$$

where f_0 is a frequency factor on the order of 10^9 cycles/sec. If the demarcation line between optimum single-domain and "super-paramagnetic" particles is taken to be one hundred seconds, then particles for which

$$kT/r^3 K_1 > 0.2$$

are super-paramagnetic. Combining this inequality with the result obtained in Appendix I for the susceptibility, the initial slope of the magnetization curve for super-paramagnetic particles satisfies the inequality

$$I/H < 7I_s^2/K_1.$$

Although the super-paramagnetic susceptibility is limited to values less than about $7I_s^2/K_1$, significant magnetization can be achieved with fields as small as $0.14K_1/I_s$, which can be much less than the fields required to give significant magnetization to large particles or optimum single-domain particles.

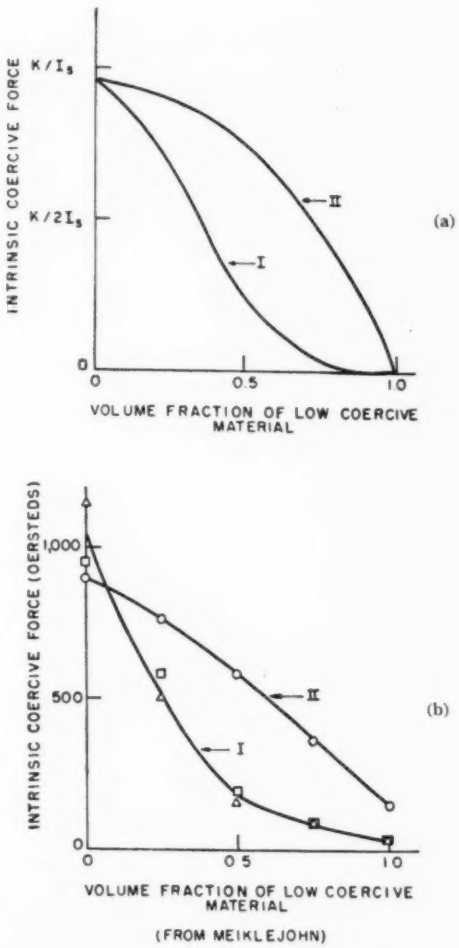

FIG. 3. (a) The coercive force derived from the curves of Fig. 1 of mixtures of optimum single-domain particles with I, "super-paramagnetic" particles, and II, multidomain particles. (b) Experimental results of Meiklejohn. Circles refer to mixtures of optimum single-domain particles and multidomain particles of iron. Triangles refer to mixtures of optimum single-domain cobalt and "super-paramagnetic" iron particles. Squares refer to optimum single-domain and "super-paramagnetic" iron particles.

[8] W. Gerlach, *Probleme der technischen Magnetisierungskurve*, edited by R. Becker (Verlag Julius Springer, Berlin, 1938), p. 141.

Letters to the Editor

Generation of Submillimeter Waves*

H. MOTZ AND K. B. MALLORY
Hansen Laboratories, Stanford University, Stanford, California
(Received July 27, 1955)

IN the course of investigation of undulator radiation during August–September, 1954,[1–3] submillimeter radiation was observed which could not be reconciled with the predictions of undulator theory. In an attempt to determine the source of this radiation, it was found that submillimeter radiation was produced when a pulsed, bunched high-energy electron beam was passed through a simple rectangular wave guide with no associated periodic structure.

The beam was supplied by a 2-Mev linear accelerator operating at 10.6 cm. It was directed along the axis of a 16-inch section of standard ½ in.×¼ in. o.d. brass wave guide. The resulting radiation was then directed through a 90° bend and through an additional wave guide of approximately 6×2.5 millimeters inside dimensions. The radiation was analyzed by an echelette grating spectrometer followed by a home-made crystal detector. A series of lines were observed at grating angles corresponding to wavelengths ranging from 8 mm to 0.16 mm. The crystal output at some wavelengths was as large as one-quarter millivolt, which was many times larger than the basic noise level of the crystal. The lines were quite sharp, with a half-power width of about 1%. They corresponded roughly to the 12th to 65th harmonics of the operating wavelength of the accelerator, but not all the lines could be identified with such harmonics.

The mechanism responsible for the generation of the radiation is not understood as yet. The wave guide was essentially a nonresonant structure, although small reflections from the ends probably existed. It is therefore unlikely that the beam was exciting resonances in the wave guide. It is possible that in some manner the phase velocity in the wave guide was retarded by a normally disregarded surface effect. In this case the observed spectrum might be caused by Čerenkov radiation. Several hypotheses have been advanced but these will require further experimental test. The experiments were discontinued owing to temporary lack of facilities but preparations for continuation of this work are underway.

* The research reported in this document was supported jointly by the U. S. Army Signal Corps, the U. S. Air Force, and the U. S. Navy (Office of Naval Research).
Present address: Engineering Laboratory, Oxford University, Oxford, England.
[1] H. Motz, J. Appl. Phys. **22**, 527–535 (1951).
[2] Motz, Thon, and Whitehurst, J. Appl. Phys. **24**, 826–833 (1953).
[3] H. Motz, "Cerenkov and undulator radiation," U.R.S.I., Michigan Symposium on Electromagnetic Wave Theory. Institute Radio Engineers Transactions, Institute Radio Engineers Professional Group on Antennas and Propagation, September, 1955.

Observations of Cathode Arc Tracks

H. S. DUNKERLEY AND D. L. SCHAEFER
General Electric Company, Schenectady, New York
(Received April 1, 1955)

IN a recent study of the effects of pulsed emission on cold cathode surfaces some interesting arc tracks were obtained which may provide some insight into the nature of the cathode spot. The tracks were obtained by using parallel anode and cathode surfaces between which the arc was initiated in the presence of a transverse magnetic field of 150 gauss. The resultant force on the arc drove it along the length of the cathode surface, resulting in well-defined tracks of the arc path. The series of experiments was carried out in air at atmospheric pressure.

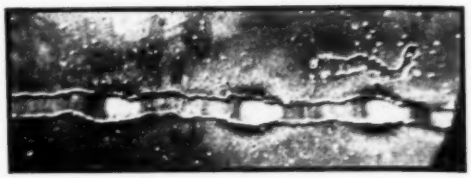

FIG. 1. 30-amp pulsed arc on tungsten.

Figure 1 illustrates the behavior of a 30-amp, 20 μsec wide pulse superimposed at 30 pps on a one-amp holding arc on a cathode of oxidized tungsten. The arc track shows evidence of broadening during the pulse and also shows that the arc "burrowed" into the clean metal beneath the oxide.

Calculations of the current density were made by assuming circular symmetry in the cathode spot, the diameter of which was taken as the measured width of the arc track. This type of calculation probably gives the lower limit of the current density. The current density for the one-amp portion of the arc was found to be 2000 amp per square centimeter.[1] A value of 45 000 amp per square centimeter was found for the pulsed density. The low value of the current density for the one-amp portion of the track can be explained by the reduced rate of propagation during the nonpulsed portion of the arc (0.03 meters/sec as compared to 2 meters/sec during the pulse). The current density for the pulsed region agrees well with the values given for tungsten cathodes. It should be noted that the requirement of high current during the 20-μsec pulse did not cause subdivision of the spot.

Figure 2 shows the effect on the arc track when the cathode spot is momentarily fixed while the plasma column continues to move under the influence of the transverse magnetic field.[2] The track shown in this photograph was made by a one-amp dc arc traveling along a surface of lightly oxidized tantalum. The track gives the appearance of a discontinuous cathode spot although the arc current was continuous. Figure 3 is an illustration of the process thought to be involved in producing this type of track.

As shown in Fig. 3(a), the arc has been formed and has anchored at point x due to the surface condition of the cathode. While the cathode spot is anchored, the plasma continues to move along the tube due to the transverse magnetic field [Fig. 3(b)]. The plasma is distorted [Fig. 3(c)] as positive ions from the plasma bombard the cathode surface preparing it for the formation of a cathode spot. The cathode spot now transfers to the "preconditioned" area at y and extinguishes at x [Fig. 3(d)]. Discontinuous tracks of this type are observed when the surface of the cathode is very lightly oxidized or oxidized nonuniformly.

It is hoped that a continued study of pulsed emission from cold cathodes can be made using very large current pulses.

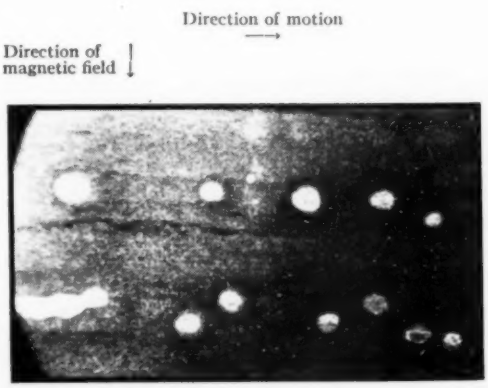

FIG. 2. Intermittent cathode spots formed by continuous-current arc.

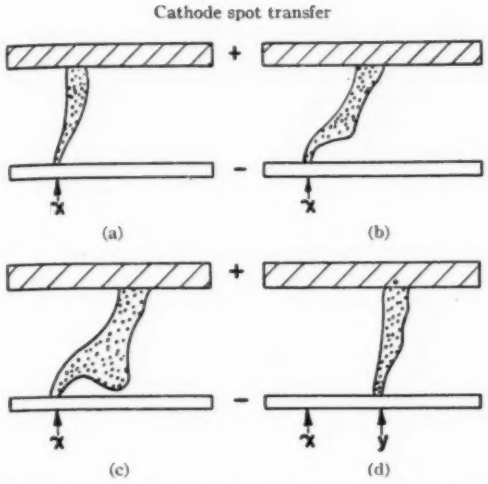

FIG. 3. Graphic illustration of phenomenon shown in Fig. 2.

We would like to express our gratitude to Dr. J. D. Cobine for several stimulating conversations and for encouragement during this work.

[1] This value is low relative to previously published data; see Cobine and Gallagher, Phys. Rev. **74**, 1524 (1948).
[2] Similar discontinuities in anode tracks have been reported by L. P. Winsor and T. H. Lee at the Gaseous Conduction Conference of the American Physical Society, New York University, October, 1954.

The Harmodotron—a Beam Harmonic, Higher-Order Mode Device for Producing Millimeter and Submillimeter Waves*

P. D. COLEMAN AND M. D. SIRKIS†
Ultramicrowave Group, Electrical Engineering Research Laboratory, University of Illinois, Urbana, Illinois
(Received July 23, 1955)

A PROPOSED method of generating high power, at millimeter and submillimeter wavelengths by exciting a single higher order TM_{omn} mode in a cylindrical cavity[1] has been successfully demonstrated in the 7–11 millimeter range. These modes were excited by a bunched 1.0–1.5 Mev electron beam obtained from a single cavity 2775 mc/sec microwave accelerator. This bunched beam contains current frequency components at high harmonics of the 2775 mc/sec fundamental frequency. The 10th through the 14th harmonic current components of the bunched beam were singly selected by means of a tunable cylindrical cavity which could allow a particular TM_{omn} mode to resonate with a particular beam harmonic frequency. Experimental power measurements using the TM_{013} mode, resonant at 8.31 millimeters, gave one watt peak power using a five milliampere pulsed beam.

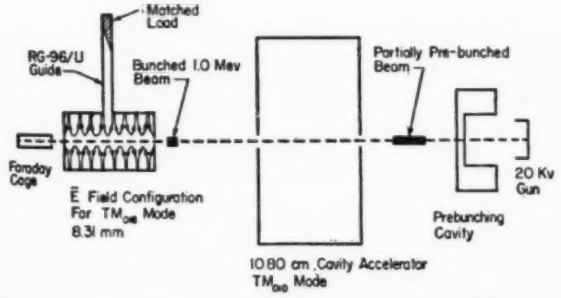

FIG. 1. Schematic drawing of higher-order mode harmonic frequency multiplier showing excitation of TM_{013} mode. Cavities drawn to same relative scale.

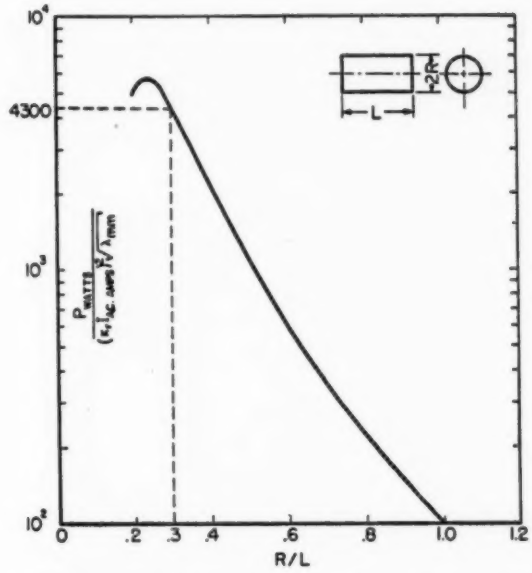

FIG. 2. Power delivered to a matched load for a silver TM_{013} cavity driven by an electron beam with $\beta=0.95$.

Figure 1 shows a schematic drawing of the experimental apparatus. Electrons from a 20-kev gun are first passed through a prebunching cavity where they are given a desired velocity distribution. They are then allowed to drift and finally enter the cavity accelerator.[2] Since the inherent bunching action of the accelerator is very large, prebunching is not necessary to obtain current harmonics up to the 14th. In fact, the power measurement of one watt at 8.31 millimeters was obtained without prebunching

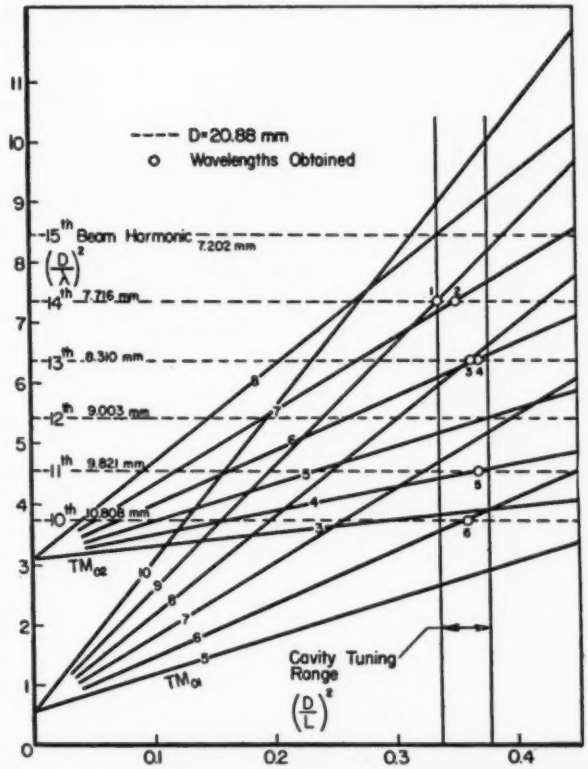

FIG. 3. Mode chart for TM_{01n} and TM_{02n} modes illustrating wavelengths excited.

the beam. The bunched 1-Mev beam passes through the tunable cylindrical cavity and excites, for example, the TM_{018} mode. Energy is coupled out to an RG-96/U guide through an iris to a matched load. The pulsed beam current is measured by means of a Faraday cage.

The accelerator produces a traveling current wave of the form

$$i(z,t)=\sum_{s=-\infty}^{s=\infty} J_s e^{is\omega_0(t-z/v)}, \tag{1}$$

with $0.94\leq v/c\leq 0.97$; $\omega_0=1.74\times10^{10}$, and a beam radius $R_0=0.5$ millimeter. Theoretically the beam should have harmonics of appreciable magnitude up to $s=1250$, which means that $J_s\simeq 2J_{Av}$ for most cases of interest.

The need for a high voltage beam[3] such as that given by Eq. (1) is evident when the beam coupling coefficient $k\pm$ (+ for forward wave, − for backward wave) is computed

$$k\pm=\tfrac{1}{2}\frac{\sin\left[\frac{n\pi}{2}\left(\frac{V_{omn}}{v}\mp1\right)\right]}{\left[\frac{n\pi}{2}\left(\frac{V_{omn}}{v}\mp1\right)\right]}, \tag{2}$$

where $V_{omn}>c$ is the phase velocity for the TM_{omn} radiation. For k_+ to be near $\frac{1}{2}$, the beam velocity v must be close to c.

A universal power curve for a TM_{018} cavity operating into a matched load is shown in Fig. 2. The coefficient k_r is the radial coupling coefficient which accounts for the finite beam radius of the beam. In our experiments $k_r\simeq1$. The power available from a cavity operating, for example, at 8.31 millimeters wavelength in the TM_{018} mode with $R/L=0.3$ is seen to be

$$P=1.2\times10^4 I_{AC\,amp}{}^2=(1.2\times10^4)(10^{-2})^2=1.2 \text{ watts}. \tag{3}$$

At 1.0 millimeter wavelength, the power would be 0.4 watt using the same electron beam.

In Fig. 3, the particular cavity dimensions and beam current harmonic wavelengths have been superimposed on a TM_{omn} mode chart. The circled points indicate the particular modes and wavelengths that were identified and measured as the cavity was tuned over a restricted range. Coupling to various modes varies somewhat as the length L is changed since the iris coupling hole does not remain in the center of the cavity.

The authors wish to thank Dr. Paul J. Ovrebo of WADC for his confidence in and encouragement of the above work. Mr. I. Kaufman contributed to the design of the electron accelerator.

* Work supported by WADC-WCLRO on Contract AF33(616)-2449.
† This letter is based in part on a doctoral thesis by M. D. Sirkis, to be submitted to the Department of Physics, University of Illinois, in partial fulfillment of the requirements for a Ph.D. degree.
[1] Quarterly Report No. 4, on Contract AF19(604)-524, September 15, 1953, Electrical Engineering Research Laboratory, University of Illinois.
[2] P. D. Coleman, "Electron acceleration and bunching with a single microwave cavity to energies of 1–1.5 Mev," AF18(600)-23, Engineering Report No. 2, Electrical Engineering Research Laboratory, University of Illinois.
[3] Quarterly Reports Nos. 2 and 4, Contract AF33(616)-2449, Electrical Engineering Research Laboratory, University of Illinois.

Breakup of Hollow Electron Beams

H. F. Webster
General Electric Research Laboratory, Schenectady, New York
(Received July 20, 1955)

In the course of measurements of the profile of a hollow electron beam produced by a hollow cathode, a surprising flow pattern has been found in which the beam breaks up into a discrete number of vortex-like current bundles. This investigation was started when it was found that a thermionic hollow cathode operating in a high vacuum produces a thin hollow beam of electrons when it is immersed in a magnetic field.

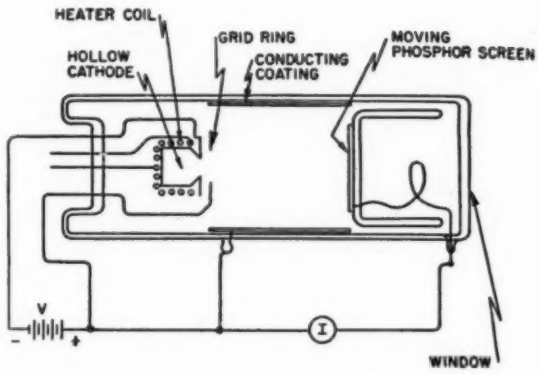

Fig. 1. Hollow beam tube and circuit.

Figure 1 is a sketch of the apparatus and circuit used for some of these measurements. The hollow cathode and grid ring project an electron beam down the axis of the tube to the phosphor screen. This screen is mounted on a separate glass cylinder which can be moved by tipping the tube. The entire tube is operated inside a solenoid to provide the confining axial magnetic field. Figures 2 and 3 are pictures of the phosphor screen at different positions along the beam. Figure 2 shows the beam 1 cm from the cathode where the beam is thin and smooth. Figure 3 was taken with the screen 8.7 cm from the cathode. There the beam has broken into discrete current bundles each of which is connected to its neighbor by thin spiral arms. Other observations at intermediate distances

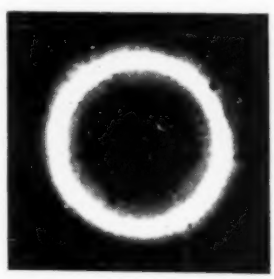

Fig. 2. Screen 1 cm from cathode. $v=15.6$ volts. $I=0.2$ ma. $B=340$ gauss.

reveal a progressive increase in size of the vortex-like disturbance as the beam moves away from the cathode. The beam voltages, beam currents, and magnetic field strengths are indicated beneath each picture.

Another tube which has a hollow beam produced by a conventional cathode was tested and this also revealed the vortex pattern at the collector. Thus this strange pattern seems not to be a property of the hollow cathode but to be a property of the hollow beam.

A considerable variety of beam oscillations have been observed over a range of frequencies. These range from audio-frequencies to indirect evidence for oscillations in the microwave range.

Fig. 3. Screen 8.7 cm from cathode. $v=15.6$ volts. $I=0.2$ ma. $B=340$ gauss.

If the beam voltage v is replaced by a pulse voltage which is on for 1 μsec and off for 300 μsec, the vortex pattern is still observed. Thus positive ions are probably not required for this effect.

As yet no complete explanation for this phenomenon has been found. A more complete description of this effect will be given in a later report.

Mass Absorption Coefficient of Carbon for CuKα Radiation*

D. R. CHIPMAN
Massachusetts Institute of Technology, Cambridge, Massachusetts
(Received August 1, 1955)

THE mass absorption coefficient of carbon for CuKα radiation has been measured and found to be in considerable disagreement with tabulated values. It is believed that the discrepancy arises from an improper consideration of the problem of small angle scattering. The measured absorption coefficient for a material which gives an appreciable amount of small angle scattering will depend on how much of this scattering is counted as part of the transmitted beam.[1] The total power in small angle scattering produced by a given material of specified thickness depends on the inhomogeneity in the distribution of scattering power within the sample. To a first approximation however, the true mass absorption coefficient depends only on the kind of atoms and not on their arrangement. Since small angle scattering robs the transmitted beam of additional power, absorption measurements which do not include the small angle scattering as part of the transmitted intensity will always give too high a value for the coefficient. This measured coefficient will decrease as an increasing percentage of the small angle scattering is counted as part of the transmitted beam.

The usual absorber to use for measuring the absorption coefficient of carbon is high purity graphite. It is quite possible for this material to give considerable small angle scattering. Many materials such as paraffin may be found, however, whose absorptions are largely due to carbon, and which will not give small angle scattering. The absorption coefficients of paraffin, polystyrene, and graphite were measured using a double crystal spectrometer. Copper radiation from the x-ray tube was limited by a 0.025 cm slit, diffracted by two calcite crystals set for first order in the antiparallel position, and passed through the absorber. A second slit, S_2, 38 cm from the absorber and directly in front of the Geiger counter, was adjustable in width. The equipment gave a fine parallel beam of copper Kα_1 the tube being run below the excitation voltage for half wavelength. With decreasing widths of slit S_2, less of the small angle scattering is counted as part of the transmitted intensity. At the maximum counting rate and minimum slit width used, the apparatus was checked for linearity and reproducibility by measuring the absorption coefficient of aluminum. At various settings for S_2 ranging from 0.005 to 0.375 cm, the absorption coefficients were measured for the aforementioned samples, using at least two thicknesses of each material. The mass absorption coefficients of carbon computed from them are plotted in Fig. 1 as a function of the angular width of S_2 as seen from the absorber. The graphite used was high purity artificial graphite of density 1.70. The mass absorption coefficient of carbon was computed from the linear absorption coefficients of paraffin and polystyrene by assuming paraffin to be CH_2 and polystyrene to be CH, and by using Compton and Allison's value[2] of 0.48 for the mass absorption coefficient of hydrogen.

Figure 1 shows clearly the existence of small angle scattering from the graphite, and its relative unimportance in paraffin and polystyrene. It also shows how previous measurements[2,3] made with instruments of high resolving power could be considerably in error on the high side. Andrew's value of 4.87 is in good agreement with our highest value showing that he must have had, as in fact he did, equipment of quite good resolving power. The value recommended for the mass absorption coefficient of carbon for CuKα is 4.15. This is quite different from the commonly used values; 4.52 Compton and Allison,[2] and 5.50.[4]

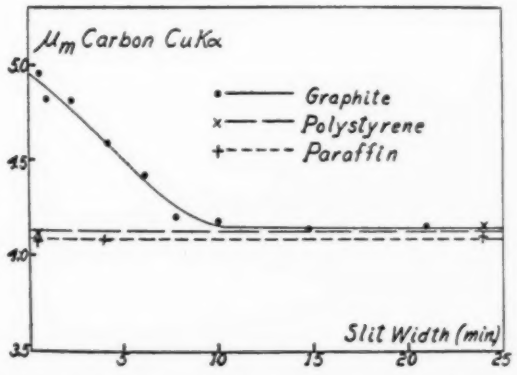

FIG. 1. Mass absorption coefficient of carbon for CuKα as a function of the counter slit width expressed in minutes. The polystyrene and paraffin measurements are corrected for the effect of hydrogen.

* Research sponsored by the Office of Naval Research.
[1] B. E. Warren, J. Appl. Phys. **20**, 96 (1949).
[2] Compton and Allison, *X-Ray in Theory and Experiment* (D. Van Nostrand Company, Inc., New York, 1955).
[3] C. L. Andrews, Phys. Rev. **54**, 994 (1938).
[4] "Internationale tabellen zur bestimmung von kristallstrukturen," Borntrager, Berlin (1935). Vol. II.

Effects of Ambient Atmosphere on the Stability of Barium Titanate

J. R. ANDERSON, G. W. BRADY, W. J. MERZ, AND J. P. REMEIKA
Bell Telephone Laboratories, Inc., Murray Hill, New Jersey
(Received July 23, 1955)

AS a part of a large number of observations we have made on the behavior of barium titanate when switched by an electric field, we have investigated the effect of ambient atmosphere on the 60-cycle hysteresis loop characteristics of this material. That there is a marked effect may be seen in Figs. 1 and 2. These experiments were made on a single crystal mounted with 4×4 mil platinum electrodes. The high slope of the top and bottom portions of the loops is due to the capacitance of the leads into the vacuum chamber. Figure 1 shows the loop of the crystal in (a) dry air, (b) after cycling with a 60 cps sine wave for 15 minutes at 10^{-6} mm Hg and, (c) after readmitting pure O_2 and cycling with a 60 cps sine wave for 45 minutes. As can be seen in Fig. 1(b) there is a definite loss of squareness when the crystal is switched *in vacuo*, although there is no significant decrease in polarization. When pure O_2 is readmitted and the 60 cps sine wave applied the loop recovers and returns essentially to its original form. None of these

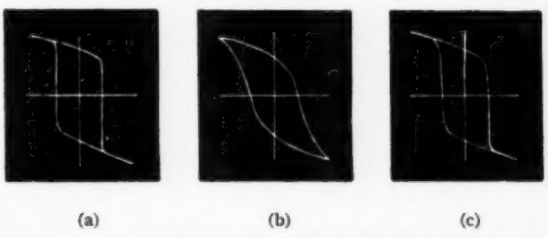

FIG. 1. 60-cps hysteresis loops of $BaTiO_3$ (a) dry air; (b) 10^{-6} mm Hg; (c) in pure O_2.

(a) (b) (c)

FIG. 2. 60-cps hysteresis loops of $BaTiO_3$ (a) dry air; (b) 350 mm N_2; (c) 350 mm O_2.

effects is immediate; it is necessary to operate the crystal in the appropriate atmosphere for some time to produce them. The specific times mentioned are not significant and there are variations from crystal to crystal.

To make sure that these effects were not due to heating or to some pressure effect we evacuated a crystal to 10^{-6} mm and admitted 350 mm of Air Reduction Research Grade N_2 and cycled at 60 cps for 15 minutes. Again there was a deterioration of the loop. The polarization decreased by about 10% and as can be seen in Fig. 2(b) the lower part of the hysteresis loop is distorted while the upper part is relatively square indicating a preferred polarization direction in the crystal. In other crystals we obtained the same deterioration as that shown in Fig. 1(b), i.e., a symmetrical distortion of the loop, in N_2 also. When the N_2 was pumped out and replaced with an equal pressure of O_2 (made by dissociating $KMnO_4$ and passing the gas through a dry ice trap to eliminate water vapor) and the crystal cycled for 15 minutes, the loop squared up again as is shown in Fig. 2(c), and the polarization returned to its original value. We have done the same experiment in pure He with the same results as in N_2. H_2 also produces marked effects as does H_2O vapor but these can be easily associated with chemical reaction of the gas and vapor with the crystal, leading to reduction of Ti^{+4} to Ti^{+3}. We feel that the effect of inert gases and O_2 is a more complex phenomenon, associated with the surface states and surface properties of $BaTiO_3$. We expect to present soon a comprehensive paper on the stability characteristics of $BaTiO_3$, in which a more complete interpretation of these interesting results, supported by other evidence, will be given.

Shot Noise in *p-n-p* Transistors*

G. H. HANSON
Department of Electrical Engineering, University of Minnesota, Minneapolis, Minnesota
(Received May 19, 1955)

THE shot noise of a *p-n-p* junction transistor operated in grounded base connection may be represented by the equivalent circuit shown in Fig. 1, in which there is a noise voltage e_s in series with the emitter junction and a noise current generator i_p in parallel with the collector junction. If a large resistance

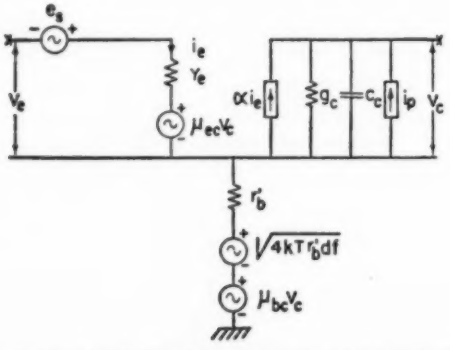

FIG. 1. Equivalent circuit for noise of a *p-n-p* junction transistor operated in grounded base connection.

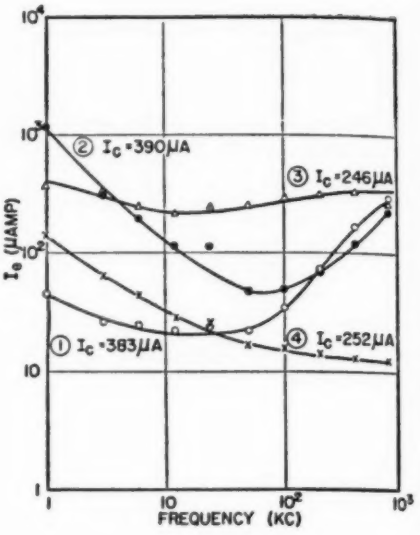

FIG. 2. Noise spectra of *p-n-p* transistors. 1—Raytheon CK727; 2—RCA TA-153; 3—RCA TA-153 with collector and emitter interchanged; 4—Philco surface barrier transistor.

(50 000 ohms) is placed in the emitter circuit, a simple calculation shows that practically all the noise comes from the current generator i_p. This method is used here for studying i_p.

Measurements of equivalent saturated diode current I_{eq} of i_p (defined by the relation $\langle i_p^2\rangle_{\rm av}=2eI_{eq}df$) have been made under these conditions on several transistors.† The measuring apparatus consisted of a preamplifier, 10 amplifier channels tuned at frequencies of 1 kc, 3 kc, 6 kc, 12 kc, 25 kc, 100 kc, 200 kc, 400 kc, and 800 kc and detecting circuits. Each measurement involved the comparison of the rectified output due to noise from the transistor with that due to noise from the transistor plus a saturated diode in parallel with the output of the transistor.

Some results are shown in Fig. 2 for collector voltages of −1 volt. Curve 1 is for a Raytheon CK727 which is a low-noise *p-n-p* junction transistor designed for use at audio-frequencies. The noise decreases from 1 kc to 50 kc because of the usual $1/f$ noise but thereafter increases with frequency. Similar transistors manufactured by the Telefunken Company of Germany have noise spectra of the same shape as Curve 1. Curves 2 and 3 are obtained from an experimental RCA transistor Type TA 153 designed such that the collector and emitter may be interchanged. Curve 2, obtained with normal biases, is similar to Curve 1. When the transistor is operated "backwards," that is with emitter and collector interchanged, the low-frequency current amplification factor α_0 is of the order of 0.6. The noise is then much greater and is almost independent of frequency. Curve 4 shows the noise spectrum of a Philco surface barrier transistor. The noise is predominantly of the $1/f$ type and there is no indication of an increase with frequency. The values of α_0 for the transistors corresponding to curves 1, 2, and 4 are about 0.974, 0.977, and 0.960, respectively.

Measurements on many other units from the same type and from different types gave similar results. The low-frequency $1/f$ noise component shows large differences between units, and Fig. 2 is not typical in that respect. Figure 2 is typical, however, in that the high-frequency shot noise of all units can be represented by formula (1), if the particular values of α_0 and of the α cut-off frequency of the unit are used.

Recently, van der Ziel[1] has calculated e_s, i_p, and the correlation between e_s and i_p.‡ According to this theory,

$$\langle i_p^2\rangle_{\rm av}=2eI_{eq}df=2eI_c df(1-|\alpha|^2/\alpha_0) \qquad (1)$$

where α is the hf current amplification factor and I_c the collector current. Thus at high frequencies ($\alpha\simeq 0$)I_{eq} should be equal to I_c, while at low frequencies ($\alpha\simeq\alpha_0$), the noise should be reduced by the factor $(1-\alpha_0)$. Since the Raytheon, Telefunken, and RCA transistors have cut-off frequencies of the order of 400 kc, the experimental dependence of I_{eq} upon frequency agrees with theory.

There should be no increase in noise for the surface barrier transistors since they have cut-off frequencies of the order of 30 mc, again in agreement with experiment. When the RCA transistor is operated backwards, the cut-off frequency is about 100 kc. Thus I_{eq} due to shot noise should equal I_e above about 100 kc and should decrease to about 0.4 of this value at lower frequencies. The addition of $1/f$ noise at low frequencies, however, should result in a total noise about equal to that measured.

The present measurements do not extend to a high enough frequency to determine whether $\langle i_p^2\rangle_{\rm av}$ reaches and remains at the value $2eI_e df$, nor to find any increase in noise in the surface barrier transistors. The measurements are now being extended to much higher frequencies.

All measurements were made at a collector voltage $V_c=-1$ volt. The cut-off frequency of the transistors increases sharply if V_c is made more negative. Therefore the increase in I_{eq} should shift to higher frequencies if V_c is made more negative. Measurements are under way to test this.

The above experiments give information about the noise current generator i_p. Further experiments are being planned to obtain information about the noise emf e_s and about the correlation between e_s and i_p and to compare the results with theory.

The author is grateful to Dr. A. van der Ziel for suggesting the experiment and for much helpful advice, and to the Graduate School of the University of Minnesota for permission to publish these results.

* Supported by the U. S. Signal Corps.
† These transistors were obtained through the courtesy of Dr. W. E. Leverton, Raytheon Manufacturing Company; Dr. H. Rothe, Telefunken A.G., Ulm Germany; Dr. E. W. Mueller, RCA Laboratories; and Dr. W. H. Forster, Philco Corporation.
‡ A. van der Ziel, Proc. Inst. Radio Engrs. (to be published).
‡ If the noise is represented by two current generators i_{p1} and i_{p2} across emitter and collector junctions, respectively, then i_{p1} and i_{p2} are found to be partially correlated and

$$i_{p2}^2)_{\rm Av}=2eI_e df$$

at all frequencies. If we transform to the equivalent circuit of Fig. 1, however, we find:

$$e_s=i_{p1}/Y_s;\quad i_p=i_{p2}+\alpha i_{p1},$$

from which the formula (1) follows.

Erratum: Elastic Constants of Germanium between 1.7° and 80°K

[J. Appl. Phys. 26, 863 (1955)]
M. E. FINE
Bell Telephone Laboratories, Murray Hill, New Jersey

AN error was made in computing the data for Fig. 4; the correct figure is hereby shown. One of the authors' names in reference 7 was also incorrect; the correct name is R. W. Hill.

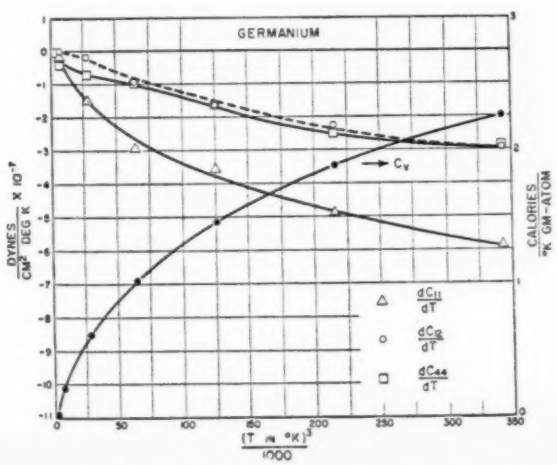

FIG. 4. dc_{ij}/dT's and C_v plotted as functions of T^3.

Books Reviewed

Chemistry of the Solid State. W. E. GARNER, Editor. Pp. 417+viii. Academic Press, Inc., New York, 1955. Price $8.80.

The subject matter of this book lies within the spheres of both physics and chemistry. The book is intended to present the experimental facts and theories of the solid state in a form useful for physical chemists. The book consists of fifteen chapters, each by a different chemist or physicist; nearly all the contributors are members or recent members of the staff of the University of Bristol. Lattice defects, semiconduction, photoconduction, surface properties, crystal growth, solid reactions, the photographic process, catalysis, and similar subjects are discussed from the point of view of the physical chemist.

Tables of the Cumulative Binomial Probability Distribution. Harvard Computation Laboratory Staff. Pp. 503+lxi. Harvard University Press, Cambridge, Massachusetts, 1955. Price: $8.00.

This volume extends by more than six times the previously available range of tabulation of the function which represents the probability that at least r successes will occur in n trials with a probability p of success in each trial. A sixty-page introduction by Frederick Mosteller is designed to make the tables useful in statistical practice and illustrates seventeen applications of the function.

Linear Feedback Analysis. J. G. THOMASON. Pp. 355+x, Figs. McGraw-Hill Book Company, Inc., New York, 1955. Price $8.50.

This book is intended as a guide to the design of servomechanisms and electronic circuitry employing feedback. The first part of the book introduces and applies circuit analysis from the point of view of the Laplace transform. The next part is a general discussion of feedback based on the work of Bode and Nyquist. Examples of applications are then discussed; some of the examples are single- and multi-stage dc amplifiers, pulse amplifiers, integrators, differentiators, and stabilized power supplies.

Production of Heavy Water. G. M. MURPHY, H. C. UREY, AND I. KIRSHENBAUM, Editors. Pp. 394+xvii, Figs. McGraw-Hill Book Company, Inc., New York, 1955. Price $5.25.

This volume in the National Nuclear Energy Series surveys the scientific and engineering problems and achievements in the isolation of deuterium. The first part of the book is devoted to the performance of the wartime heavy water plants at Trail, British Columbia (catalytic exchange) and at Morgantown, West Virginia (water distillation), and to pilot-plant studies of the hydrogen-distillation process. The second part presents the results of laboratory studies of the various possible ways of separating deuterium.

Laplace Transforms for Electrical Engineers. B. J. STARKEY. Pp. 279. Philosophical Library, New York, 1955. Price $10.00.

Laplace transforms are introduced in this book through the language of the electrical engineer. Although there are no problems for the student, the book is intended as a textbook or as a supplement to more rigorously mathematical texts.

Fifth Symposium on Combustion. B. LEWIS, H. C. HOTTEL, AND A. J. NERAD, EDITORS. Pp. 802+xxiv. Reinhold Publishing Corporation, New York, 1955. Price $15.00.

This volume presents 101 papers presented at the Fifth International Combustion Symposium held at the University of Pittsburgh, August 30 to September 3, 1954. The papers are grouped under the following headings: review of problems on combustion in engines and kinetics of combustion processes, combustion of fuel droplets, propellant burning, combustion of solids, diffusion flames and carbon formation, combustion in engines, special techniques, kinetics of combustion reactions, flame spectra and dissociation energies, panel discussions on heterogeneous burning, and theory of the kinetics of combustion reactions.

Harmonic Analysis and the Theory of Probability. S. BOCHNER. Pp. 176+viii. University of California Press, Berkeley, 1955. Price $4.50.

This is a tract on some topics in Fourier analysis of finitely and infinitely many variables and on some topics in the theory of probability. The book emphasizes the connections and interchange of stimuli between probability and analysis.

Principles of Nuclear Reactor Engineering. SAMUEL GLASSTONE. Pp. 861+ix. D. Van Nostrand Company, Inc., New York, 1955. Price $7.95.

The aim of this book is to present the physics, chemistry, and engineering principles involved in the design, construction, and operation of nuclear reactors. Reactor engineering calls for the cooperation of many kinds of scientists and engineers in solving a wide variety of problems. This book is intended to aid in such cooperation. About one-fourth of the book is devoted to nuclear physics and the theory of reactors. Another fourth is concerned with instrumentation, control and the processing of reactor fuel. The rest of the book considers materials technology, radiation protection and shielding, thermal aspects of reactor systems, design theory, and descriptions of existing reactors.

Introductory Nuclear Physics. DAVID HALLIDAY. Pp. 493+ix. John Wiley and Sons, Inc., New York, 1955. Second edition. Price $7.50.

The revised edition, like the original edition, is intended as a textbook in nuclear physics for undergraduates who already have studied some atomic physics. A chapter on wave mechanics and derivations of many of the formulas have been added, and the author has sought to bring the first edition up to date by revisions throughout the text. Such topics as fundamental particle physics, cosmic rays, and molecular beams are treated in addition to the topics of "classical" nuclear physics.

Nuclear and Radiochemistry. G. FRIEDLANDER AND J. W. KENNEDY. Pp. 468+ix. John Wiley and Sons, Inc., New York, 1955. Price: $7.50.

This book is based on the authors' *Introduction to Radiochemistry* and is essentially an expanded and revised second edition of their 1949 book. The heart of the new book is the systematic discussion of radioactivity, nuclear reactions, radiation detection, and the applications of tracers to chemical research and chemical engineering. The final chapters present recent information on nuclear reactors, energy production in stars, cosmic rays, radio-dating, and the origin of the elements. The book is intended as a textbook for seniors or graduate students and includes about 150 problems and extensive reference lists.

Books Received

Dictionary of Mechanical Engineering Terms. J. G. HORNER. Pp. 417+iv. Philosophical Library, New York, 1955. Seventh edition. Price $6.50.

Electro-Magnetic Machines. R. LANGLOIS-BERTHELOT. Pp. 535+xvi. Philosophical Library, New York, 1955. Price $15.00.

Magnetic Materials in the Electrical Industry. P. R. BARDELL. Pp. 288+xiv. Philosophical Library, New York, 1955. Price $10.00.

The Ordnance Department: Planning Munitions for War. GREEN, THOMSON, and ROOTS. Pp. 542+xviii, photographs, tables and charts. Office of the Chief of Military History, Department of the Army, Washington, D. C., 1955. Price $4.25.

Announcements

Nuclear Engineering and Science Congress

The major U. S. organizations concerned with nuclear science, engineering, industry, and government are sponsoring a **Nuclear Engineering and Science Congress.** December 12–16, Public Auditorium, Cleveland, Ohio. Further information may be obtained from the Engineers Joint Council, 29 West 39th Street, New York 18, New York.

International Colloquium on Spectroscopy

The **Sixth International Colloquium on Spectroscopy** will be held in Amsterdam, Netherlands, May 14–19, 1956. The colloquium will cover emission and absorption spectroscopy and emphasize analytical applications. Persons wishing to attend or contribute should correspond with the Secrétary, Colloquium Spectroscopicum Internationale, Laboratorium voor Analytische Chemie, 125 Nieuwe Achtergracht, Amsterdam-C4.

Soviet Physics—JETP

The American Institute of Physics, 57 East 55th Street, New York, will shortly commence publication of *Soviet Physics—JETP*, a periodical translation of research reports appearing in the Russian language *Journal of Experimental and Theoretical Physics*. The National Science Foundation of the Federal Government has granted funds to help finance the first year's operations. The editor will be Professor Robert T. Beyer of the Department of Physics, Brown University, where the editorial office will be located. The American Institute of Physics is the publisher of essentially all of the American physics journals.

Publication of *Soviet Physics—JETP* is being undertaken because few physicists in the western world are able to read Russian and yet it is important for them to know the results of researches everywhere as a basis for their own researches. General dissemination of the results of research is essential to the vigorous advancement of science. It will appear every two months, the first issue being scheduled for publication in October. The subscription price in the U. S. and Canada is $30.00 per year (six issues).

Proceedings of the Electron Microscope Society of America

The annual meeting of the Electron Microscope Society of America was held at Pennsylvania State University, University Park, Pennsylvania, on October 27, 28, and 29, 1955. Titles and abstracts of the papers are presented below.

PROGRAM

THURSDAY MORNING

Welcome: DEAN E. F. OSBORN

Introductory Remarks: T. F. ANDERSON

Session A. Contributed Industrial Papers

1. Fine Structure of Submicron Alpha Iron Particles. JOHN H. L. WATSON, *Edsel B. Ford Institute for Medical Research, Henry Ford Hospital, Detroit 2, Michigan,* AND MICHAEL W. FREEMAN, *M. W. Freeman Company, Detroit 11, Michigan.*—Well-resolved micrographs of a series of in-process, submicron, alpha iron materials, produced electrolytically from a continuous, controlled process are shown to illustrate their fine structures. According to manufacturing conditions, the samples occur as (1) particulates, which might find their best application in medicine, (2) large, well-formed dendrites, useful wherever dendrite strength is important, (3) shorter, fragile dendrites, (4) serrated rods, or (5) needles, important for their magnetic properties. Representative dimensions are given for the various measurable units. The dendrites are 3-dimensional with branches forming a "V" on one side only of the main stem, and the central and side stems are arrangements of single crystals. The serrated rods and needles tend to become monolithic. A laminar structure is seen in some of the dendrites and particulates and also in hexagonal platelets which occur in the background of the micrographs. X-ray diffraction detects alpha iron and certain forms of Fe_2O_3.

2. A Technique for a Profile Study of Evaporated Metallic Films. H. U. RHOADS * AND A. H. WEBER, *Department of Physics, St. Louis University, St. Louis, Missouri.*—A technique has been developed for the microtomy of metallic films evaporated on glass which yields a profile view (perpendicular to evaporating direction) of sectioned metallic film. The essential technique includes choice of both proper transfer and embedding materials. Micrographs showing thickness structure of bismuth films are presented.

3. Microstructure of Titanium-Aluminum-Hardened Nickel-Base Alloys. W. C. BIGELOW, J. A. AMY, AND L. O. BROCKWAY, *Department of Chemistry, University of Michigan.*—Electron microscopic studies show that aging the titanium-aluminum hardened nickel base alloys, such as Inconel-X, Waspalloy, and Udimet, at temperatures of 1200° to 1600°F produces a fine dispersion of a precipitate particle within the matrix grains. The identity of these particles and their influence on the metallurgical properties of the alloys will be discussed.

4. The Use of Carbon Replicas in Electron Microscopic Studies of Magnesium Alloys. C. A. MOE, *Electron Microscopist, Metallurgical Laboratories, Dow Chemical Company.*—A modified version of Bradley's[1] carbon replica technique has been developed for replicating magnesium and magnesium alloy surfaces. This modified technique consists of preparing a polystyrene block negative, evaporating carbon onto this, and removing the positive carbon replicas by dissolution of the polystyrene in ethyl bromide. This procedure is less complicated and introduces less strain in the replicas than the technique proposed by Bradley. Very thin carbon replicas (<100 A) are stronger under intense electron bombardment than silica films of comparable thickness. It was possible to resolve particles down to 50 A without shadowing.

[1] D. E. Bradley, "A high-resolution evaporated-carbon replica technique for the electron microscope," J. Inst. Metals (September, 1954).

5. Electron Microscope and Electron Diffraction Studies of Vanadiferous Clays from the Colorado Plateau. EDWARD J. DWORNIK* AND MARTIN S. TISCHLER, *U. S. Geological Survey, Washington 25, D. C.*—A suite of chemically analyzed vanadium-bearing clays was studied to determine whether the vanadium was structurally held or occurred as a separate mineral phase. Systematic study of each sample was made by both electron microscopy and electron diffraction methods. Electron micrographs, selected area diffraction patterns, and study of calculated interplanar spacings indicate that the vanadium is present as an integral part of the clay mineral structure.

6. Interpretation of Transmission Electron Diffraction Spot Patterns of Certain Monoclinic Crystals. MALCOLM ROSS, *U. S. Geological Survey, Washington 25, D. C.*—A method has been devised for interpreting transmission electron diffraction spot patterns of monoclinic crystals which orient with two crystallographic axes parallel to the specimen mount. Patterns of $KClO_3$ ($\beta = 109° 38'$) were obtained from specimens which crystallized with the (001) face parallel to the substrate. Analysis of these patterns shows that they represent a projection of the a^* b^* reciprocal net plane. This projection foreshortens the spot pattern in the a^* direction causing the apparent d_{100} to be equal to a_0. As a result the a and b unit cell constants may be determined directly from

measurements of these diffraction patterns. Colemanite ($2CaO \cdot 3B_2O_3 \cdot 5H_2O$, $\beta = 110° 7'$) has perfect 010 cleavage. Spot patterns of this mineral give directly the d_{200}, d_{001}, and β^* angle. These patterns thus represent the a^* c^* reciprocal net plane.

7. Comparator for Measuring Electron Diffraction Patterns. C. Poehlman and L. M. Niebylski, *Research Laboratories, Ethyl Corporation, Detroit, Michigan,* and W. C. Bigelow, *Department of Chemistry, University of Michigan, Ann Arbor, Michigan.*—A comparator has been designed especially for measuring electron diffraction patterns. This instrument incorporates a rotating stage for carrying the diffraction pattern to permit the pattern to be rotated during measurement. It is therefore particularly well suited for measuring patterns of spots or discontinuous rings such as are frequently obtained by reflection from surfaces and by selected area diffraction techniques. The details of the design will be described and the performance of the instrument will be discussed.

8. Techniques in the Electron Micrography of Storage Battery Plates and of Finely Ground Carbons. G. L. Clark, A. E. Vatter, and G. W. Bailey, *Department of Chemistry and Chemical Engineering and Electron Microscope Laboratory, University of Illinois, Urbana, Illinois.*—Successful electron micrographs of spongy storage battery plates, cured, formed, and discharged, have been obtained for the first time by the carbon replica technique. Other methods of replication and of sectioning are described and compared. The very spectacular results are illustrated with examples. A series of powdered graphite samples ground up to 144 hours is investigated by a sectioning technique of a polymerized dispersing medium made with the new Swedish microtome. These results are compared with micrographs of carbon blacks and with x-ray diffraction patterns to indicate clearly the stages of deterioration in crystalline arrangement. The persistence of crystalline forms even in extreme cases of deterioration are clearly indicated. The superiority of the impregnation and sectioning technique for carbons over earlier techniques is illustrated.

9. On the Electron Microscopy of Air-Borne Particles.† H. Froula,* A. F. Bush, and E. S. C. Bowler, *University of California, Department of Engineering, Los Angeles 24, California.*—A description is given of thermal precipitation methods used by the authors in the collection of air-borne particles for electron microscopy. Results of the microscopical study are presented in terms of particle counts and particle-size distributions for samples obtained from the open atmosphere and from various sources of pollutants. Consideration is given to the nature of collected particles and to the problem of establishing a numerical balance between the number of particles in a local atmosphere and the number of particles from local sources.

† Sponsored in part by the following University of California sources: Institute of Geophysics Research Grants, Department of Engineering Research Grants, and Sanitary Engineering Research Project.

10. Submicroscopic Structure of Polyethylene. G. C. Claver, *Monsanto Chemical Company, Plastics Division, Springfield, Massachusetts.*—Through electron micrographs and sample preparative techniques it is shown that structure in polyethylene heretofore reported as fibrillar is in reality small platelets. It is further shown that the arrangement of these platelets can be altered markedly by various preparative procedures. The differences observed in microstructure of various commercial polyethylene is thought to be related to molecular weight and/or degree of branching of the polymer molecule. The dimensions of polyethylene microstructure as measured on electron micrographs are compared to those obtained by light scattering techniques on solid material.

11. Use of Monodisperse Latexes in an Electron Microscope Investigation of the Mechanism of Emulsion Polymerization. E. B. Bradford,* J. W. Vanderhoff, T. Alfrey, Jr., and J. F. Vitkuske, *Physical Research Laboratory, The Dow Chemical Company, Midland, Michigan.*—Monodisperse polystyrene latexes are useful in electron microscope investigations of the mechanism of emulsion polymerization: (1) as calibration standards in particle diameter determinations, and (2) in determining the relative rates of growth of different size particles, and the effect of varying emulsifier concentration in seeded emulsion polymerizations. Previously measured monodisperse latexes, dispersed on a substrate along with the particles to be measured, were used as a calibration standard. The accuracy, reproducibility, and limitations of this method of measurement are discussed. The relative rates of growth of different size particles in a seeded emulsion polymerization were determined by polymerizing monomer in a seed latex comprised of a mixture of two monodisperse latexes. The total particle volume increase was in stoichiometric agreement with the volume of added monomer. A mathematically derived relationship of relative particle growth is presented. The effect of varying emulsifier concentration is shown. Too high concentrations yield "new" particles, and too low concentrations result in excessive coagulum.

12. Electron Microscope Studies of Silicon Produced by Vapor Phase Decomposition. Alvin E. Bills,* Robert Lefker, and William F. Nye, *Signal Corps Engineering Laboratories, Fort Monmouth, New Jersey.*—Electron microscope studies of silicon samples formed by vapor phase decomposition of silicon compounds, primarily halides, have revealed a variety of morphologies. The silicon thus produced occurs as fibrous and acicular crystallites, prismatic particles, euhedral and subhedral platelets, or chained spheroids resembling "structure" carbon black. The majority of the products of these reactions appear, visually, as spiny masses of blue-gray needles. Other states are discernible through differences in color and texture. Morphologies are distinguishable as characteristic to the particular state from which they come.

Session B. Contributed Biological Papers

13. Electron Microscopic Researches during 1954–1955 at the Department of Anatomy, Nara Medical College, Naraken, Japan. G. Yasuzumi, *Department of Anatomy, Nara Medical College, Naraken, Japan.*—The work of the Electron Microscope Laboratory at the Department of Anatomy, Nara Medical College, Naraken, Japan, will be reported briefly. It includes the following: A comparative study between Kinocili, stereocilia and sperm-tails; helical structure of euchromatic bands and interband filaments in salivary gland chromosomes of *Drosophila melanogaster;*

double helical structure of mitotic chromosomes and its significance in ganglion cell nuclei of *Drosophila virilis;* spermiogenesis of albino rat, sparrow, and *Drosophila melanogaster.* The observations have been performed with Shimazu's electron microscope (50–80 kv) and Shimazu's microtome provided with a glass knife.

14. Fine Structure of Alveoli and of Bronchiolar Epithelial Cells of Normal Mouse Lung. H. E. KARRER, *Johns Hopkins University, Baltimore, Maryland.*—The alveoli of lungs fixed by intratracheal infusion of osmium tetraoxide were uncollapsed. Specimens embedded by polymerization at 80°C appeared to be much better preserved than those embedded at 45°C. The epithelium of alveoli appears to be an uninterrupted layer of thin cells. The endothelial cells of capillaries may be as thin as 100° A. The fine structure of the basement membrane will be discussed. The nonciliated cells of terminal bronchioles contain numerous characteristic, apparently spherical, mitochondria and an extensive system of cytoplasmic membranes (endoplasmic reticulum).

15. An Electron Microscope Study of the Epidermis of Mammalian Skin in Thin Sections. II. Superficial Cell Layers. CECILY CANNAN SELBY,† *Sloan-Kettering Institute for Cancer Research, New York 21, New York.*—The fine structure of cytoplasmic filaments and intercellular bridges in the *stratum granulosum, stratum lucidum,* and *stratum corneum* of human skin will be described. Similar studies on the dermo-epidermal junction and basal cell layer have already been reported.[1] Some specimens were stained in 1% phosphotungstic acid (PTA), following the usual osmium fixation, to increase the electron density of fibrous components. Cytoplasmic filaments < 100 A in diameter, and believed to represent the fibrous keratin-like protein "epidermin," are more densely packed and organized into fibers in the "prickle" and granular than in the basal cell layers. They increase in diameter and decrease in density in the *stratum lucidum,* while in the *stratum corneum* the solid masses of keratin show no filamentous fine structure within the resolution limits of this study. Intercellular bridges, consisting of two electron-dense areas separated by a constant-diameter, less-dense space, are found in all cell layers. Cytoplasmic filaments are attached to the dense areas (shaped like narrow disks) but do not cross through the space between the disks separating one cell from the other. Cell membranes are still visible in the *stratum corneum,* separating the keratin of one cell area from that of the other and possessing regularly spaced densities which are matched by corresponding densities of adjacent cells but separated from them by a space which is narrower than that in intercellular bridges of the lower cell layers. These observations will be correlated, as much as possible, with known properties of epidermin and keratin and histochemical studies of skin.

† Present address: Department of Anatomy, Cornell Medical School, New York 21, New York.
[1] J. Biophys. and Biochem. Cyt. (to be published, October, 1955).

16. Electron Microscopy of Thin Sections of Yeast. HILDA D. AGAR* AND H. C. DOUGLAS, *Department of Microbiology, University of Washington School of Medicine, Seattle 5, Washington.*—Section of a tetraploid Saccharomyces, prepared from cells grown on glucose yeast extract medium, yield good detail of cell wall, bud, and birth scar structure but are unsuitable for study of internal cellular details.[1] Sections prepared from cells grown on Lindegren's presporulation medium[2] are more satisfactory for this purpose. The cell wall is a laminated structure composed of several distinct layers. Adjacent to the inner layer of the cell wall is a thin, sinuate structure bounding the cytoplasm which we interpret as the cytoplasmic membrane. Oriented peripherally in the cytoplasm in close proximity to the cytoplasmic membrane are rod-shaped (1×0.25 micron) and ovoid (0.3×0.2 micron) structures which possess the characteristic "cristae mitochondriales" described for mitochondria from many sources. Two larger bodies surrounded by double membranes are observed in the cytoplasm. The smaller of these is approximately the same diameter (1.5 microns) as the nucleus in stained unsectioned cells.[3]

[1] Agar and Douglas, J. Bacteriol. (to be published).
[2] C. C. Lindegren, *The Yeast Cell, Its Genetics and Cytology* (St. Louis Educational Publishers, 1949).
[3] D. C. Hawthorne, *Genetics* (to be published, 1955).

17. Electron Microscope Study of Bacterial Phagocytosis by Human Leucocytes. JOSEPH R. GOODMAN, ROGER E. MOORE, AND RICHARD F. BAKER, *Investigative Medicine Service, Veterans Administration Hospital, Long Beach, California, and the Department of Experimental Medicine, School of Medicine, University of Southern California, Los Angeles, California.*—Techniques of ultrathin sectioning of human leucocytes were used to examine the relationship between leucocytes and ingested bacteria. Virulent and nonvirulent strains of *Staphylococcus* were mixed with suspensions of human buffy coat and incubated at 37°C. Aliquots were removed at 5-min, 15-min, 30-min, 1-hr, and 2-hr intervals for fixation, dehydration, embedding, and sectioning. Bacteria were observed on the surface of the neutrophils and in various stages of phagocytosis. The osmophilia of the nonvirulent organisms decreased as the bacteria were digested. Vacuolation developed within the bacteria during digestion and the bacterial cell wall was one of the last identifiable structures. The virulent strain ingested by the neutrophils resulted in the development of vacuoles around the bacteria, a retention of their osmophilia, and some bacterial fission within the cytoplasm. Continued growth of the bacteria resulted in large vacuoles in the neutrophils with subsequent rupture and eventual destruction of the leucocyte. Lymphocytes present in the suspension were apparently unaffected during the 2-hr incubation.

18. A Filamentous Macromolecular Component of Meiotic Chromosomes. EDUARDO DE ROBERTIS AND HUMBERTO CASAROTTI, *Department of Cell Ultrastructure, Instituto de Investigación de Ciencias Biológicas.*—High-resolution electronmicrographs of thin sections of the testicular follicles of a locust of the genus *Aleuas* have been obtained. Within the nuclei of primary spermatocytes the areas corresponding to chromosomes in different stages of the meiotic prophase and metaphase have been identified. This preliminary report is intended to give a description of a filamentous macromolecular component visualized within those areas and which seems to constitute the bulk of the chromosomic material. These filaments are irregularly coiled, describing tight gyri and undulations. Their length cannot be determined because of the thinness of the section, but they certainly must be several thousand angstroms or more in length. The thickness of these filaments seems to vary with different stages of the prophase and metaphase. In an early prophase a considerable proportion of filaments are 28 ± 7 A in diameter and the thicker ones are 84 A ± 7 A. In the metaphase chromosomes the filaments are definitely thicker, varying between 60 and 170 A with a mean of 100 A. In all the spaces interspersed among the prophasic chromosomes and near the nuclear membrane another component can be recognized. This is composed of dense particles and short threads of 100 to 240 in diameter (mean of 160 A). Evidence will be presented that similar dense particles can be observed within granules resulting from the activity (or disintegra-

tion) of the nucleolus. Our finding of a macromolecular filamentous component of chromosomes will be discussed on the basis of the existing literature about electronmicroscopy of nucleoproteins and nucleic acids. This correlation leads to the suggestion that the thinnest chromosomic filaments (28 ±7 A) represent single desoxyribonucleoprotein molecules.

19. Preparation of Self-Supporting Monomolecular Protein Films.† RICHARD E. HARTMAN AND ROBERTA S. HARTMAN, *Virus Laboratory, Department of Epidemiology, School of Public Health, University of Michigan, Ann Arbor, Michigan.*—The loss of contrast and the introduction of extraneous structure which results from the use of supporting membranes in electron microscopy makes it desirable when possible to use specimens which are capable of self-support. It has been found that monomolecular protein films transferred to membranes are self-supporting over holes in the membranes provided these holes have diameters of one micron or less. Such preparations can be examined without further treatment or can be first shadowed or stained with osmic acid. Electron micrographs of such preparations show structures comparable in size to the molecular dimensions of the protein, as obtained by other methods. Fine structure is also observed which appears to be limited primarily by photographic artifact at levels of the order of 10 a.u. Representative electron micrographs selected to demonstrate applications of the technique will be shown.

† Aided by a grant from the National Foundation for Infantile Paralysis, Inc.

20. Serial Sectioning in Analysis of Fine Cell Structure.† HELEN GAY, *Department of Genetics, Carnegie Institution, Cold Spring Harbor, Long Island, New York.*—The method of serial sectioning for electron microscopy has facilitated determination of the three-dimensional structural configurations of individual cellular organelles and has revealed their associations and interrelations with other cellular structures. By way of illustration, the continuity afforded by serial sections has permitted identification in salivary-gland cells of *Drosophila* of an association between chromosomes and outpocketings of the nuclear membrane. This has led to formulation of a mechanism for nucleocytoplasmic interchange in which segments of the nuclear membrane lying in association with specific chromosomal regions are detached into the cytosome together with materials of nuclear origin. Reconstruction of three-dimensional models of the endoplasmic reticulum and secretion granules in these cells has afforded evidence about their interrelations and, indirectly, about their possible method of origination. Serial sections of intact cells and smears of salivary-gland chromosomes have revealed structural patterns indicating that the chromosomes consist of a hierarchical array of pairs of intertwined pairs of chromonemata.

† This research was supported in part by a research grant (RG-149) from the National Institutes of Health, U. S. Public Health Service, to Dr. Berwind P. Kaufmann.

21. Effects of the Microtome Knife and the Electron Beam on Thin Sections of Methacrylate Embedded Tissue. COUNCILMAN MORGAN,* DAN H. MOORE, AND HARRY M. ROSE, *Departments of Microbiology and Medicine, College of Physicians and Surgeons, Columbia University, New York.*—Impact of the microtome knife produces variable compression, gouging, and scratching of sections. Comparison of sections examined in the electron microscope at low beam intensity and at the intensities commonly employed indicates that extensive sublimation and limited flow of the methacrylate obliterates or masks much of the distortion caused by the knife. Some interpretations of serial sections based on the foregoing observations will be discussed.

22. Phase Contrast Microscope Study of Gross Structural Changes Occurring during the Preparation of Cells for Thin Sectioning by Means of the Methacrylate Embedding Technique.† EMIL BORYSKO, *Department of Pathobiology, Johns Hopkins University School of Hygiene and Public Health, Baltimore, Maryland.*—The appearance of living cells, grown in tissue culture, was compared with the appearance of the same cells after each phase of processing. Gross changes were not observed after fixation. Dehydration with ethanol produced a general shrinkage, large spherical cells suffering a decrease in volume of as much as 30%. However, there did not appear to be any destruction of cytological detail during dehydration. The most severe changes occurred during the polymerization of the embedding matrix when a polymerization temperature of 45°C was employed. Damage during polymerization had the following characteristics: 1. It varied in degree from one preparation to the next. Some preparations were not visibly damaged while others were completely destroyed. 2. It varied in degree within the same preparation. Nucleoli in a single cell were completely destroyed while nucleoli in neighboring cells appeared to be well preserved. 3. It always took the form of a swelling of the cells. In some preparations, nuclei increased in volume by 114%. 4. Neither the occurrence nor the degree of damage were affected by alterations in the treatment of the specimens prior to the polymerization of the embedding matrix. The pattern of damage could be altered only by changing the conditions of polymerization. It was found that the use of high polymerization temperatures (60–80°C) minimized the damage. Optical and electron micrographs will be present illustrating damage phenomenon and the successful results obtained when high polymerization temperatures were used.

† Based on doctoral dissertation. Work supported by The Damon Runyon Memorial Fund for Cancer Research.

23. Hypothesis for the Mechanism of Polymerization Damage Occurring during the Embedding of Cells in Methacrylates.† EMIL BORYSKO, *Department of Pathobiology, Johns Hopkins University School of Hygiene and Public Health, Baltimore, Maryland.*—The observed characteristics of polymerization damage and the known changes in the physical properties of methacrylates taking place during polymerization permit the formation of the following hypothesis for the mechanism of polymerization damage. During polymerization, there is a decrease in volume of the methacrylate of about 15%. However, polymerization does not proceed at a uniform rate throughout the embedding mass, resulting in local variations in the rate of contraction within the matrix. Hence, internal forces are set up in the hardening mass which mechanically disrupt the cells. By using a high polymerization temperature, the polymerizing mass is maintained in a "fluid" state by virtue of its thermoplastic nature. In this condition, internal stresses can be relieved by flow, minimizing damage to the cells. The hypothesis will be illustrated diagrammatically and applied to explain various damage phenomenon.

† Based on doctoral dissertation. Work supported by The Damon Runyon Memorial Fund for Cancer Research.

THURSDAY AFTERNOON

Contributed Papers

24. An X-Ray Microscope. W. A. LADD,* *Ladd Research Industries, Inc., Roslyn Heights, New York,* W. M. HESS, *Columbian Carbon Company, New York, New York,* AND M. W. LADD, *Guggenheim Foundation, Institute of Dental Research, New York, New York.*—High-resolution x-ray micrographs have been obtained by combining the high penetrating power of x-rays with the high resolving power of the electron microscope. The technique involves making relief images in crystals or plastics by means of x-rays. From these, suitable replicas then can be taken for electron microscope examination. X-ray micrographs of carbon-black particles showing variation in dispersion have been obtained at useful magnifications of 10 000 to 25 000 diameters. The overlapping of lead particles and structural differences indiscernible in either light or electron micrographs have been demonstrated. Specimens now can be examined in air or growing media, thus eliminating the desiccating and destructive effects caused by the high vacuum and electron beam of the electron microscope.

25. Modification of the RCA EMU Electron Microscope for X-Ray Microscopy. BENJAMIN M. SIEGEL* AND KENNETH C. KNOWLTON, *Department of Engineering Physics, Cornell University, Ithaca, New York.*—An RCA EMU-2B electron microscope has been modified so that it may be used alternately as an x-ray projection microscope operating at a series of voltages from 6 to 16.7 kv. The electron gun, condenser lens, and objective lens of the electron microscope form the electron optical components of the x-ray microscope. The intermediate lens and bellows are removed, and the space between objective and projector lens accommodates a special holder for x-ray target and specimens, as well as the fluorescent screen for focusing and the photographic plate for recording the image. The electron gun geometry has been modified to produce a source of adequate brightness for exposure times of 5 to 10 minutes at magnification of 50–100 ×. With the appropriate switches installed, the conversion from an electron to x-ray microscope may be accomplished in fifteen minutes. A resolution of better than 1 micron is obtained.

26. Modification of the RCA Model B for X-Ray Microanalysis. R. M. FISHER AND H. E. KNECHTEL, *U. S. Steel.*—Progress on the modification of an RCA Model B electron microscope for microanalysis by point-probe x-ray emission spectroscopy will be discussed. The description will include the specimen holder and stage mechanism, optical viewing system, focusing of electron probe, and detection and analysis of emitted x-rays.

Symposium on Electron Optics

CHAIRMAN: CECIL E. HALL, *Department of Biology, Massachusetts Institute of Technology, Cambridge, Massachusetts*

SPEAKERS: W. GLASER, *Farrand Optical Company, New York, New York.* **Instrumental Limitations to Resolution**

L. A. MARTON, *National Bureau of Standards, Washington, D. C.* **Limitations on Resolution Imposed by Interaction of Electrons with Specimen**

FRIDAY MORNING

Symposium on Preservation and Interpretation of Structure in Biological Materials

CHAIRMAN: FRANCIS O. SCHMITT, *Department of Biology, Massachusetts Institute of Technology, Cambridge, Massachusetts*

SPEAKERS: FRITIOF SJOSTRAND, *Karolinska Institute, Stockholm, Sweden*

ALBERT J. DALTON, *National Institutes of Health, Bethesda, Maryland*

BETTY BEN GEREN, *Childrens Medical Center, Boston, Massachusetts*

Invited Lecture

27. Speculations Concerning Some Approaches to the Development of Histochemical Methods for Electron Microscopy. ARNOLD M. SELIGMAN, *Johns Hopkins University School of Medicine.*—(Invited lecture and discussion —1 hour.)

FRIDAY AFTERNOON

Symposium on Emission Microscopy

CHAIRMAN: T. F. ANDERSON, *University of Pennsylvania Hospital, Philadelphia, Pennsylvania*

SPEAKERS: E. W. MÜLLER, *Pennsylvania State University, University Park, Pennsylvania*
R. D. HEIDENREICH, *Bell Telephone Laboratories, Inc., Murray Hill, New Jersey*
R. GOMER, *University of Chicago, Chicago, Illinois*

Annual Business Meeting, Assembly Hall, Hetzel Union Building

Reception, Elks Club, University Park, Pennsylvania

Annual Banquet, Ballroom, Hetzel Union Building

SATURDAY MORNING

Contributed Papers

28. Structure and Development of Influenza Virus in Cells of Chick Chorioallantoic Membranes Examined in Ultrathin Sections. COUNCILMAN MORGAN,* HARRY M. ROSE, AND DAN H. MOORE, *Departments of Microbiology and Medicine, College of Physicians and Surgeons, Columbia University, New York.*—Influenza virus has been observed at various stages of development from 6 to 44 hours after infection. Rods and spheres could be identified. The spheres appeared to develop at the cell surface, either within dense amorphous material or from cytoplasmic extensions of variable length. The rods also formed at the cell surface. Both spheres and rods were composed of granular material enclosed by a dense, sharply defined membrane and a diffuse, amorphous peripheral zone. No particles considered to be virus were encountered either in the cytoplasm or the nuclei of host cells. Nor were specific changes in the cytoplasm observed.

29. Some Effects of Oncolytic and Other Viruses on Ehrlich Ascites Tumor Cells. MARLENE FRIEDLAENDER,* DAN H. MOORE, AND HILARY KOPROWSKI, *Department of Microbiology, College of Physicians and Surgeons, Columbia University, New York, and Lederle Laboratories Division, American Cyanamid Company, Pearl River, New York.*—Ehrlich ascites mouse tumor cells were used as host, and a preliminary report will be given of some results of infection with mengo, anopheles A, neurotropic influenza and different strains of Newcastle Disease virus, respectively. The first two viruses lyse the cell, the most virulent, Mengo, causing cellular breakdown within 24 hours, whereas influenza virus multiply but do not destroy the cell. Problems of identification, morphological characteristics, and virus location will be discussed.

30. Stages in the Development of a Polyhedral Virus Disease. M. F. DAY, J. L. FARRANT, AND CORALIE POTTER, *Division of Entomology, C.S.I.R.O., Canberra and Chemical Physics Section, Division of Industrial Chemistry, C.S.I.R.O., Melbourne, Australia.*—Studies of a nuclear polyhedral disease of an Australian pasture caterpillar *Pterolocera amplicornis* have established the sequence of events leading to polyhedron formation and have revealed several features hitherto unobserved in polyhedroses. The elementary virus rods proliferate within the chromatin mass which releases rods into the nuclear sap where enveloping membranes are deposited about them. These membraneous envelopes contain up to six rods, even numbers occurring with twice the frequency of odd numbers, suggesting that virus multiplication continues after encapsulation. Polyhedron formation then occurs by deposition of protein about the encapsulated virus particles. In thin sections the crystal lattice of the polyhedral protein has been resolved and the virus rods have been shown to contain an axial concentration of dense material.

31. Electron Microscopic Study of Dispersion in Virus Particle Suspensions. D. GORDON SHARP,* *Biophysicist, Department of Surgery,* AND M. J. BUCKINGHAM, *Department of Physics, Duke University, Durham, North Carolina.*—Inherent in the method of counting virus particles by direct sedimentation is the possibility of determining their state of dispersion as well. Little information is available on this subject although many anomalies in sedimentation rate analyses and certain discrepancies between biological results and particle count by other methods have been attributed to aggregation. The method is briefly that of sedimenting virus from a dilute suspension directly upon agar. On pseudoreplicas from such surfaces, single particles, pairs, triplets, etc., can be counted. These various numbers, expressed as fractions of the total number of particles, are then compared with analogous numbers calculated from the probability that they would, by chance, fall that way. The degree of aggregation which existed in the suspension can then be expressed as a dispersion coefficient. Dispersion coefficients for virus in plasma and in various buffers are given, as well as time changes in the coefficient for virus in the presence of specific antiserum.

32. Structural and Functional Differentiation in T2 Bacteriophage. ROBLEY C. WILLIAMS AND DEAN FRASER, *Virus Laboratory, University of California, Berkeley, California.*—Structural components of T2 bacteriophage have

been disunited in order to investigate the morphology of the parts and to establish their function in the adsorption stage of bacterial invasion. The phage have been disjoined by treatment to alternate freezing and thawing and released DNA enzymatically degraded. Separate, identifiable components are: intact heads, intact tails, ghosted heads, a central tail element termed the "core," appendages of the tail called "fibers," and broken sections of the tail resembling perforated discs. The intact tails and the tail fibers adsorb to sensitive bacteria. The intact and ghosted heads and the cores do not adsorb. It is postulated that the tail fibers are the structures responsible for the primary stage of adsorption of phage to bacteria.

33. Ultrastructure of Maize Chloroplasts. A. J. Hodge, J. D. McLean, and F. V. Mercer, *Chemical Physics Section, Division of Industrial Chemistry, C.S.I.R.O., Melbourne, and Botany Department, Sydney University, Sydney, Australia.*—The parenchyma sheath chloroplasts of maize (*Zea mays*) are lamellated, devoid of grana, and accumulate large numbers of starch grains in the mature plant. The mesophyll chloroplasts contain typical grana and few starch grains. Both chloroplast types are limited by a thin double membrane. The lamellae in both types are *ca.* 125 A thick and exhibit a characteristic compound structure in thin sections. A thin dense line (P zone) is sandwiched between two less dense layers (L zones), the outer borders of which are edged by thin dense lines (C zones). In the grana, these compound lamellae are stacked with high precision, the spacing being about 125 A, and thin dense intermediate lines (I zones) are situated midway between P zones. These appear to arise by close apposition of the C zones of adjacent lamellae. The P zones of the grana lamellae are continuous with those of the intergrana (stroma) lamellae. In *Zea mays,* the ratio of the number of intergrana to grana lamellae is about 1:2. This is caused by "forking" of the lamellae as they enter the granum, the relationships involved being more complex than those described elsewhere for *Aspidistra.* A model of the structure is proposed in which P zones represent protein layers, L zones mixed lipid layers, and chlorophyll is present as a monolayer over the entire hydrophilic face area of the compound lipoprotein lamellae.

34. Chloroplast Development and a Mechanism of Lamellar Growth. A. J. Hodge, J. D. McLean, and F. V. Mercer, *Chemical Physics Section, Division of Industrial Chemistry, C.S.I.R.O., Melbourne, and Botany Department, Sydney University, Sydney, Australia.*—The structural changes occurring in *Zea mays* chloroplasts during both normal development and recovery from etiolation have been followed by thin-sectioning procedures. The sequence of events is similar for both mesophyll and parenchyma sheath chloroplasts, except that grana appear at an early stage in the former while the latter lack grana at all stages. Lamellae appear to arise by a process involving the "fusion" of small vesicular elements to give closed double-membrane structures. In *Zea,* during normal development, the minute vesicles are aggregated into one or more "dense granular bodies," which often appear "crystalline." Lamellae appear to grow out from these bodies. In etiolated leaves, lamellae are absent, and the granular bodies become quite large, presumably because of inhibition of the "fusion" step, which apparently requires chlorophyll. Lamellae develop rapidly on exposure to light, and subsequent development closely parallels that seen under normal conditions. The plastids of several chlorophyll-deficient *Zea* mutants similarly lack lamellae and contain only vesicular elements. A specialized peripheral zone immediately below the double limiting membrane in *Zea* chloroplasts exhibits faint lamellae which arise by "fusion" of vesicles and, later, after structural modification, are added to the existing system of compound lamellae. A similar "fusion" process has been observed in the cytoplasm of young *Nitella* cells by which large elements of the endoplasmic reticulum are formed from small microsomal vesicles. The observations suggest that such a "fusion" process may represent a general mechanism for the formation of lamellar structures.

35. Electron Microscope Studies of Human Urine. George W. Cochran,* *Utah State Agricultural College, Logan, Utah,* and George M. Fister, *Ogden, Utah.*—Preparations of human urine were made by atomizing urine-polystyrene latex mixtures on 7% agar blocks covered with thin collodion membranes. A two-step procedure was devised to remove the dialyzable components without redistributing the colloids in the microdroplet patterns. Dialysis was initiated by the diffusion of distilled water through the agar and collodion membranes from below for 48 hours. The membranes were floated on the surface of distilled water for an additional 24 hours to complete the dialysis. They were then picked up on specimen screens, shadowed with uranium, and observed in the electron microscope. When known concentrations of polystyrene latex were mixed with urines, the concentrations of urinary colloids could be determined by making particle counts in the microdroplet patterns. At least five types of urinary colloids were found occurring regularly as components of normal urines. Marked changes in the colloids were found in urinary disease.

36. Electron Microscope Study of Mycobacteria in Spinal Fluid of Multiple Sclerosis. Theodor Wanko, *University Clinic of Psychiatry and Neurology, Vienna, Austria.*—The spinal fluid from six cases of multiple sclerosis—ten milliliters each—were fixed with osmic acid[1] and observed under the Siemens Microscope at 100 kv in order to demonstrate the mycobacteria isolated in this disease also by other methods.[2] In every case the spinal fluid was shown to contain mycobacteria ranging in length from 900–4000 mmμ and in thickness from 200–500 mmμ and manifestations of spherical and polygonal forms 200–500 mmμ in diameter adhered and dissociated from the bacteria, sometimes not completely demarcated from one another. Comparing these studies with electron microscope investigations of other authors[3–6] it would appear certain that the bacilli described belong to the group of mycobacteria, and the evidence of developmental phases leads us to suppose that there is a growth cycle in the human central nervous system affected with multiple sclerosis.

[1] G. E. Palade, J. Exptl. Med. **95**, 285 (1952).
[2] Tschabitscher, Wanko, Schinko, and Fust, Schweiz. med. Wochschr. **85**, 556 (1955).
[3] F. J. Bassermann, Beitr. Klin. Tuberk. **113**, 134 (1955); *Probleme der Morphologie, Cytochemie und Wuchsform des Tuberkuloseerregers* (Thieme-Verlag, Stuttgart, 1953).
[4] Brieger, Cosslett, and Glauer, J. Gen. Microbiol. **10**, 294 (1954).
[5] Ruska, Bringmann, Neckel, and Schuster, Z. wiss. Mikroskop. **60**, 425 (1952).
[6] G. H. Werner, Fortschr. Tuberkuloseforsch. Fasc. 5. Bibl. Tuberc. Basel (1951).

Contributed Electron Micrograph Demonstration

37. Fine Structure of the Cortex in Paramecium Multimicronucleatum. (Presented as a demonstration.) ALBERT W. SEDAR[1] AND KEITH R. PORTER, *The Rockefeller Institute for Medical Research, New York 21, New York.*—Micrographs will be displayed to illustrate the three-dimensional relationships of body cortical components in *Paramecium.* The cortex is covered by two closely apposed membranes constituting the pellicle. Beneath the pellicle the plasma membrane is molded into a ridgework forming a pattern of polygons with depressed centers. The trichocysts are located in the centers of the anterior and posterior ridges of each polygon. The cilia, extending singly from the depressed centers of the surface polygons, show two axial and nine peripheral and parallel double filaments embedded in a matrix surrounded by a membrane. At the level of the plasma membrane, the peripheral filaments of the cilium become continuous with its tube-shaped basal body or kinetosome. The kinetodesma connecting the ciliary kinetosomes of the light microscopist is composed of a number of discrete striated fibrils each of which arises independently from a kinetosome of a particular meridional array. A fibrous network of irregular polygons, the infraciliary lattice system, runs roughly parallel to the surface of the animal at the level of the ciliary kinetosomes. The structure corresponding to *cristae mitochondriales* appear as microvilli extending into the matrix of the organelle from the inner member of the paired mitochondrial membrane. The cortical cytoplasm also contains a system of vesicles and a particulate component.

[1] U. S. Public Health Service Research Fellow of the National Cancer Institute. Present address: The Daniel Baugh Institute of Anatomy, Jefferson Medical College, Philadelphia, Pennsylvania.

Author Index to Abstracts †

Agar, H.—16
Alfrey, Jr., T.—11
Amy, J. A.—3
Bailey, G. W.—8
Baker, R. F.—17
Bigelow, W. C.—3, 7
Bills, A. E.—12
Borysko, E.—22, 23
Bowler, E. S. C.—9
Bradford, E. B.—11
Brockway, L. O.—3
Buckingham, M. J.—31
Bush, A. F.—9
Casarotti, H.—18
Clark, G. L.—8
Claver, G. C.—10
Cochran, G. W.—35
Dalton, A. J.—page 8
Day, M. F.—30
De Robertis, E.—18
Douglas, H. C.—16
Dwornik, E. J.—5
Farrant, J.—30
Fisher, R. M.—26
Fister, G. M.—35
Fraser, D.—32
Freeman, M. W.—1
Friedlaender, M.—29
Froula, H.—9
Gay, H.—20
Geren, B. B.—page 8
Glaser, W.—page 8
Gomer, R.—page 8
Goodman, J. R.—17
Hartman, R. E.—19
Hartman, R. S.—19
Heidenreich, R. D.—page 8
Hess, W. M.—24
Hodge, A. J.—33, 34
Karrer, H. E.—14
Knechtel, H. E.—26
Knowlton, K. C.—25
Koprowski, H.—29
Ladd, M. W.—24
Ladd, W. A.—24
Lefker, R.—12
Marton, L. A.—page 8
McLean, J. D.—33, 34
Mercer, F. V.—33, 34
Moe, C. A.—4
Moore, D. H.—21, 28, 29
Moore, R.—17
Morgan, C.—21, 28
Müller, E. W.—page 8
Niebylski, L. M.—7
Nye, W. F.—12
Pohlman, C.—7
Porter, K. R.—37
Potter, C.—30
Rhoads, H. U.—2
Rose, H. M.—21, 28
Ross, M.—6
Sedar, A. W.—37
Selby, C. C.—15
Seligman, A. M.—27
Sharp, D. G.—31
Siegel, B. M.—25
Sjostrand, F.—page 8
Tischler, M. S.—5
Vanderhoff, J. W.—11
Vatter, A. E.—8
Vitkuske, J. F.—11
Wanko, T.—36
Watson, John H. L.—1
Weber, A. H.—2
Williams, R. C.—32
Yasuzumi, G.—13

† Note: Numbers after author's name correspond to number of paper.